MODELLING AND SIMULATION STUDIES OF BULK HETERO-JUNCTION ORGANIC SOLAR CELLS

A **THESIS**

submitted to the



UNIVERSITY of CALICUT

for the award of the degree

of

DOCTOR of PHILOSOPHY

in

PHYSICS

by

DENET DAVIS



OPTO-ELECTRONICS DEVICE SIMULATION RESEARCH LAB

POST GRADUATE and RESEARCH DEPARTMENT of PHYSICS

CHRIST COLLEGE (AUTONOMOUS), IRINJALAKUDA,

THRISSUR, KERALA

November 2025

Dedicated to my family,

For their endless love and support.

Certificate

This is to certify that the thesis titled **"Modelling and Simulation Studies of Bulk Hetero-junction Organic Solar Cells"** submitted by **Denet Davis** to the **University of Calicut** for the award of the degree of **Doctor of Philosophy**, is a bonafide record of the research work done by her under my supervision. The contents of this thesis, in full or in parts, have not been submitted to any other Institute or University for the award of any other degree.

Prof. Dr. Sudheer Sebastian K,
Research Supervisor,
Department of Physics,
Christ College(Autonomous), Irinjalakuda.
680125

Place:

Date:

Declaration

I hereby declare that the work presented in the thesis entitled **"Modelling and Simulation Studies of Bulk Hetero-junction Organic Solar Cells"** is based on the original work done by me under the guidance of **Dr. Sudheer Sebastian K** and has not been included in any other thesis submitted previously for the award of any degree. The contents of the thesis have undergone plagiarism check using **iThenticate**-software at **C.H.M.K. Library, University of Calicut**, and the similarity index is found to be within the permissible limit. I also declare that the thesis is free from AI generated contents.

Denet Davis

Dr. Sudheer Sebastian K

Place:

Date:

Acknowledgements

"My flesh and my heart may fail, but God is the strength of my heart and my portion forever"-says the lord. First and foremost, I would like to express my deepest gratitude to God for strengthening me, with wisdom, and perseverance to complete my dream. Without his blessings, none of this would have been possible.

I am deeply grateful to Dr.Sudheer Sebastian K, Professor and Head, Department of Physics, Christ College (Autonomous) Irinjalakuda, for his unwavering guidance, expertise and support throughout the duration of this endeavor. His mentorship has been invaluable in shaping the direction and execution of this research.

I would like to take this opportunity to express my sincere gratitude to the Christ College Principal and Associate Professor of Department of Physics, Fr. Dr. Jolly Andrews CMI, for his motivational words.

I am also gratful to Dr. Antony Joseph, retired Professor, Department of Physics for his valuable suggestions in the initial stage of my reserach. I would like to sincerely thank Dr. Pradyumnan P P, Professor and Head, Department of Physics, University of Calicut for his support and careful suggestions for my research work. I am also thankful to Dr. Sonia Sunny, Associate Professor, Dept. of Computer Science, Prajyoti Niketan College, Pudukkad.

I thank the management of Christ College (Autonomous), Irinjalakuda for providing the CCRF scholarship for doing my research. I would like to use a special word to extend a heartfelt thanks to Ms. Nithya K S, Ms. Shamna M S, Ms. Kavitha M V, Mr. Ramabadran C D, Mr. Dandapani K R and Mr. Vijay Joy P research scholars of Department of Physics for their constant and valuable support. I would also like to express my sincere gratitude to Ms. Anju Sebastian, Ms. Aswathy P V, Ms. Sikha K simon, research scholars of the Physics Department at Christ College (Autonomous) Irinjalakuda. Their valuable support from the very beginning to the completion of this project, have been incredibly valuable and sincerely appreciated very much.

I take this opportunity to thank the office staff, non teaching staff, the administrative staff, Physics department faculties, physics department lab staff and my dearest juniors from all sectors.

I would like to express my sincere gratitude to Prof. Marc Burgelman of Gent University for generously providing access to the SCAPS-1D simulation software. His commitment to supporting the academic and research community has been invaluable.

I would also like to thank my father K. P. Davis, my mother Sophy Davis, my brother Delphrin Davis, whose endless support and encouragement have been my anchor. I would

like to express my heartfelt gratitude to my grandparents, who continue to watch over me from heaven. I thank for your understanding, patience, and faith in me. Your love and motivation have been crucial during the challenging times. I humbly thank all my cousins and close friends for their motivation throughout this entire journey.

I take this opportunity to thank my relatives, neighbours and my dearest nephews and nieces for just being there as a blessing. I am truly blessed to have a family that always stood with me, in all my ups and downs and strengthened me to give out my best. I extend my sincere gratitude to all those who have helped me for the completion of this project.

Denet Davis

Abstract

Solar cells (SCs), an indispensable energy-harvesting devices, have always been at the forefront of cutting-edge research. Bulk hetero-junction organic solar cells (BHJOSCs) offer a promising pathway for developing affordable, flexible, and customizable solar energy solutions. Extensive research has been carried out in this field to enhance device performance through various design modifications and the implementation of advanced technologies.

Although traditional SCs continue to dominate the market due to their high efficiency, ongoing research to identify novel materials is essential to minimize toxicity, improve durability, and reduce overall degradation. This research primarily focuses on understanding the complexities of existing BHJOSC designs and addressing their major limitations.

Fullerene and non-fullerene acceptor (NFA) materials are considered highly promising candidates for BHJOSCs because of their excellent opto-electronic properties. Their suitable band gap and high absorption capability make them particularly attractive for device optimization. Furthermore, an in-depth investigation into their physical properties and environmental impact is crucial for sustainable development.

The thesis entitled "Modelling and Simulation Studies of Bulk Hetero-junction Organic Solar Cells" explores the design and simulation of BHJOSCs based on P3HT:PCBM, PBDB-T:NCBDT and PBDB-T:INTIC systems. Key parameters such as layer thickness, doping concentration, band gap, temperature, and defect density have been systematically analyzed. The simulation results reveal potential efficiency enhancements through custom- engineered device architectures.

Comprehensive studies were conducted using SCAPS-1D software to identify more efficient and environmentally friendly BHJOSC structures. Special emphasis is placed on the incorporation of graphene derivatives as carrier transport interfacial layers. A novel device structure exhibiting maximum efficiency was designed, where reduced graphene oxide (rGO) demonstrated superior performance as a hole transport layer (HTL).

This research underscores the potential of graphene derivatives in overcoming current challenges and advancing both the efficiency and stability of BHJOSCs

Keywords: Numerical simulation study, organic solar cells, bulk hetero-junction, graphene derivatives

സംഗ്രഹം

സോളാർ സെൽ, പകരംവെക്കാനാകാത്ത ഒരു ഊർജ ശേഖരണ ഉപകരണമെന്ന നിലയിൽ, എപ്പോഴും ശ്രദ്ധാകേന്ദ്രമായ് നിലകൊള്ളുകയും, ഏറ്റവും മുൻനിര ഗവേഷണങ്ങൾക്ക് വഴികാട്ടിയായി മാറുകയും ചെയ്യുന്നു. ബൾക്ക് ഹെറ്ററോ-ജങ്ഷൻ ഓർഗാനിക് സോളാർ സെല്ലുകൾ, കുറഞ്ഞ ചെലവിൽ, സൗകര്യപ്രദവും ഇഷ്ടാനുസൃതവുമായ സോളാർ എനർജി പരിഹാരങ്ങൾ സൃഷ്ടിക്കുന്നതിനുള്ള പ്രതീക്ഷാജനകമായ ഒരു മാർഗമാണ്. ഈ മേഖലയിലെ വ്യാപകമായ ഗവേഷണപ്രവർത്തനങ്ങൾ ഇപ്പോഴും നടന്നുകൊണ്ടിരിക്കുന്നുണ്ട്. ഉപകരണത്തിന്റെ പ്രകടനം മെച്ചപ്പെടുത്തുന്നതിനായി നിരവധി ഡിസൈൻ മാറ്റങ്ങൾ നടപ്പിലാക്കുകയും, ഏറ്റവും പുതിയ സാങ്കേതികവിദ്യകൾ പ്രയോഗിക്കുകയും ചെയ്യുന്നത് ഗവേഷണ സമൂഹത്തിന്റെ ഇടയിൽ വലിയ താത്പര്യം സൃഷ്ടിച്ചിട്ടുണ്ട്. ഉയർന്ന കാര്യക്ഷമതയുള്ളതുകൊണ്ട് പരമ്പരാഗത സോളാർ സെല്ലുകൾ വിപണിയിൽ ആധിപത്യം പുലർത്തുന്നുണ്ടെങ്കിലും, വിഷാംശം കുറയ്ക്കുന്നതിനും ദൈർഘ്യം ഉറപ്പാക്കുന്നതിനും, ദുർബലീകരണം കുറയ്ക്കുന്നതിനുമായി പുതിയ വസ്തുക്കളുടെ ആവശ്യകത ഇപ്പോഴും നിലനില്ക്കുന്നു. നിലവിലുള്ള സാങ്കേതിക രൂപകൽപ്പനകളുടെ സങ്കീർണതകളെയും അവയിലെ പ്രധാനമായ കുറവുകളെയും പഠിക്കുകയെന്നതാണ് ഈ ഗവേഷണത്തിന്റെ പ്രധാന ലക്ഷ്യം.

ബൾക്ക് ഹെറ്ററോ-ജങ്ഷൻ ഓർഗാനിക് സോളാർ സെല്ലുകളുടെ കൂടുതൽ കാര്യക്ഷമവും പരിസ്ഥിതി സൗഹൃദവുമായ ഘടനകൾ കണ്ടെത്താൻ വിശകലനപരമായ പഠനങ്ങൾ ഈ ഗവേഷണത്തിൽ നടത്തിയിട്ടുണ്ട്. ഫുള്ളറീൻ ആക്സപ്റ്റർ വസ്തുക്കളും നോൺ- ഫുള്ളറീൻ ആക്സപ്റ്റർ വസ്തുക്കളും ബൾക്ക് ഹെറ്ററോ-ജങ്ഷൻ ഓർഗാനിക് സോളാർ സെല്ലുകൾക്കായി വളരെ സാധ്യതയുള്ള ഘടകങ്ങൾ ആണ്. അവയുടെ ഉത്തമ ഓപ്റ്റോ-ഇലക്ട്രോണിക് ഗുണങ്ങളാൽ യോജിച്ച ബാൻഡ് ഗ്യാപും മികച്ച പ്രകാശശോഷണ ശേഷിയും ഇവയുടെ പ്രധാന പ്രത്യേകതകളാണ്. വസ്തുക്കളുടെ ഭൗതിക ഗുണങ്ങളും, പരിസ്ഥിതി വ്യത്യാസങ്ങൾക്കും മൂല്യങ്ങൾക്കും ഇടയാക്കുന്ന പ്രത്യാഘാതങ്ങളും വിശദമായി പരിശോധിക്കുന്നത് ഈ ഗവേഷണ പഠനത്തിന് അത്യന്താപേക്ഷിതമാണ്.

ഈ ഗവേഷണം എസ്.സി.എ.പി.എസ് - 1ഡി എന്ന സോഫ്റ്റ്വെയർ ഉപയോഗിച്ച് ബൾക്ക് ഹെറ്ററോ-ജങ്ഷൻ ഓർഗാനിക് സോളാർ സെല്ലുകളുടെ ഡിസൈൻ ചെയ്യലിനെയും സിമുലേഷനിനെയും അടിസ്ഥാനമാക്കിയുള്ളതാണ്. ഞങ്ങളുടെ പഠനത്തിൽ ഉപയോഗിച്ച ഫോട്ടോആക്റ്റീവ് ലെയറുകൾ പി3എച്ച്ടി: പിസിബിഎം, പി.ബി.ഡി.ബി-ടി: എൻ.സി.ബി.ഡി.ടി, പി.ബി.ഡി.ബി-ടി: ഐ.എൻ.ടി.ഐ.സി എന്നിവയാണ്. ചാർജ് ട്രാൻസ്പോർട്ട് ലെയറുകളായി ഗ്രാഫീൻ ഡെറിവേറ്റീവുകൾ ഉൾപ്പെടുത്തുന്നതിന് പ്രത്യേകമായ ശ്രദ്ധ നൽകിയിട്ടുണ്ട്.

ഈ തെസിസ്, പി3എച്ച്ടി: പിസിബിഎം, പിബിഡിബി-ടി: എൻസിബിഡിടി, പിബിഡിബി-ടി: ഐ.എൻ.ടി.ഐ.സി എന്നിവയിൽ അടിസ്ഥാനമാക്കിയുള്ള ബൾക്ക് ഹെറ്ററോ-ജംഗ്ഷൻ ഓർഗാനിക് സോളാർ സെല്ലുകളുടെ പ്രകടനവും ഉപകരണങ്ങളുടെ രൂപകൽപ്പനയും സിമുലേഷൻ ഉപയോഗിച്ച് പരിശോധിക്കുന്നു. ലെയറുകളുടെ കനം, ഡോപ്പിങ് കൺസെൻട്രേഷൻ, ബാൻഡ് ഗാപ്, താപനില, ദോഷ സാന്ദ്രത എന്നീ പ്രധാന ഘടകങ്ങൾ ഈ ഗവേഷണത്തിൽ വിശകലനം ചെയ്യുന്നു. സിമുലേഷനുകൾ, കസ്റ്റം-ഡിസൈൻ ചെയ്ത ഉപകരണങ്ങൾ മുഖേന സാധ്യതയുള്ള പ്രവർത്തനക്ഷമത വർദ്ധനവ് വെളിപ്പെടുത്തുന്നു. കസ്റ്റം ഡിസൈൻ ചെയ്ത ഉപകരണങ്ങളിലൂടെ പ്രകടനത്തിൽ വലിയ മെച്ചപ്പെടൽ സാധ്യമാകുമെന്ന് സിമുലേഷൻ ഫലങ്ങൾ സൂചിപ്പിക്കുന്നു.

ഈ ഗവേഷണം, നിലവിലുള്ള പരിധികളെ മറികടക്കാനും, ബൾക്ക് ഹെറ്ററോ-ജംഗ്ഷൻ ഓർഗാനിക് സോളാർ സെലുകളുടെ പ്രവർത്തനക്ഷമതയും സ്ഥിരതയും മുൻനിർത്താൻ ഗ്രാഫീൻ ദ്രവ്യങ്ങളുടെ സാധ്യതയെ ഉയർത്തുന്നു.

Contents

Acknowledgements i

Abstract iii

1 Introduction 1
- 1.1 Solar Energy . . . 3
- 1.2 Solar Cell . . . 5
  - 1.2.1 Absorption of Light and Generation of Carriers . . . 6
  - 1.2.2 Separation of Generated Carriers . . . 7
  - 1.2.3 Collection of Photogenerated Carriers . . . 7
- 1.3 P-N Junction Semiconductor Theory . . . 7
  - 1.3.1 Working of a P-N Junction . . . 7
- 1.4 Equivalent Circuit of an SC . . . 9
  - 1.4.1 Short Circuit Current Density . . . 11
  - 1.4.2 Open Circuit Voltage . . . 12
  - 1.4.3 Fill Factor . . . 12
  - 1.4.4 Power Conversion Efficiency . . . 13
  - 1.4.5 Quantum Efficiency . . . 14
- 1.5 Different Recombination Mechanisms . . . 15
  - 1.5.1 Band to Band Recombination (Radiative Recombination) . . . 15
  - 1.5.2 Trap Assisted Recombination (Shockley-Read-Hall Recombination) . . . 16
  - 1.5.3 Auger Recombination . . . 17
  - 1.5.4 Surface Recombination . . . 18
- 1.6 Understanding Light-Matter Interaction in SCs . . . 18
  - 1.6.1 Electromagnetic Waves . . . 18
  - 1.6.2 Optics and Absorption . . . 20
- 1.7 Fundamental Semiconductor Equations Solved in an SC . . . 22
  - 1.7.1 Poisson's Equation . . . 23
  - 1.7.2 Continuity Equations . . . 23
  - 1.7.3 Drift-Diffusion Current Equations . . . 24
    - 1.7.3.1 Drift Current Inside an SC . . . 24

1.7.3.2 Diffusion Current Inside an SC . . . 26
1.7.3.3 Total Current Density in an SC . . . 26
1.8 History of SCs . . . 27
1.9 Different Types of SCs . . . 28
1.9.1 First Generation SCs . . . 28
1.9.2 Second Generation SCs . . . 29
1.9.2.1 Amorphous Silicon SC . . . 29
1.9.2.2 Copper Indium Gallium Selenide SC . . . 30
1.9.2.3 Cadmium Telluride SC . . . 31
1.9.3 Third Generation SCs . . . 31
1.9.3.1 Copper Zinc Tin Sulfide SC . . . 32
1.9.3.2 Gallium Arsenide SC . . . 32
1.9.3.3 Organic SC . . . 33
1.9.3.4 Perovskite SC . . . 34
1.9.3.5 Quantum Dot SC . . . 34
1.9.3.6 Dye Sensitized SC . . . 36
1.9.3.7 Multi-Junction SC . . . 36
1.9.3.8 Hybrid SC . . . 37
1.9.3.9 Carbon NanoTube SC . . . 37
1.9.4 Fourth Generation SCs . . . 39
1.9.4.1 Graphene Derivatives Based SCs . . . 39

2 Bulk Hetero-Junction Organic Solar Cells 42
2.1 OSCs-Their Significance and Advantages . . . 43
2.2 Organic Semiconductors . . . 44
2.2.1 Major Classes of Organic Semiconductors . . . 44
2.2.2 Fundamental Structure and Properties of Organic Semiconductors . . . 47
2.2.3 Charge Transport Mechanisms in Organic Semiconductors . . . 48
2.3 The Operational Mechanism of OSCs . . . 48
2.4 History of OSCs . . . 49
2.4.1 Major Types of OSCs . . . 51
2.4.1.1 Single Layer OSC . . . 51
2.4.1.2 Bilayer Hetero-Junction OSC . . . 51
2.4.1.3 Bulk Hetero-Junction OSC . . . 53
2.4.1.4 Ternary Blend OSC . . . 53
2.4.1.5 Tandem OSC . . . 54
2.4.1.6 Organic DSSC . . . 54
2.5 Bulk Hetero-Junction OSC . . . 55
2.5.1 Layers of BHJOSC . . . 55
2.5.1.1 Active Layer . . . 55
2.5.1.2 Electron Transport Layer . . . 56
2.5.1.3 Hole Transport Layer . . . 57
2.5.1.4 Electrodes . . . 57
2.5.2 Fundamental Principle of BHJOSC . . . 57

2.5.3 Historical Timeline of BHJOSCs . . . 59
2.5.4 Structural Variants of BHJOSCs . . . 60

3 Graphene Derivatives in Bulk Hetero-Junction Organic Solar Cells 62
3.1 Graphene and its Derivatives:Familiarization of the Wonder Material . . . 63
3.2 Important Graphene Derivatives in BHJOSCs . . . 64
3.2.1 Graphene Oxide . . . 65
3.2.2 Reduced Graphene Oxide . . . 66
3.2.3 Graphene Quantum Dots . . . 66
3.2.4 Doped Graphene Derivatives . . . 67
3.3 Graphene Derivatives in BHJOSCs:Enhancing Efficiency . . . 68
3.3.1 Graphene Derivatives as an Anode Material in BHJOSCs . . . 68
3.3.2 Graphene Derivatives as a Cathode Material in BHJOSCs . . . 69
3.3.3 Graphene Derivatives as an HTL in BHJOSCs . . . 70
3.3.4 Graphene Derivatives as an ETL in BHJOSCs . . . 71
3.3.5 Graphene Derivatives as a Photoactive Material in BHJOSCs . . . 73

4 Methodology for Device Modelling and Simulation:SCAPS-1D 76
4.1 Basic Semiconductor Equations Solved in SCAPS-1D . . . 77
4.1.1 Poisson's Equations . . . 77
4.1.2 Continuity Equations . . . 78
4.2 Steps and Analysis Performed using SCAPS-1D . . . 80
4.3 Basic Operation of SCAPS-1D . . . 82
4.3.1 The Working of SCAPS-1D . . . 88
4.4 Limitations of SCAPS-1D . . . 90

5 Numerical Investigation of P3HT:PCBM BHJOSC with Diverse Graphene Derivative HTLs and ETLs 92
5.1 P3HT:PCBM BHJOSCs . . . 94
5.2 Numerical Investigation of P3HT:PCBM BHJOSC with Graphene as an HTL 95
5.2.1 Study of P3HT:PCBM BHJOSC with Graphene as HTL, PDINO and PFN-Br as ETLs . . . 99
5.2.1.1 Influence of Thickness Variation of Active Layer on the Device Performance of Structures I and II . . . 100
5.2.1.2 Influence of Electron Mobility and Hole Mobility Variation in Active Layer on the Device Performance of Structures I and II . . . 102
5.2.1.3 Influence of Defect Density Variation in P3HT:PCBM on the Device Performance of Structures I and II . . . 105
5.2.2 Numerical Investigation of Active Layer BHJOSC with Graphene as HTL, ZnO and TiO_2 as ETLs . . . 106
5.2.2.1 Influence of Thickness Variation of Active Layer on the Device Performance of Structures III and IV . . . 106

5.2.2.2 Influence of Electron Mobility and Hole Mobility Variation in Active Layer on the Device Performance of Structures III and IV . . . 109
5.2.2.3 Influence of Defect Density Variation in Active Layer on the Device Performance of Structures III and IV . . . 113
5.3 Numerical Investigation of P3HT:PCBM BHJOSC with GO as HTL, Diverse ETLs and Different Cathode Materials . . . 113
5.3.1 Standardization . . . 115
5.3.2 Optimization . . . 115
5.3.2.1 Influence of Varying Input Parameters of Active Layer on Device Output Performance . . . 116
5.3.2.2 Influence of Various Parameters of HTL . . . 118
5.3.2.3 Influence of Varying Interface Defect Density, Operating Temperature, Series Resistance and Shunt Resistance . . . 120
5.3.3 Study of ITO/GO/P3HT:PCBM/ETL/Al with Diverse ETLs and Different Cathodes . . . 123
5.4 Numerical Investigation of P3HT:PCBM BHJOSC with rGO as HTL, Diverse ETLs and Cathode Materials . . . 127
5.4.1 Standardization . . . 128
5.4.2 Optimization . . . 129
5.4.2.1 Influence of Varying Input Parameters of Active Layer on the Device Performance . . . 131
5.4.2.2 Influence of Varying Input Parameters of rGO (HTL) on the Device Performance . . . 132
5.4.2.3 Influence of Varying Interface Defect Density, Series Resistance, Shunt Resistance and Operating Temperature on the Device Performance . . . 134
5.4.3 Study of ITO/rGO/P3HT:PCBM/ETL/ Metal Electrode with Diverse ETLs and Different Metal Electrodes . . . 138
5.5 Comparison of P3HT:PCBM based BHJOSCs with Efficiency Exceeding 10% 139
5.6 Conclusion . . . 140

6 Numerical Investigation of PBDB-T:NCBDT BHJOSCs with Diverse Graphene HTLs and Different ETLs 141
6.1 PBDB-T:NCBDT BHJOSCs . . . 142
6.2 Numerical Investigation of PBDB-T:NCBDT BHJOSC with Diverse Graphene HTLs and ETLs . . . 144
6.2.1 Standardization . . . 144
6.2.2 Study of ITO/HTL/PBDB-T:NCBDT/ETL/Al with Graphene Derivative HTLs and Diverse ETLs . . . 147
6.2.3 Optimization . . . 150
6.2.3.1 Influence of Varying Work Function of ITO . . . 150
6.2.3.2 Influence of Thickness of Active Layer . . . 151
6.2.3.3 Influence of Defect Density of Active Layer . . . 152
6.2.3.4 Influence of Thickness of HTL . . . 152

6.2.3.5 Influence of Defect Density of HTL . . . 153
6.2.3.6 Influence of Hole Mobility of HTL . . . 155
6.2.3.7 Influence of Acceptor Density of HTL . . . 155
6.2.3.8 Influence of Thickness of ETL . . . 156
6.2.3.9 Influence of Defect Density of ETL . . . 157
6.2.3.10 Influence of Electron Mobility of ETL . . . 157
6.2.3.11 Influence of Donor Density of ETL . . . 158
6.2.4 Influence of Varying Interface Defect Densities, Series Resistance, Shunt Resistance and Operating Temperature . . . 158
6.2.4.1 Influence of Varying Defect Densities of Interface I and interface II . . . 158
6.2.4.2 Influence of Series Resistance and Shunt Resistance . . . 159
6.2.4.3 Influence of Operating Temperature . . . 161
6.3 Numerical Investigation of PBDB-T:NCBDT based BHJOSC with Double Layered HTLs and Diverse ETLs . . . 162
6.3.1 Optimization . . . 165
6.3.1.1 Influence of Varying Input Parameters of PBDB-T:NCBDT (Active Layer) . . . 165
6.3.1.2 Influence of Varying Input Parameters of MoS_2 (HTL-II) . . . 171
6.3.1.3 Influence of Varying Input Parameters of PDINO (ETL) . . . 172
6.4 Comparison of PBDB-T:NCBDT based BHJOSCs . . . 174
6.5 Conclusion . . . 175

7 Numerical Investigation of PBDB-T:INTIC BHJOSC with Diverse Graphene Derivative HTLs and ETLs 176
7.1 PBDB-T:INTIC BHJOSC . . . 177
7.2 Numerical Investigation of PBDB-T:INTIC BHJOSC with PEDOT:PSS:rGO HTL and n-graphene ETL . . . 178
7.2.1 Influence of Thickness of Active Layer . . . 180
7.2.2 Influence of Band Gap of Active Layer . . . 181
7.2.3 Influence of Electron Affinity of Active Layer . . . 181
7.3 Numerical Investigation of PBDB-T:INTIC BHJOSC with Diverse Graphene Derivative HTLs and Different ETLs . . . 182
7.3.1 Standardization . . . 183
7.3.2 Study of ITO/HTL/PBDB-T:INTIC/ETL/Al . . . 185
7.3.3 Optimization of ITO/rGO/PBDB-T:INTIC/PDINO/Al . . . 193
7.3.3.1 Influence of Thickness and Defect Density Variation of Active Layer . . . 193
7.3.3.2 Influence of Varying Electron and Hole Mobility Variation of Active Layer . . . 198
7.3.3.3 Influence of Varying Thickness and Defect Density of HTL 199
7.3.3.4 Influence of Varying Electron and Hole Mobilities of HTL . 201
7.3.3.5 Influence of Varying Thickness and Defect Density of ETL 202
7.3.3.6 Influence of Varying Electron and Hole Mobilities of ETL . 203
7.3.3.7 Influence of Varying Doping Densities of HTL and ETL . . 204

7.3.3.8 Influence of Varying Interface Defects on the Device Performance . . . 210
7.4 Comparison of Device Performance of PBDB-T:INTIC BHJOSCs . . . 215
7.5 Conclusion . . . 216

8 Conclusion **217**
8.1 Major Inferences . . . 218
8.1.1 Limitations and Future Directions . . . 220

9 Recommendations and Scope for Future Work **222**
9.1 Recommendations for Future Work . . . 223

Bibliography **224**

List of Publications **263**

Conference Presentations **264**

List of Figures

1.1 Growth in global energy demand . . . 2
1.2 Figure showing tilt angle of elevation for PV cells. . . . 4
1.3 Figure showing solar spectrum spread in various wavelength. . . . 5
1.4 Working principle of an SC. . . . 6
1.5 Electron excitation occurring in an SC. . . . 6
1.6 Formation of a simple p-n junction. . . . 8
1.7 Typical I-V graph of p-n junction diode. . . . 8
1.8 Equivalent circuit of an SC. . . . 10
1.9 I-V graph of SC in dark, and illuminated condition. . . . 11
1.10 Typical J-V graph obtained for an SC. . . . 14
1.11 Quantum efficiency graph. . . . 15
1.12 (a) Band to band, (b) trap assisted and (c) Auger recombination. . . . 17
1.13 The propagation of light through two different media. . . . 20
1.14 First generation SCs. . . . 29
1.15 Amorphous silicon SC. . . . 29
1.16 CIGS SC. . . . 30
1.17 CdTe SC. . . . 31
1.18 CZTS SC. . . . 32
1.19 GaAs SC. . . . 33
1.20 Organic SC. . . . 34
1.21 Perovskite SC. . . . 35
1.22 Quantum Dot SC. . . . 35
1.23 Dye sensitized SC. . . . 36
1.24 Multi-Junction SC. . . . 37
1.25 Hybrid SC. . . . 38
1.26 CNT based solar cell. . . . 38
1.27 Graphene derivatives based SC with graphene derivative as (a) anode and (b) cathode. . . . 39
1.28 Graphene derivative based SC with graphene derivative as (a) HTL and (b) ETL. . . . 40
1.29 Graphene derivative based SC with graphene derivative in active layer. . . . 41

2.1 Chemical structure of P3HT. . . . 45
2.2 Chemical structure of PBDB-T. . . . 45
2.3 Chemical structure of PCBM. . . . 46

2.4 Chemical structure of NCBDT. . . . 46
2.5 Chemical structure of INTIC. . . . 46
2.6 (a) Single layer, (b) bilayer and (c) BHJOSC 52
2.7 (a) Ternary OSC and (b) Tandem OSC 54
2.8 DSSC. . . . 55
2.9 (a) Steps involved in exciton generation to charge carriers collection. (b) Band diagram of the photocurrent generation mechanism. . . . 58
2.10 (a) Conventional and (b) inverted BHJ structures 61

3.1 Chemical structures of (a) graphene, (b) graphene oxide and (c) reduced graphene oxide. . . . 65
3.2 Chemical structures of graphene and graphene quantum dot 67
3.3 Graphene derivative as (a) anode and (b) cathode. . . . 70
3.4 Graphene derivative as (a) HTL and (b) ETL. . . . 72
3.5 Graphene derivative in photoactive layer. . . . 74

4.1 Opening action panel 83
4.2 Panel showing layer addition 83
4.3 Panel showing parameters of layers 84
4.4 Operating conditions panel 85
4.5 Solar spectrum selection panel 86
4.6 Selection of solar spectrum from files 86
4.7 Output parameter setting panel 86
4.8 Batch recorder panel I 87
4.9 Batch recorder panel II 87
4.10 Panel showing energy band diagrams 88
4.11 I-V graph 88
4.12 QE graph 89

5.1 Chemical structures of P3HT and PCBM. . . . 94
5.2 Schematic representation of P3HT:PCBM BHJOSC with graphene as HTL and diverse ETLs 95
5.3 Energy band alignment of the layers used for the simulation study of ITO/-graphene/P3HT:PCBM/ETL/Al. . . . 96
5.4 Influence of variation of V_{oc} with varying thickness of P3HT:PCBM on device structures I and II. . . . 98
5.5 Influence of variation of J_{sc} with varying thickness of P3HT:PCBM on device structures I and II. . . . 98
5.6 Influence of variation of FF with varying thickness of P3HT:PCBM on device structures I and II. . . . 99
5.7 Influence of variation of efficiency with varying thickness of P3HT:PCBM on device structures I and II. . . . 99
5.8 Variation of device output parameters with varying electron mobility of P3HT:PCBM on device structure I. . . . 101

5.9 Variation of device output parameters with varying hole mobility of P3HT:PCBM on device structure I. . . . 101
5.10 Variation of device output parameters with varying electron mobility of P3HT:PCBM on device structure II. . . . 102
5.11 Variation of device output parameters with varying hole mobility of P3HT:PCBM on device structure II. . . . 102
5.12 Influence of variation of device output parameters with varying defect density of P3HT:PCBM on device structure I. . . . 104
5.13 Influence of variation of device output parameters with varying defect density of P3HT:PCBM on device structure II. . . . 104
5.14 Influence of variation of V_{oc} with varying thickness of P3HT:PCBM on device structures III and IV. . . . 107
5.15 Influence of variation of J_{sc} with varying thickness of P3HT:PCBM on device structures III and IV. . . . 107
5.16 Influence of variation of FF with varying thickness of P3HT:PCBM on device structures III and IV. . . . 108
5.17 Influence of variation of efficiency with varying thickness of P3HT:PCBM on device structures III and IV. . . . 108
5.18 Influence of varying electron mobility of P3HT:PCBM on the device performance of structure III. . . . 109
5.19 Influence of varying hole mobility of P3HT:PCBM on the device performance of structure III. . . . 110
5.20 Influence of varying electron mobility of P3HT:PCBM on the device performance of structure IV. . . . 110
5.21 Influence of varying hole mobility of P3HT:PCBM on the device performance of structure IV. . . . 111
5.22 Influence of varying defect density of P3HT:PCBM on the device performance of structure III. . . . 112
5.23 Influence of varying defect density of P3HT:PCBM on the device performance of structure IV. . . . 112
5.24 Device structure used in the experimental study of ITO/GO/P3HT:PCBM/Al [336]. . . . 114
5.25 Matching EQE graph. . . . 114
5.26 Influence of varying active layer thickness on device output parameters. . . . 116
5.27 Influence of varying active layer defect density on device output parameters. 116
5.28 Influence of varying active layer electron mobility on device output parameters. . . . 117
5.29 Influence of varying active layer hole mobility on device output parameters. 117
5.30 Influence of varying HTL thickness on device output parameters. . . . 118
5.31 Influence of varying HTL defect density on device output parameters. . . . 119
5.32 Influence of varying HTL electron mobility on device output parameters. . . . 119
5.33 Influence of varying HTL hole mobility on device output parameters. . . . 120
5.34 Influence of varying interface defect density on device output parameters. . . . 121
5.35 Influence of varying operating temperature on device output parameters. . . . 121
5.36 Influence of varying series resistance on device output parameters. . . . 122

5.37 Influence of varying shunt resistance on device output parameters. 122
5.38 Device design used for the simulation study. 123
5.39 Energy band diagram of layers used in the simulation study of the device structure ITO/GO/P3HT:PCBM/ETL/Al. 124
5.40 The device structure used for the experimental study of ITO/rGO/P3HT:PCBM/Al [336]. 127
5.41 Matched EQE graph for the device structure ITO/rGO/P3HT:PCBM/Al. . 128
5.42 Variation of device output parameters vs active layer thickness. 129
5.43 Variation of device output parameters vs active layer defect density. 129
5.44 Variation of device output parameters vs active layer electron mobility. . . . 130
5.45 Variation of device output parameters vs active layer hole mobility. 130
5.46 Variation of device output parameters vs thickness of HTL. 132
5.47 Variation of device output parameters vs defect density of HTL. 132
5.48 Variation of device output parameters vs electron mobility of HTL. 133
5.49 Variation of device output parameters vs hole mobility of HTL. 133
5.50 Variation of device output parameters vs interface defect density. 134
5.51 Variation of device output parameters vs series resistance. 135
5.52 Variation of device output parameters vs shunt resistance. 135
5.53 Variation of device output parameters vs operating temperature. 136
5.54 Schematic illustration of the device structure of ITO/rGO/P3HT:PCBM/ETL/cathode. 137
5.55 Schematic illustration of the energy band diagram of materials used for the simulation study of ITO/rGO/P3HT:PCBM/ETL/cathode. 137

6.1 PBDB-T and NCBDT. 143
6.2 Figure illustrating the experimental device structure- ITO/PEDOT:PSS/PBDB-T:NCBDT/ PDINO/Al [368]. 145
6.3 Matching simulation and experimental J-V graph of ITO/PEDOT:PSS/PBDB-T:NCBDT/PDINO/Al. 146
6.4 Matching simulation and experimental EQE graph of ITO/PEDOT:PSS/PBDB-T:NCBDT/ PDINO/Al. 146
6.5 Device structure for the simulation of ITO/HTLs/PBDB-T:NCBDT/ ETL-s/Al 147
6.6 Energy band diagram of layers used for the simulation of ITO/HTLs/PBDB-T:NCBDT/ETLs/Al 148
6.7 Effect of varying ITO work function on device performance 150
6.8 Effect of active layer thickness on device performance. 151
6.9 Effect of active layer defect density on device performance. 152
6.10 Effect of HTL thickness on device performance. 153
6.11 Effect of HTL defect density on device performance. 153
6.12 Effect of HTL hole mobility on device performance. 154
6.13 Effect of HTL acceptor density on device performance. 154
6.14 Effect of ETL thickness on device performance. 155
6.15 Effect of ETL defect density on device performance. 156
6.16 Effect of ETL electron mobility on device performance. 156
6.17 Effect of ETL donor density on device performance. 157

6.18 Effect of interface I defect density on device performance. 159
6.19 Effect of interface II defect density on device performance. 159
6.20 Effect of series resistance on device performance. 160
6.21 Effect of shunt resistance on device performance. 160
6.22 Effect of operating temperature on device performance. 161
6.23 Device structure used for the simulation study of ITO/HTL-I/HTL-II/PBDB-T:NCBDT/ETL/Al. 163
6.24 Energy band diagram of the layers used in the simulation study of ITO/HTL-I/HTL-II/PBDB-T:NCBDT/ETL/Al. 164
6.25 Effect of thickness and defect density of active layer on V_{oc}. 166
6.26 Effect of thickness and defect density of active layer on J_{sc}. 166
6.27 Effect of thickness and defect density of active layer on FF. 167
6.28 Effect of thickness and defect density of active layer on efficiency. 167
6.29 Effect of electron mobility and hole mobility of active layer on V_{oc}. 168
6.30 Effect of electron mobility and hole mobility of active layer on J_{sc}. 168
6.31 Effect of electron mobility and hole mobility of active layer on FF. 169
6.32 Effect of electron mobility and hole mobility of active layer on efficiency. . . 169
6.33 Influence of varying thickness of HTL-I (PEDOT:PSS) on the device output parameters. 170
6.34 Influence of varying defect density of HTL-I (PEDOT:PSS) on the device output parameters. 170
6.35 Influence of varying thickness of HTL-II (MoS_2) on the device output parameters 171
6.36 Influence of varying defect density of HTL-II (MoS_2) on the device output parameters. 172
6.37 Influence of varying thickness of ETL (PDINO) on the device output parameters. 173
6.38 Influence of varying defect density of ETL (PDINO) on the device output parameters. 173

7.1 PBDB-T and INTIC. 177
7.2 Device structure of ITO/PEDOT:PSS:rGO/PBDB-T:INTIC/n-graphene/Al. 179
7.3 Energy band diagram of the layers used in the device structure-ITO/PEDOT:rGO/PBDB-T:INTIC/n-graphene/Al. 179
7.4 Influence of varying thickness of the active layer on the device output parameters 180
7.5 Influence of varying band gap of the active layer on the device output parameters 181
7.6 Influence of varying electron affinity of the active layer on the device output parameters. 182
7.7 Device structure used for standardization [368]. 183
7.8 Matched J-V graph of experimental and simulation work of ITO/PEDOT:PSS/PBDB-T:NCBDT/PDINO/Al. 184
7.9 Matched EQE graph of experimental and simulated data of ITO/PEDOT:PSS/PBDB-T:NCBDT/PDINO/Al [368]. 184

7.10 Device structure used for the simulation study of ITO/HTL/PBDB-T:INTIC/ETL/Al. 186
7.11 Energy band diagram of the layers used in the device structure used for the simulation study of ITO/HTL/PBDB-T:INTIC/ETL/Al. 186
7.12 Influence of thickness and defect density variation of active layer on V_{oc} of the device. 189
7.13 Influence of thickness and defect density variation of active layer on J_{sc} of the device. 190
7.14 Influence of thickness and defect density variation of active layer on FF of the device. 191
7.15 Influence of thickness and defect density variation of active layer on efficiency of the device. 192
7.16 Influence of varying electron and hole mobilities of active layer on V_{oc}. . . . 194
7.17 Influence of varying electron and hole mobilities of active layer on J_{sc}. . . . 195
7.18 Influence of varying electron and hole mobilities of active layer on FF. . . . 196
7.19 Influence of varying electron and hole mobilities of active layer on efficiency. 197
7.20 Influence of varying thickness of HTL on the device output parameters. . . 198
7.21 Influence of varying defect density of HTL on the device output parameters. 199
7.22 Influence of varying electron mobility of HTL on the device output parameters. 200
7.23 Influence of varying hole mobility of HTL on the device output parameters. 201
7.24 Influence of varying thickness of ETL on the device output parameters. . . 202
7.25 Influence of varying defect density of ETL on the device output parameters. 203
7.26 Influence of varying electron mobility of ETL on the device output parameters. 204
7.27 Influence of varying hole mobility of ETL on the device output parameters. 205
7.28 Influence of varying doping density of HTL and ETL on V_{oc}. 206
7.29 Influence of varying doping density of HTL and ETL on J_{sc}. 207
7.30 Influence of varying doping density of HTL and ETL on FF. 208
7.31 Influence of varying doping density of HTL and ETL on efficiency. 209
7.32 Influence of varying defect densities of interface I and II on V_{oc}. 210
7.33 Influence of varying defect densities of interface I and II on J_{sc}. 211
7.34 Influence of varying defect densities of interface I and II on FF. 212
7.35 Influence of varying defect densities of interface I and II on efficiency. 213

List of Tables

5.1 Input parameters of active layer (P3HT:PCBM) and HTL (graphene). . . . 97
5.2 Input parameters of ETLs used for the simulation study. 97
5.3 Input parameters of P3HT:PCBM and GO used for the simulation study of ITO/GO/P3HT:PCBM/Al. 114
5.4 Matched output parameters of experimental and simulation study. 115
5.5 Input parameters of the active layer (P3HT:PCBM) and HTL (GO) used for the simulation of ITO/GO/P3HT:PCBM/Al. 125
5.6 Input material parameters used for ETLs-PDINO, PFN-Br, LiF, and ZnO. 125
5.7 Input parameters of ETLs-IGZO, PCBM, C_{60}, TiO_2:gr, and n-graphene. . . 125
5.8 Output parameters of various device configurations simulated using GO as HTL, diverse ETLs and different cathodes. 126
5.9 Input material parameters of P3HT:PCBM and rGO. 127
5.10 Matching experimental and simulation results. 128
5.11 Input material parameters of P3HT:PCBM and rGO. 138
5.12 Input parameters used for the ETLs-PDINO, PFN-Br, LiF, and ZnO. . . . 138
5.13 Input parameters of ETLs-IGZO, PCBM, C_{60}, TiO_2:gr, and n-graphene. . . 138
5.14 Device output parameters attained for different configurations. 139

6.1 Input parameters of PBDB-T:NCBDT, PEDOT:PSS and PDINO for the simulation of ITO/PEDOT:PSS/PBDB-T:NCBDT/PDINO/Al. 145
6.2 Comparison of simulated output with experimental result of ITO/PEDOT:PSS/PBDB-T:NCBDT/ PDINO/Al. 146
6.3 Input parameters of PBDB-T:NCBDT and various HTLs. 148
6.4 Input parameters of the various ETLs used for the simulation study. 149
6.5 Photovoltaic parameters of devices using different HTL and ETL combinations. 149
6.6 Optimized device input parameters for ITO/rGO/PBDB-T:NCBDT/ PDINO/Al. 162
6.7 Optimized device output parameters for ITO/rGO/PBDB-T:NCBDT/PDINO/Al. 162
6.8 Input parameters for PEDOT:PSS, MoS_2, GO, and PBDB-T:NCBDT for the simulation study. 164
6.9 Input parameters of ETLs used for the simulation study. 165
6.10 Output parameters of device configurations with double HTLs after the simulation study of ITO/HTL-I/HTL-II/PBDB-T:NCBDT/ETL/Al 165
6.11 Optimized input parameters of the simulated device structure. 174

6.12 Optimized output parameters of the simulated device structure. 174
6.13 Comparison of previous works done on PBDB-T:NCBDT BHJOSCs with our study. 175

7.1 Input parameters for PEDOT:PSS:rGO, PBDBT:INTIC and n-graphene . . 180
7.2 Input parameters of PBDB-T:NCBDT and PEDOT:PSS used for the simulation of ITO/PEDOT:PSS/PBDB-T:NCBDT/PDINO/Al. 183
7.3 Matching experimental and simulation output parameters. 185
7.4 Input parameters of PBDB-T:INTIC and HTLs used for the simulation of ITO/HTL/PBDB-T:INTIC/ETL/Al. 187
7.5 Input parameters of ETLs used for the simulation of ITO/HTL/PBDB-T:INTIC/ETL/Al. 187
7.6 Device output parameters after the simulation study with graphene derivative HTLs and diverse ETLs. 187
7.7 Optimized input parameters of the device structure simulated. 214
7.8 Optimized output parameters of the simulated device structure. 214
7.9 Comparison table of PBDB-T:INTIC NFABHJOSCs. 215

Symbols

θ	Elevation angle falling on solar panel
E	Energy of incident light
h	Planck's constant
ν	Frequency of light absorbed by the solar cell
I_d	Diode current
I_0	Reverse saturation current
V_D	Diode Voltage
η	Ideality Factor
V_T	Thermal Voltage
R_{sh}	Shunt resistance
R_s	Series resistance
I_{sh}	Additional Shunt resistance current
J_{sc}	Short circuit current density
V_{oc}	Open circuit voltage
FF	Fill factor
PCE	Power Conversion Efficiency
K	Boltzmann's Constant
n	Number of electron carriers
p	Number of hole carriers
T	Temperature
q	Charge
I_{ph}	Photocurrent
P_{in}	Incident light power
V_{mp}	Voltage at maximum powerpoint
J_{mp}	Current at maximum powerpoint
τ_n	Lifetime of electrons
τ_p	Lifetime of holes

n_i	Electron concentration
n_p	Hole concentration
E	Electric Field
B	Magnetic Field
ρ	Charge density
Ω	Angular Frequency
ε_0	Vacuum Permittivity
I_0	Incident Intensity
α	Absorption Coefficient
x	Depth of material
n_1, n_2	Refractive indices of two seperate mediums
θ_i	Angle of Incidence
θ_t	Angle of Transmission
θ_{crit}	Critical angle
R	Reflectance
T	Transmittance
ε'	Real part of permittivity
ε''	Imaginary part of permittivity
k	Extinction Coefficient
λ_0	Wavelength in vacuum
I_z	Intensity after propogation
ϕ	Electrostatic Potential
U	Recombination rate
J_n	Electron current density
J_p	Hole current density
e	Electron charge
τ	Relaxation time
D_e	Diffusion constant of electron
D_p	Diffusion constant of holes
G_e	Generation rate of electrons
R_e	Recombination rate of electrons
G_p	Generation rate of holes
R_p	Recombination rate of holes

Chapter 1

Introduction

This chapter delves into the importance of renewable energy, focusing on solar power and the indispensable role of solar cells (SCs). It explores the fundamental physics behind the SC operation, outlining the steps involved in converting sunlight into electricity. The chapter also traces the historical development of SCs and examines the evolution of different SC generations. Finally, it provides a concise introduction to this thesis and an overview of the subsequent chapters.

Energy is a fundamental requirement of modern civilization, leading to economic growth, industrial activity and improved living standards. As the global population continues to increase from about 3 billion in 1960 to nearly 8 billion today, understanding global energy requirements is vital to ensure a sustainable, equitable and secure energy future. Furthermore, technological advancements and widespread digitalization have significantly increased energy demand, particularly from infrastructures like data centers and communication networks. The transportation sector also contributes substantially to this rise, driven by an increasing number of vehicles on the roads and a boom in air travel.

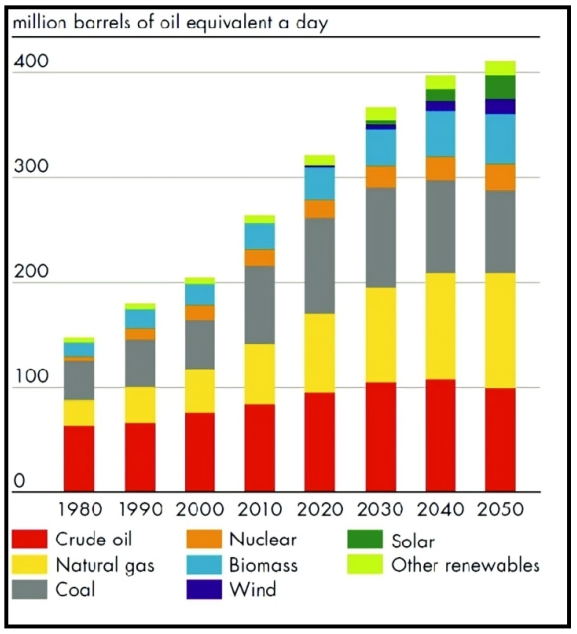


FIGURE 1.1: Growth in global energy demand

Fig. 1.1 shows data published by the International Energy Agency (IEA) [1], presented in their world energy outlook reports. The plot illustrates measure of energy demand in million barrels of oil equivalent per day (Mboe/d). Measurements range from approximately 0 to 400 Mboe/d [1]. The total energy demand growth is seen to increase significantly from approximately 250 Mboe/d in 1990 to 400 Mboe/d by 2050 as shown in the figure.

The relative contribution of non-renewable energy resources such as oil, gas and coal declines after the year 2020, though they might still hold major shares. Due to the depletion of accessible oil resources, the proportion of crude oil in the world's energy balance will continue to decline, while the proportion of natural gas will increase. Even though these fossil energy sources seem to be plenty in the world, the increasing demand for environmental protection impels transformation from oil and gas to new energy sources.

All these concerns have prompted researchers worldwide to search for renewable energy resources. This has led to significant energy research efforts aiming to resolve the challenges of energy availability, cost, and sustainability. Renewable energy produced from natural sources like sun, light, wind, water, and biomass that continuously replenish is a primary, domestically sourced, clean and inexhaustible option. Most common types of renewable energy resources include solar, wind, hydroelectric, geothermal, and bioenergy. Among all of these, solar energy shows a practically inexhaustible nature and stands out as one of the finest renewable energy resource [2, 3, 4, 5, 6, 7, 8, 9, 10, 11, 12, 13, 14, 15, 16].

Solar energy is one of the most abundant and cleanest energy resources. As we face the challenges of climate change, environmental degradation and depletion of fossil fuels, solar energy emerges as the most favourable solution to meet our energy demand, with its immense potential to deliver a renewable, eco-friendly and possibly inexhaustible power supply.

1.1 Solar Energy

Solar energy is the energy harnessed from the sun's rays using diverse technologies. The most common technologies include, the implementation of solar photovoltaic (PV) systems and solar thermal systems. Solar PV panels convert sunlight directly into electricity with the help of semiconductor materials that generate an electric current when exposed to sunlight. Solar thermal systems, on the other hand, use mirrors or lenses to concentrate sunlight to heat a fluid, which is then used to generate steam and produce electricity. Both of these technologies provide a means of capturing the solar energy and converting it into electrical power [17, 18].

The sun behaves as a fusion reactor where hydrogen nuclei at the center of it are converted into helium under extremely high temperature and pressure by the process of thermonuclear fusion. The energy released during the fusion reaction is radiated outward into space as electromagnetic radiation. This radiant spectrum can be compared to a blackbody spectrum at a temperature of 5760 K [19]. The energy received from the sun per unit area per unit time is called solar irradiance, which mainly belongs to the near-ultraviolet (UV), visible and near-infrared (NIR) regions with its peak in the blue-green region of the visible wavelength. The solar power radiated per unit area received at the mean distance from the earth to the sun is known as the solar constant with a power of 1.353 kW/m^2 [19]. Upon passing the earth's atmosphere, the incoming sunlight gets

attenuated by various factors, mainly scattering and absorption. The sunlight that reaches the atmosphere is partially absorbed by constituents like oxygen, nitrogen and ozone. The absorbed light is scattered, and this attenuation is defined by the quantity called air mass (AM) (unitless quantity), which is explained using the Equation (1.1) [20, 21].

$$AM = \frac{Optical\ pathlength\ to\ incident\ sunlight}{Optical\ pathlength\ when\ the\ sun\ is\ incident\ directly\ overhead} \tag{1.1}$$

The relation between AM and θ is given using Equation (1.2), where θ is the angle between the sun and the vertical direction in degrees. Fig. 1.2 illustrates the solar elevation angle.

$$AM = \frac{1}{cos\theta} \tag{1.2}$$

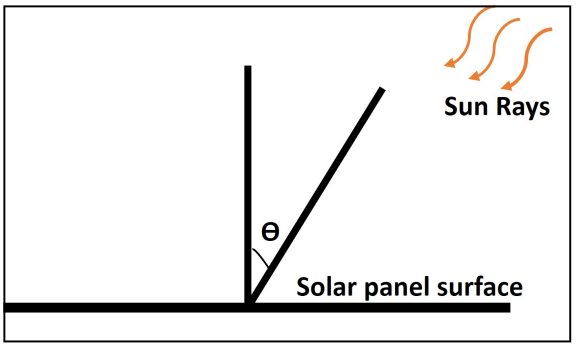


FIGURE 1.2: Figure showing tilt angle of elevation for PV cells.

The scattering of incident sunlight results in diffusion of radiation, where sunlight is incident on the earth from all directions along with the direct beam. Thus the total radiation reaching the earth consists of both the direct and diffused radiation. The variation of incident angles differs according to latitudes, due to which the varying concentration of diffused light has been a challenge for PVs.

Fig. 1.3 shows the global solar spectrum in the broad range of wavelengths [19]. AM 1.5 (Air mass 1.5 global spectrum), comprising both the direct and diffuse radiation, is the standard AM value with an incident power of 1000 W/m^2 [21].

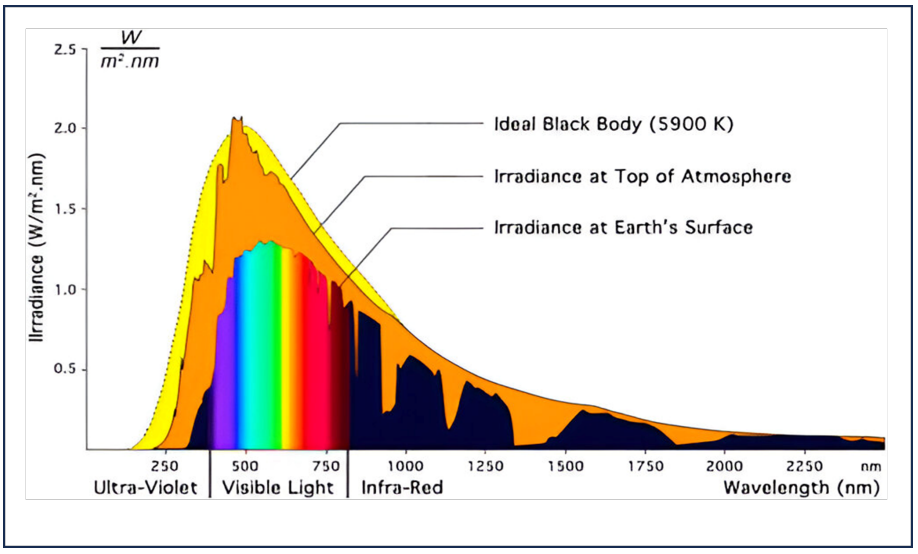


FIGURE 1.3: Figure showing solar spectrum spread in various wavelength.

1.2 Solar Cell

Harvesting solar energy using SC technology for the modern era and diving into the working of an SC is of high significance. The basic working principle of an SC is the PV effect, in which sunlight is converted into electricity. When sunlight (in the form of photons) strikes the surface of a semiconducting material, such as silicon, its electrons gets excited, causing them to be knocked loose from their atoms. This creates electron-hole (e-h) pairs. The internal electric field, usually created by a p-n junction (a junction between two types of semiconductor materials), inside the semiconducting material drives the electrons towards the negative side and the holes towards the positive side. This movement of charges generates an electric current, which in turn is used as electricity [22]. The energy of the incident photon responsible for the effect is expressed in Equation (1.3).

$$E = h\nu \tag{1.3}$$

where E corresponds to the energy of the photon, h denotes the Planck's constant and ν corresponds to the frequency of the light. When the photon has an energy greater than or equal to the band gap of a semiconductor, it gets absorbed and the light energy is eventually converted into electrical energy. This is the basic principle of an SC [22]. Fig. 1.4 illustrates the basic working principle of an SC and Fig. 1.5 illustrates a basic electron excitation occurring in an SC.

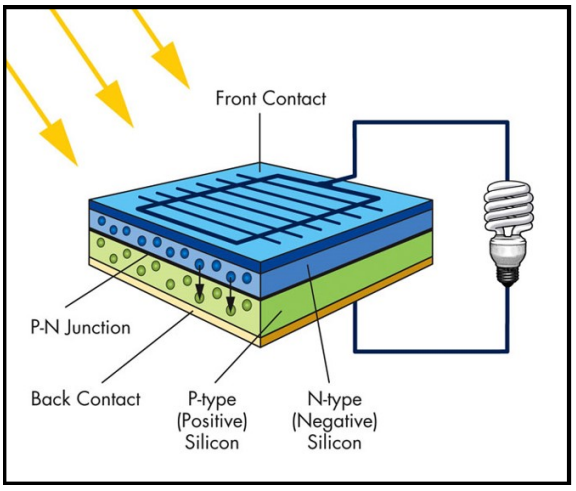


FIGURE 1.4: Working principle of an SC.

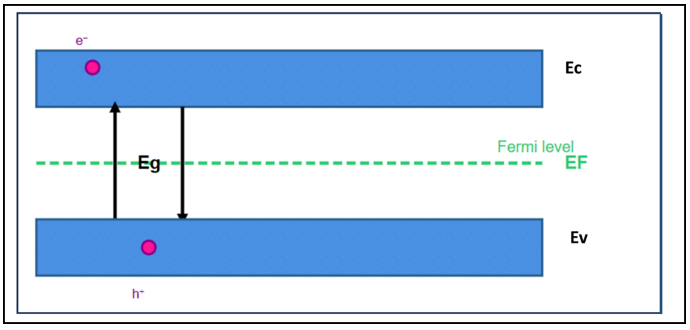


FIGURE 1.5: Electron excitation occurring in an SC.

The major processes involved in the working of an SC can be explained using the following three major steps.

- Absorption of light and generation of carriers.
- Separation of generated carriers.
- Collection of photogenerated carriers.

1.2.1 Absorption of Light and Generation of Carriers

The operation of an SC is initiated with the absorption of light. When sunlight strikes the SC, photons possessing energies at or above the semiconductor's band gap are absorbed by the active layer. This absorption process excites electrons from the valence band (V_B) into the conduction band (C_B), thereby generating e-h pairs. The effectiveness of this charge carrier generation hinges on the material's absorption coefficient and the

specific spectral distribution of the incident light [22, 23, 24]. Maximizing the number of absorbed photons, while simultaneously minimizing reflection and transmission losses, is crucial at this stage. Efficient absorption ensures a high yield of charge carriers, which is the underlying cause for producing photocurrent. This is often achieved through the use of anti-reflective coatings and light trapping structures [25, 26].

1.2.2 Separation of Generated Carriers

Once photogenerated, the short lifetime of electrons in the C_B makes them fall back quickly to their initial state, leading to recombination. To efficiently extract these charge carriers, a specialized junction is essential. This junction must ensure that electrons are directed to one side while holes are guided to the other. This separation is typically accomplished by creating a p-n junction between n-type and p-type semiconductor materials [22, 23, 24].

1.2.3 Collection of Photogenerated Carriers

Once separated, the electrons and holes are collected at terminal electrodes, enabling current to flow through a connected load. This process directly converts solar energy into electrical energy within the SC.

An SC can be fundamentally understood as a simple p-n junction diode. However, its function as an SC is contingent upon illumination. Therefore, a thorough understanding of p-n junction theory and operation is essential to grasp how the device works. Given that the SC's main absorber layer is also a semiconductor material, comprehending the working principle of a p-n junction semiconductor is highly significant [22, 23, 24, 27].

1.3 P-N Junction Semiconductor Theory

1.3.1 Working of a P-N Junction

Fig. 1.6 depicts the formation of a simple p-n junction in a semiconductor and Fig. 1.7 shows how the I-V characteristics of an SC would behave in different quadrants.

As a result, electrons begin to diffuse from the n-side to the p-side, while holes diffuse in the opposite direction. This diffusion continues until equilibrium is reached. At this

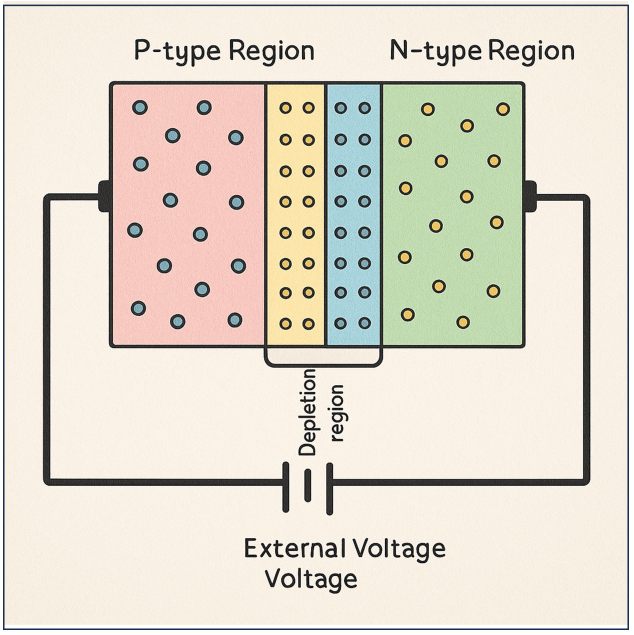


FIGURE 1.6: Formation of a simple p-n junction.

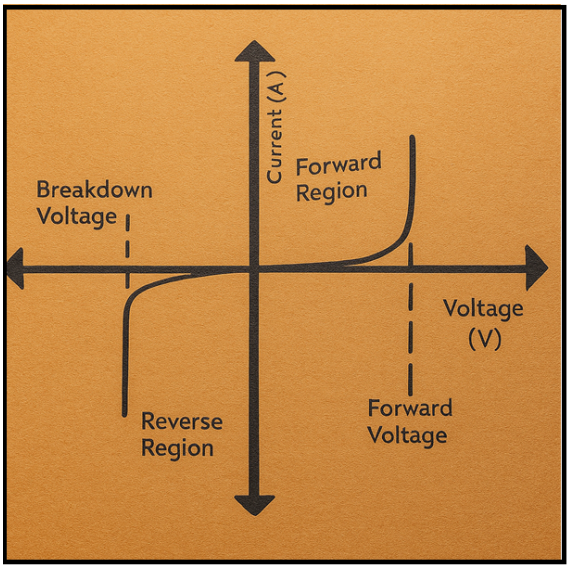


FIGURE 1.7: Typical I-V graph of p-n junction diode.

point, the movement of carriers stops, leading to an accumulation of electrons on the p-side and holes on the n-side. This charge separation creates an electric field that opposes further diffusion, forming a depletion region at the junction, where no free charge carriers are present, and carrier transport is effectively halted [22, 28, 29].

The accumulation of charges on either side of the p–n junction creates an electric field that gives rise to a barrier potential, effectively preventing further charge movement across

the depletion region. This region becomes devoid of free charge carriers. For current to flow across the junction, an external voltage greater than the barrier potential must be applied [22, 28, 29].

To allow external connection, the p–n junction diode is fitted with metal contacts: the anode on the p-side and the cathode on the n-side. When the diode is forward biased, the n-type region is connected to the negative terminal, and the p-type region is connected to the positive terminal of the voltage source. Once the applied voltage exceeds the barrier potential, the depletion region narrows, allowing charge carriers to cross the junction. As a result, current begins to flow through the semiconductor [22, 28, 29].

In reverse bias, the diode's depletion region widens as the applied voltage increases the barrier potential. Under this condition, majority carriers are pulled away from the junction, and no significant current flows through the diode because of the very low concentration of minority carriers in both the p and n regions. However, a small reverse saturation current flows, primarily due to these minority carriers. As the reverse voltage increases, this current remains nearly constant until the breakdown voltage is reached.

The relationship between the diode current and the applied voltage is described by the Shockley diode equation as depicted in Equation (1.4), which defines the I–V characteristics of a p–n junction semiconductor diode [22, 28, 29].

$$I = I_0 \left(e^{\frac{V_D}{\eta V_T}} - 1 \right) \tag{1.4}$$

where I corresponds to the diode current, I_0 corresponds to the reverse saturation current, V_D corresponds to the diode voltage, η is the ideality factor, V_T is the thermal voltage. As already mentioned, an SC is basically a p-n junction diode without illumination. The illumination by sunlight could turn it into an SC.

1.4 Equivalent Circuit of an SC

An SC can be represented by an electrically equivalent circuit, as shown in Fig. 1.8. This circuit consists of a constant current source in parallel with a diode, modelling the movement of electrons through the external circuit. The total current at the SC output is given by Equation (1.5). The current source represents the photocurrent generated by incident light. I_{ph} denotes the photocurrent, and I_D is the diode current. A practical

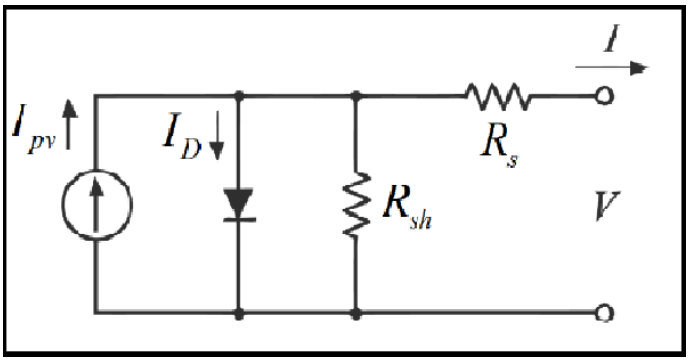


FIGURE 1.8: Equivalent circuit of an SC.

SC is non-ideal, and two additional components, called series resistance (R_s) and shunt resistance (R_{sh}), must be included in the circuit. The R_s results from the resistance offered by the device to current flow, primarily at the front surface, while R_{sh} arises from the leakage of current at the edges of the device. This leads to an additional shunt resistance current, denoted by I_{sh}.

The total current at the SC output is given by Equation (1.5).

$$I = I_{ph} + I_D - I_{sh} \tag{1.5}$$

V_D can be written as given in Equation (1.6)

$$V_D = V + IR_s \tag{1.6}$$

As already mentioned in section 1.3.1, the diode equation is given by Equation (1.7).

$$I_D = I_0 \left[\exp\left(\frac{V_D}{\eta V_T}\right) - 1 \right] \tag{1.7}$$

I_D denotes the diode current, I_0 is the reverse saturation current, V_D denotes the diode voltage, η is the ideality factor and V_T corresponds to the thermal voltage. The shunt resistance current can be written in the form of Equation (1.8).

$$I_{sh} = \frac{V_D}{R_{sh}} \tag{1.8}$$

Thus the modified diode equation becomes as shown in Equation (1.9).

$$I = I_{ph} - I_0 \left[\exp\left(\frac{V_D}{\eta V_T}\right) - 1 \right] - \frac{V + IR_s}{R_{sh}} \tag{1.9}$$

The I–V characteristics of an SC is essentially the superposition of the PV device under dark and illuminated conditions. The graphical representation is given in Fig. 1.9. The I–V characteristics of an SC under dark conditions is identical to that of a p–n junction semiconductor diode. The illumination of the device shifts the I–V curve into its fourth quadrant and the amount of shift is proportional to the intensity of incident light on the SC [30].

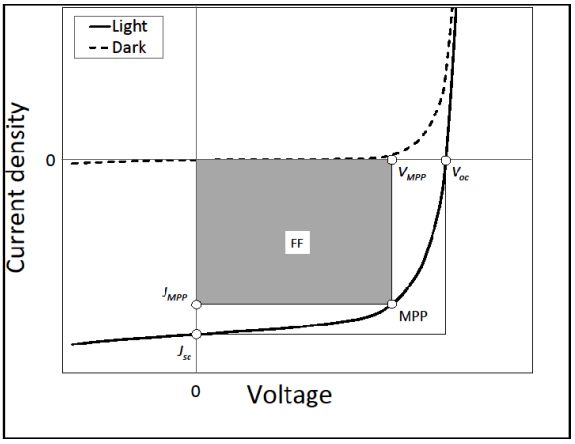


FIGURE 1.9: I-V graph of SC in dark, and illuminated condition.

1.4.1 Short Circuit Current Density

It can be defined as the current per unit area generated by the SC when the terminals are shorted (i.e., when the voltage across the cell is zero). Essentially, J_{sc} represents the maximum current density that an SC can deliver under illumination, measured in units of mA/cm^2. The J_{sc} quantifies the ability of the SC to generate and collect these photogenerated carriers efficiently [22, 30].

Mathematically, J_{sc} is measured under standard test conditions (typically under AM 1.5G illumination at 1000 W/m^2) with the cell terminals shorted. Factors affecting the short circuit current density include incident light intensity, spectrum, light absorption efficiency, band gap of the semiconductor, charge carrier generation and recombination, charge carrier mobility and transport, device architecture, thickness of each layer, surface and interface quality. The ability of the active layer to absorb incident photons directly affects J_{sc}. Materials with a broad and strong absorption spectrum generate more e-h pairs,

increasing J_{sc}. The semiconductor band gap determines the range of photon energies that can be absorbed. A smaller band gap allows absorption of longer wavelengths (lower energy photons), potentially increasing J_{sc}, but it must be balanced against voltage considerations [22, 30].

1.4.2 Open Circuit Voltage

Open circuit voltage (V_{oc}) is the maximum voltage an SC can produce when no current is drawn from the device (i.e., when the circuit is open). It represents the difference in electrochemical potential between the cell's electrodes under illumination and is crucial for determining the cell's power output. V_{oc} depends on the balance between photogenerated carrier generation and recombination losses within the SC [22]. Equation (1.10) gives the basic equation of V_{oc} [22, 30].

$$V_{oc} = \frac{\eta k T}{q} \ln\left(\frac{I_{\text{ph}}}{I_0} + 1\right) \tag{1.10}$$

where, η is the ideality factor, k is Boltzmann's constant, T is the absolute temperature (in Kelvin), q is the elementary charge, I_{ph} is the photocurrent and I_0 is the reverse saturation current.

Factors affecting the V_{oc} include material band gap, recombination rates, temperature and quality of interfaces and contacts. A wider band gap generally leads to a higher V_{oc} because it increases the maximum possible energy difference between electrons and holes. Higher recombination of charge carriers reduces the quasi-Fermi level splitting and lowers V_{oc} [31]. Increasing temperature typically decreases V_{oc} due to enhanced carrier recombination and changes in semiconductor properties [22]. Defects and poor quality interfaces increase recombination, leading to a reduction in V_{oc} [22, 30].

1.4.3 Fill Factor

Fill factor (FF) is a crucial parameter that measures the quality of an SC's current-voltage (I-V) characteristic. It is defined as the ratio of the maximum power output, to the product of V_{oc} and J_{sc}. A higher FF indicates better device performance and efficiency [22, 32]. Equation (1.11) gives the general equation of FF.

$$FF = \frac{V_{mp} \times J_{mp}}{V_{oc} \times J_{sc}} \tag{1.11}$$

In this equation, FF represents the fill factor, which is a measure of the 'squareness' of the SC's current–voltage (I-V) curve. V_{mp} is the voltage at the maximum power point and J_{mp} is the corresponding current density at that point. V_{oc} denotes the open circuit voltage, which is the maximum possible voltage from the SC when the current is zero. Finally, J_{sc} refers to the short circuit current density, defined as the current density when the voltage is zero.

Factors affecting the FF include series resistance (R_s), shunt resistance (R_{sh}), charge carrier recombination, material quality, interface quality and temperature. Increased R_s causes a drop in voltage and FF. Low R_{sh} leads to leakage currents that lower FF. Higher recombination decreases current and voltage, thus reducing FF. Defects and poor contacts increase resistive losses, lowering FF. Elevated temperatures typically reduce FF due to increased resistive losses and recombination [22, 32].

1.4.4 Power Conversion Efficiency

Power conversion efficiency (PCE) is the primary metric for assessing how efficiently an SC transforms incident sunlight into usable electrical energy. It is formally defined as the ratio of the SC's maximum electrical power output to the incident solar power input, typically expressed as a percentage.

Applying the equation, PCE can be defined by the Equation (1.12).

$$\eta = \frac{J_{sc} \cdot V_{oc} \cdot \mathrm{FF}}{P_{in}} \tag{1.12}$$

P_{in} denotes the incident light power per unit area, usually expressed in mW/cm^2, and is often taken as 100 mW/cm^2 under standard test conditions.

Higher photocurrent improves PCE by generating more charge carriers. Higher voltage increases the maximum power output, thus enhancing PCE. Good FF indicates less resistive loss and better device performance, improving PCE. Defects, impurities, and recombination centers reduce charge carrier lifetime and lowers efficiency. Optimized layer

thicknesses, interfaces and contact materials influence charge collection efficiency and overall PCE. Variations in sunlight intensity and spectrum can impact the generated current and efficiency [22]. Fig. 1.10 shows a simple J-V curve.

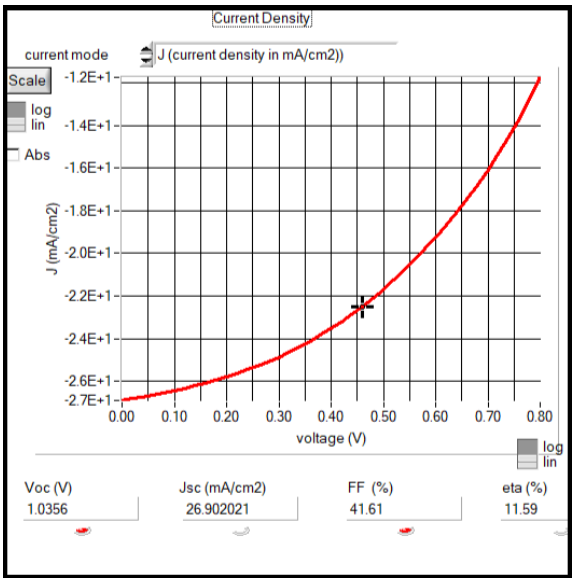


FIGURE 1.10: Typical J-V graph obtained for an SC.

In addition to these parameters, the quantum efficiency (QE) attained for an SC is important for the analysis of the output obtained by the device.

1.4.5 Quantum Efficiency

The quantum efficiency (QE) of an SC is defined as the ratio of the number of electrons in the device's external circuit to the number of incident photons. The QE of an SC is categorized into two types: External quantum efficiency (EQE) and internal quantum efficiency (IQE). EQE is the ratio of the number of electrons in the external circuit to the total number of photons incident on the cell, whereas IQE is the ratio of the number of electrons in the external circuit to the number of incident photons that are absorbed by the SC [22]. The output parameters obtained for an SC are largely influenced by certain mechanism occurring inside the SCs. These are due to recombination mechanisms to a large extent. Fig. 1.11 shows a typical QE graph.

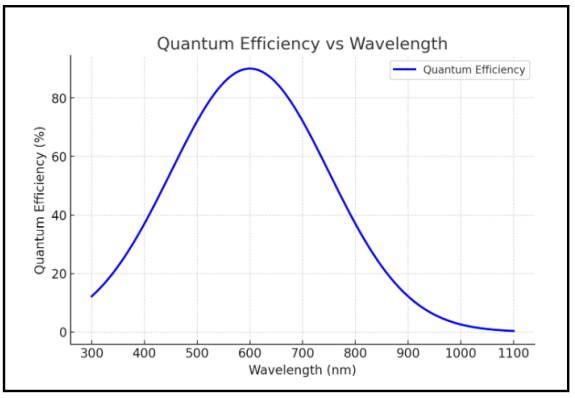


FIGURE 1.11: Quantum efficiency graph.

1.5 Different Recombination Mechanisms

The photogenerated electrons can decay back to their equilibrium states, and this process involves recombining with the opposite carriers. The major recombination mechanisms are explained in this section [22].

1.5.1 Band to Band Recombination (Radiative Recombination)

Radiative recombination, also known as spontaneous emission, is an unavoidable recombination mechanism within semiconductors. When an electron absorbs a photon with energy equal to or exceeding the semiconductor's band gap, it gets excited from the valence band to the conduction band, leaving behind a hole. However, the electron's lifetime in the conduction band is extremely short. It will inevitably decay back into the valence band, causing the electron and hole to recombine. The energy difference between these two bands is then emitted as light. This process is particularly dominant in direct band gap semiconductors [22, 33]. Recombination rate is given by Equation (1.13).

$$R = Bnp \tag{1.13}$$

where B is a constant based on absorption coefficient of the semiconductor, n and p denotes the concentration of electrons in the conduction band and holes in the valence band. Fig. 1.12 (a) exhibits band-to-band recombination [22, 33].

1.5.2 Trap Assisted Recombination (Shockley-Read-Hall Recombination)

Shockley-Read-Hall (SRH) recombination is a crucial process where charge carriers recombine through trap states, or defects in a semiconductor material. These defects introduce intermediate energy levels. SRH recombination occurs as two distinct steps. First, a photogenerated electron from the conduction band is captured by a trap, decaying into its intermediate energy level. Secondly, the trapped carrier could then be released due to thermal activation. However, if that same trap captures a carrier of the opposite polarity before the first carrier is thermally released, the two carriers will then recombine. The total recombination rate in SRH recombination process is given by the relation below [22, 33]. Equation (1.14) gives the equation for SRH recombination. Fig. 1.12 (b) exhibits trap assisted recombination [22, 33].

$$R_{SRH} = \frac{np - n_i^2}{\tau_p(n + n_1) + \tau_n(p + p_1)} \tag{1.14}$$

where R_{SRH} is the SRH recombination rate, expressed as the number of carriers recombining per unit volume per unit time. The terms n and p represent the electron and hole concentrations, respectively, while n_i is the intrinsic carrier concentration. The parameters τ_n and τ_p denote the lifetimes of electrons and holes, respectively, which are related to the capture cross-sections of trap states for these carriers. The quantities $n_1 = n_i \exp\left(\frac{E_t - E_i}{kT}\right)$ and $p_1 = n_i \exp\left(\frac{E_i - E_t}{kT}\right)$ represent the electron and hole concentrations, respectively, when the trap is half-filled. E_t is the energy level of the trap state, and E_i is the intrinsic Fermi level. Finally, k is the Boltzmann's constant and T is the absolute temperature in Kelvin [22, 33]. τ and L is given by the Equation (1.15) and Equation (1.16).

$$\tau = \frac{1}{\sigma V_{th} N_t} \tag{1.15}$$

$$= \sqrt{D\tau} \tag{1.16}$$

where, τ is carrier lifetime (due to traps), σ denotes capture cross-section, V_{th} stands for thermal velocity of the carriers, N_t is defect density, L is carrier diffusion length and D is the diffusion constant.

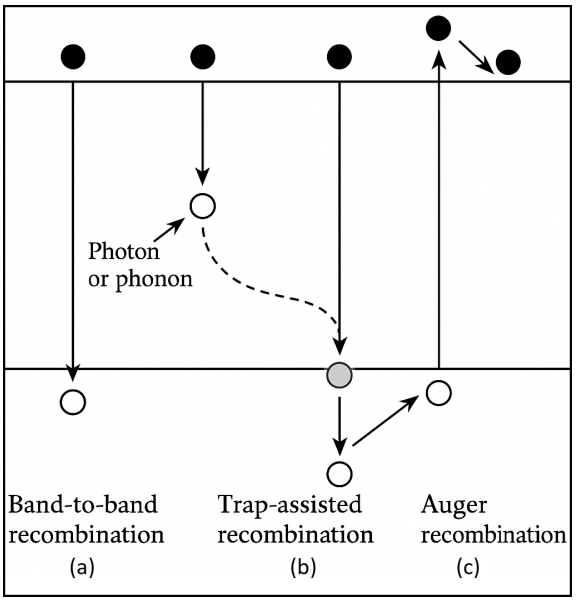


FIGURE 1.12: (a) Band to band, (b) trap assisted and (c) Auger recombination.

For efficient collection of photogenerated carriers, the absorber thickness d should satisfy Equation (1.17).

$$d \lesssim L_D \tag{1.17}$$

where d is the thickness of the absorber layer.

- If $d \ll L_D$, nearly all carriers are collected, but absorption may be weak.
- If $d \gg L_D$, many carriers recombine before reaching the junction, reducing efficiency.

.

1.5.3 Auger Recombination

Auger recombination occurs as a result of a collision between two charge carriers, which can be either similar or dissimilar. During this collision, one carrier is excited to a higher energy state, while the other decays across the band gap and recombines with a carrier of opposite polarity. The newly excited carrier will then eventually decay back towards the band edge [22, 33]. The carrier lifetime of electrons and holes corresponding to the Auger recombination process is given by Equation (1.18) and Equation (1.19).

$$\frac{1}{\tau_n} = Cnp + Dn^2 \tag{1.18}$$

$$\frac{1}{\tau_p} = Cnp + Dp^2 \tag{1.19}$$

where C and D are constants and n, p corresponds to the concentration of electrons and holes respectively. The above equations are applicable based on the dominant carrier in the semiconductor.

Fig. 1.12 (c) displays Auger recombination [22, 33].

1.5.4 Surface Recombination

Surface recombination is a process that happens because of the defects present on the surfaces of semiconductor crystals. These defects create intermediate energy levels within the forbidden energy gap, and these intermediate levels then act as sites where recombination occurs [22, 34]. Surface recombination rate is given by Equation (1.20).

$$R_s = \frac{s_n s_p \left(np - n_i^2\right)}{s_n \left(n + n_t\right) + s_p \left(p + p_t\right)} \tag{1.20}$$

n_t, p_t are carrier concentrations of electrons and holes respectively, s_n, s_p are electron and hole surface recombination velocities (cm/s), n, p are electron and hole concentrations at the surface (cm^{-3}), n_i stands for intrinsic carrier concentration (cm^{-3}), E_t is trap energy level and E_i is intrinsic Fermi level [22, 34].

1.6 Understanding Light-Matter Interaction in SCs

1.6.1 Electromagnetic Waves

As solar energy is fundamentally electromagnetic radiation emitted from the sun towards the earth, a grasp of the essential principles of electrodynamics is necessary to comprehend the propagation of light and its related properties.

The electromagnetic waves (EM) consist of electric and magnetic field vectors which are parpendicular to each other and also perpendicular to the direction of propagation.

EM waves can be described by the following relations for the electric and magnetic field using Equation (1.21) and Equation (1.22).

$$\frac{\partial^2 \vec{E}}{\partial x^2} + \frac{\partial^2 \vec{E}}{\partial y^2} + \frac{\partial^2 \vec{E}}{\partial z^2} - \frac{n^2}{c^2}\frac{\partial^2 \vec{E}}{\partial t^2} = 0 \tag{1.21}$$

$$\frac{\partial^2 \vec{B}}{\partial x^2} + \frac{\partial^2 \vec{B}}{\partial y^2} + \frac{\partial^2 \vec{B}}{\partial z^2} - \frac{n^2}{c^2}\frac{\partial^2 \vec{B}}{\partial t^2} = 0 \tag{1.22}$$

where $\vec{E}$ and $\vec{B}$ corresponds to the electric and magnetic field vectors, n corresponds to the refractive index of the medium and c is the speed of light in vacuum.

The solutions for the above equations are obtained in the form of plane harmonic wave propagating in a single direction and are given by Equation (1.23) and Equation (1.24).

$$\vec{E}(r,t) = \vec{E}_0 e^{ik_z z - i\omega t} \tag{1.23}$$

$$\vec{B}(r,t) = \vec{B}_0 e^{ik_z z - i\omega t} \tag{1.24}$$

where k_z is the wave vector in the direction of propagation and ω is the angular frequency of the wave. Comparing the equations, we obtain Equation (1.25) and Equation (1.26).

$$k_z - \frac{n^2}{c^2}\omega^2 = 0 \tag{1.25}$$

$$k_z = \frac{n\omega}{c} \tag{1.26}$$

where ω is related to the frequency ν as shown in Equation (1.27).

$$\omega = 2\pi\nu \tag{1.27}$$

The wavelength is defined by the Equation (1.28).

$$\lambda = \frac{2\pi}{k_z} = \frac{2\pi c}{n\omega} = \frac{c}{n\nu} \tag{1.28}$$

These relations indicate that the wave vector and wavelength depend on the refractive indices of the media through which the EM wave travels, while the frequency remains the same.

1.6.2 Optics and Absorption

In an SC, light is absorbed by a material medium and charge carriers are generated upon the photon absorption eventually leading to production of electricity. Therefore, it is essential to comprehend the optical characteristics of a medium in order to fully grasp the processes occurring within an SC. When an electromagnetic wave propogates from medium 1 to medium 2, the wave may get reflected at the interface, while transmitted portion undergoes refraction transmitted or refracted. The graphical representation is given in Fig. 1.13.

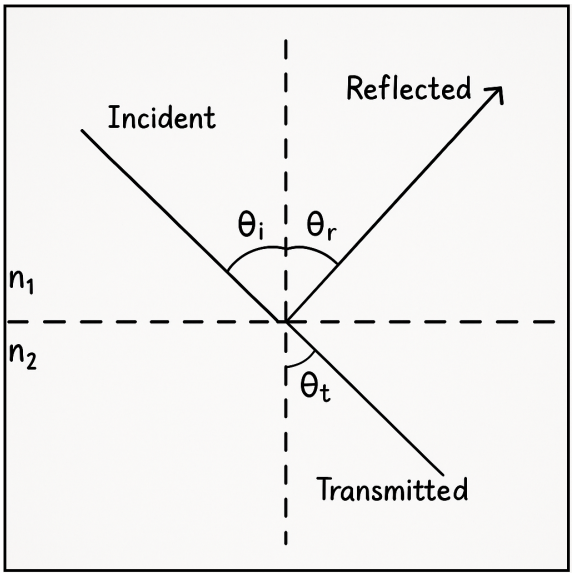


FIGURE 1.13: The propagation of light through two different media.

Considering only the real parts of the refractive indices, let the refractive index of medium 1 be n_1 and that of medium 2 be n_2. When the angle of incidence and angle of reflection are the same, the wave is reflected back to the first medium and the remaining part will get transmitted to the second medium at an angle of transmittance given by θ_t. Based on energy conservation, the reflectance R and transmittance T is related by the Equation (1.29).

$$R + T = 1 \tag{1.29}$$

The Snell's law and critical angle for reflectance have to be understood to learn about the propagation of light through the cell. Snell's law for interface between two different media is given by Equation (1.30).

$$n_1 \sin\theta_i = n_2 \sin\theta_t \tag{1.30}$$

The critical angle is defined as the incident angle at which the refraction angle is 90 °. The Snell's law can be modified as given in the equation below. When θ_i is larger than the critical angle θ_{crit}, the light wave won't be transmitted to the second medium, instead it will be reflected back to the first medium itself. The relation connecting n_1, n_2 and θ_{crit} is given by Equation (1.31).

$$\sin\theta_{\text{crit}} = \frac{n_2}{n_1} \tag{1.31}$$

where $n_1 > n_2$.
Dielectric permittivity of the material defines the medium properties and is given by the Equation (1.32).

$$\tilde{\epsilon} = \epsilon' + i\epsilon'' \tag{1.32}$$

The dielectric permittivity in a medium is defined by its real and imaginary part. where $\tilde{\epsilon}$ is the complex permittivity, ϵ' is the real part representing energy storage in the medium, and ϵ'' is the imaginary part representing dielectric losses. The refractive index of a medium depends on the dielectric permittivity as shown in Equation (1.33).

$$\tilde{n} = \sqrt{\tilde{\epsilon}} = n + ik \tag{1.33}$$

where $\tilde{n}$ is the complex refractive index, n is the real refractive index governing phase velocity, and k is the extinction coefficient describing optical absorption. The equation for k-vector can be modified as shown in Equation (1.34).

$$k_z = \frac{\tilde{n}\omega}{c} = \frac{n\omega}{c} + i\frac{k\omega}{c} = k_z' + ik_z'' \tag{1.34}$$

where k_z is the complex wave vector, ω is the angular frequency of light, and c is the speed of light in vacuum. The terms k_z' and k_z'' represent the real (phase) and imaginary (attenuation) components respectively. Thus, the component of electric field can be explained in terms of the k-vector by the Equation (1.35).

$$\vec{E_x}(r,t) = \vec{E_{x0}} e^{ik_z z - i\omega t} = E_{x0} e^{-k_z'' z} e^{ik_z' z - i\omega t} \tag{1.35}$$

where $\vec{E}_x(r,t)$ is the electric field component, E_{x0} is the initial amplitude, z is the propagation distance, and t is time. The term $e^{-k_z'' z}$ represents exponential attenuation due to absorption. From the above equation, it is clear that the electric field is attenuated upon passing through a material medium. The attenuation of electric field intensity is defined by Beer-Lambert law given by Equation (1.36).

$$I(z) = I_0 e^{-2k_z'' z} = I_0 e^{-\alpha z} \tag{1.36}$$

where $I(z)$ is the intensity at depth z, I_0 is the incident intensity, and α is the absorption coefficient of the material, where $\vec{E}_x(r,t)$ is the electric field component, E_{x0} is the initial amplitude, z is the propagation distance, and t is time. The attenuation of electric field intensity depends on the absorption coefficient α which differ among materials. Thus the spectral response of an SC depends on the absorption profile of the material medium used in it.

1.7 Fundamental Semiconductor Equations Solved in an SC

The operation of an SC is governed by the fundamental equations of semiconductor physics, which describe how charge carriers (electrons and holes) are generated, transported and collected within the device. These equations include Poisson's equation, the carrier continuity equations, and the drift-diffusion current equations. Together, they form a system of coupled partial differential equations that must be solved to accurately simulate the behaviour of an SC.

1.7.1 Poisson's Equation

The general form of Poisson's equation is given by Equation (1.37).

$$\nabla^2 V = -\frac{\rho}{\varepsilon} \tag{1.37}$$

where $\nabla^2 V$ is the Laplacian of the electrostatic potential V, ρ is the space charge density (C/m^3), ε is the permittivity of the material (F/m), defined as $\varepsilon = \varepsilon_r \varepsilon_0$, ε_0 is permittivity in vacuum and ε_r is the relative permittivity of the semiconductor material.

In a semiconductor, the total charge density ρ is given by Equation (1.38).

$$\rho = q\left(p - n + N_D^+ - N_A^-\right) \tag{1.38}$$

where q is the elementary charge, n is the electron concentration (cm^{-3}), p is the hole concentration (cm^{-3}), N_D^+ is the ionized donor concentration and N_A^- is the ionized acceptor concentration.

In one-dimensional analysis (along the x-axis), which is commonly used in SC modelling, Poisson's equation simplifies to Equation (1.39).

$$\frac{d^2 V(x)}{dx^2} = -\frac{\rho(x)}{\varepsilon} \tag{1.39}$$

This equation must be solved in conjunction with the carrier continuity equations and current equations to fully describe the behaviour of an SC under various conditions [22].

1.7.2 Continuity Equations

These equations ensure charge conservation for electrons and holes. Equation (1.40) and Equation (1.41) gives the continuity equations for electrons and hole[22].

For electrons:

$$\frac{\partial n}{\partial t} = \frac{1}{q}\nabla \cdot \vec{J}_n + G_n - R_n \tag{1.40}$$

For holes:

$$\frac{\partial p}{\partial t} = -\frac{1}{q}\nabla \cdot \vec{J}_p + G_p - R_p \tag{1.41}$$

where J_n and J_p are the electron and hole current densities, G_n and G_p are the generation rates of carriers (e.g., due to incident light), R_n and R_p are the recombination rates and q is the elementary charge.

$$\frac{\partial n}{\partial t} = \frac{\partial p}{\partial t} = 0. \tag{1.42}$$

Equation (1.42) can be written under steady-state conditions in an SC.

1.7.3 Drift-Diffusion Current Equations

These equations describe carrier transport due to electric fields and concentration gradients [22].

Electron current density:

$$\vec{J_n} = q\mu_n n\vec{E} + qD_n\nabla n \tag{1.43}$$

Hole current density:

$$\vec{J_p} = q\mu_p p\vec{E} - qD_p\nabla p \tag{1.44}$$

Equation (1.43) and Equation (1.44) gives electron current density and hole current density respectively. Where μ_n and μ_p are the carrier mobilities, D_n and D_p are the diffusion coefficients, $\vec{E} = -\nabla\phi$ denotes the electric field and n, p denotes the carrier concentrations [22].

1.7.3.1 Drift Current Inside an SC

In an SC, drift current refers to the movement of charge carriers under the influence of an electric field. This field is naturally established in the depletion region of the p-n junction. When the SC is exposed to light, incident photons generate e-h pairs. If these carriers are generated within or close to the depletion region, they are immediately separated by the internal electric field.

- Electrons are driven toward the n-type region,
- Holes are driven toward the p-type region.

This motion of carriers due to the electric field gives rise to the drift current, which is crucial for the efficient collection of photogenerated carriers. To evaluate this we need to find equations for drift velocity and mobility.

The drift velocity and mobility equations are given by Equations (1.45), (1.46), and (1.47).

$$v_{\text{drift}} = a\tau = \frac{qE\tau}{m_e^*} \tag{1.45}$$

$$v_{\text{drift}} = \mu E \quad \Rightarrow \quad \mu = \frac{v_{\text{drift}}}{E} \tag{1.46}$$

$$\mu = \frac{v_{\text{drift}}}{E} = \frac{\left(\frac{q\tau}{m^*}\right) E}{E} = \frac{q\tau}{m^*} \tag{1.47}$$

where a is the carrier's acceleration, t = τ is the average time between scattering events, q is elementary charge, μ is mobility and m* is the effective mass of the charge carrier.

The drift current densities for electrons and holes are described by Equation (1.48) and Equation (1.49).

$$J_{n,\text{drift}} = q\mu_n n\vec{E} \tag{1.48}$$

$$J_{p,\text{drift}} = q\mu_p p\vec{E} \tag{1.49}$$

where $J_{n,\text{drift}}$ and $J_{p,\text{drift}}$ are the drift current densities of electrons and holes (A/cm^2), q is elementary charge, μ_n and μ_p represent mobilities of electrons and holes (cm^2/V·s), n and p denotes carrier concentrations (cm^{-3}) and $\vec{E}$ stands for the electric field (V/cm).

Drift current is significant primarily within the depletion region, where the built in electric field exists. It is responsible for the initial separation and movement of charge carriers generated by light and it plays a fundamental role in the overall current generation of the SC [22].

1.7.3.2 Diffusion Current Inside an SC

In an SC, diffusion current is caused by the movement of charge carriers (electrons and holes) from regions of higher concentration to regions of lower concentration, driven by concentration gradients. This mechanism is particularly important in the quasi-neutral regions of the SC, where the electric field is negligible.

When light is absorbed by the SC, it generates e-h pairs throughout the semiconductor material. This leads to non-uniform carrier distributions, especially in the quasi-neutral n and p-type regions. The excess carriers diffuse toward the depletion region, where they are separated and collected by the built in electric field. The flow of these carriers due to concentration gradients constitutes the diffusion current [22].

The diffusion current densities for electrons and holes are given by Equation (1.50) and Equation (1.51).

$$J_{n,\text{diffusion}} = qD_n \frac{dn}{dx} \tag{1.50}$$

$$J_{p,\text{diffusion}} = -qD_p \frac{dp}{dx} \tag{1.51}$$

where $J_{n,\text{diffusion}}$ and $J_{p,\text{diffusion}}$ are the diffusion current densities for electrons and holes (A/cm^2), D_n and D_p are diffusion coefficients for electrons and holes (cm^2/s) and $\frac{dn}{dx}, \frac{dp}{dx}$ are the spatial gradients of electron and hole concentrations. The negative sign in the hole diffusion current reflects that holes move in the direction opposite to the gradient of their concentration [22].

1.7.3.3 Total Current Density in an SC

The total current density inside an SC is the sum of both drift and diffusion current components for electrons and holes. These two mechanisms describe the complete carrier transport behaviour in the device.

The total current density due to electrons is given by Equation (1.52).

$$J_n = q\mu_n n\vec{E} + qD_n \frac{dn}{dx} \tag{1.52}$$

where J_n is the electron current density (A/cm^2), D_n is the electron diffusion coefficient (cm^2/s) and $\frac{dn}{dx}$ is the electron concentration gradient.

Similarly, the total current density due to holes is given by Equation (1.53).

$$J_p = q\mu_p p\vec{E} - qD_p\frac{dp}{dx} \tag{1.53}$$

where J_p is the hole current density (A/cm^2), D_p is the hole diffusion coefficient (cm^2/s),

$\frac{dp}{dx}$ is the hole concentration gradient.

The total current density in the SC is the sum of the electron and hole current densities, depicted by Equation (1.54).

$$J_{\text{total}} = J_n + J_p \tag{1.54}$$

Substituting from the above expressions J_{total} changes to Equation (1.55).

$$J_{\text{total}} = q\mu_n n\vec{E} + qD_n\frac{dn}{dx} + q\mu_p p\vec{E} - qD_p\frac{dp}{dx} \tag{1.55}$$

This equation comprehensively describes charge transport in an SC, incorporating both drift due to the electric field and diffusion due to carrier concentration gradients. Accurate modelling of this total current is essential for analyzing and optimizing SC performance [22].

1.8 History of SCs

The discovery of the PV effect is commonly ascribed to Becquerel, who discovered a photocurrent when platinum (Pt) electrodes, covered with silver bromide (AgBr) or silver chloride (AgCl), were illuminated in aqueous solution (strictly speaking this is a photoelectrochemical effect) [35]. Smith and Adams made the first reports on photoconductivity, in 1873 and 1876, respectively, working on selenium [36]. Anthracene was the first organic compound in which photoconductivity was observed by Pochettino in 1906 [37] and Volmer in 1913 [38]. The first inorganic SC was developed at Bell laboratories in 1954 [39]. In

the early 1960s, it was discovered that many common dyes, such as methylene blue, had semiconducting properties [40]. Later, these dyes were among the first organic materials to exhibit the PV effect [41]. Today, silicon (Si)-based SCs are by far the most dominant type of PVs used and account for 99% of all PVs [42]. Around 3% efficiency was attained by Shaheen et al. in 2001 [43]. In 2004 4.2% efficiency was obtained by jiangeng et al. [44].

In the 2000s and 2010s, perovskite SCs revolutionized PVs with their rapid increase in efficiency from 3.8% in 2009 to around 25% by 2020 [45, 46, 47, 48]. These cells, based on organic-inorganic halide materials, offered low-cost, high-performance possibilities. Meanwhile, tandem SCs, particularly perovskite-silicon combinations, began to exceed the single-junction Shockley–Queisser efficiency limit [49]. By 2022, tandem cells had surpassed 29% efficiency [50], and four-junction SCs had reached a world record of 47.6% at Fraunhofer ISE [51].

In 2024, multiple records were broken. LONGi achieved 27.4% efficiency using commercial size hetero-junction (HJT) cells [52], and Oxford PV reported a 26.9% efficiency for large-area perovskite-silicon tandem modules [53]. By 2025, solar technology had reached new milestones. Trina Solar set a world record with a 25.44% efficiency for large area n-type HJT modules [54], and LONGi achieved 34.85% efficiency for a 1cm^2 perovskite-silicon tandem cell, certified by National Renewable Energy Laboratory (NREL) [55]. In the same year, Singapore's Solar Energy Research Institute of Singapore (SERIS) produced a flexible perovskite organic tandem cell with 26.4% efficiency, a world record for flexible devices [56]. Emerging technologies also included quantum dot enhanced solar panels, designed to improve light absorption and energy yield [57].

1.9 Different Types of SCs

1.9.1 First Generation SCs

The first generation SCs comprise of crystalline and poly-crystalline silicon materials. The first silicon SC made of crystalline silicon was introduced by Chaplin and Fuller in 1954. It had an efficiency of 6% [58].

The crystalline silicon is an indirect band gap material (1.1 eV) [58]. The conventional crystalline silicon SC is made up of a homo-junction between p-type and n-type [58] silicon. Two electrodes are connected at each terminal completing the device structure. Similarly

the polycrystalline silicon SCs also feature p-n junction with properly doped n and p regions. The polycrystalline silicon SC [59, 60, 61, 62] was first developed in 1970 recording an efficiency of 1.5%. Crystalline silicon SCs have been extensively used for electricity generation in space vehicles and satellites. Despite their immense popularity in the global market, the cost of silicon SCs remain high for large-scale commercialization. Fig. 1.14 shows first generation SCs.

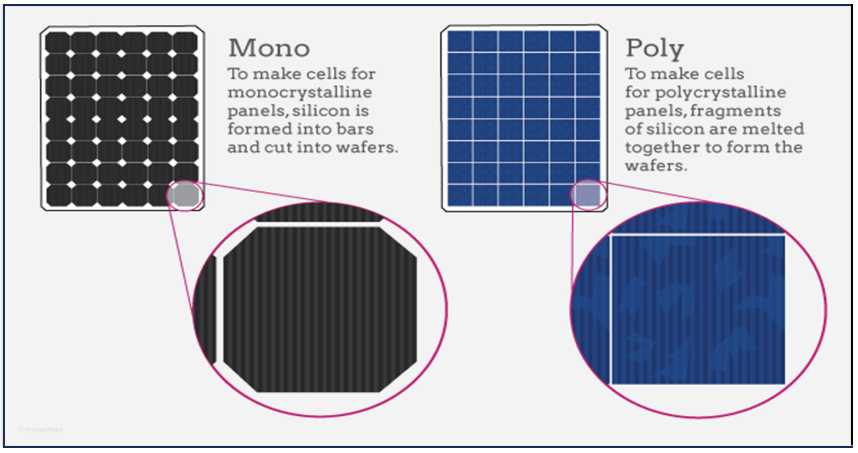


FIGURE 1.14: First generation SCs.

1.9.2 Second Generation SCs

1.9.2.1 Amorphous Silicon SC

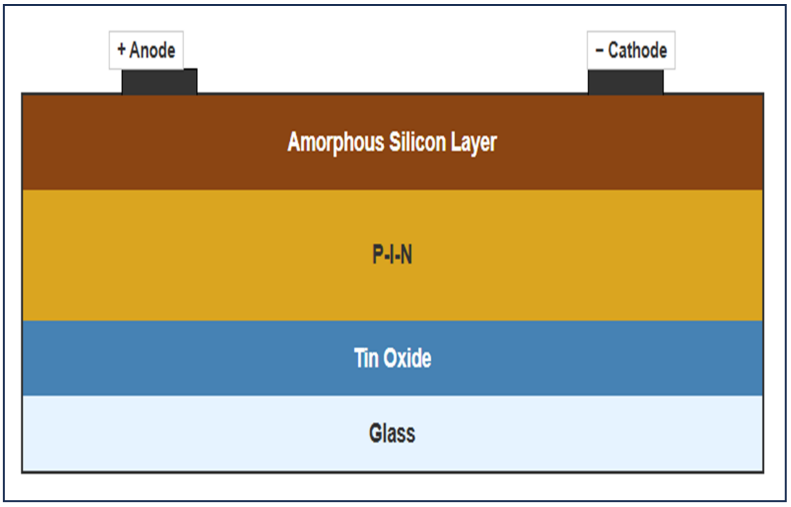


FIGURE 1.15: Amorphous silicon SC.

Amorphous silicon is a non-crystalline silicon (a-Si SC), and as the name suggests, the silicon atoms don't have a long range order [63, 64, 65]. It is also an indirect band gap material having a band gap of 1.7 eV [63, 64, 65]. The first ever Amorphous silicon SC (a-Si SC) was introduced by Charlson and Wronski in 1976 recording an efficiency of 2.4% [63, 64, 65]. Though a-Si is relatively inexpensive, the dangling bonds inside the material reduces the efficiency of the device. Fig. 1.15 shows amorphous silicon SC (a-Si) [63, 64, 65, 66].

1.9.2.2 Copper Indium Gallium Selenide SC

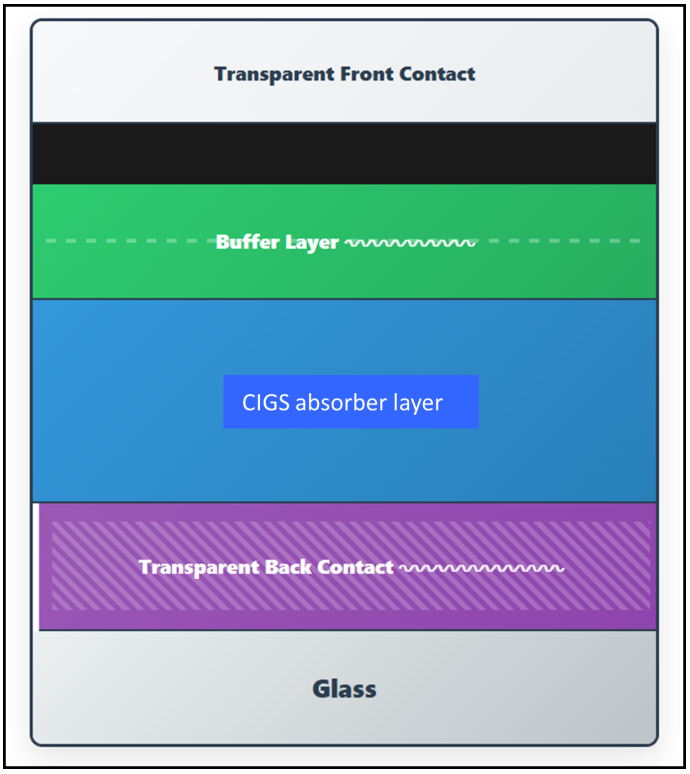


FIGURE 1.16: CIGS SC.

CIGS semiconductors comprise copper (Cu), indium(In), gallium(Ga) and selenium (Se). The material's band gap varies from 1 to 1.7 eV by altering its composition [66, 67, 68]. CIGS SCs are a type of thin-film SC, notable for their very thin absorber layer, which contributes to their reduced manufacturing cost. However, their significant drawback is a higher degradation rate. Although their production began in 1953, CIGS SCs were first utilized by Bell laboratories in the 1970s [66, 67, 68]. Among all SCs, CIGS holds the distinction of having the widest spectral response [67]. Fig. 1.16 exhibits a typical CIGS SC [66].

1.9.2.3 Cadmium Telluride SC

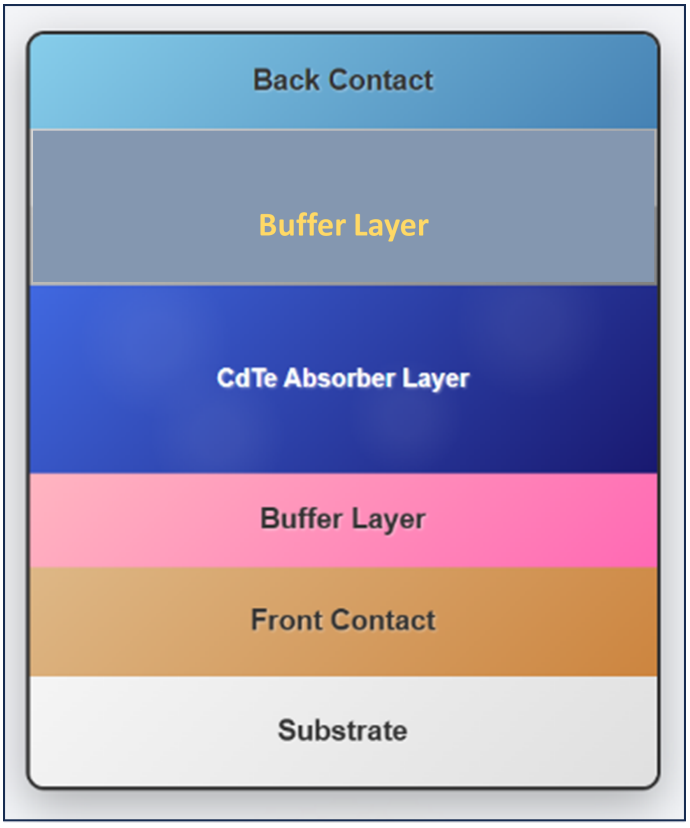


FIGURE 1.17: CdTe SC.

The photoconductivity inside cadmium telluride solarcell (CdTeSC) was first recognised in 1955 and the first CdTe SC was fabricated in 1963 by Cusano [69]. CdTe is a direct band gap semiconductor having a band gap of 1.5 eV and it has the structure similar to zinc blend [69]. The absorption coefficient of CdTe is exceptionally high and only a thin layer of absorption material is needed for the SC. The highest efficiency for CdTe SC was recorded at 21.5% in 2015 [70]. Fig. 1.17 displays a basic CdTe SC [71].

1.9.3 Third Generation SCs

The third generation SCs, also known as emerging PVs, include recent developments in SCs like copper zinc tin sulfide (CZTS SC), gallium arsenide SC (GaAs SC), organic SC (OSC), perovskite SC, quantum dot SC (QDSC), dye sensitized SC (DSSC), multi-junction SC (MJSC), hybrid SC and carbon nanoTube SC (CNT SC).

1.9.3.1 Copper Zinc Tin Sulfide SC

CZTSSCs are a promising thin film PV technology, composed entirely of earth abundant, non toxic elements, offering a sustainable alternative to conventional solar materials containing scarce or toxic elements like Indium or Cadmium [72]. With an optimal



FIGURE 1.18: CZTS SC.

direct band gap of 1.4-1.5 eV and high optical absorption coefficients exceeding 10^4 cm^{-1}, CZTS can efficiently harvest light in thin films of just 1-2 micrometers, theoretically enabling efficiencies above 30% [72]. However, current laboratory devices achieve efficiencies of only 12-13% [72] efficiency due to challenges in controlling secondary phase formation, managing defect states that cause voltage losses, and optimizing the complex four element composition. Despite these obstacles, ongoing research in synthesis methods, defect physics understanding and device architecture improvements positions CZTS as a potentially cost-effective pathway for large scale sustainable solar energy implementation [72]. Fig. 1.18 shows a simple CZTS SC.

1.9.3.2 Gallium Arsenide SC

GaAs SC is a direct band gap material with a band gap of 1.42 eV and has been revelation in the field of thin film SCs [73, 74]. The relatively high absorption coefficient

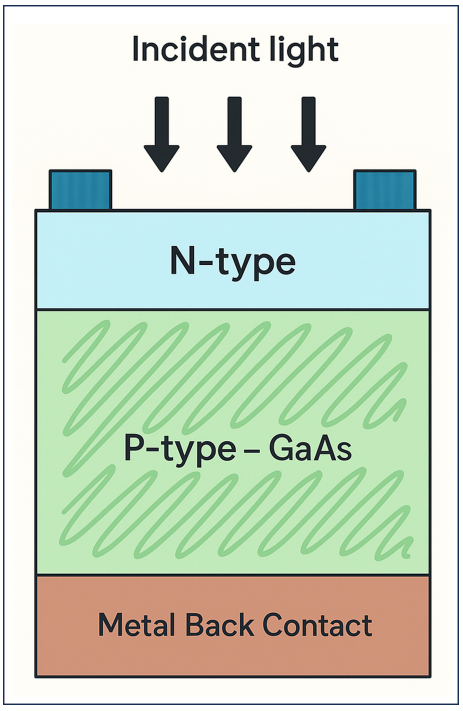


FIGURE 1.19: GaAs SC.

of gallium arsenide allows only a thin layer of absorber layer in the device [75]. The major advantages of gallium arsenide include the radiation resistant nature which makes it easier to operate the SC even at very high temperature. The GaAs SC has recorded the highest efficiency for any single-junction SC with a record PCE of 29.1% [74]. Fig. 1.19 illustrates a basic structure of GaAs SC.

1.9.3.3 Organic SC

OSCs use conjugated organic semiconductors, which are carbon based molecules with alternating single and double bonds for light absorption and charge transport. These materials form π and π^* molecular orbitals, with their energy gap acting as the band gap [76, 77, 78, 79, 80, 81, 82, 83]. Due to their low dielectric constant, absorbed light creates bound e-h pairs called excitons, which must be separated to generate current. The first OSC, developed in 1978 using merocyanine, achieved 0.5% efficiency. Later advancements introduced the bilayer cell (1986) and the bulk hetero-junction (1995), which is now the most common design. Despite their low cost, OSCs face challenges like limited stability and low efficiency [76, 77, 78, 79, 80, 81, 82, 83]. Fig. 1.20 illustrates the basic OSC device structure [84].

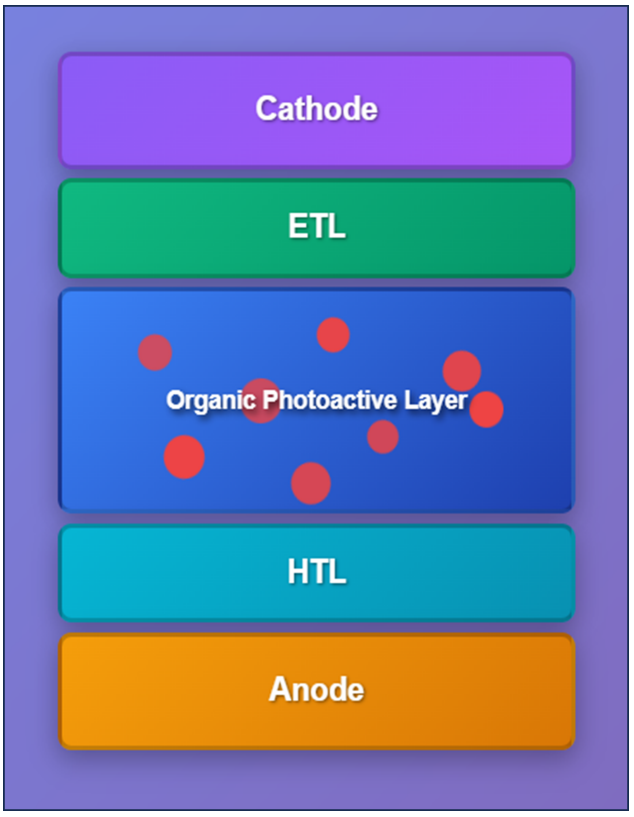


FIGURE 1.20: Organic SC.

1.9.3.4 Perovskite SC

The emergence of perovskite SC is considered as a landmark in PVs due to their very high PCE. The first ever perovskite material discovered was calcium titanium oxide in 1839 [85]. Materials having a similar structure of calcium titanium oxide and with the chemical formula ABX_3 are considered as perovskites [85].

In the formula, A and B represent bigger and smaller cations, while X represents the anion [85]. The first perovskite SC was introduced in 2009 by Miyasaka. The organometal halides used were methyl ammonium lead iodide and methyl ammonium lead bromide, recording efficiencies of 3.81% [45, 86] and 3.13% [45, 86]. Fig. 1.21 shows the device structure of a simple perovskite SC.

1.9.3.5 Quantum Dot SC

The concept of QDSC was first introduced in 1990 by Burnham and Duggan. QDs are extremely tiny semiconductor particles with a size resembling that of Bohr radius of an

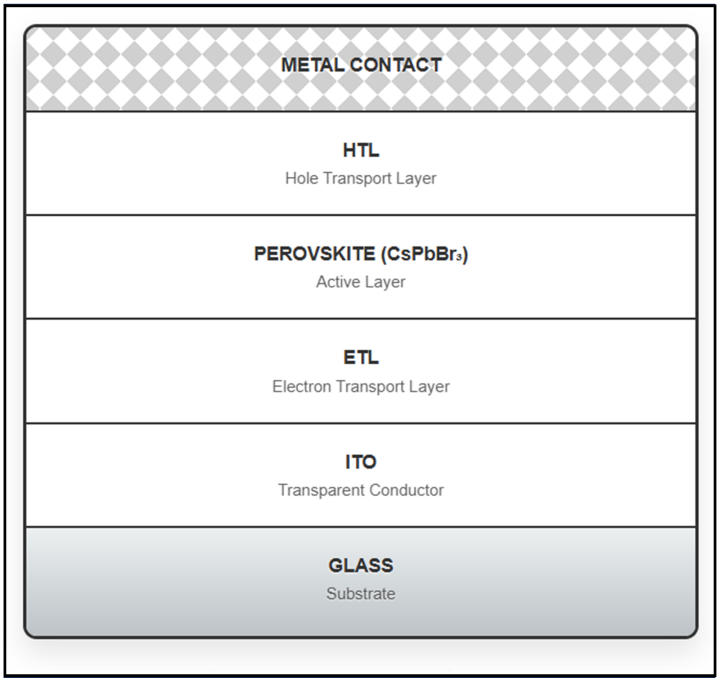


FIGURE 1.21: Perovskite SC.

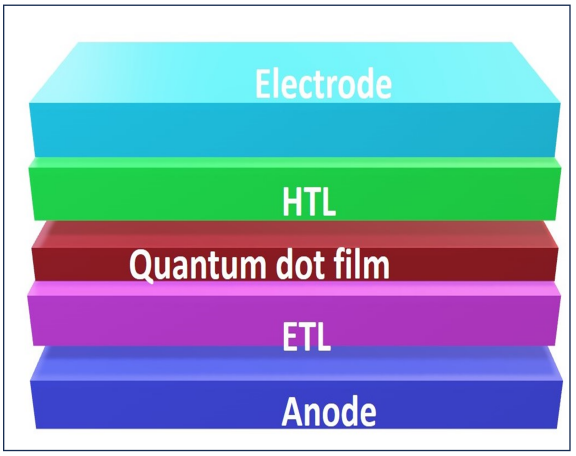


FIGURE 1.22: Quantum Dot SC.

exciton [46, 87, 88, 89]. Since QDs are only a few nanometers in size, quantum confinement leads to discrete electron energy levels. These energy levels can be tuned by varying the particle size, and it results in tunability of the band gap [46, 87, 88, 89]. This feature enables quantum dots to form multi-junction SCs where semiconductors of different band gaps can be incorporated. The major feature of QDs is their potential to generate more than one pair of electron and hole upon the absorption of a photon [46, 87, 88, 89]. Fig. 1.22 shows a typical QDSC.

1.9.3.6 Dye Sensitized SC

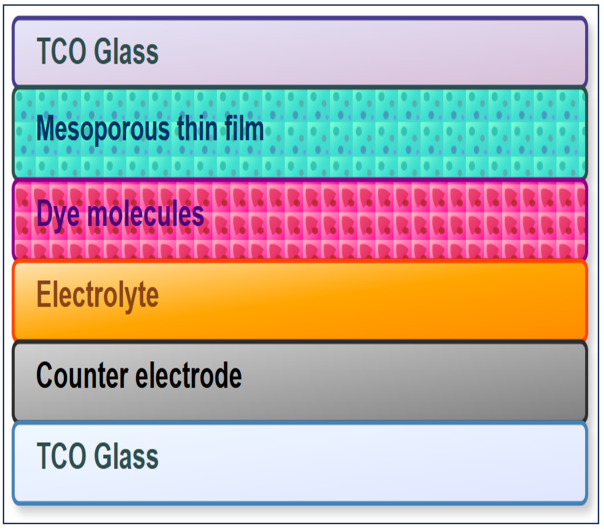


FIGURE 1.23: Dye sensitized SC.

DSSCs use organic dyes as their absorbing materials. DSSC was developed in 1970s and is easily processable even at very low temperatures. The structure of a DSSC starts with a front electrode most commonly transparent conducting oxide (TCO) coated on a substrate followed by porous titanium dioxide coating. Here the titanium dioxide (TiO_2) being a wide band gap material functions as the window layer [90, 91, 92, 93]. Porous TiO_2 is a network of TiO_2 nanoparticles, and the porous layer is coated with the absorber material. The organic dye and a back electrode completes the structure [90, 91, 92, 93]. The back electrode is commonly TCO on a dye coated electrode and an electrolyte medium is included in between them. The key limitation of DSSCs is their instability of the device [90, 91, 92, 93]. Fig. 1.23 displays a typical DSSC [94]. The working principle of this SC is explained briefly in section.

1.9.3.7 Multi-Junction SC

MJSCs stack multiple semiconductor layers, with varying band gaps to capture a broader range of the solar spectrum. This helps in achieving efficiencies far beyond the Shockley–Queisser limit of single-junction cells (33%) [95]. Developed in the late 1970s, early MJSCs reached 20% efficiency, with major milestones in the 1990s pushing efficiencies above 40% using GaInP/GaAs/Ge architectures [96]. In 2020, a six-junction device set a record efficiency of 47.1% under concentrated sunlight [97]. These are primarily used in space due to their high performance, ongoing research into low-cost materials such as

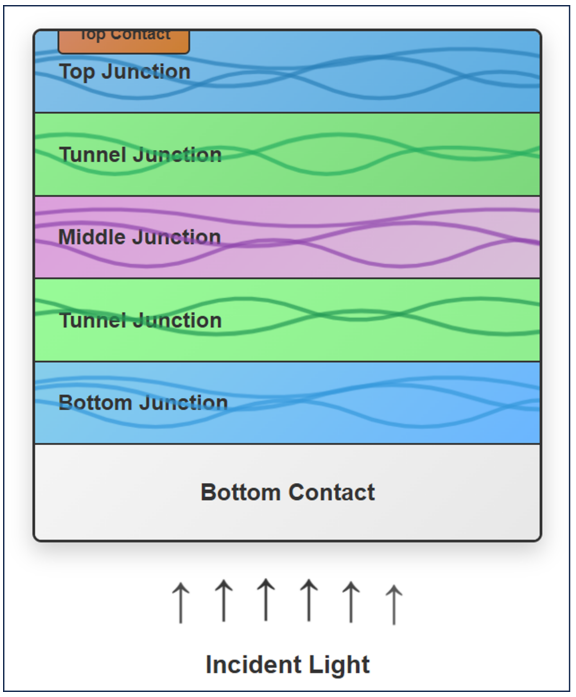


FIGURE 1.24: Multi-Junction SC.

perovskites, and can enable broader terrestrial adoption [98]. Fig. 1.24 shows a typical MJSC [99].

1.9.3.8 Hybrid SC

Hybrid SCs comprise a combination of organic and inorganic materials to improve efficiency and stability while keeping costs low. Emerging in the early 2000s, they use inorganic nanoparticles or quantum dots (QDs) to enhance charge separation and transport [100, 101, 102]. Recent advancements in perovskites seem to boost their performance, making hybrid SCs a promising option for flexible and affordable PVs [100, 101, 102, 103]. Fig. 1.25 displays a hybrid SC device structure.

1.9.3.9 Carbon NanoTube SC

CNTSC carry the remarkable electrical, mechanical and optical properties of CNTs to significantly boost PV performance. CNTs are particularly effective as charge transport materials due to their high conductivity and large surface area, which facilitates efficient electron collection and transport within the SC [104, 105, 106]. These cells often combine CNTs with polymers or inorganic materials to improve light absorption and charge

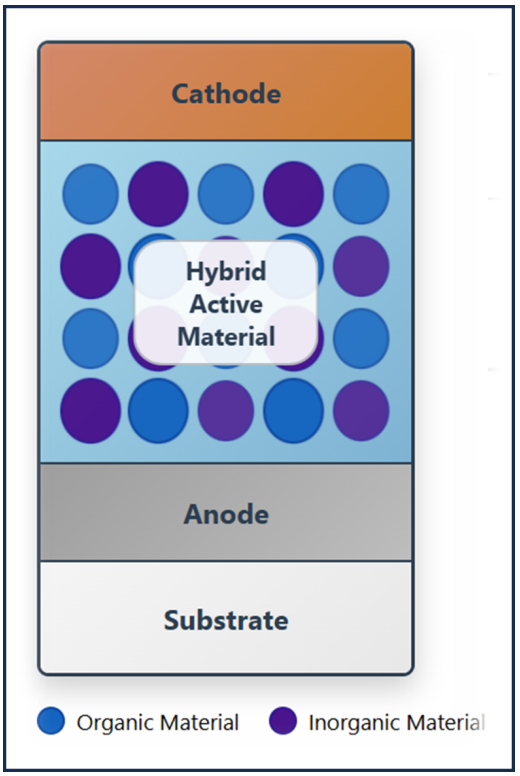


FIGURE 1.25: Hybrid SC.

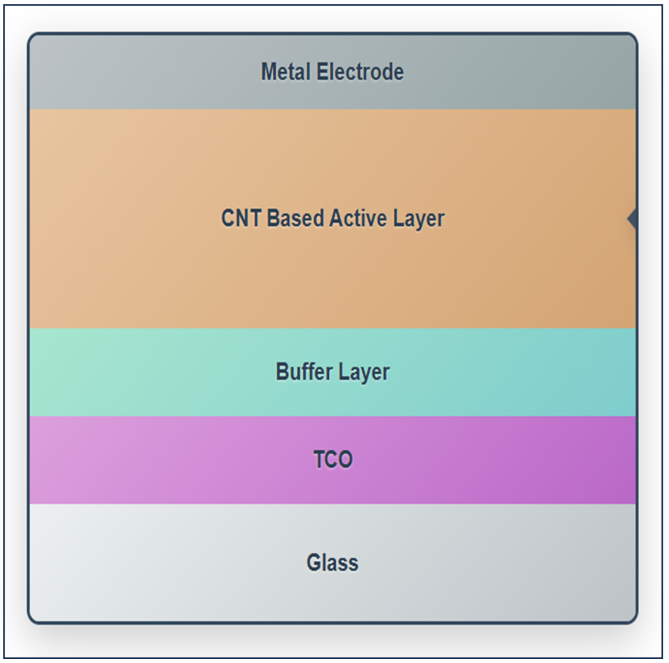


FIGURE 1.26: CNT based solar cell.

separation. Research studies since the early 2000s illustrates incorporating CNTs can improve device efficiency and stability, making them promising candidates for flexible and lightweight SC technologies [104, 105, 106]. Fig. 1.26 illustrates CNT based OSC device structure.

1.9.4 Fourth Generation SCs

1.9.4.1 Graphene Derivatives Based SCs

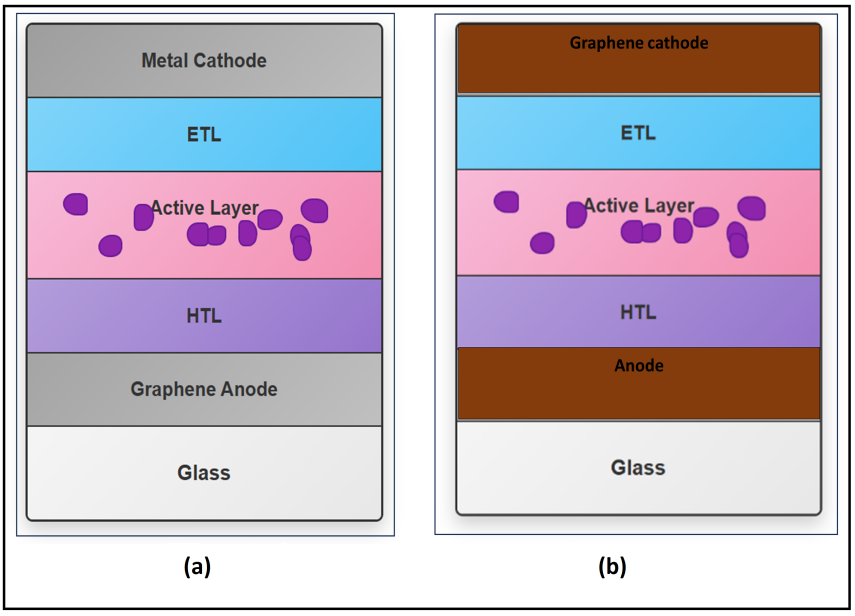


FIGURE 1.27: Graphene derivatives based SC with graphene derivative as (a) anode and (b) cathode.

Graphene derivatives, such as graphene oxide (GO) and reduced graphene oxide (rGO), have exhibited considerable interest in OPV technology [107, 108]. Their widespread adoption is attributed to their undeniable unique properties such as good electrical conductivity, large surface area, and mechanical flexibility. Fig. 1.27 (a) and Fig. 1.27 (b) show typical SCs with graphene anode and graphene cathode respectively. Fig. 1.28 (a) and Fig. 1.28 (b) show typical SCs with graphene HTL and graphene ETL respectively. Fig. 1.29 shows graphene derivative based SC with graphene derivative in active layer. These figures exhibit how graphene derivatives are introduced as electrodes, interfacial layers and in absorber layers of OSC [107]. These materials are frequently incorporated as charge transport layers or as additives to enhance charge extraction, and minimize recombination in both organic and perovskite SCs [109, 110, 111]. Since the early 2010s,

implementing graphene derivatives in OSCs has enhanced device stability and efficiency, making them promising future components for next-generation PV devices especially in OSCs [109, 110, 111]. These SCs are explained elaborately in chapter 3.

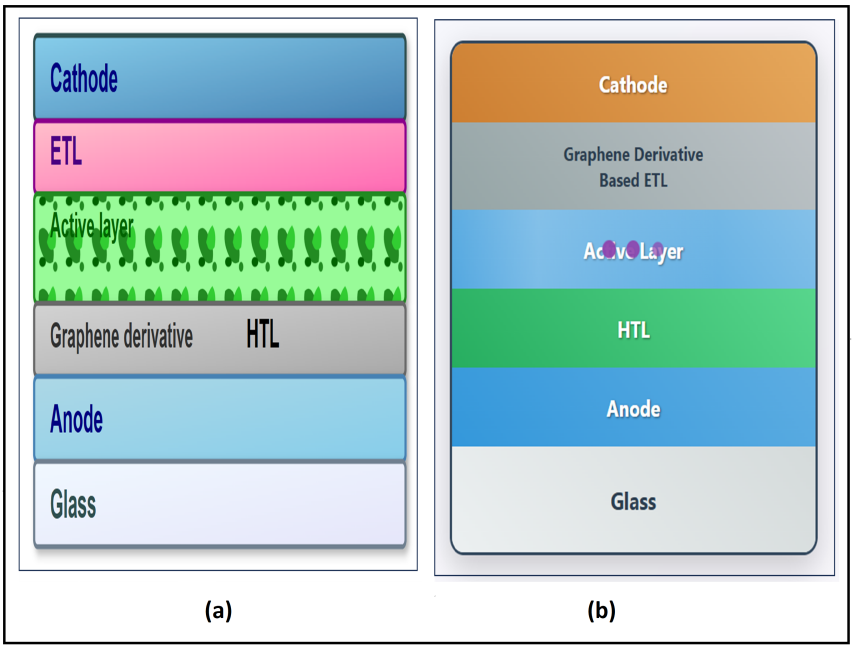


FIGURE 1.28: Graphene derivative based SC with graphene derivative as (a) HTL and (b) ETL.

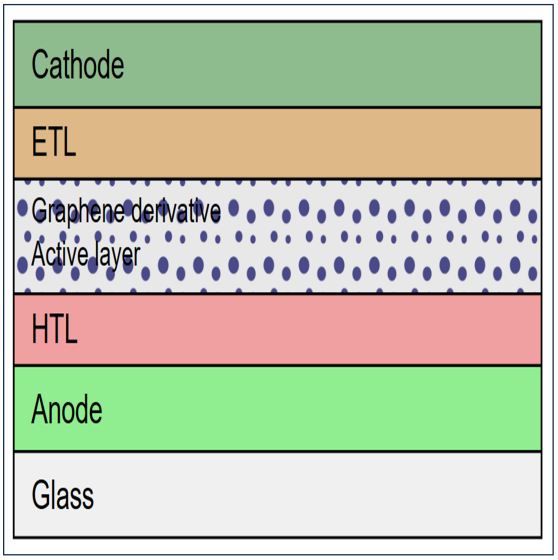


FIGURE 1.29: Graphene derivative based SC with graphene derivative in active layer.

Chapter 2

Bulk Hetero-Junction Organic Solar Cells

This chapter provides a comprehensive overview on organic solar cells (OSCs), with a special emphasis on bulk hetero-junction organic solar cells (BHJOSCs). The discussion begins with a general overview of OSCs and later explores the history, working principles and core concepts of OSCs. BHJOSC, one of the most extensively researched area of organic photovoltaics (OPVs) is discussed meticulously in this chapter.

OSCs are a groundbreaking PV technology that harnesses carbon-based organic semiconductors like conjugated polymers and small molecules to transform sunlight into electricity via the PV effect. These differ from traditional silicon-based SCs by offering distinct benefits such as lightweight, mechanical flexibility and solution processability at low temperatures. This leads to low-cost manufacturing through roll-to-roll printing on flexible substrates [112, 113, 114, 115, 116].

Among various architectures, the bulk hetero-junction (BHJ) design has proven to be the most effective for OSCs. This BHJ structure significantly increases the interfacial area between the donor and acceptor, which is crucial because photogenerated excitons in organic materials have short diffusion lengths, typically only 10-20 nanometers (nm). Contemporary BHJOSCs often use conjugated polymer donors mixed with fullerene-acceptors (FAs). More recently, NFAs including small molecule non-fullerene acceptors (SM-NFAs) have been employed, pushing PCE beyond 18% in laboratory environments, while retaining the benefits of mechanical flexibility, lightweight design and the potential for large area and cost effective manufacturing.

2.1 OSCs-Their Significance and Advantages

OSCs offer extraordinary advantages, as already mentioned in section 1.9.3.3 and the beginning of this chapter, which allows them to be manufactured on bendable substrates [117]. This property makes them the best choice for portable electronic devices with curved surfaces. Another significant advantage lies in their tunable optical properties. The band gap of organic materials can be engineered at the molecular level, enabling precise customization of their light absorption ranges. Many OSCs are also semi-transparent, making them suitable to be integrated seamlessly into windows and building facades without obstructing natural light.

OSCs perform well under low or diffuse light conditions, such as indoors or on cloudy days, sometimes even outperforming silicon SCs in these environments. The energy payback time for OSCs is also notably short, so they can recoup the energy invested in their production more quickly. Their versatility is another advantage. They come in various colors and levels of transparency, allowing for more architectural creativity. Furthermore, their lightweight construction reduces the structural load on buildings. Finally, some organic solar materials can be engineered for biodegradability, enhancing their environmental friendliness at the end of their lifecycle [77, 82, 117, 118, 119, 120, 121, 122, 123, 124, 125, 126, 127, 128, 129].

Organic semiconductors comprise the major components of OSCs. Understanding their importance, types, structure and working is of utmost significance to discover more about OSCs.

2.2 Organic Semiconductors

Organic semiconductors are carbon-based materials that exhibit semiconducting behaviour, featuring π-conjugated systems interconnected through Van der Waals forces [130, 131, 132, 133, 134]. They form a distinct group between inorganic semiconductors (e.g., silicon) and insulators. They combine the electronic functionality of semiconductors with the mechanical and chemical advantages of organic materials. These characteristics enable innovative applications in flexible electronics, Organic Light Emitting Diodes (OLEDs) [135], Organic Field Effect Transistors (OFETs) [136] and Organic PhotoVoltaics (OPVs) [130, 131].

2.2.1 Major Classes of Organic Semiconductors

The major classes of organic semiconductors are small molecules and conjugated polymers. Small molecules are discrete, low molecular weight organic compounds [137, 138]. Examples of small molecules organic semiconductors include pentacene, rubrene, anthracene, fullerenes (example: Phenyl-C61-butyric acid methyl ester (C_{60} fullerene functionalized with a phenyl-butyric acid methyl ester side chain) (PCBM)) and various dye molecules like phthalocyanine. Conjugated polymers are long chain molecules with many repeating units. Examples of polymers are common conductive polymers such as polyacetylene, polyaniline, polythiophene (example: Poly(3-hexylthiophene) (P3HT)) and poly(p-phenylene vinylene) (PPV), which are used in electronics. Polymers often exhibit properties similar to conventional organic polymers, and their electrical properties can be tuned through synthesis.

Conjugated polymers are long chain macromolecules with repeating conjugated units which include (P3HT) [139, 140], polyfluorenes, poly(p-phenylene vinylene) derivatives and (Poly[(2,6-(4,8-bis(5-(2-ethylhexyl)thiophen-2-yl)-benzo[1,2-b:4,5 -b']dithiophene))-alt-(5,5-(1',3'-di-2-thienyl-5',7'-bis(2-ethylhexyl)benzo[1',2'-c:4,5-c'] dithiophene4,8-dione))]) (PBDB-T) derivatives [141, 142]. Advantages of conjugated polymers are flexibility, solution processability and tunable properties achieved through side chain engineering. P3HT and PBDB-T are the two major donor materials that were used in our study. Fig. 2.1 and

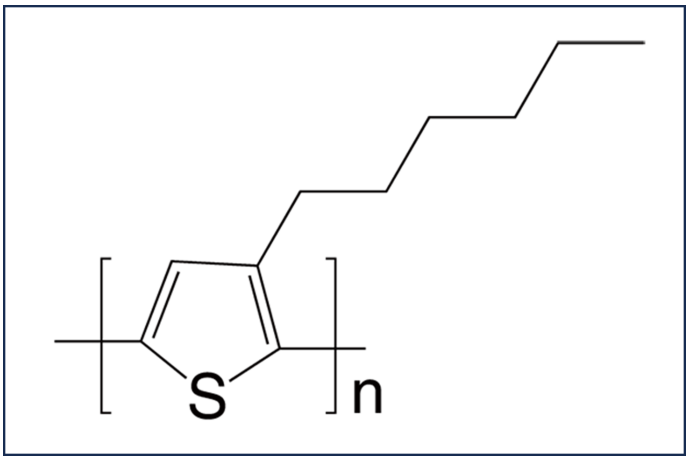


FIGURE 2.1: Chemical structure of P3HT.

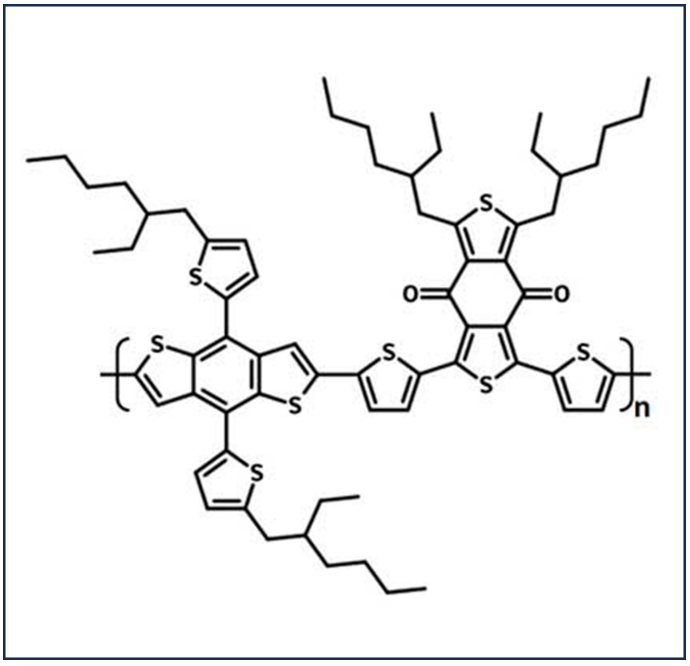


FIGURE 2.2: Chemical structure of PBDB-T.

Fig. 2.2 show the chemical structures of P3HT and PBDB-T respectively. Fig. 2.3 shows the chemical structure of phenyl-C61-butyric acid methyl ester (PCBM-fullerene derivative). 2,9-bis(2-methylene-(3(1,1-dicyanomethylene)benz[f]indanone))-7,12-dihydro-(4,4,10,10-tetrakis
(4-hexylphenyl)-5,11-diocthylthieno [3 ,2 :4,5]cyclopenta[1,2-b]thieno[2 ,3 :3 ,4]cyclopenta[1 ,2 :4,5]

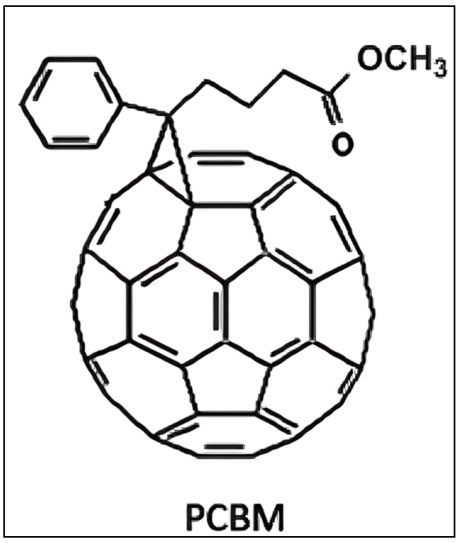


FIGURE 2.3: Chemical structure of PCBM.

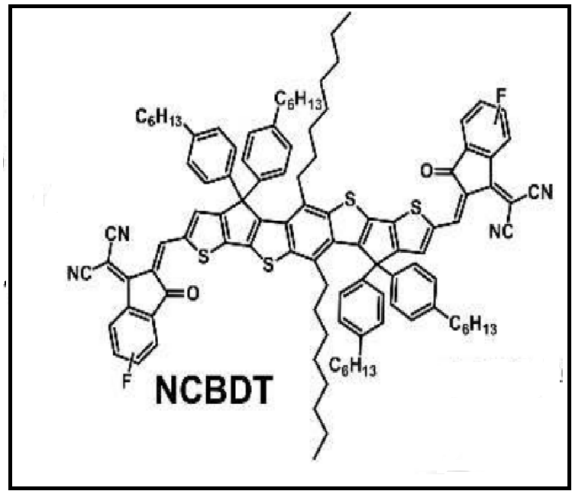


FIGURE 2.4: Chemical structure of NCBDT.

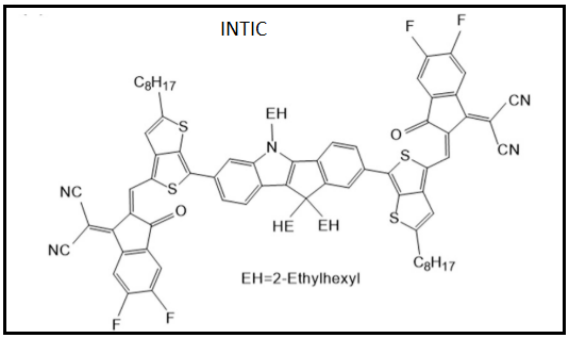


FIGURE 2.5: Chemical structure of INTIC.

thieno[2,3-f]benzothiophene) (NCBDT) and 2,2'-((2Z,2'Z)-((6,6'-(5,10,10-tris(2-ethylhexyl)-5,10-dihydroindeno[1,2-b]indole-2,7-diyl)bis(2-octylthieno[3,4-b]thio-phene-6,4-diyl))bis(methanylylidene)difluoro-3-oxo-2,3-dihydro-1H-indene-2,1-diylidene))dimalononitrile (INTIC) (SMNFA derivative) are used as acceptors in our study. Fig. 2.4 and Fig. 2.5 show the chemical structures of NCBDT [143, 144] and INTIC [145] respectively.

2.2.2 Fundamental Structure and Properties of Organic Semiconductors

Conjugated materials have alternating single and double bonds between adjacent carbon atoms formed by the sp^2 hybridized orbitals [132, 133, 134]. The sp^2 hybridization in carbon atoms consists of one s orbital along with two p_x and p_y orbitals forming three sp^2 hybridized orbitals of equal energy, whereas the p_z orbital remains unhybridized. The hybridized sp^2 orbitals form σ bonds, while the unhybridized p_z orbitals overlap to form π bonds [133]. The π orbital electrons are delocalized over the carbon atoms, and these delocalized electrons are responsible for the conducting behaviour of organic semiconductors. The unhybridized p_z orbitals overlap resulting in the formation of bonding and antibonding molecular orbitals. Antibonding orbitals have higher energy than bonding orbitals [132, 133, 134].

Small molecule organic semiconductors are low molecular weight compounds with well defined π-conjugated structures, typically consisting of electron rich donor units, electron deficient acceptor units, and conjugated π-bridges connecting them. This architecture, often in an A–D–A or D–A–D form facilitates efficient charge transport and energy level tuning. The core donor units (such as benzodithiophene or triphenylamine) provide electron density and structural rigidity, while acceptor end groups (like dicyanomethylene or rhodanine) lower the LUMO energy levels to enhance electron affinity. The π-bridges, such as thiophene or phenylene, extend conjugation and improve planarity, promoting strong π–π stacking in the solid state. Side chains, often alkyl groups, are introduced to enhance solubility, control crystallinity, and influence film morphology. The planarity and conjugation length of the molecule are crucial for narrowing the band gap and improving charge mobility. Examples of small molecule semiconductors include pentacene and rubrene for p-type transport, Tris(8-hydroxyquinolinato)aluminium(III) or aluminum tris(8-hydroxyquinoline) (Alq_3) for n-type transport, and A–D–A type acceptors like ITIC and Y6, which are commonly used in NFA based OSCs [132, 133, 134].

In comparison to inorganic semiconductors, the highest occupied molecular orbital known as the HOMO and the lowest unoccupied molecular orbital known as the LUMO

are analogous to the V_B and C_B, respectively [133]. Charge transport in organic semiconductors takes place through these HOMO and LUMO levels. The energy gap between the HOMO and the LUMO levels defines the band gap of an organic semiconductor (which typically ranges from 1.5 to 3.5 eV). The band gap of a semiconductor plays a critical role in determining light absorption and electronic transitions [132, 133, 134].

In contrast to their inorganic counterparts, organic semiconductors often lack long range crystalline order and instead exhibit substantial structural disorder. This structural disorder influences their charge transport, which primarily occurs via thermally activated hopping between localized states [132, 133, 134]. These materials exhibit lower charge carrier mobilities (on the order of 10^{-6} to $10^{-1}\text{cm}^2/\text{Vs}$), yet offer advantages such as mechanical flexibility, large area processability and compatibility with solution based and printing technologies [146, 147, 148, 149, 150].

2.2.3 Charge Transport Mechanisms in Organic Semiconductors

Charge transport in organic semiconductors is specific and differs significantly from their inorganic counterparts. Transport mechanisms occurring in organic semiconductors are hopping transport, polaronic transport and disorder effects [146, 148, 149]. Hopping transport occurs when charge carriers move by thermally activated hopping between localized states, rather than through delocalized bands [146, 148, 149]. Polaronic transport of charge carriers arise when charge carriers deform the surrounding molecular structure, thus leading to the formation of a polaron—charge carrier coupled with associated lattice distortions. Whereas, disorder effects encompass both energetic and positional irregularities and substantially influence charge carrier mobility [147].

2.3 The Operational Mechanism of OSCs

The working principle of an OSC is based on the generation, diffusion and separation of e-h pairs known as excitons. When a photon with energy equal to or greater than the band gap of the organic semiconductor is absorbed, an electron in the HOMO is excited to the LUMO, leaving behind a hole in the HOMO [22, 133, 151, 152, 153, 154, 155]. When an exciton is generated in the donor material, it diffuses to the hetero-junction (interface formed between two different materials) driven by the energy offset, where the e-h (exciton) pair is separated [22, 152, 154, 155]. After exciton dissociation, the generated electrons and holes must be transported to the cathode and anode, respectively, where they are collected

to produce electrical current [22, 131, 151, 154, 155]. The charge transport within an OSC primarily involves drift and diffusion. Drift current arises from the movement of charge carriers under the influence of an internal electric field (potential gradient) established inside the device, while diffusion current results from the movement of carriers along concentration gradients [22]. The internal electric field is created by employing electrodes with a high work function anode and a low work function cathode which generates a built in potential across the active layer [22, 151, 152, 154, 155]. Diffusion currents develop due to variations in carrier concentration, which are generally highest near the D-A hetero-junction [22, 133, 154, 155].

2.4 History of OSCs

The modern era of OPVs began in 1986 with the pioneering work of Dr. Ching W. Tang at Eastman Kodak. Tang developed the first two-layer OPV cell by stacking copper phthalocyanine (CuPc) as the electron donor and a perylene tetracarboxylic derivative as the electron acceptor [156]. This architecture achieved a PCE of approximately 1%, representing a significant improvement over previous designs and introducing the D-A hetero-junction concept, which remains a cornerstone of OSC design [156].

The 1990s marked a pivotal shift in OPVs with the advent of polymer-based SCs, which introduced the potential for low-cost, solution-processed manufacturing. In 1992, a research group at the University of California, Santa Barbara, led by Alan Heeger, demonstrated the first polymer SC using poly[2-methoxy-5-(2 -ethylhexyloxy)-p-phenylene vinylene] (MEH-PPV) as the active layer [157].

A major breakthrough followed in 1995 when Heeger's team, in collaboration with the University of Groningen, introduced the BHJ concept. This innovation involved blending electron-donating and electron-accepting materials to form a nanoscale interpenetrating network, greatly enhancing charge separation and transport. This replaced less efficient planar bilayers and became the foundation of most modern OSC designs. The approach was further strengthened with the development of fullerene derivatives such as PCBM as electron acceptors, which, when blended with conjugated polymer donors, dominated throughout the late 1990s and early 2000s [151, 158].

In 2001, researchers at the University of Linz demonstrated that thermal annealing of the active layer could enhance morphology, improving charge transport and device performance [159]. A significant leap came in 2005 with the introduction of low-band gap

polymers such as P3HT, which, when blended with fullerene derivatives like PCBM, enabled PCEs of around 5% [160]. In 2006, researchers began using processing additives such as 1,8-diiodooctane (DIO) to fine-tune morphology, further boosting device performance [161]. In 2007, tandem OSC devices stacking multiple active layers to absorb different regions of the solar spectrum were demonstrated, achieving higher efficiencies [162].

In 2009, the inverted device architecture emerged, reversing electrode polarity to improve stability and operational lifetime. By 2010, researchers at Solarmer Energy reported a certified efficiency of 8.13% for a single-junction OSC, marking a major milestone [163]. In 2012, small molecule OSCs began to rival polymer devices in efficiency, offering advantages such as higher purity and batch-to-batch consistency [164]. In 2013, the German company Heliatek announced a record 12% efficiency for a tandem OSC, highlighting commercialization prospects [165].

A pivotal breakthrough occurred in 2015 with the introduction of NFAs, particularly fused-ring acceptors such as ITIC, which improved light absorption and energy level tunability [166]. The development of Y-series NFAs such as Y6 during 2016–2017 further boosted single-junction device efficiencies beyond 15% [167].

By 2018, commercialization progress accelerated, with OPV module production by Heliatek in Germany, Advanced Solar Cells Alliance (ASCA) by ARMOR in France, and Sunew in Brazil [168]. In 2019, researchers at Nankai University in China achieved 17.3% efficiency in a single-junction OSC using a novel acceptor material, underscoring OPV's competitiveness [99].

The 2020s have witnessed remarkable progress. In 2020, researchers from the University of Michigan and NREL reported 18.2% PCE for a two-terminal tandem OSC [169]. This was surpassed in 2021 when the Chinese Academy of Sciences achieved 18.7% efficiency in a single-junction OSC. In 2022, Shanghai Jiao Tong University set a new record of 19.0% for a single-junction device, nearing the 20% threshold considered crucial for broad commercialization. By 2023, stability became a primary focus, with several groups demonstrating devices maintaining over 80% of initial efficiency after thousands of hours under real-world conditions [169].

By 2024, commercial organic solar modules exceeding 12% efficiency were available, targeting applications in building integrated photovoltaics (BIPV), wearable electronics, and IoT devices. Looking ahead, ongoing research seeks to design new donor and acceptor materials with enhanced optical and electronic properties [170].

2.4.1 Major Types of OSCs

The major types of OSCs include single layer OSCs, bilayer (planar hetero-junction) OSCs, BHJOSCs, tandem OSCs and DSSCs.

2.4.1.1 Single Layer OSC

The simplest OSC design consists of a single layer of organic material sandwiched between two different electrodes. The working principle of this particular design is that, the difference in work function between the electrodes creates an electric field that helps separate excitons [167]. However, this field is rarely strong enough for efficient charge separation. Materials usually used in single layer OSCs are small molecules like phthalocyanines or conjugated polymers like polythiophene [167]. The efficiency of single layer OSCs typically exhibit very low PCE(<1%) due to poor exciton dissociation and high recombination rates. They are primarily of historical interest rather than practical application. Fig. 2.6 (a), (b) and (c) show single layer, bilayer and BHJOSC respectively [167].

2.4.1.2 Bilayer Hetero-Junction OSC

Bilayer (planar hetero-junction) OSC structures consist of distinct organic layers—an electron donor and an electron acceptor that are stacked between electrodes. The working principle of bilayer (planar hetero-junction) OSC is that the interface between donor and acceptor materials facilitates exciton dissociation [171, 172]. After separation, electrons travel through the acceptor material to one electrode, while holes travel through the donor material to the opposite electrode. Materials used in bilayer OSCs are common donor materials including copper phthalocyanine (CuPc), P3HT, and MEH-PPV. Acceptor materials often include fullerene derivatives like PCBM or perylene derivatives. Efficiency and limitations of bilayer OSCs achieve 1-5% efficiency [171, 172]. Their performance is limited by the short exciton diffusion length (10-20 nm) in organic materials, meaning only excitons generated near the D-A interface contribute to photocurrent [171, 172].

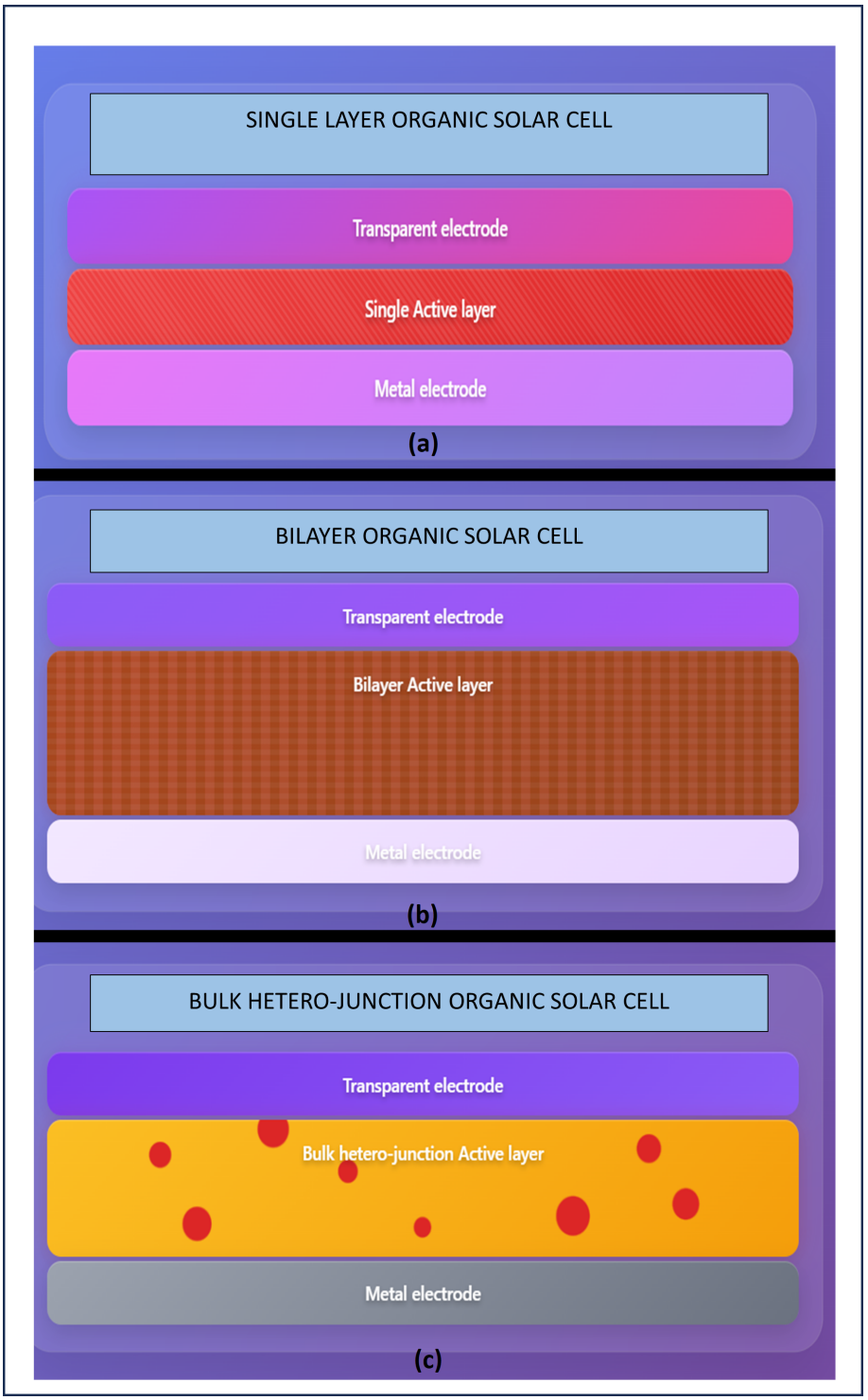


FIGURE 2.6: (a) Single layer, (b) bilayer and (c) BHJOSC

2.4.1.3 Bulk Hetero-Junction OSC

BHJOSCs comprise a blend of donor and acceptor materials blended together. They create a three-dimensional (3D) interpenetrating network with significantly increased interfacial area. Working principle of the BHJOSC can be defined using the following processes. The increased D-A interfacial area ensures most excitons reach an interface within their diffusion length, dramatically improving exciton dissociation efficiency. Major blend materials used in BHJOSCs include P3HT:PCBM [172], PTB7:$PC_{70}BM$, and PBDB-T:ITIC [172]. Recently NFAs have pushed efficiencies higher. Efficiency and advantages of BHJ cells are among the most efficient OSC designs, achieving 8-17% efficiency [172]. Their performance heavily depends on morphology control, and the phase separation between donor and acceptor materials must be on the scale of exciton diffusion length [172].

2.4.1.4 Ternary Blend OSC

Ternary Blend OSCs have a structure with three components (typically two donors and one acceptor or one donor and two acceptors) blended together. The working principle of ternary blend OSCs is that the third component enhances light absorption, improves morphology, and facilitates energy/charge transfer [173]. Materials used in ternary blend OSCs include (Poly[(2,6-(4,8-bis(5-(2-ethylhexyl-3-fluoro)thiophen-2-yl) benzo [1,2-b:4,5-b']dithiophene))-alt-(5,5-(1′,3′-di-2-thienyl-5′,7′-bis(2-ethylhexyl) benzo[1′,2′-c:4′,5′-c'] dithiophene-4,8-dione))]:2,2′-((2Z,2′Z)-((12,13-bis(2-ethylhexyl)-3,9-diundecyl-12,13 -dihydro- [1,2,5]thiadiazolo[3,4-e]thieno[2″,3″:4′,5′] thieno[2′,3′:4,5]pyrrolo[3,2-g] thieno[2′,3′:4,5] thieno[3,2-b]indole-2,10-diyl)bis(methanylylidene))bis(5,6-difluoro-3-oxo-2,3- dihydro-1H-indene-2,1-diylidene))dimalononitrile:[6,6]-Phenyl-C_{71}-butyric acid methyl ester) [174] (PM6:Y6:PC71BM) or (Poly[(2,6-(4,8-bis(5-(2-ethylhexyl)thiophen-2-yl) benzo[1,2-b:4,5-b']dithiophene))-alt-(5,5-(1′,3′-di-2-thienyl-5′,7′-bis(2-ethylhexyl) benzo[1′,2′-c:4′,5′-c']dithiophene-4,8-dione))]):3,9-bis(2-methylene-(3-(1,1-dicyanomethylene)-indanone))-5,5,11,11-tetrakis(4-hexylphenyl)-dithieno[2,3-d:2′,3′-d′]-s-indaceno[1,2-b:5,6-b'] dithiophene:[6,6]-Phenyl-C_{71}-butyric acid methyl ester) (PBDB-T: ITIC:PC71BM) [174]. Enhanced efficiency and advantages of ternary blends can improve efficiencies beyond binary counterparts by, broadening absorption spectra and optimizing morphology. Recent ternary OSCs have achieved efficiencies near to 18% [174]. Fig. 2.7 (a) and (b) show ternary and tandem OSC respectively [174].

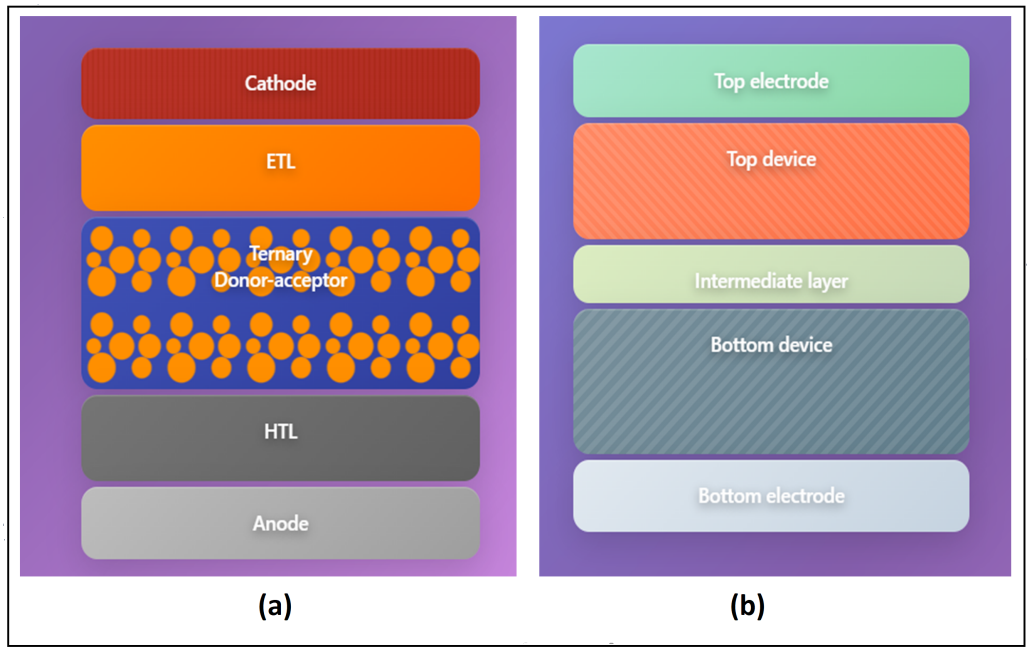


FIGURE 2.7: (a) Ternary OSC and (b) Tandem OSC

2.4.1.5 Tandem OSC

Tandem OSCs consist of multiple SCs with complementary absorption spectra stacked and connected in series. The working principle of tandem OSCs is such that the subcells harvest distinct parts of the solar spectrum, maximizing overall light utilization [162, 174]. Interconnection layers facilitate charge recombination between subcells. Materials used in tandem OSCs are various D-A combinations with complementary absorption profiles [174]. Recent high efficiency devices use NFAs with tunable absorption properties. Efficiency and advantages of tandem designs can surpass the Shockley-Queisser limit for single-junction cells [174]. State of the art tandem OSCs have achieved efficiencies over 18%, with theoretical limits approaching 25% [174].

2.4.1.6 Organic DSSC

Organic DSSCs have a structure representing a hybrid approach using organic dye molecules anchored to a mesoporous inorganic semiconductor (typically TiO_2), immersed in an electrolyte [175, 176]. Working principle of DSSCs can be explained as follows: dye molecules absorb light and inject electrons into the conduction band of TiO_2. The electrolyte regenerates the oxidized dye and completes the circuit. Materials used in DSSCs include ruthenium based complexes (N_3, N_{719}) [176] were early standards, but organic dyes



FIGURE 2.8: DSSC.

and metal free sensitizers have become increasingly common. Efficiency and advantages of DSSCs offer 10-14% [176] efficiency and perform well in diffuse light conditions. They can be made semi-transparent and in various colors, making them suitable for building integrated PVs.

2.5 Bulk Hetero-Junction OSC

Since this thesis primarily aims to carry out simulation studies on organic BHJSC with multilayer architecture, it is worth mentioning about the different layers within them. The fundamental structure of a multilayer BHJOSC includes the active layer with D-A blend, electron and hole transport layers along with the front and back electrodes.

2.5.1 Layers of BHJOSC

2.5.1.1 Active Layer

The active layer, also known as the absorber layer, is the material responsible for photon absorption and photocurrent generation in OSCs. Excitons are generated within

this active layer, and efficient separation of these excitons into free charge carriers is essential for current flow. For effective photon absorption, the active layer should possess a relatively low band gap and a suitable absorption spectrum [131, 151, 177]. The thickness of the active layer must be compatible with the exciton diffusion length of the materials used, with BHJ devices typically requiring thinner active layers due to efficient exciton harvesting [152, 177]. Donor materials in BHJSCs are generally conjugated polymers such as P3HT, Poly[[4,8-bis[(2-ethylhexyl)oxy]benzo[1,2-b:4,5-b]dithiophene-2,6-diyl][3-fluoro-2-[(2-ethylhexyl)carbonyl]thieno[3,4-b]thiophenediyl]] (PTB7), Poly[[4,8-bis[(2-ethylhexyl)oxy]benzo[1,2-b:4,5-b]dithiophene-2,6-diyl][3-fluoro-2-[(2-ethylhexyl)carbonyl]thieno[3,4-b]thiophene-2,6-diyl]] (also called PCE10) (PTB7-Th), Poly(dithienobenzodithiophene-alt-thieno[3,4-b]thiophene) derivative (low-bandgap D–A polymer) (PDBT-T1), PBDB-T, and Poly[2-methoxy-5-(2 -ethylhexyloxy)-1,4-phenylene vinylene] (MDMO-PPV) [137]. Acceptor materials include fullerene derivatives such as PC71BM and PC61BM, as well as NFAs like 3,9-Bis(2-methylene-(3-(1,1-dicyanomethylene)-indanone))-5,5,11,11-tetrakis(4-hexylphenyl)dithieno[2,3-d:2 ,3 -d]-s-indaceno[1,2-b:5,6-b]dithiophene (ITIC), PDI, Indacenodithiophene-based fused-ring acceptor with barbituric acid end groups (IDTBR), and Indacenodithieno[3,2-b]thiophene-based acceptor with ethylhexyl end groups (ITIC-variant NFA) (IEIC) [178].

2.5.1.2 Electron Transport Layer

The electron transport layer (ETL) is the layer incorporated between the active layer and the cathode in OSCs. After exciton dissociation, electrons migrate to the ETL, facilitating their transport and collection at the cathode. The ETL serves two main functions. It provides a selective and efficient pathway for electron transport, and blocks holes from reaching the cathode [179, 180]. To achieve this, the C_B of the ETL is aligned close to the C_B of the active layer, while the V_B of the ETL is positioned significantly lower than that of the active layer, effectively blocking hole transport [181]. Common ETL materials used in BHJOSCs include conjugated polyelectrolytes like Poly(9,9-bis(3'-N,N-dimethyl)-N-ethylammonium-propyl-2,7-fluorene)-alt-2,7-(9,9-dioctylfluorene))dibromide (PFN-Br), metal oxides such as titanium dioxide (TiO_2), zinc oxide (ZnO), tin dioxide (SnO_2), fullerene derivatives like phenyl-$C_6$1-butyric acid methyl ester (PCBM) and C_{60}, as well as indium gallium zinc oxide (IGZO) [182, 183].

2.5.1.3 Hole Transport Layer

The hole transport layer (HTL) facilitates the efficient transport of holes to the anode following exciton dissociation. For optimal performance, the V_B of the HTL should align closely with the valence band of the active layer, while its C_B should lie significantly higher than that of the active layer. This band alignment allows the HTL to selectively accept holes from the active layer, enhancing carrier transport towards the anode [179, 181]. Commonly used hole transport materials (HTMs) in OSCs include Poly(3,4-ethylenedioxythiophene):poly(styrene sulfonate) (PEDOT:PSS), copper iodide (CuI), nickel oxide (NiO), P3HT and MEH-PPV [184, 185].

2.5.1.4 Electrodes

The top and bottom electrodes, namely the anode and cathode connect the OSC to the external circuit. These electrodes are selected such that the work function of the anode is higher than that of the cathode, allowing the anode to extract holes and the cathode to extract electrons from the active layer [131, 137]. Indium tin oxide (ITO) is the most commonly used anode in OSCs, while typical cathode materials include low work function metals such as calcium (Ca), aluminum (Al), silver(Ag) and gold (Au) [186, 187, 188, 189].

2.5.2 Fundamental Principle of BHJOSC

Fig. 2.9 (a) and (b) show the working principle of BHJOSC. BHJOSCs operate via four fundamental stages [22, 152, 190] which are photon absorption and exciton generation, exciton diffusion and dissociation, charge transport and charge collection. Fig. 2.9 (a) shows the steps involved in exciton generation to charge carriers collection. Fig. 2.9 (b) displays band diagram of the photocurrent generation mechanism. Incident sunlight is primarily absorbed by the donor polymer (e.g., P3HT), promoting an electron from the HOMO to the LUMO and creating a tightly bound Frenkel exciton [133, 151]. The D-A energy offset, typically 0.1–1.4 eV, ensures that the exciton binding energy can be overcome. The neutral exciton diffuses (over a few nanometers) to a D-A interface. Where the LUMO–LUMO (or HOMO–HOMO) offset provides sufficient driving force to split the exciton into a Coulombically bound charge–transfer (CT) state [147, 152]. This CT state then separates into free polarons (hole on donor, electron on acceptor). Once free, electrons and holes percolate through their respective phases via hopping (or band-like) transport towards the ETL and HTL. Finally, electrons and holes are extracted at the cathode and

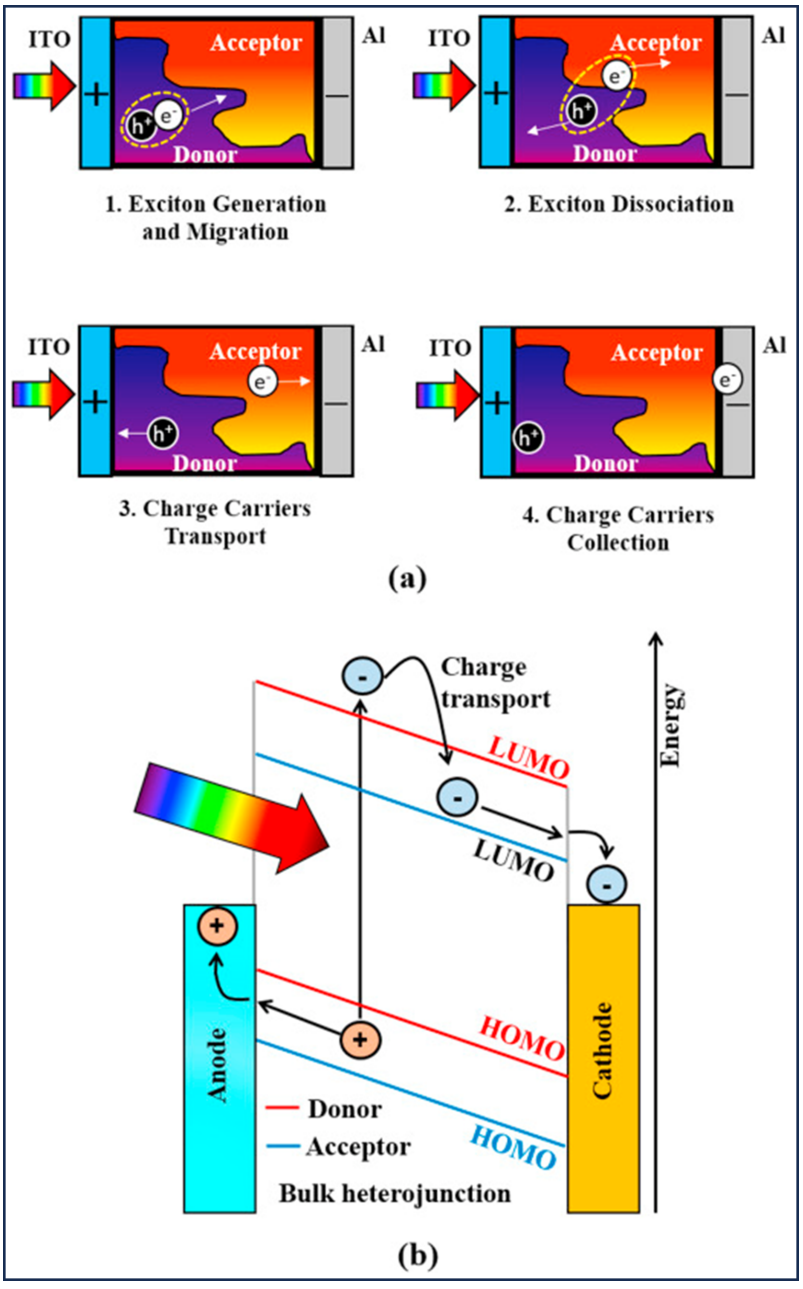


FIGURE 2.9: (a) Steps involved in exciton generation to charge carriers collection. (b) Band diagram of the photocurrent generation mechanism.

anode, respectively, via the ETL and HTL layers (e.g., ZnO and PEDOT:PSS), completing the circuit [22, 190].

2.5.3 Historical Timeline of BHJOSCs

The advancement of bulk hetero-junction organic solar cells (BHJOSCs) highlights one of the most revolutionized areas of materials science and renewable energy research. Although Hiramoto *et al.* first described a hetero-junction in 1991, the modern BHJ structure emerged in 1995 when Yu *et al.* demonstrated MEH-PPV:C_{60} blends achieving approximately 2.9% PCE under simulated sunlight [191]. Initially, donor polymers used in BHJOSCs included poly(phenylene vinylene) (PPV) and MEH-PPV, where pristine C_{60} served as the first electron acceptor [186].

However, the limited solubility of C_{60} as an electron acceptor prompted development of soluble fullerene derivatives. In 1995, Hummelen *et al.* introduced $PC_{61}BM$ ([6,6]-phenyl-C_{61}-butyric acid methyl ester), which rapidly became the standard acceptor [192]. By the early 2000s, P3HT:$PC_{61}BM$ BHJs frequently achieved 3-4% PCE, cementing fullerene derivatives as the benchmark acceptors. Notable donor polymers at this stage included MDMO-PPV, P3HT [360] and PCDTBT [194].

Between 2002-2005, breakthroughs in P3HT revealed that regioregularity, optimized molecular weight and thermal annealing were critical for good device performance. By 2005, optimized P3HT:$PC_{61}BM$ devices achieved nearly 5% PCE [360, 195]. Researchers elucidated how polymer backbone design affected band gap, energy level alignment (HOMO/LUMO matching), and nanoscale morphology, guiding rational D-A design [133, 152].

In the late 2000s and early 2010s, polymers engineered for optimal PV properties emerged. PTB7, with an alternating D-A architecture, yielded PCEs above 7%. PBDTTT-C (Poly[(4,8-bis(5-(2 -ethylhexyl)thiophen-2-yl)benzo[1,2-b;4,5-b']dithiophene)-alt-(4-(2-
ethylhexyl)-3-fluorothieno[3,4-b]thiophene)]) exhibited excellent charge mobility [196], and (Poly[N-9′-heptadecanyl-2,7-carbazole-alt-5,5-(4′,7′-di-2-thienyl-2′,1′,3′-benzo
thiadiazole)]) (PCDTBT) offered superior thermal stability [194]. The introduction of high-boiling-point additives (e.g., 1,8-diiodooctane [DIO] and 1-chloronaphthalene [CN]) dramatically improved BHJ morphology, enabling finer D-A phase separation and boosting PCEs by 20-50% in many systems [161]. Meanwhile, inverted BHJ structures employing metal oxides (e.g., TiO_2) as ETLs and alternative HTLs improved air stability, reducing cathode oxidation and enhancing device lifetimes [197, 198].

Later, highly tailored donor polymers appeared. PTB7-Th (a thiophene analog of PTB7) improved charge transport and absorption breadth. PBDB-T combined benzodithiophene and thieno[3,4-b]thiophene units for superior performance, and PffBT4T-2OD achieved mobilities that pushed PCEs beyond 10%.

A paradigm shift occurred with the emergence of NFAs. In 2015, Lin *et al.* introduced ITIC (3,9-bis(2-methylene-(3-(1,1-dicyanomethylene)-indanone))- 5,5,11,11-tetrakis(4-hexylphenyl)-dithieno[2,3-d:2′,3′-d′]-s-indaceno[1,2-b:5,6-b′]dithiophene), a fused-ring electron acceptor with strong visible absorption and tunable energy levels [199, 200]. Fluorinated derivatives such as IT-4F further boosted device performance. Within just two years, NFA-based BHJs surpassed fullerene-based systems, with PCEs jumping from about 11% to over 13% [201].

The most significant leap came with the introduction of BTP-4F-12 (also called Y6; a fused-ring acceptor based on benzothiadiazole–core A–D–A structure) (Y6) and its derivatives. The PM6:Y6 blend achieved PCEs above 17% in single-junction devices [202]. Subsequent Y6 variants pushed efficiencies to 18-19%. Donors optimized for NFA pairing, such as PM6, Fluorinated derivative of PBDB-T (with difluorinated acceptor units in backbone side chains) (PBDB-T-2F) and Poly[(2,6-(4,8-bis(5-(2-ethylhexyl)-thiophen-2-yl)benzo[1,2-b:4,5-b]dithiophene))-alt-(5,5-(1 ,3 -di-2-thienyl-5 ,7 -bis(2-ethylhexyl)benzo[1,2-c:4,5-c]dithiophene-4,8-dione))] (D18), enabled unprecedented performance. D18:Y6 devices exceeded 18% PCE by 2021.

Finally, ternary BHJ blends incorporating two donors or multiple acceptors offered complementary absorption and improved morphology, further enhancing efficiency and stability.

2.5.4 Structural Variants of BHJOSCs

BHJOSCs employ a variety of structural configurations to optimize charge generation, separation and collection in the device. Such variants help to maximize the D-A interface while maintaining effective charge transport pathways. These structures significantly contribute to determining the efficiency, stability and scalability of the devices. Fig. 2.10 (a) and (b) show the conventional and inverted structural variants used in BHJOSCs.

The layer sequence of the conventional device structure is as follows: Anode/HTL/the D-A blend photoactive layer/ETL/low work function cathode [182, 184, 203, 204, 205].

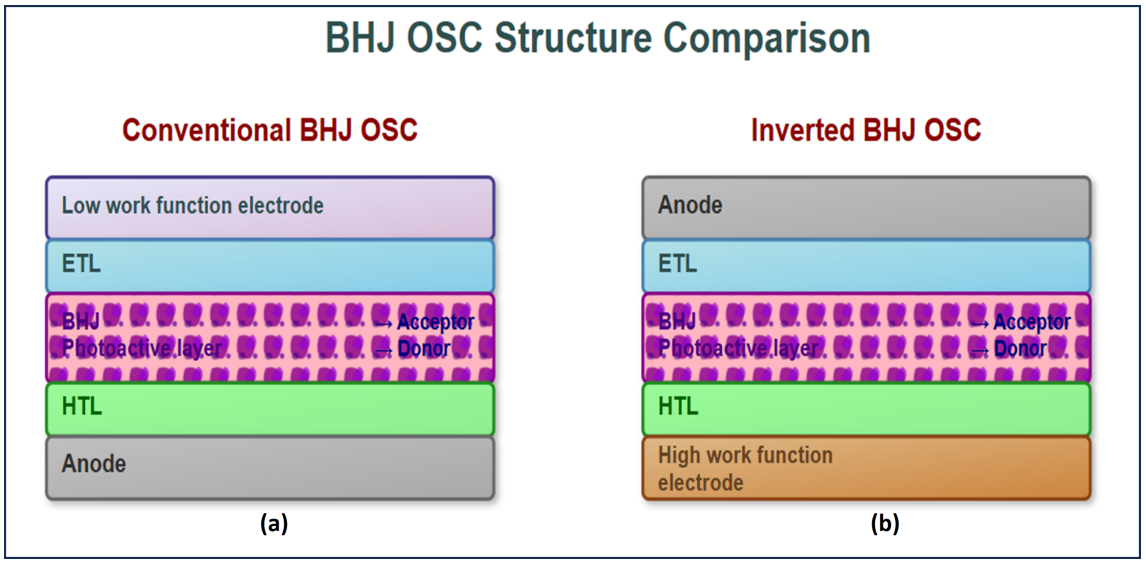


FIGURE 2.10: (a) Conventional and (b) inverted BHJ structures

Advantages of this structure include facile, low temperature solution processing and thermal evaporation [131, 179]. However, conventional devices often suffer from stability issues caused by cathode oxidation and moisture/oxygen ingress, particularly at the metal/ETL interface, which can lead to rapid performance degradation over time.

The layer sequence of inverted BHJOSC structure is as follows: Anode/ETL/the D-A blend photoactive layer/HTL/high work function cathode [206, 207]. In the inverted device structure, the polarity of the electrodes is reversed to enhance air stability [206, 207]. Advantages of this inverted structure includes improved environmental stability. Its limitations include complex fabrication steps (e.g., deposition of oxide ETLs and HTLs) and reduced compatibility with certain traditional organic materials that do not tolerate the required processing conditions [206, 207].

In this research study we have carried out designing and simulation study of BHJOSCs with a conventional device structure, aiming to incorporate materials that can address the stability issues and will eventually enhance device performance.

Chapter 3

Graphene Derivatives in Bulk Hetero-Junction Organic Solar Cells

This chapter offers a comprehensive overview of the applications of graphene derivatives in BHJOSCs. The chapter explores the employment of graphene derivatives across diverse components, including anode, cathode, hole transport layer (HTL), electron transport layer (ETL) and the photoactive absorber layer. Integration of graphene derivatives in BHJOSCs mitigates degradation and enhances their stability. Modern BHJ design and fabrication of BHJOSCs, with graphene derivatives have gained attention among researchers and scientists ubiquitously.

Carbon materials, especially the two dimensional graphene-based material, have garnered significant research interest in recent years due to their exceptional electrical, optical, and mechanical properties making them promising candidates for the next-generation energy-harvesting technologies, particularly in PV applications [208, 209, 210, 211, 212, 213, 214, 215, 216]. While pristine graphene possesses exceptional electrical, thermal and mechanical properties, its limited solubility, lack of functional groups, and processing challenges have prompted the development of its functionalized forms, collectively known as graphene derivatives. These include graphene oxide (GO), reduced graphene oxide (rGO), graphene quantum dots (GQDs) and various chemically modified graphene derivatives [208, 209, 210, 213, 214, 215].

3.1 Graphene and its Derivatives:Familiarization of the Wonder Material

Graphene possesses unique properties including zero band gap, ambipolar transporting property, ultrahigh mobility, exceptional optical transparency, exceptional thermal conductivity and high tensile strength [217] making it a wonder material and hence one of the attractive candidate as a significant layer in the BHJOSCs.

Graphene exhibits ultrahigh electron mobility exceeding 200,000 cm^2/Vs [213, 214, 218, 219, 220, 221, 222] which can be attributed to its linear band structure and minimal defect scattering.

A monolayer of graphene absorbs minimal visible light, transmitting 97.7% light [213, 214, 215, 223]. Graphene's thermal conductivity exceeds 3000-5000 W/mK, surpassing most metals and carbon based materials [208, 213, 214, 215]. It can withstand a temperature four times of that of diamond [208, 213, 214, 215]. Graphene has a Young's modulus of approximately 1 TPa and intrinsic tensile strength of 130 GPa making it one of the strongest materials ever found [208, 213, 214, 215].

The zero band gap of pristine graphene makes it unsuitable to be directly used in the organic electronics. So it has to be made tunable, thus developing derivatives with properties similar to that of graphene [208, 213, 214, 215]. Graphene derivatives represent a rapidly expanding class of materials derived from graphene, a single layer of carbon atoms arranged in a 2D honeycomb lattice. Its tunable derivatives are being used in organic electronics widely, especially BHJOSCs [211].

Researchers use graphene derivatives in BHJOSCs to improve mobility and charge transport, which are currently the major issues faced by BHJ based OPVs. Recent studies have demonstrated that graphene-based materials can achieve high electrical conductivity while maintaining excellent optical transparency. This makes graphene derivative an excellent option for TCO electrode.

Thin and mechanically strong graphene derivatives can be developed to resolve the cracks that appear on commercialized OPVs. Many opto-electronic devices available in the market are already implementing the flexible yet strongest devices, that has graphene derivatives incorporated in them. The continuous exposure to sunlight, extreme heat and U-V radiation could significantly damage not only the exterior parts of OPVs, but also alter the chemical composition of the layers used in OPVs. Graphene derivatives with high thermal conductivity are already halfway in solving these issues currently faced by the OPVs [211].

Their amazing ability to transport both electrons and holes make them suitable as both ETL and HTL. This improves the overall device performance [211].

3.2 Important Graphene Derivatives in BHJOSCs

The practical use of pristine graphene is often limited by its zero band gap property, hydrophobicity, chemical inertness, and challenges in large scale production and dispersion [208, 213, 214, 215]. These limitations have driven the development of graphene derivatives, a versatile family of modified graphene based materials designed to retain many of graphene's remarkable properties while enhancing its functionality and processability [208, 213, 214, 215]. To explore the possibilities of this propitious material to desired applications, it is required to control the electronic structures and properties of graphene [208, 211, 213, 214, 215]. Some of the most common derivatives include GO, rGO and GQDs. Improving the device stability, mobility and efficiency in BHJOSCs could be achieved by the incorporation of graphene derivatives in the layers of BHJOSCs [211]. GO and rGO are currently the emerging graphene derivatives used in electrodes, interfacial layers and active layers. Our research study involves implementation of graphene, GO, rGO and p-graphene as HTLs in fullerene acceptor (FA) BHJOSCs and NFA BHJOSCs. We have also incorporated n type doped graphene (n-graphene) and TiO_2:graphene composite as ETLs in our current studies on BHJOSCs. Despite these excellent characteristics of graphene derivatives, challenges remain in terms of scalability, reproducibility and understanding their long-term environmental and biological impacts. Nonetheless, ongoing

research continues to expand their potential, making them a cornerstone of next-generation materials science [224, 225, 226, 227] .

3.2.1 Graphene Oxide

Graphene oxide (GO) is a chemically modified derivative of graphene with oxygen containing functional groups attached to the basal plane and edges [228, 229, 230, 231, 232, 233, 234, 235, 236, 237]. It is essentially the oxygenated form of graphene that combines the unique characteristics of graphene and related 2D materials, such as high mechanical strength and large surface area [232, 233, 234, 235, 236].

The presence of oxygen-rich functional groups in GO offers excellent water dispersibility and facilitates both covalent and non-covalent functionalization. These modifications significantly alter the electronic properties of GO compared to pristine graphene [228]. The addition of oxygen functionalities creates a band gap ranging from 1.5 to 4.0 eV, depending on the degree of oxidation [229]. The sp^3 hybridization introduced by oxygen atoms disrupts the π-conjugation, significantly reducing electrical conductivity [230].

The hydrophilic nature of GO enables solution based processing techniques compatible with OSC fabrication [231, 237]. Fig. 3.1 (a), (b) and (c) display the chemical structures of graphene, GO and rGO.

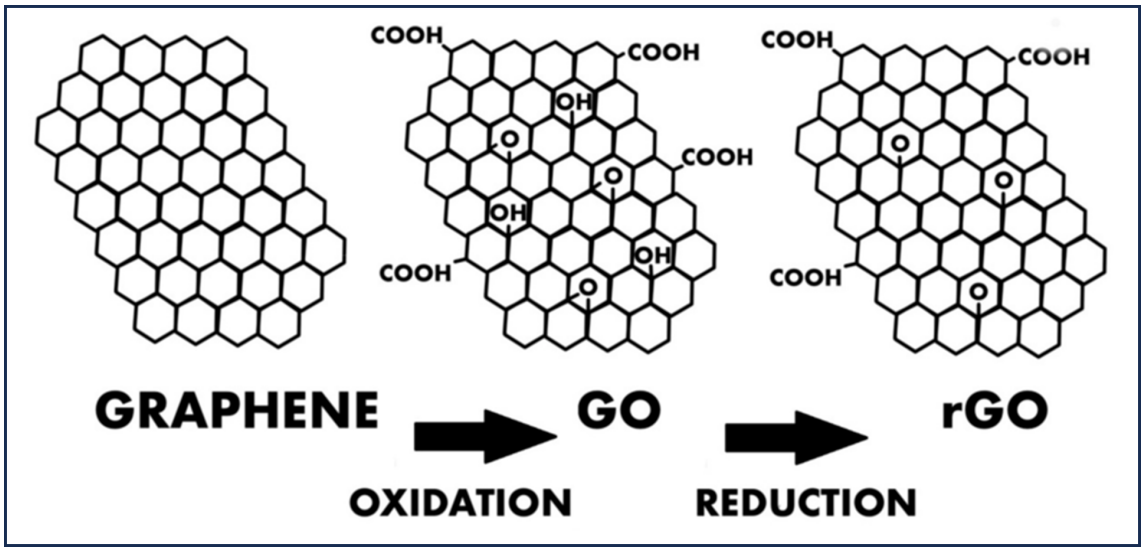


FIGURE 3.1: Chemical structures of (a) graphene, (b) graphene oxide and (c) reduced graphene oxide.

3.2.2 Reduced Graphene Oxide

Reduced graphene oxide (rGO) is obtained through various reduction processes by removing oxygen-containing functional groups of GO while partially restoring the sp^2 carbon network [232, 233, 234, 235, 236, 238, 239, 240, 241, 242]. The electronic properties of rGO can be tailored by controlling the degree of reduction [242]. In its reduced form, rGO displays enhanced conductivity, reaching sheet resistances of a few tens of Ω/sq. Restored conductivity, tunable work function and improved charge carrier mobility are the key features of rGO.

Partial restoration of the π-conjugated network increases electrical conductivity, though it typically remains lower than that of pristine graphene [238]. The work function can be adjusted from 4.3 to 5.1 eV by controlling the reduction extent [240] and mobility values can reach 1-100 cm^2/Vs depending on the reduction method and processing conditions [241].

3.2.3 Graphene Quantum Dots

Graphene quantum dots (GQDs) are nanoscale graphene fragments that exhibit quantum confinement in all three spatial dimensions. Graphene itself is a semiconductor with an effectively infinite exciton Bohr diameter [239]. Consequently, quantum confinement can arise in any fragment, though GQDs typically have dimensions below 20 nm in diameter. The experimental and theoretical study of GQDs has closely followed the research on graphene [239, 243, 244, 245, 246, 247, 248, 249, 250].

GQDs have been fabricated by fragmentation or 'cutting' of graphene sheets (top-down approach) [239, 245, 246, 248, 249, 250], as well as by bottom-up chemical synthesis of large graphene like molecules with well defined molecular structures [243].

Excitons in graphene have an effectively infinite Bohr diameter [244], so graphene fragments of any size exhibit quantum confinement effects. As a result, GQDs possess a non-zero band gap and show luminescence upon excitation, which can be tuned by modifying the size and surface chemistry. Early work on GQDs focused on their physical properties. More recently, GQDs have been chemically modified and applied in energy conversion, bioanalysis and sensing [239, 245, 246, 247, 248, 249, 250, 251]. Fig. 3.2 displays chemical structures of graphene and GQDs.

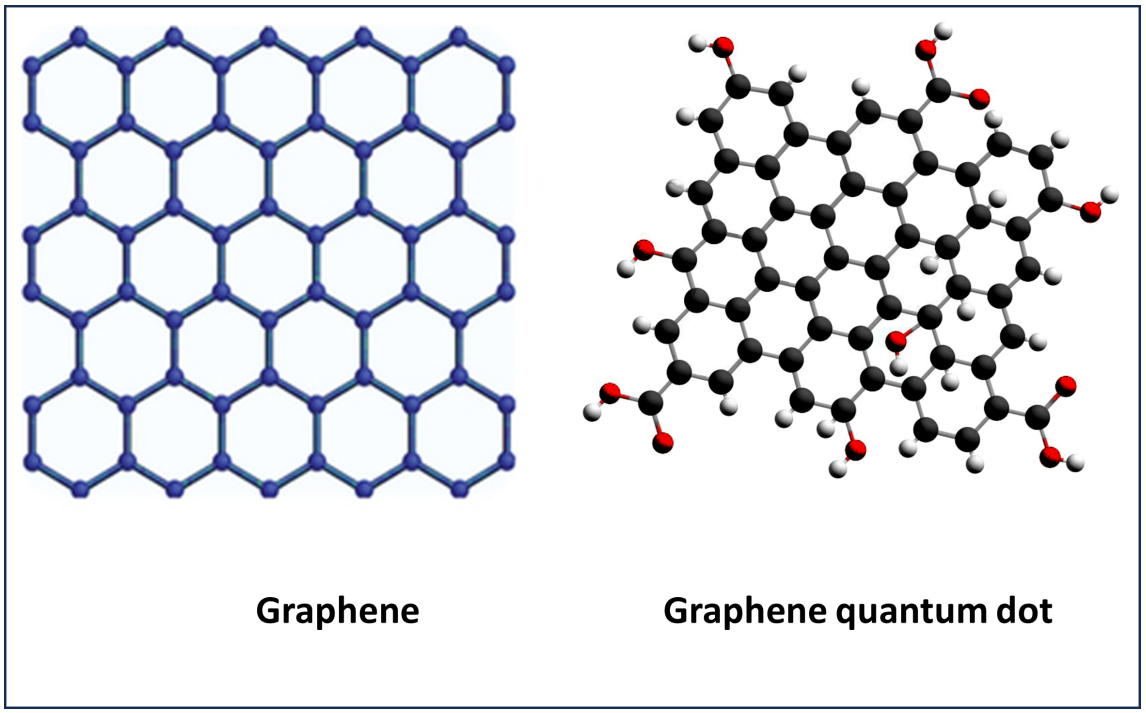


FIGURE 3.2: Chemical structures of graphene and graphene quantum dot

3.2.4 Doped Graphene Derivatives

Graphene is a semi-metal with an intrinsic zero band gap and does not provide high conductance compared to other metallic or semiconducting materials. Doping is a practical and widely adopted approach for tailoring the electronic properties of graphene. Single-atom and hetero-atom doping can be used to modify both the structural and electrical properties of graphene. Doping opens the zero band gap of graphene and allows tuning of the Fermi level [252, 253, 254, 255]. This Fermi level tuning helps control the charge carrier concentration, enabling tunable p-type and n-type semiconducting behaviour suitable for potential applications of graphene in BHJ OSCs [255].

Precise and effective control of n-type or p-type doping in graphene with desired charge carrier concentration is achievable. Applications of doped graphene derivatives include photodetectors, PVs, OLEDs, supercapacitors [252], OTFTs [253], catalytic applications and sensors [254].

3.3 Graphene Derivatives in BHJOSCs:Enhancing Efficiency

Graphene derivatives serve as excellent ETLs, HTLs, active layer materials and electrodes in BHJOSCs.

3.3.1 Graphene Derivatives as an Anode Material in BHJOSCs

One of the most advanced developments in the incorporation of graphene derivatives in BHJOSCs is their integration of graphene derivatives as anode materials [256]. The unique combination of high electrical conductivity ($\sim 10^6$ S/m), high optical transparency (>97% in visible range) and good mechanical flexibility has made graphene as an ideal candidate for transparent conducting electrodes, especially as anode [257, 258].

During the period 2004-2008, ITO was the dominant transparent conducting electrode in OSCs, despite its limitations including brittleness, scarcity of Indium and high processing temperatures [259]. The first theoretical studies emerged around 2007-2008, suggesting that graphene's work function (~4.5 eV) and transparency could make it suitable as a transparent electrode [260]. However, pristine graphene's work function did not match with the HOMO levels of common organic donor materials, signifying the need for work function modification of pristine graphene to be implemented as an anode. Graphene is a promising alternative to ITO as a transparent electrode in OSCs, since it addresses several limitations inherent to ITO, such as brittleness and scarcity of Indium [261, 262].

The first experimental demonstrations on graphene as an electrode in OSCs appeared around the year 2009 [263]. Early work by Wu et al. demonstrated the use of chemical vapor deposition (CVD) grown graphene as a transparent electrode [264], though it has limited success due to high sheet resistance (~1000 Ω/sq) and poor work function alignment. Key challenges identified during this period include high sheet resistance of single-layer graphene [265], work function mismatch with organic semiconductors [266], difficulty in large area [267], uniform graphene synthesis and poor adhesion to plastic substrates [268]. Researchers began exploring GO as an alternative to ITO, recognizing that its tunable electronic properties and solution processability could address some of these limitations [269]. The first reports of GO based anodes appeared in 2010, showing improved performance over pristine graphene but still lagging behind ITO [270]. In 2012, several groups demonstrated that rGO films could achieve sheet resistances comparable to ITO while offering superior flexibility. The work by Li et al. showed that thermally reduced GO films could achieve PCE approaching those of ITO based devices in

P3HT:PCBM BHJSCs [271]. Optimization of reduction processes to balance conductivity and transparency [272], development of solution based deposition techniques for large area processing [273], introduction of doping strategies to further enhance conductivity [274] and recognition of the importance of work function engineering [275] are some of the crucial investigations done.

Chemical doping emerged as a powerful tool for work function modification. Studies demonstrated that both p-type doping (using molecules like MoO_3, PEDOT:PSS, or organic acids) and n-type doping (using alkali metals or organic amines) could effectively tune the work function of graphene based anodes to match different organic semiconductor systems [276, 277]. Covalent functionalization also gained attention, with researchers attaching various functional groups to graphene sheets to modify their electronic properties [278, 279].

The introduction of machine learning approaches began to accelerate materials discovery and optimization during this period, allowing researchers to more efficiently explore the vast parameter space of graphene functionalization and processing conditions [280]. Fig. 3.3 (a) shows graphene derivative incorporated as anode in a BHJOSC.

Today, graphene derivatives represent a promising alternative to ITO as anode in BHJOSCs. Graphene based anodes have found commercial applications in flexible and lightweight SCs where ITO's brittleness is prohibitive [281, 282].

3.3.2 Graphene Derivatives as a Cathode Material in BHJOSCs

Unique properties of graphene derivatives that render them highly suitable for cathode applications in BHJOSCs. Notably, its high electrical conductivity, with carrier mobilities exceeding 15,000 cm^2/Vs at room temperature, ensures efficient electron transport and minimizes resistive losses [283]. Fig. 3.3 (b) shows graphene derivative used as cathode in BHJOSC.

Pristine graphene exhibits a work function around 4.6 eV, but this can be modulated through chemical doping (e.g., with PEI or alkali metals), surface functionalization, or the insertion of buffer layers (e.g., LiF or ZnO), optimizing energy-level alignment for efficient electron extraction [284, 285, 286]. This tunability is essential to minimize energy barriers between the cathode and the lowest unoccupied molecular orbital (LUMO) of the electron acceptor, enhancing charge selectivity and extraction [284, 285, 286].

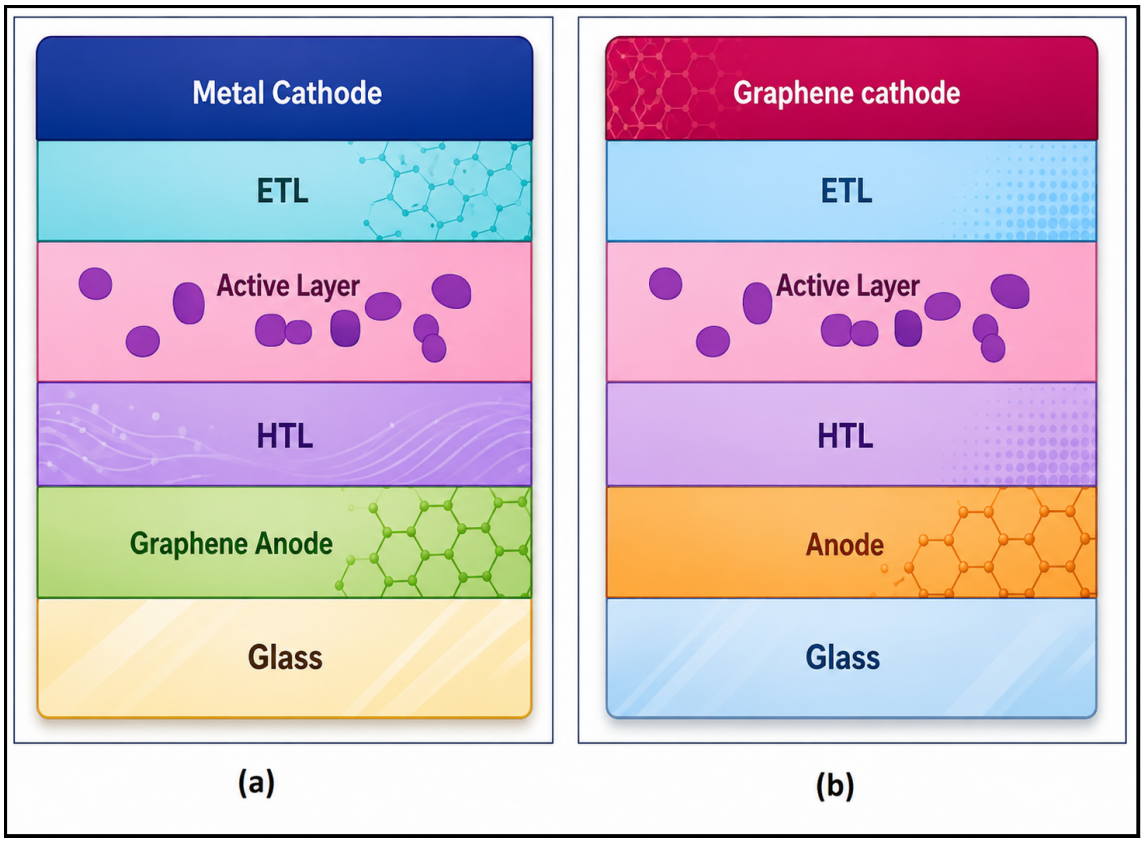


FIGURE 3.3: Graphene derivative as (a) anode and (b) cathode.

In BHJOSCs, the cathode plays a pivotal role in the selective extraction of photogenerated electrons from the active layer while simultaneously blocking holes, thereby ensuring unidirectional charge flow. Efficient electron collection requires a cathode with low contact resistance to reduce R_s and avoid charge buildup that may lead to recombination losses [284, 285, 286]. Moreover, the work function of the cathode must be properly aligned with the LUMO of the electron acceptor material (commonly fullerene derivatives like PCBM) to facilitate barrier-free electron transfer [191]. Mismatched energy levels introduce barriers that lower the V_{oc} and PCE. In addition to electrical properties, the cathode must also exhibit chemical and environmental stability under illumination [284, 285, 286, 287].

3.3.3 Graphene Derivatives as an HTL in BHJOSCs

The incorporation of graphene derivative as an HTL in BHJOSCs represents a fascinating work in the broader narrative of OPV development. Unlike its application as a

cathode material, graphene's role as an HTL leverages its intrinsic properties more naturally, as its work function and transparency make it inherently suitable for hole extraction and transport [257, 258].

However, conventional HTLs like PEDOT:PSS presented limitations including hygroscopicity, acidity and limited thermal stability [284, 288]. Researchers recognized that graphene's work function of approximately 4.6 eV was well suited for hole extraction from common organic donor materials, while its exceptional transparency minimized optical losses (a critical advantage over traditional transparent conducting oxides) [284]. Initial experimental explorations focussed on graphene as a transparent anode rather than explicitly as an HTL. Nonetheless, these early studies established important foundational knowledge about graphene organic semiconductor interfaces and the potential for more sophisticated charge transport applications [258]. Between 2010 and 2012, the first systematic investigations specifically targeting graphene derivative as an HTL in OSCs were conducted.

GO and rGO emerged as promising candidates as HTLs due to their solution processability and favourable energy level alignment facilitated by oxygen containing functional groups [284]. Chemical doping with electron withdrawing molecules such as F4-TCNQ and functionalization with organic groups were employed to increase graphene's work function, facilitating more efficient hole extraction [289]. Researchers led by Bumjoon Kim and Lei Jiang demonstrated that controlled chemical modification improved energy level alignment and interfacial charge transfer [289, 290, 291]. Fig. 3.4 (a) displays BHJOSC with graphene derivative as HTL.

Patterned graphene structures via lithography and laser processing also gained attention, offering enhanced charge collection and additional functionalities [292]. During this period, graphene HTLs were integrated into complex device architectures including ternary blends, NFAs and tandem SCs [293, 294, 295, 296, 297, 298, 299, 300].

3.3.4 Graphene Derivatives as an ETL in BHJOSCs

The electron transport layer (ETL) plays a crucial role in BHJOSCs as discussed in chapter 2, section 2.5.1.2. An effective ETL is characterized by a low work function, enabling for optimal energy level alignment between the LUMO of the acceptor material and the cathode work function [179, 301]. This alignment promotes the formation of an Ohmic contact at the active layer–cathode interface, thereby enabling rapid and efficient electron extraction and transport to the cathode [179, 301]. Concurrently, the ETL functions

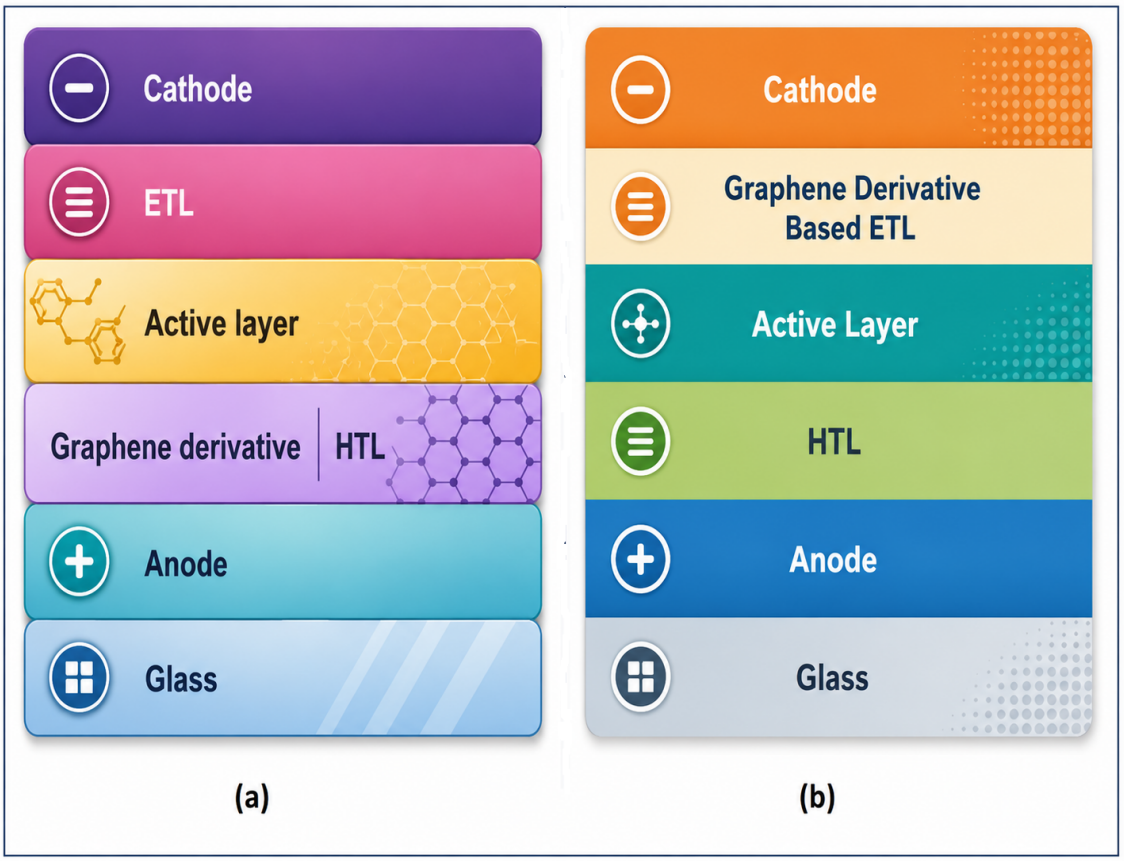


FIGURE 3.4: Graphene derivative as (a) HTL and (b) ETL.

as a hole blocking layer, effectively suppressing undesired charge carrier recombination and thus enhancing overall device performance [302]. Common ETL materials employed in BHJOSCs include inorganic semiconductors such as zinc oxide (ZnO) and titanium dioxide (TiO_2) [303, 304], organic semiconductors like bathocuproine (BCP) [305] and conjugated polyelectrolytes such as Poly[(9,9-bis(3'-((N,N-dimethyl)-N-ethylammonium)-propyl)-2,7-fluorene)-alt-2,7-(9,9-dioctylfluorene)]dibromide (PFN-Br) and N,N'-Bis(N,N-dimethylpropan-1-amine oxide)
perylene-3,4,9,10-tetracarboxylic diimide (PDINO) [306, 307]. However, many of these solution processed ETLs require complex synthetic procedures and exhibit limitations in terms of morphological uniformity, optical transparency and long-term environmental stability [308, 309, 310].

As the field progressed, researchers increasingly focussed on optimizing ETL performance through ternary composite systems and interfacial engineering strategies aimed at overcoming the limitations of individual components. A pivotal development was reported by Huang et al., [309], who introduced a ternary ETL composed of ZnO, polyethyleneimine

ethoxylated (PEIE), and rGO. This combination synergistically improved both electronic and morphological properties. Recent years have focussed on improving long term stability and exploring novel graphene derivatives for scalable manufacturing. Doping and functionalization of GO and rGO to tailor their work function can improve compatibility with adjacent layers. Development of solution processed, low temperature ETLs, makes OSC fabrication more viable for flexible substrates [311]. Exploration of Nitrogen doped graphene (N-G) and functionalized rGO, offer better control over electronic properties [311]. Fig. 3.4 (b) displays BHJOSC with graphene derivative as ETL.

3.3.5 Graphene Derivatives as a Photoactive Material in BHJOSCs

The historical development of graphene derivatives as photoactive layers in BHJOSCs needs to be discussed, since it is essential to comprehend the role of absorber layers in such devices. The absorber layer must efficiently capture photons across the solar spectrum, generate excitons, facilitate exciton dissociation at D-A interfaces, and provide pathways for charge transport to electrodes [312, 313, 314, 315, 316]. Traditional organic absorbers, primarily conjugated polymers and small molecules, have limitations in spectral coverage, particularly in the NIR region where significant solar irradiance exists [312, 313, 314, 315, 316]. The quest for materials that could extend absorption beyond conventional organic semiconductors while maintaining compatibility with solution processing methods set the stage for exploring graphene derivatives as absorber components.

The initial period of graphene research in PVs (2008-2010) was marked by the recognition that pristine graphene's zero band gap and weak light absorption (approximately 2.3% per monolayer) rendered it unsuitable as a primary absorber material. However, theoretical work during this period began to suggest that chemical modification could transform graphene into a viable absorber material. A breakthrough occurred in 2010 when *Liu et al.* demonstrated the first use of GO as a photoactive absorber component in OSCs. Their work showed that GO could function as an electron acceptor in P3HT:GO blends, achieving a PCE of 1.4% [313]. Research during 2010-2012 began to elucidate the absorption mechanisms in GO [314]. UV-vis spectroscopy studies revealed that GO exhibited strong absorption in the UV region (200-300 nm) with a tail extending into the visible region [314]. The absorption was attributed to π-π^* transitions of aromatic domains and n-π^* transitions of carbonyl groups. Concurrent with absorption studies, researchers investigated the morphology of polymer:GO blends [314]. Transmission electron microscopy (TEM) studies revealed that GO sheets could form well dispersed networks within polymer matrices, providing both absorption enhancement and charge transport

pathways. However, the tendency of GO sheets to aggregate posed significant challenges for achieving optimal morphologies [314]. Fig. 3.5 shows graphene derivative incorporated in photoactive layer of a BHJOSC [300].

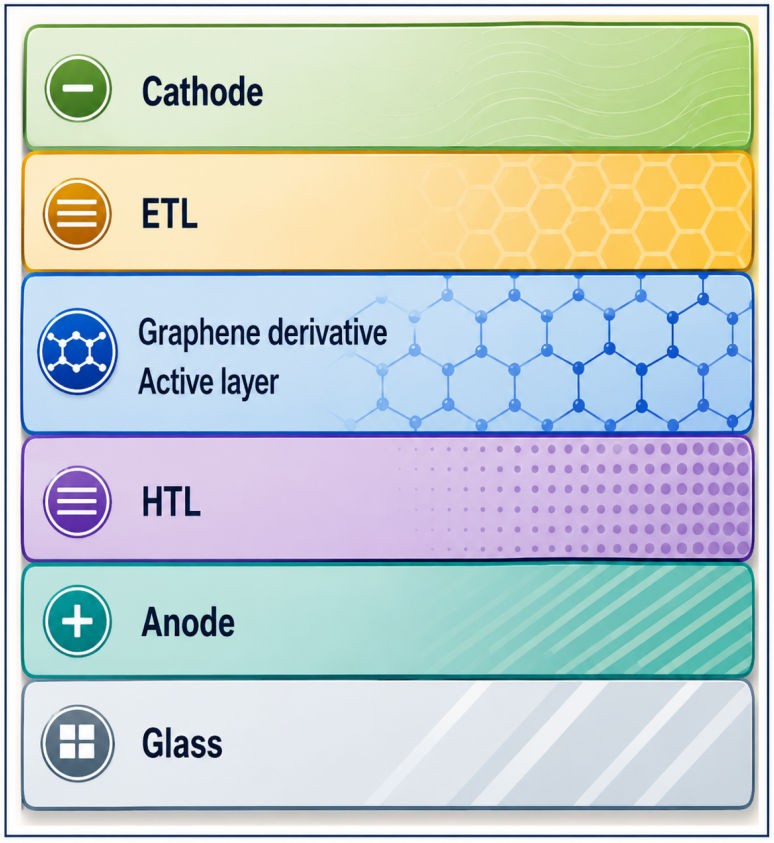


FIGURE 3.5: Graphene derivative in photoactive layer.

A major advancement came in 2012 with the systematic exploration of rGO as an absorber material. Thermal reduction of GO was shown to significantly improve electrical conductivity while maintaining electronic properties suitable for PV operation [315, 316]. Devices utilizing P3HT:rGO blends achieved efficiencies of 2.6%, representing a significant improvement over GO based devices [315, 316]. The period 2012-2014 saw the development of various chemical reduction methods for converting GO to rGO [315, 316]. Hydrazine reduction became a standard method, but concerns about hydrazine's toxicity led to the development of alternative reducing agents. Notably, Fernández-Merino *et al.* introduced vitamin C (ascorbic acid) as a green reducing agent, demonstrating that environmentally friendly reduction could produce high quality rGO suitable for PV applications. This approach achieved efficiencies of 3.2% in P3HT:rGO blends [315, 316].

Advanced spectroscopic studies during 2013-2015 provided crucial insights into the electronic structure of graphene derivatives [315, 316]. X-ray photoelectron spectroscopy (XPS) and UV-vis absorption studies revealed that the absorption spectrum of graphene derivatives could be systematically tuned by controlling the types and concentrations of functional groups [315, 316]. This led to the development of "designer" graphene derivatives with tailored absorption properties. A significant development in 2014-2015 was the introduction of ternary blend systems where graphene derivatives served as secondary absorbers alongside traditional polymer fullerene blends. Incorporating small amounts (1-5 wt%) of GO or rGO, significantly enhanced absorption in the NIR region, leading to improved photocurrent generation [315, 316].

The period 2015-2018 marked the emergence of sophisticated functionalized graphene derivatives designed specifically for absorber applications [317]. Researchers began attaching various organic chromophores and functional groups to graphene sheets to enhance absorption and control energy levels. For instance, porphyrin functionalized graphene exhibited strong absorption across the visible spectrum with additional NIR absorption, achieving efficiencies of 6.8% [317].

A revolutionary development occurred in 2016-2017 with the emergence of graphene quantum dots (GQDs) as absorber materials. Unlike larger graphene derivatives, GQDs exhibited size dependent band gaps due to quantum confinement effects, enabling precise band gap tuning through size control [318, 319]. Devices utilizing GQDs achieved efficiencies of 4.2%, demonstrating excellent spectral tunability [318, 319].

In summary, while graphene derivatives based layers of BHJOSCs may not yet universally outperform other high efficiency devices, their unique advantages position them as a critical component in the next generation BHJOSCs.

Chapter 4

Methodology for Device Modelling and Simulation:SCAPS-1D

Computational tools serve as a powerful tool for scientific discovery, equipping researchers to explore, learn and optimize complex systems in ways that would be challenging with tedious experimental techniques alone. One dimensional Solar Cell Capacitance Simulator (SCAPS-1D) has emerged as a widely utilized and powerful 1D simulation tool for studying vast area of SC technologies, including thin-film, crystalline, and amorphous SCs. This chapter examines into the role of numerical simulation studies for designing and optimization of PV devices, using SCAPS-1D. The fundamental principles by which SCAPS-1D operates and its key features are explored in this chapter.

Simulation studies utilize computational tools and mathematical models to analyze physical systems in a virtual environment, helping us understand their behaviour under various conditions. In PVs, device modelling and analysis are vital for developing new designs and analyze their performance, which provides a deeper understanding of the device's theoretical aspects. Numerical simulation has emerged as a powerful tool in the study and optimization of SCs. It reduces the gap between material properties and the device performance. It helps to create experimental design, and helps to reduce trial and error iterations in the lab. As computational tools and physical models improve, simulation studies will play an even larger role in the development of next generation OSC technologies. Numerical simulations offer analytical solutions and enhance our understanding of SCs, providing valuable information for designing efficient systems and yielding important results for future experimental and theoretical studies on OSCs.

One-dimensional Solar Cell Capacitance Simulator (SCAPS-1D) is implemented for our research study. We chose SCAPS-1D, since extensive literature is available on its usage and it has a broad range of applicability in the analysis of various types of SCs. SCAPS-1D is the simulation tool created by Prof. Marc Burgelman and his team at the Department of Electronics and Information systems (ELIS), University of Gent, Belgium. Initially designed for the studies of CdTe, $CuInSe_2$ SCs, SCAPS-1D has become the most popular tool for simulating SCs including CIGS, silicon, Perovskite and OSCs. SCAPS-1D provides an effective platform to analyze the working of OSCs and optimize the structure in a virtual environment. Along with the free availability of the software for the PV community, the main features of SCAPS-1D include modelling upto seven layers, separate provisions for direct, auger and trap assisted recombination mechanisms, grading features for all input parameters etc. Though the simulations of other SCs using SCAPS-1D have dominated the computational studies in PV research for the last decade, the use of SCAPS-1D for OSC simulation studies has not been explored much by the PV community. This chapter details the working principle and basic semiconductor equations solved by the software [320].

4.1 Basic Semiconductor Equations Solved in SCAPS-1D

4.1.1 Poisson's Equations

To analyze the working of SCs using SCAPS-1D numerical analysis software, it is essential that the software is capable of solving the fundamental semiconductor equations.

These equations determine the performance and output characteristics of SCs. Among the major semiconductor equations solved in SCAPS-1D, the governing one for electrostatic potential is the Poisson's equation. This equation describes how the potential varies in space due to a distribution of electric charge and is critical for understanding the internal electric fields within the SC device [320].

Equation (4.1) represents Poisson's equation for electrostatic potential:

$$\frac{d^2V}{dx^2} = -\frac{\rho}{\varepsilon} \tag{4.1}$$

where, V is the electrostatic potential, ρ is the charge density and ε is the permittivity of the semiconductor material, which is the product of the dielectric constant of the semiconductor and the permittivity of free space. Using the charge neutrality condition and assuming that all dopants are fully ionized, the charge density ρ can be further expressed as given in Equation (4.2):

$$\rho = q(p - n + N_D^+ - N_A^-) \tag{4.2}$$

where, q is the elementary charge, p stands for the hole concentration, n stands for electron concentration, N_D^+ is the concentration of ionized donor atoms and N_A^- is the concentration of ionized acceptor atoms. This formulation forms the basis of self-consistent numerical simulations in the SC modeling, allowing for the calculation of electric fields and potential profiles within semiconductor devices [320]. Substituting Equation (4.2) into Poisson's Equation gives Equation (4.3).

$$\frac{d^2V}{dx^2} = \frac{q(p - n + N_D^+ - N_A^-)}{\varepsilon} \tag{4.3}$$

To solve equation for the electrostatic potential V as a function of position x, the expressions for the carrier concentrations p and n must be known or approximated [320].

4.1.2 Continuity Equations

The continuity equations constitute another set of governing equations, as they simultaneously account for drift, diffusion, generation and recombination of carriers. The continuity equation for electron concentration is given by Equation (4.4).

$$\frac{\partial n}{\partial t} = \frac{1}{q}\frac{\partial J_n}{\partial x} + (G_n - R_n) \tag{4.4}$$

Similarly, the continuity equation for hole concentration is given by Equation (4.5)

$$\frac{\partial p}{\partial t} = \frac{1}{q}\frac{\partial J_p}{\partial x} + (G_p - R_p) \tag{4.5}$$

where J_n and J_p are the electron and hole current densities respectively. G_n and G_p are the generation rates for electrons and holes. R_n and R_p are the recombination rates for electrons and holes and t denotes time. These equations are the basis for modelling carrier transport in SCs using numerical simulations. The output attained using Equation Equations (4.6) and (4.7) exhibits nonlinear dependencies on the charge carrier concentrations (p and n). Consequently, these equations should be solved using numerical techniques using standard approaches such as discretization of equations, discretization of the device and by applying boundary conditions. To evaluate the current characteristics of an SC, the simulator must solve the drift-diffusion equations for current [320]. The drift-diffusion equations for charge carriers are given by Equations (4.6) and (4.7).

$$J_n = q\mu_n n\mathcal{E} + qD_n\frac{\partial n}{\partial x} \tag{4.6}$$

$$J_p = q\mu_p p\mathcal{E} - qD_p\frac{\partial p}{\partial x} \tag{4.7}$$

Where q denotes charge, J_n and J_p denotes the current densities for electrons and holes respectively. n and p stands for electron and hole concentrations respectively. μ_n and μ_p are the mobilities of electrons and holes. D_n and D_p are the diffusion coefficients of electrons and holes [320]. E denotes the electric field. According to the Einstein relation, the diffusion coefficients can be expressed in relation to the mobilities of charge carriers by Equation (4.8).

$$D_{(n,p)} = \mu_{(n,p)}\frac{kT}{q} \tag{4.8}$$

where k is Boltzmann's constant, T is the absolute temperature, and q is the electronic charge. To solve Equations (4.3), (4.4), and (4.5), it is also necessary to determine the generation and recombination rates (G, R), which are collectively expressed as the net

recombination rate U [320]. For an n-type semiconductor, the recombination rate can be expressed using Equation (4.9).

$$U = \frac{p - p_0}{\tau_p} \tag{4.9}$$

where p_0 is the equilibrium hole concentration and τ_p is the carrier lifetime for holes [320].

4.2 Steps and Analysis Performed using SCAPS-1D

The design of SC structure and the analysis of their electrical properties and spectral response can be performed using SCAPS-1D. SCAPS-1D is based on solving the fundamental carrier transport semiconductor equations using finite difference methods [320].

The action panel of SCAPS-1D: core control interface for SC simulation

The main interface that facilitate effective user interaction with this software is the action panel. This panel serves as the operational command center, where users control the execution of simulations. The action panel allows users to perform electrical characterization of SCs, initiate different types of simulations, and visualize the internal physical processes of the device. Each button or option within the action panel corresponds to a specific function, such as J–V analysis, QE analysis, capacitance measurement and plotting energy band diagram plotting [320]. The key functionalities of SCAPS-1D action panel are given below.

Current-Voltage calculations (I-V) - Dark J-V curve and illuminated J-V curve

The dark J-V curve gives the J-V curve without illumination. It provides insights into R_s and R_{sh}, diode ideality factor, recombination mechanisms in the dark, injection barriers and interface effects. Illuminated J-V curve analysis gives the J-V graph under standard illumination conditions (AM1.5G). From this analysis users can extract V_{oc}, J_{sc}, FF and PCE [320].

Capacitance-Frequency calculations (C-f)

In SCAPS-1D, the capacitance–frequency (C–f) curve is a useful diagnostic tool for analyzing the electrical response of an SC to AC signals of varying frequency. This feature

simulates how the capacitance of the device changes with frequency, revealing key insights into the device's charge storage, carrier dynamics, and defect states [320].

Quantum efficiency calculation (QE)

This action computes both the EQE and IQE. It evaluates how efficiently each wavelength of light generates current. It also reveals spectral response limitations due to absorption or recombination. Parasitic losses could be pinpointed by this action [320].

Capacitance-Voltage measurement (C-V)

By mimicking experimental C–V profiling, this action helps to analyze doping concentrations, examine depletion widths and detect interface traps or charge accumulation [320].

Plot bands and levels

This option provides the graphical representations of the energy band diagram, including C_B and V_B profiles, quasi-Fermi levels, electrostatic potential, band bending and interface discontinuities [320].

Running SCAPS-1D Software: A Step-by-Step Overview

This section outlines the process of running SCAPS-1D software, from installation to simulation execution, and emphasizes the importance of accurate input and thoughtful device configuration [320].

1- Launch SCAPS-1D.
2- Define the problem, including the device structure and the internal properties of materials.
3- Specify the operating conditions in which you want to do the simulation, i.e. specify the working point.
4- Select the measurements and curves to be calculated.
5- Start the calculation(s).
6- Display and analyze the simulated curves [320].

Installation and launch

SCAPS-1D is a Windows based executable program. It does not require complex installation procedures. The first step involves downloading the software. Later installation is done, and the action panel interface is set to run [320].

Device configuration

The first step before running a simulation is to define the device structure. SCAPS-1D models a device as a stack of layers, each with specific material properties. Each layer is defined separately and each layer can be assigned key parameters that include thickness (d), band gap (Eg), electron affinity (χ), dielectric permittivity (ε), doping concentration of acceptors (N_A), doping concentration of donors (N_D), mobility of electrons (μ_n), mobility of holes (μ_p) and recombination parameters (SRH, radiative and Auger). Other parameters include absorption spectrum for each layers, defect levels within layers, interface defect densities, trap density, capture cross sections and interface recombination velocities. Before running the simulations certain operating conditions should be set up. It includes light source (Typically AM 1.5G with defined intensity), bias conditions (start and end voltages, voltage step size), scan directions (forward or reverse bias) and temperature (default is 300 K, but it can be adjusted for thermal analysis) [320].

Analysis and saving output

After setting these conditions, the analysis of the SC parameters mentioned in the previous section are done. Followed by analysis and saving the entire simulation and saving the output results obtained.

4.3 Basic Operation of SCAPS-1D

The basic action window (simulator panel) of the simulation program is shown in Fig. 4.1.

The window is divided into different portions based on the functions in the simulation process. The set problem tab used to open the problem definition window for layer addition is shown in Fig. 4.2.

This window primarily serves to define the device structure of the SC along with the relevant material parameters. At the lower right-hand side of the window, icons for loading and saving are present. The load icon allows users to upload a previously saved file containing specific structure and parameters. Users can analyze some examples that are already available in the SCAPS-1D database by loading and executing them. The user can enter the desired device structure and its parameters, subsequently saving the file into the database using the save icon. The device structure of an SC is divided into various layers. Each layer can be detailed with material parameters and absorption profiles by

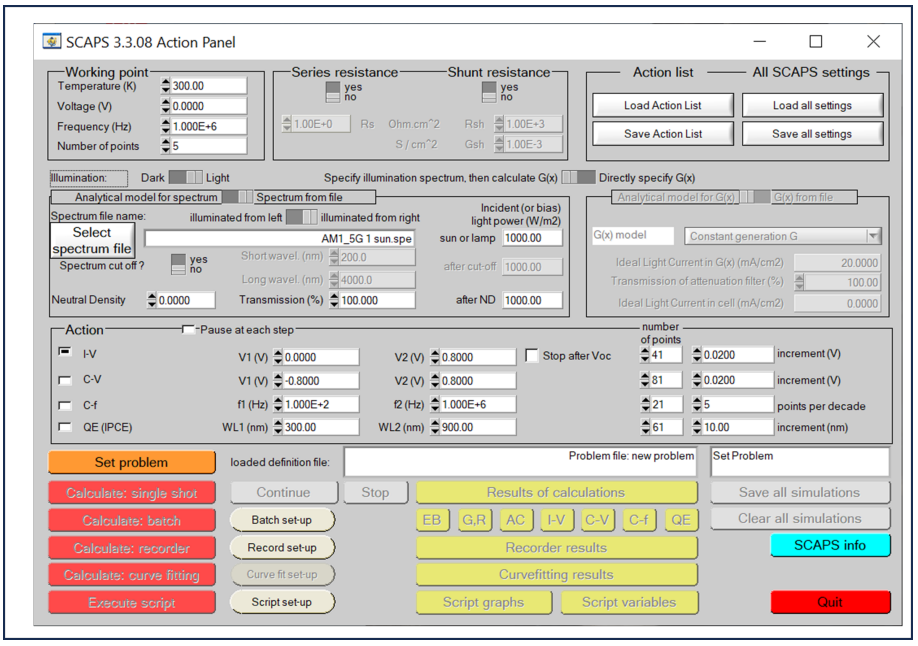


FIGURE 4.1: Opening action panel

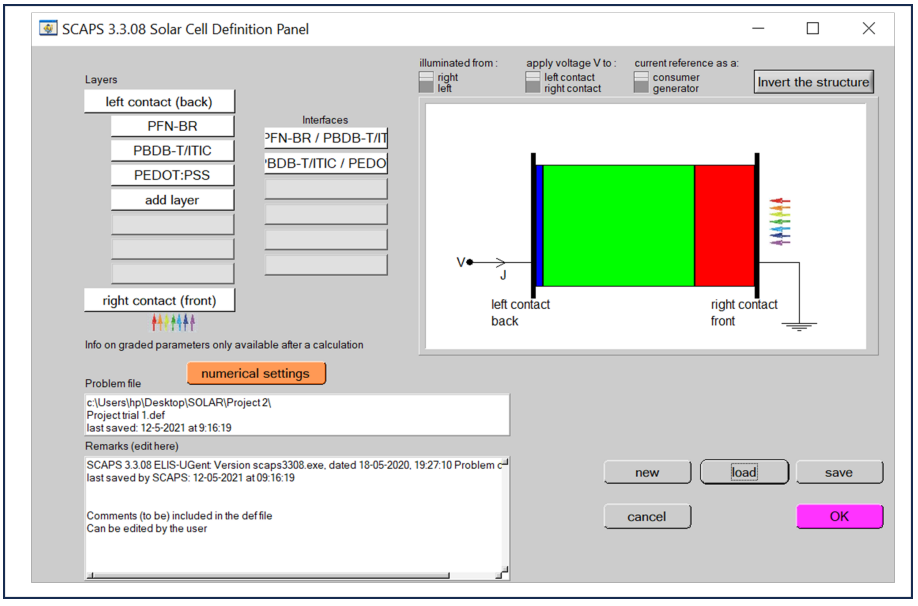


FIGURE 4.2: Panel showing layer addition

clicking under the layers tab [320]. The layer definition window showing parameters of layers opens up as shown in Fig. 4.3.

At the bottom of the LHS, there exists a tab labeled 'set absorption model' which is used to provide the absorption profile of the material. The SCAPS-1D database already

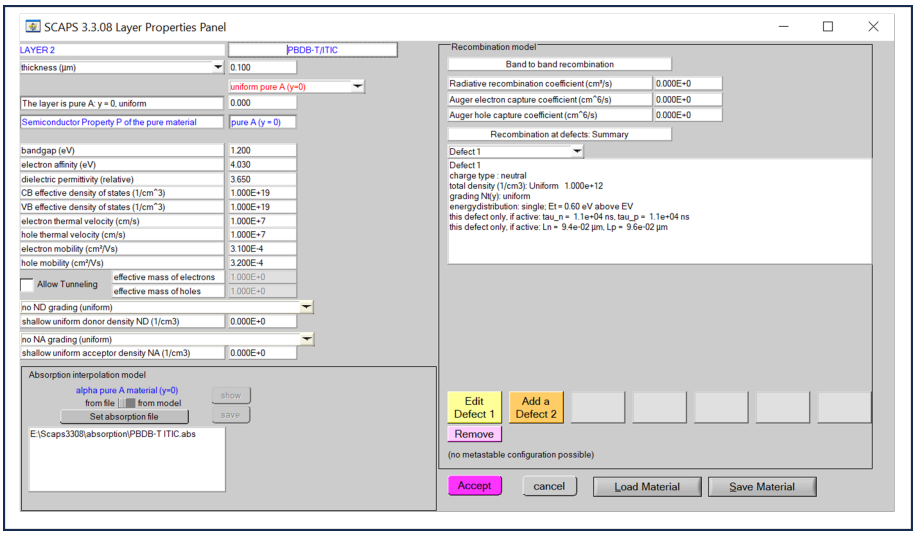


FIGURE 4.3: Panel showing parameters of layers

contains absorption profiles for certain materials. Users can select these profiles by clicking on the option from the file menu. Additionally, it is possible to upload an external absorption profile by creating a new one. The absorption profile must be uploaded as a text file with the .abs extension. This process is typically accomplished by digitizing the graph that represents the relationship between the material's absorption coefficient and the wavelength, which ranges from approximately 300 to 900 nm. The digitized data is converted to a text file with two columns where the first column corresponds to wavelength in nm and second column corresponds to the absorption coefficient in 1/m [320].

The defects and recombination occurring within the specific layer are detailed on the right-hand side (RHS) of the layer definition window. SCAPS-1D permits the addition of up to seven defects for a single layer; a new window appears upon selecting the Add/Edit tab. After saving the defect parameters, the layer definition window displays the corresponding carrier lifetime and diffusion length for both electrons and holes. Additionally, options to input the capture coefficient values related to Auger recombination and the coefficient for radiative recombination are available at the top of the RHS of the layer definition window. In the case of OSCs, these fields are typically left empty, as the primary recombination mechanism is predominantly SRH recombination. Each of the aforementioned characteristics must be specified individually for every layer within the device structure. There are also options to add, remove, or duplicate any of the created layers. Once all parameters for the layer have been defined, the properties for the front and back contacts can be incorporated. This can be accomplished by clicking on the front contact tab and back contact tab, which will launch a new window for contact properties.

The key characteristic of the contact electrode is its work function, which can be directly entered in the contact properties panel. Also, another way of getting work function of the electrode is to use the tab 'flat bands' already present in the action panel [320].

The final details required as input in the layer definition panel pertain to the interface defects. By clicking the tab adjacent to layers, a window appears where we must enter the input properties for interface defect densities. Once the interface defect properties are saved, the problem is successfully defined. The user can upload the device into the SCAPS-1D database by selecting the save tab located at the bottom right-hand side of the window. The left side of the action window addresses the simulation environment. The working point establishes the conditions that remain constant during the simulations. The operating temperature must be specified manually given for all the simulations [320]. Operating conditions can be chosen using the operating conditions panel as shown in Fig. 4.4.

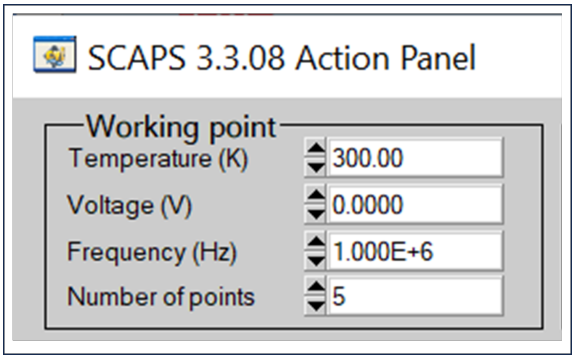


FIGURE 4.4: Operating conditions panel

The initial voltage of SCAPS-1D is always set at 0 V and it eventually reaches the input voltage after a few steps. The frequency f is necessary for the Capacitance-Voltage simulations, if any. The most important tab for the working of the PV cell is the illumination. The user can use the input light conditions as dark or under illumination, then choose the spectrum. The device structure can be illuminated from either from the front or the back electrode. The standard spectrum used in most of the simulation studies is AM 1.5G spectrum with incident power of $1000 W/m^2$ [320]. The spectrum selection panel is depicted in Fig. 4.5 and selection of spectrum from existing files appears as shown in Fig. 4.6.

Now we have to specify the type of simulation to be performed by the program. It could be of any output form (current-voltage (I-V), Capacitance-frequency (C-f), capacitance-Voltage (C-V) and Quantum efficiency (QE). Output parameter setting panel is shown in Fig. 4.7.

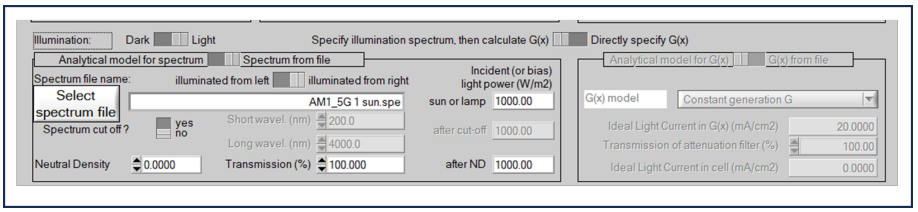


FIGURE 4.5: Solar spectrum selection panel

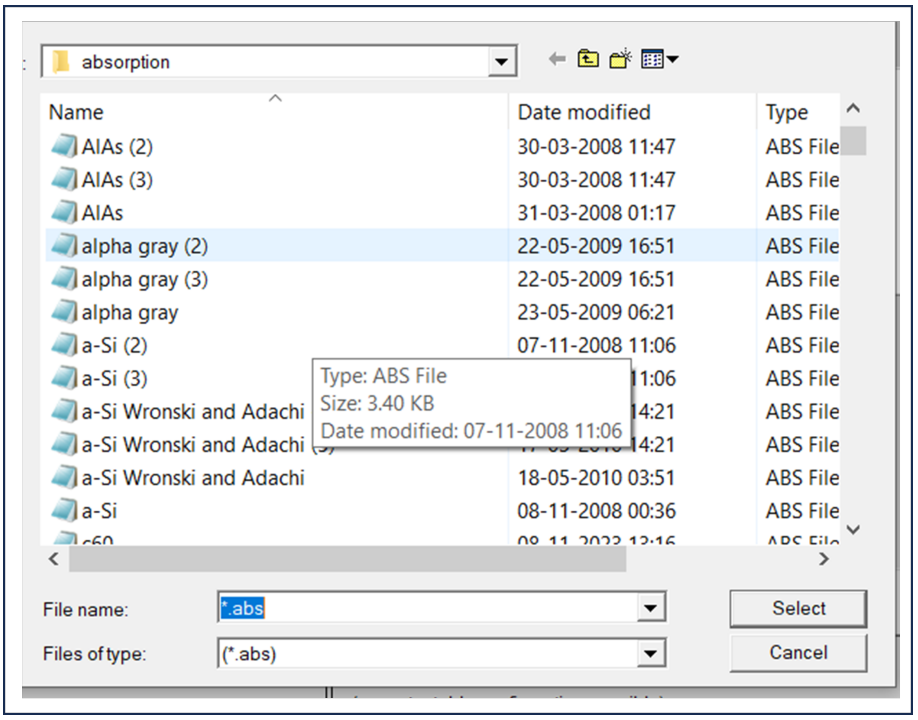


FIGURE 4.6: Selection of solar spectrum from files

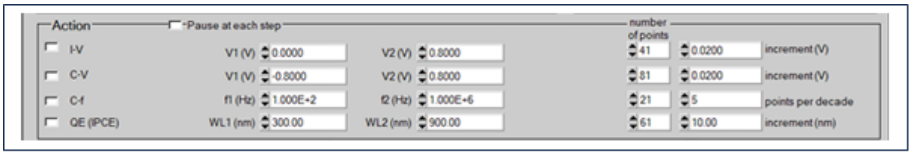


FIGURE 4.7: Output parameter setting panel

After clicking on the box near to the desired type of simulation, the user has to click on the tab-'calculate single shot' to start the simulations. There is also provision for batch simulations in the action window as shown in Fig. 4.8 and these batch calculations can be recorded as shown in Fig. 4.9.

Finally by choosing 'run the programme' and looking at the simulation output characteristics results, we can analyse the plots and graphs obtained as output results. Fig.

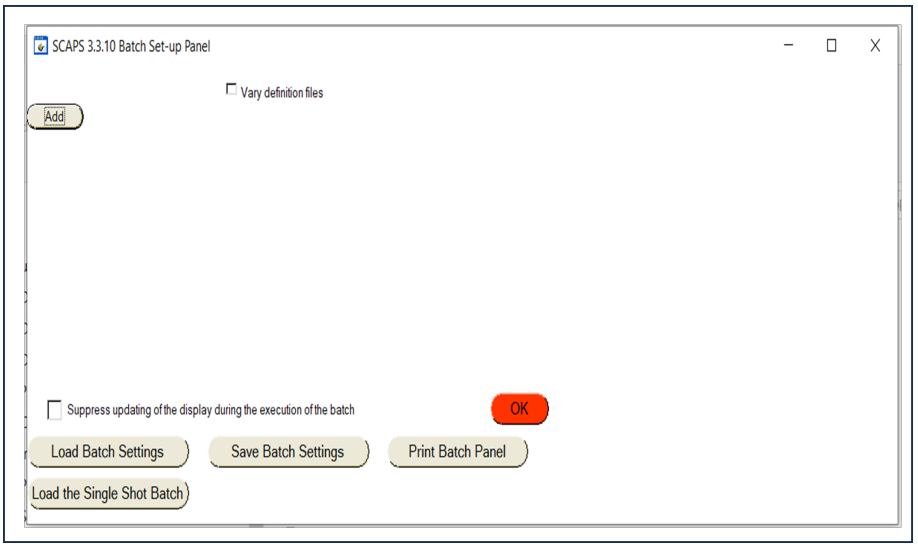


FIGURE 4.8: Batch recorder panel I

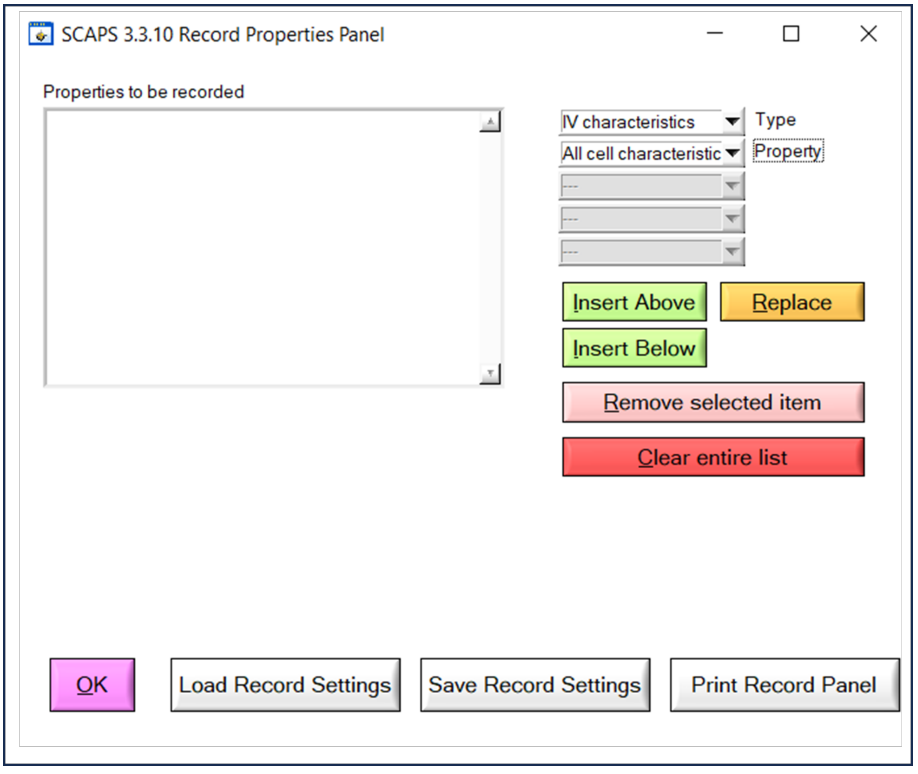


FIGURE 4.9: Batch recorder panel II

4.10 exhibits the panel displaying energy band diagrams. Fig. 4.11 and Fig. 4.12 show simple I-V and QE graphs obtained in SCAPS-1D respectively.

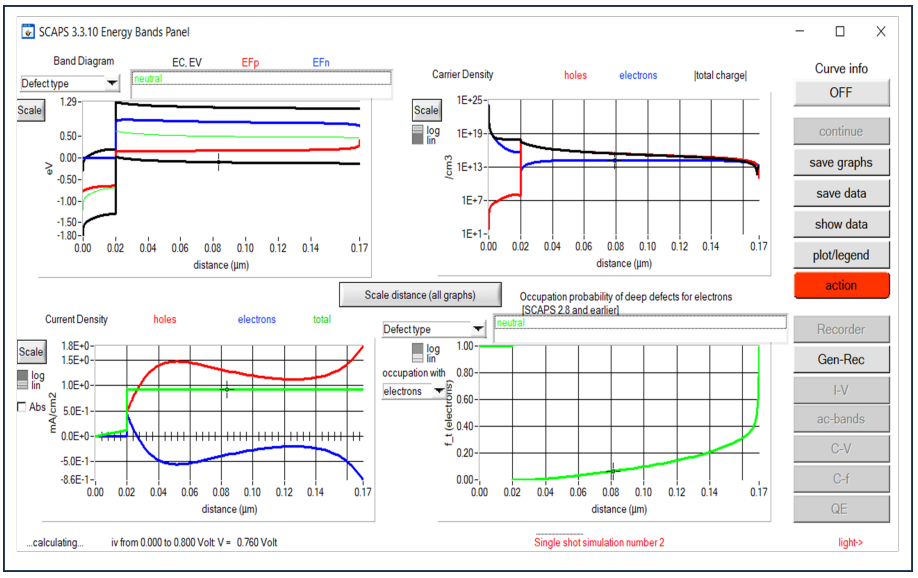


FIGURE 4.10: Panel showing energy band diagrams

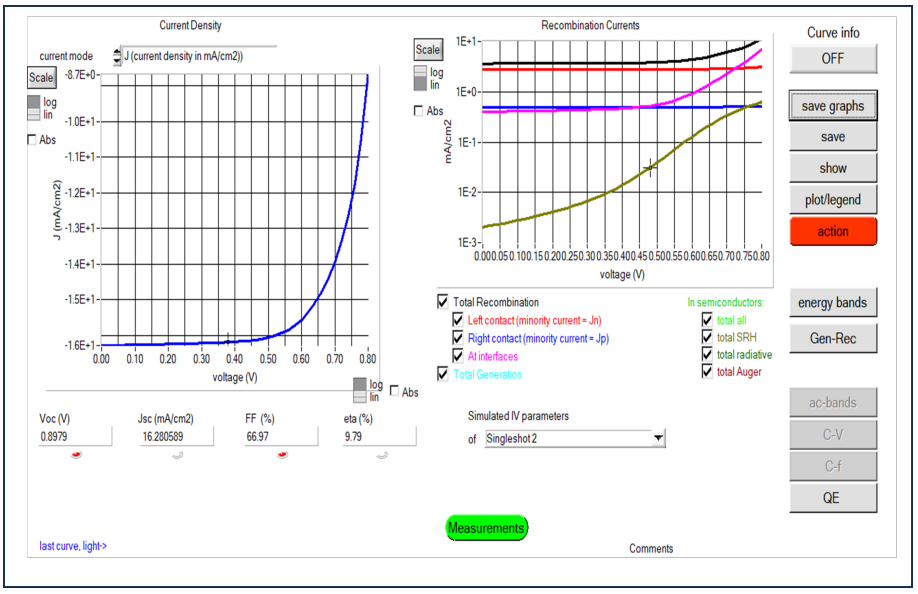


FIGURE 4.11: I-V graph

4.3.1 The Working of SCAPS-1D

By applying suitable boundary conditions, SCAPS-1D solves a batch of coupled differential equations. Then steady state solutions of the system are calculated numerically.

Discretization of the structure in SCAPS-1D

Discretization of the device structure is performed by generating a mesh. The mesh generation inside SCAPS-1D follows specific criteria to ensure numerical accuracy. At

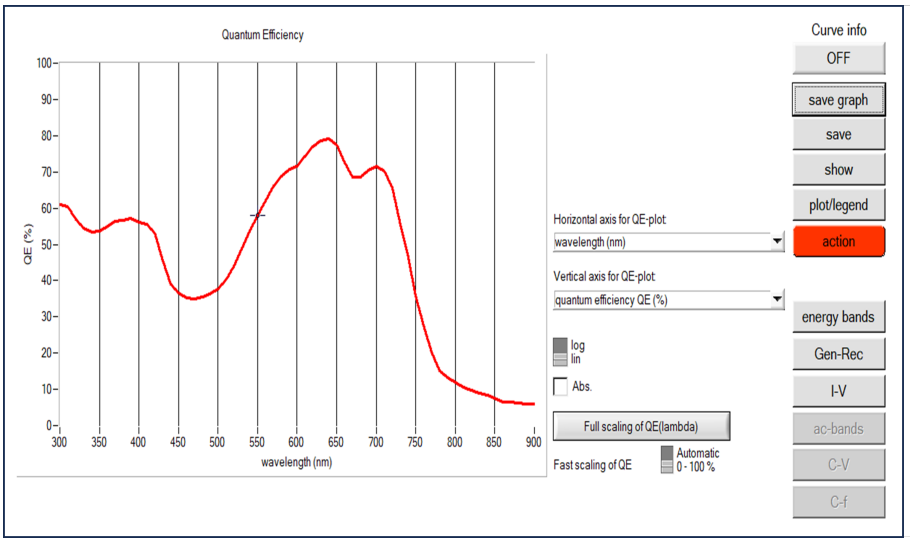


FIGURE 4.12: QE graph

the centre of a layer, a coarse mesh is generated while more finer mesh is generated at the device interface and contact electrodes. The meshing at the interface of the structure involves two points for discretization. Mesh is optimized at the time of calculation. Also, there is provision for optimizing the mesh for each iteration which can be made possible by setting the tab recalculate the mesh during iterations in the numerical window. If the recalculating mesh option is activated in the numerical window the programme calculates the ratio of recombination rate R and generation rate G between two adjacent meshpoints. A maximum ratio value is already set in the numerical panel. If the ratio is higher than this value, more meshpoints will be added to the simulation and if the ratio is lower, a meshpoint will be deleted by the program [320].

Steps to reach the solution in SCAPS-1D

The calculations commence when we select the calculate single shot tab from the action window, following the successful specification of the desired simulation type. The initial phase involves solving the governing semiconductor equations described in the section through numerical techniques. The primary numerical methods employed are the Gummel's iteration method and the Newton-Raphson method. The parameters that govern these methods can be found in the numerical window. It is advisable to utilize a large number of iteration steps to ensure a smooth calculation process. An initial guess is essential to arrive at the solution. This guess should be very close to the actual solution of the system, as any deviation from the actual value may lead to convergence failure after a few iteration steps. Thus, extreme care is needed while choosing the initial guess value [320].

However, it is not necessary for the user to provide the initial guess value to the program. SCAPS-1D operates under various scenarios to derive a solution value at the working point conditions and arrives at the first calculation point. The initial assumptions made by SCAPS-1D include quasi-Fermi levels of zero throughout the device structure, and it is also assumed that the electrostatic potential across the structure is zero. These assumptions facilitate the acquisition of the initial guess under dark equilibrium conditions with zero applied voltage. Under illumination, SCAPS-1D calculates the short circuit condition in between an intermediate level to get an initial guess value [320].

Extracting output parameters from SCAPS-1D

The output of the simulation performed can be obtained by navigating the results panel from the action window itself. The primary option for result analysis is the I-V panel. The current density voltage curve (J-V curve) is seen at the top of LHS of the panel. The RHS of the panel shows recombination currents. The output parameters of the SC are shown below the J-V curve with V_{oc}, J_{sc}, FF and PCE are displayed below the I-V curve in four columns. The QE of the simulated device can be analysed by clicking on the QE panel tab. Here QE refers to external quantum efficiency (EQE). We can save the J-V curve and QE curve directly into any other folder by clicking on the save tab on the top-right corner of the window [320].

4.4 Limitations of SCAPS-1D

Although SCAPS-1D is a powerful and computationally efficient tool for investigating and optimizing PV devices, it possesses several limitations when applied to BHJOSCs. SCAPS-1D treats the photoactive layer as a homogeneous medium and therefore cannot explicitly capture the complex nanoscale D-A morphology, phase separation, percolation pathways, and interfacial area that critically govern charge generation and transport in BHJOSCs.

Furthermore, the simulator is based primarily on drift–diffusion formalism and does not rigorously account for excitonic processes such as exciton generation, diffusion, charge-transfer state formation, and exciton dissociation, which are fundamental to the operation of OSCs. The substantial energetic and positional disorder present in organic semiconductors, leading to hopping-mediated charge transport and localized states, is also represented only through simplified effective parameters.

In addition, SCAPS-1D employs a 1D approximation that neglects lateral inhomogeneities, 3D morphology effects, and spatial variations in charge transport pathways. Consequently, the simulation results provide valuable insights into device trends, material selection, and parameter optimization, but may not fully reproduce the intricate physical processes occurring in real BHJOSC devices.

Chapter 5

Numerical Investigation of P3HT:PCBM BHJOSC with Diverse Graphene Derivative HTLs and ETLs

This chapter explores an extended numerical simulation study of P3HT:PCBM BHJOSC with graphene derivatives as HTL. Three significant simulation studies were carried out and analyzed. The simulation of P3HT:PCBM BHJOSC utilizing graphene as the HTL along with different ETLs were carried out in the initial study. The subsequent research study involved are numerical simulation of P3HT:PCBM BHJOSC, employing GO as the HTL, with different ETLs and metal electrodes (cathodes). Lastly, the numerical simulation of P3HT:PCBM BHJOSC with rGO serving as the HTL, incorporating various ETLs and distinct cathodes were done.

P3HT:PCBM based BHJOSCs have played a vital role in the field of OPVs over the years. Their flexibility, simplicity, processability, and reproducibility have made them a standard for investigating light harvesting mechanisms [140, 321]. Simulation studies on P3HT:PCBM based BHJOSCs have significantly helped in understanding the charge transport, morphology, and efficiency limitations of these BHJOSCs [140, 321].

The most common HTL PEDOT:PSS shows good performance as an HTL in P3HT:PCBM BHJOSCs [322, 323, 324]. Despite its good performance, its unavoidable limitations have prompted researchers to search for a better HTL [322, 323, 324]. Its limitations include hygroscopicity and acidic nature that deteriorates both the active layer and the electrode [322, 323, 324]. Therefore, a stable and efficient HTL is required to enhance device performance and address stability concerns. These problems can be resolved by the incorporation of graphene and graphene derivatives [322, 324, 325, 326, 327].

Numerical simulation studies of P3HT:PCBM BHJOSCs with graphene derivatives as HTLs are rarely reported. The novelty of the present work lies in the systematic SCAPS-1D based simuation study using non-zero band gap graphene, GO, and rGO as the HTL. In our initial simulation study, we employed graphene with a non-zero band gap as the HTL to harness its enhanced charge transport properties while addressing the inherent limitations of pristine graphene. Pristine graphene, with its zero band gap, exhibits metallic conductivity, which leads to inefficient charge injection and significant recombination in opto-electronic devices.

Simulation studies of P3HT:PCBM blends focus on optimizing the input parameters including layer thickness, electron mobility, hole mobility, conduction band density, valence band density, defect density, acceptor concentration, donor concentration, and interfacial defects. One of the challenges with modelling and simulating P3HT:PCBM BHJOSCs lies in accounting for their blend morphology. Effective medium approximations or spatially resolved model attempt is employed to simulate phase separation and charge pathways.

Numerical simulation has proven to be an advanced and reliable methodology for studying and optimizing P3HT:PCBM BHJOSCs. In the following sections, discussions of numerical simulation studies of P3HT:PCBM BHJOSCs with graphene/GO/rGO as an HTL is done. It is of utmost importance to understand and learn about P3HT:PCBM as a photoactive layer to deal with its numerical simulation study.

5.1 P3HT:PCBM BHJOSCs

P3HT:PCBM is a blend of Poly(3-hexylthiophene) (P3HT) (donor) and [6,6]-phenyl-C_{61}-butyric acid methyl ester (PCBM) (acceptor). The P3HT:PCBM blend forms a BHJ, a nanostructured interpenetrating network of donor (P3HT) and acceptor (PCBM) domains, which significantly enhances charge separation and transport efficiency [328, 329].

P3HT is a semiconducting polymer known for its high hole mobility, solution processability and thermal stability. The energy band gap (1.9 eV) and HOMO-LUMO levels of P3HT makes it suitable for photon absorption in the visible range and effective charge transfer to PCBM. PCBM, a fullerene derivative, acts as an efficient electron acceptor and transporter, providing good miscibility with P3HT and facilitating charge extraction. Fig. 5.1 illustrates the chemical structures of P3HT and PCBM. The conjugated polymer structure of P3HT and the fullerene cage like structure of PCBM complement each other by providing efficient D-A interface that facilitate exciton dissociation and charge transport in BHJOSCs [140, 321].

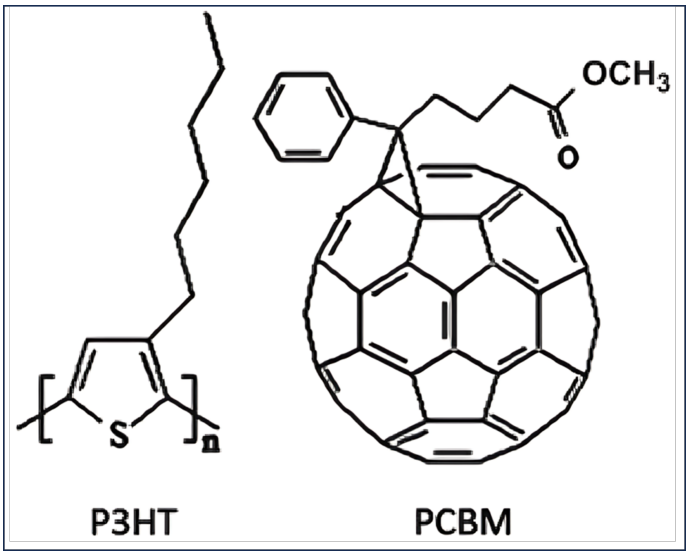


FIGURE 5.1: Chemical structures of P3HT and PCBM.

The performance of P3HT:PCBM BHJOSC is highly sensitive to their morphology. Devices based on P3HT:PCBM blends have achieved efficiencies exceeding 5% under optimized conditions, making them a benchmark system for OPVs [328]. Key factors influencing the efficiency include film thickness, D to A ratio (typically 1:1 by weight), and post-processing treatments. Despite their popularity, P3HT:PCBM system suffers from innate limitations like limited absorption range, energetic losses and morphological instability [328, 329].

To overcome these limitations, researchers continue to develop new donor polymers and NFAs with better absorption, energy level alignment, and morphological stability [328, 329]. However, P3HT:PCBM remains a model system for studying the fundamental physics of OPVs and for benchmarking new material systems.

5.2 Numerical Investigation of P3HT:PCBM BHJOSC with Graphene as an HTL

Recently, the field of FA based BHJOSC devices has shown a great deal of interest in incorporating graphene and graphene related materials (GRMs) as interfacial layers. Their unique properties like high electrical and thermal conductivity, large specific surface and unique combination of mechanical strength and flexibility [330, 331, 332, 333, 334, 335] makes them a good candidate material for future applications in BHJOSCs.

In this study graphene was incorporated as the HTL and a simulation study with diverse ETLs were carried out. Fig. 5.2 illustrates the device design used for the simulation study.

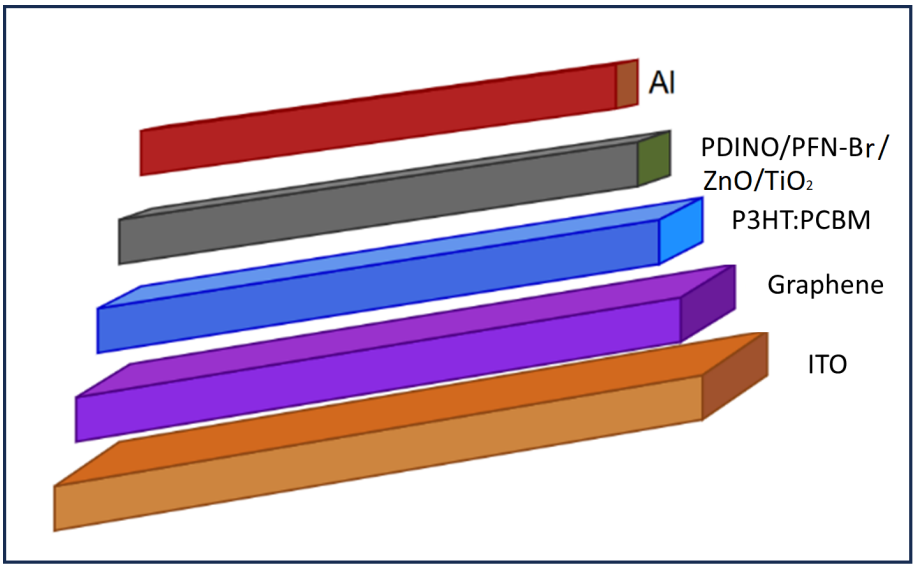


FIGURE 5.2: Schematic representation of P3HT:PCBM BHJOSC with graphene as HTL and diverse ETLs

Graphene is consistently used as the HTL across all four configurations studied. An in-depth analysis and extensive numerical simulation study of P3HT:PCBM BHJOSC with graphene as HTL and various ETLs has not been reported to date.

In the four configurations analyzed, we used diverse ETLs, namely 2,9-bis[3-(dimethyl oxidoamino)propyl]anthra(2,1,9-def:6,5,10-d'e'f')diisoquinoline-1,3,8,10(2H,9H)-tetrone (PDINO), PFN-Br, ZnO and TiO_2. The four configurations studied are as follows:

- ITO/graphene/P3HT:PCBM/PDINO/Al (Device structure I)
- ITO/graphene/P3HT:PCBM/PFN-Br/Al (Device structure II)
- ITO/graphene/P3HT:PCBM/ZnO/Al (Device structure III)
- ITO/graphene/P3HT:PCBM/TiO_2/Al (Device structure IV)

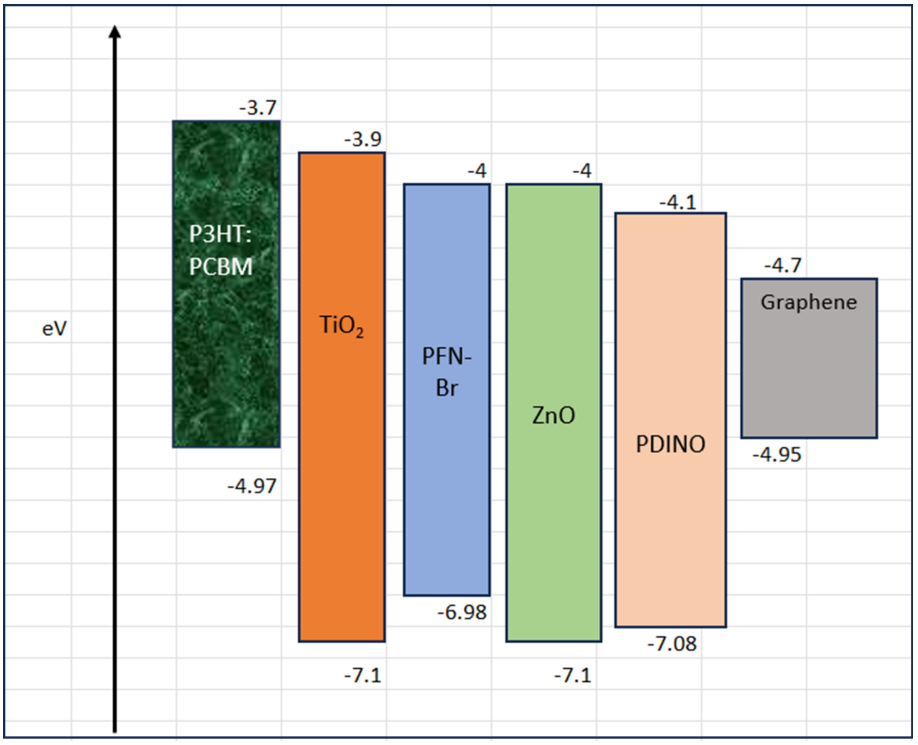


FIGURE 5.3: Energy band alignment of the layers used for the simulation study of ITO/-graphene/P3HT:PCBM/ETL/Al.

Fig. 5.3 shows the energy band distribution of the layers used for the study. To align the numerical model with real-world device operation, the HOMO and LUMO levels derived from the material band gaps and electron affinities were extracted from previously published experimental data. This integration of empirical literature values anchors the band diagram in realistic material physics, reinforcing the practical validity of the simulated SC performance.

The material input parameters of the layers used for the simulation study which are listed in Table 5.1 and Table 5.2 were chosen from previous literature of experimental and simulation works done on P3HT:PCBM based BHJOSCs. Input numerical parameters given in the table include thickness of the layer (d), band gap (E_g), electron affinity (χ), relative permittivity (ϵ_r), conduction and valence band densities (C_B and V_B), electron and hole thermal velocities (V_e and V_h), electron and hole mobility (μ_e and μ_h), donor density and acceptor density (N_D and N_A), and defect density (N_t). ITO was used as the anode and Al as the cathode. Processing and availability of ITO anodes are much easier these days and always stands as a good option for current and future experimental works. The work function of ITO used in this study is 4.5 eV [336]. Al is the most commonly used cathode in OSCs due to its easier availability. The work function of Al used for this study is 4.2 eV [336].

TABLE 5.1: Input parameters of active layer (P3HT:PCBM) and HTL (graphene).

Parameter	P3HT:PCBM	Graphene
Thickness (d) (nm)	100 [336]	20 [337]
Band gap (E_g) (eV)	1.27 [338]	0.25 [337]
Electron affinity (χ) (eV)	3.7 [338]	4.7 [337]
Dielectric constant (ε_r)	3.5 [339]	13 [337]
Conduction band density (C_B) (cm^{-3})	7.8×10^{19} [339]	2×10^{20} [337]
Valence band density (V_B) (cm^{-3})	7.8×10^{19} [339]	1.8×10^{20} [337]
Thermal velocity of electrons (V_e) (cm/s)	1×10^{7} [340]	1×10^{7} [337]
Thermal velocity of holes (V_h) (cm/s)	1×10^{7} [340]	1×10^{7} [337]
Electron mobility (μ_e) (cm^2/Vs)	2×10^{-3} [340]	1×10^{4} [337]
Hole mobility (μ_h) (cm^2/Vs)	2×10^{-3} [340]	1×10^{4} [337]
Doping concentration of donor (N_D) (cm^{-3})	0 [339]	1.0×10^{15} [337]
Doping concentration of acceptor (N_A) (cm^{-3})	0 [339]	0 [337]
Defect density (N_t) (cm^{-3})	6.847×10^{15}	1.9×10^{9} [337]

TABLE 5.2: Input parameters of ETLs used for the simulation study.

Parameter	PDINO	PFN-Br	ZnO	TiO_2
Thickness (d) (nm)	5 [341]	5 [341]	20 [341]	5 [341]
Band gap (E_g) (eV)	2.98 [341]	2.98 [341]	3.1 [341]	3.2 [341]
Electron affinity (χ) (eV)	4.1 [341]	4 [341]	4 [341]	3.9 [341]
Dielectric constant (ε_r)	5 [341]	5 [341]	9 [341]	9 [341]
Conduction band density (C_B) (cm^{-3})	1×10^{19} [341]	1×10^{19} [341]	2×10^{18} [341]	1×10^{19} [341]
Valence band density (V_B) (cm^{-3})	1×10^{19} [341]	1×10^{18} [341]	1.8×10^{19} [341]	1×10^{19} [341]
Thermal velocity of electrons (V_e) (cm/s)	1×10^{7} [341]	1×10^{7} [341]	1×10^{7} [341]	1×10^{7} [341]
Thermal velocity of holes (V_h) (cm/s)	1×10^{7} [341]	1×10^{7} [341]	1×10^{7} [341]	1×10^{7} [341]
Electron mobility (μ_e) (cm^2/Vs)	2×10^{-6} [341]	2×10^{-6} [341]	1×10^{2} [341]	20 [341]
Hole mobility (μ_h) (cm^2/Vs)	1×10^{-3} [341]	1×10^{-4} [341]	2.5×10^{2} [341]	0.1 [341]
Doping concentration of donor (N_D) (cm^{-3})	2×10^{21} [341]	9×10^{18} [341]	1×10^{18} [341]	0 [341]
Doping concentration of acceptor (N_A) (cm^{-3})	0 [341]	0 [341]	0 [341]	1×10^{18} [341]
Defect density (N_t) (cm^{-3})	1×10^{9} [341]	1×10^{14} [341]	1×10^{14} [341]	1.0×10^{14} [341]

The following input parameters were chosen as default value from the SCAPS-1D software. Operating temperature of 300 K was set and simulation was done under AM 1.5 G light with an intensity of 100 mW/cm^2. Capture cross-section, electron and hole thermal

velocities for all layers were set to 1×10^{-15} cm^2 and 1×10^{7} cm/s respectively. Furthermore, the capture cross-section for the HTL/active layer interface, and active layer/ETL interface were chosen as 1×10^{-15} cm^2. The characteristic energy value for a defect with a neutral Gaussian distribution was set to 0.1 eV. The energy level with respect to the reference (eV) was kept constant for all layers at 0.6 eV.

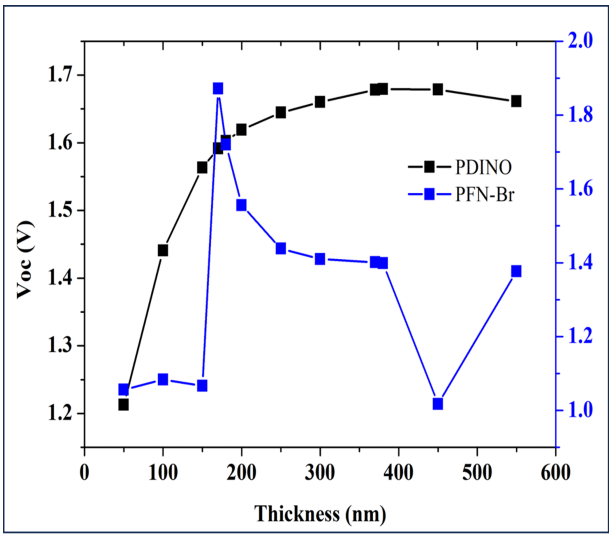


FIGURE 5.4: Influence of variation of V_{oc} with varying thickness of P3HT:PCBM on device structures I and II.

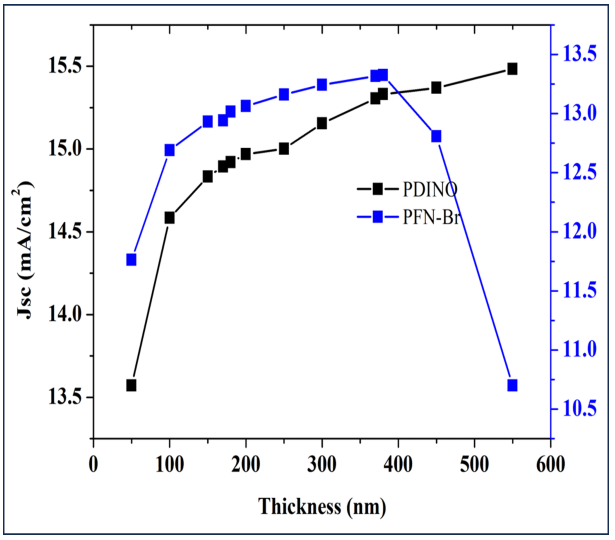


FIGURE 5.5: Influence of variation of J_{sc} with varying thickness of P3HT:PCBM on device structures I and II.

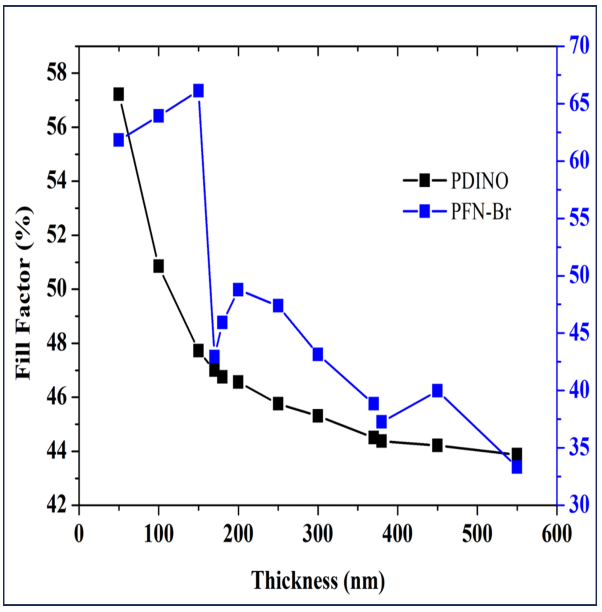


FIGURE 5.6: Influence of variation of FF with varying thickness of P3HT:PCBM on device structures I and II.

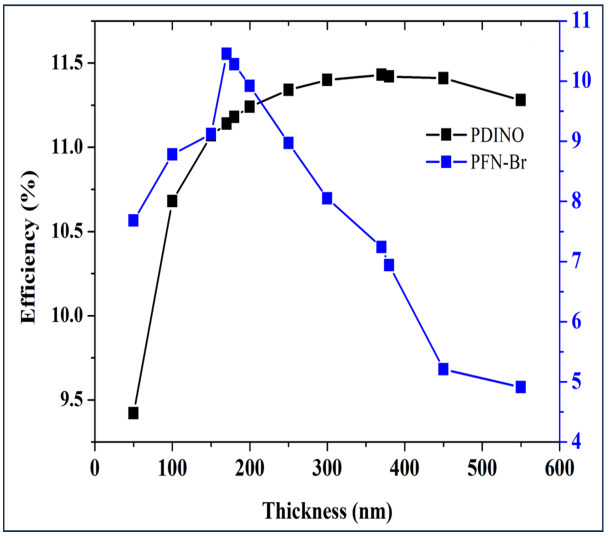


FIGURE 5.7: Influence of variation of efficiency with varying thickness of P3HT:PCBM on device structures I and II.

5.2.1 Study of P3HT:PCBM BHJOSC with Graphene as HTL, PDINO and PFN-Br as ETLs

The configurations ITO/graphene/P3HT:PCBM/PDINO/Al (device structure I) and ITO/graphene/P3HT:PCBM/PFN-Br/Al (device structure II) are simulated and analyzed in this study. In both device structures (I and II), graphene is consistently incorporated

as the HTL. PDINO is used as the ETL in structure I and PFN-Br is used as the ETL in structure II.

5.2.1.1 Influence of Thickness Variation of Active Layer on the Device Performance of Structures I and II

Thickness of the active layer (P3HT:PCBM) was varied from 50 to 550 nm and its influence on output device parameters of device structure I and device structure II were studied.

After the simulation, following device output parameters were obtained for device structure I. Highest V_{oc} of 1.6792 V was attained at a thickness of 420 nm (Fig. 5.4), J_{sc} of 15.4836 mA/cm^2 at 550 nm (Fig. 5.5), an FF of 57.22% at 50 nm (Fig. 5.6) and a peak efficiency of 11.43% was achieved at 370 nm (Fig.5.7).

For device structure II, highest V_{oc} of 1.6720 V was attained at 170 nm (Fig. 5.4). J_{sc} reached a value of 13.3077 mA/cm^2 at 300 nm (Fig. 5.5). Highest FF of 67.91% was achieved at 170 nm (Fig. 5.6) and peak efficiency of 11.51% was obtained at a thickness of 170 nm (Fig. 5.7).

For device structure I, V_{oc}, J_{sc} and FF exhibited a systematic pattern of variation across a wide range of thickness. This can be attributed to good optical absorption, efficient and consistent charge transport, low recombination losses and robust interfacial properties between PDINO and the active layer. The higher V_{oc} obtained could be attributed to certain factors. Favourable energy-level alignment between the low band gap graphene HTL, the P3HT:PCBM active layer, and the ETLs, which reduces interfacial recombination losses and improves charge selectivity. Additionally, increasing the active layer thickness enhances light absorption and carrier generation up to an optimum value, contributing to the increase in V_{oc}.

For device structure II, peak efficiency occurred at lower thickness of the active layer. Efficiency dropped significantly beyond this point due to sharp decrease in V_{oc} and FF at higher thicknesses. Inefficient charge extraction in thicker films, heightened recombination, energetic discrepancies at the interface and the accumulation of space charge may account for this behaviour observed in PFN-Br based devices (structure II).

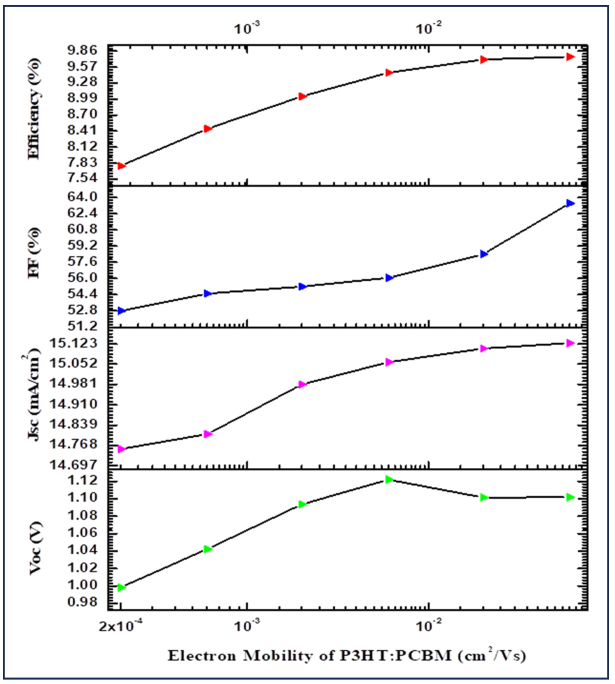


FIGURE 5.8: Variation of device output parameters with varying electron mobility of P3HT:PCBM on device structure I.

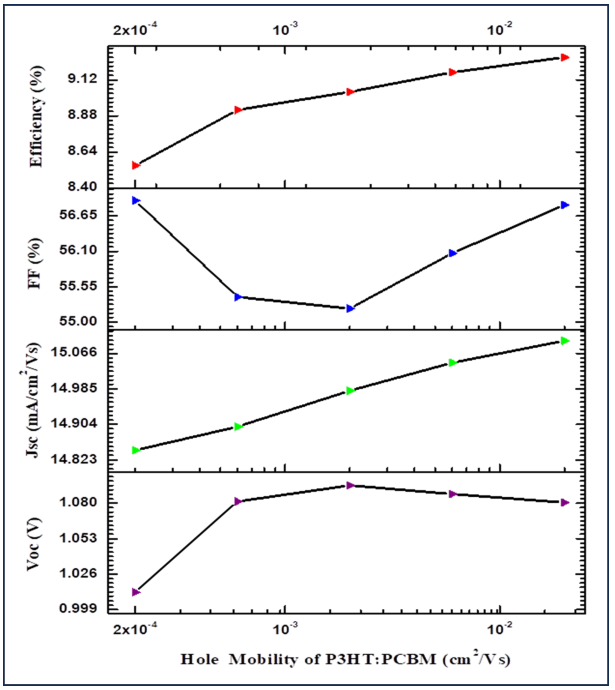


FIGURE 5.9: Variation of device output parameters with varying hole mobility of P3HT:PCBM on device structure I.

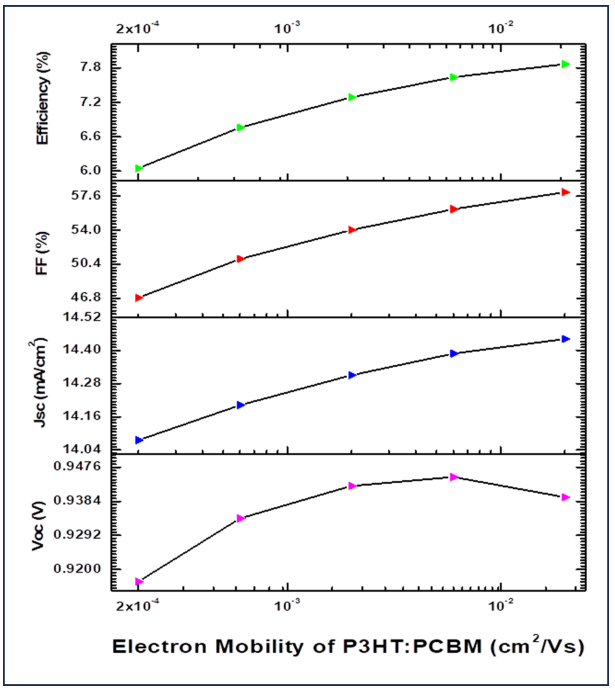


FIGURE 5.10: Variation of device output parameters with varying electron mobility of P3HT:PCBM on device structure II.

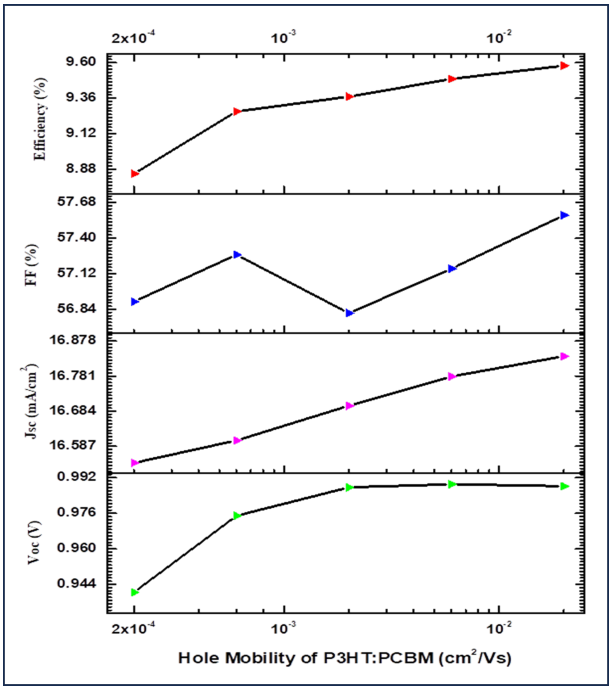


FIGURE 5.11: Variation of device output parameters with varying hole mobility of P3HT:PCBM on device structure II.

5.2.1.2 Influence of Electron Mobility and Hole Mobility Variation in Active Layer on the Device Performance of Structures I and II

Fig. 5.8 and Fig. 5.9 displays the influence of varying electron mobility and hole mobility of active layer (P3HT:PCBM) on device output parameters of device structure I.

Simulation was done for electron mobilities ranging from 2×10^{-4} to 2×10^{-2} cm^2/Vs. Highest V_{oc} of 1.1219 V was obtained at 6×10^{-3} cm^2/Vs. A maximum J_{sc} of 15.126 mA/cm^2 was acquired at 6×10^{-2} cm^2/Vs. The highest FF of 63.42% was attained at 6×10^{-2} cm^2/Vs. Maximum efficiency of 9.76% was obtained for 6×10^{-2} cm^2/Vs. As the electron mobility of P3HT:PCBM increased, the device output parameters improved in device structure I. These results showed that the increasing electron mobility resulted in improved device performance. Increased electron transport helps in reducing charge recombination and efficient charge collection which collectively contributes to higher V_{oc}, J_{sc}, FF, and efficiency.

Simulation study on the influence of varying hole mobility of P3HT:PCBM for device structure I was done and plotted in Fig. 5.9. Hole mobility was varied from 2×10^{-4} to 2×10^{-2} cm^2/Vs. V_{oc} of 1.0936 V is achieved at 2×10^{-3} cm^2/Vs. At 6×10^{-2} cm^2/Vs, a J_{sc} of 15.115 mA/cm^2, an FF of 57.12% and an efficiency of 9.31% were achieved. The improvement in device performance with increasing hole mobility was due to more efficient hole transport and extraction, which reduces charge recombination within the active layer. Consequently, enhanced charge collection leads to higher J_{sc}, FF, and overall device efficiency.

For device structure II, as electron mobility was varied, highest V_{oc} of 0.9883 V was obtained at 6×10^{-3} cm^2/Vs, maximum current density of 16.852 mA/cm^2 was shown at 2×10^{-2} cm^2/Vs, highest FF of 61.61% was attained for 2×10^{-2} cm^2/Vs, and highest efficiency of 10.15% was obtained for 2×10^{-2} cm^2/Vs as shown in Fig. 5.10. Incorporation of PFN-Br as ETL in P3HT:PCBM BHJOSC helps to improve device performance as PFN-Br energy level is well aligned with that of P3HT:PCBM and graphene.

In the BHJOSC, with device structure II, simulations were done for varying hole mobilities and V_{oc} of 0.9891 V was achieved at 6×10^{-3} cm^2/Vs. A current density of 16.859 mA/cm^2 was acquired at 6×10^{-2} cm^2/Vs. FF of 57.67% was attained at 6×10^{-2} cm^2/Vs. Efficiency of 9.62% was obtained at 6×10^{-2} cm^2/Vs. The influence of varying hole mobility of active layer in device structure II is displayed in Fig. 5.11.

The mobility of P3HT:PCBM is of smaller range, and incorporating ETLs improves the electron extraction towards the respective electrodes.

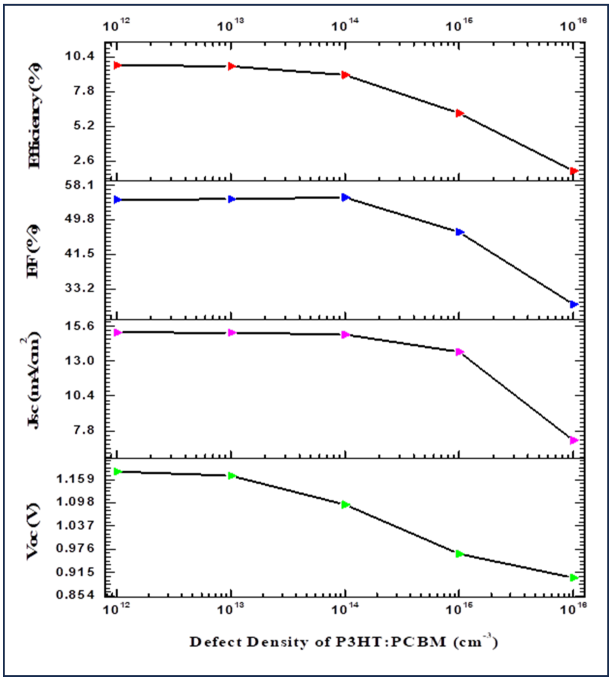


FIGURE 5.12: Influence of variation of device output parameters with varying defect density of P3HT:PCBM on device structure I.

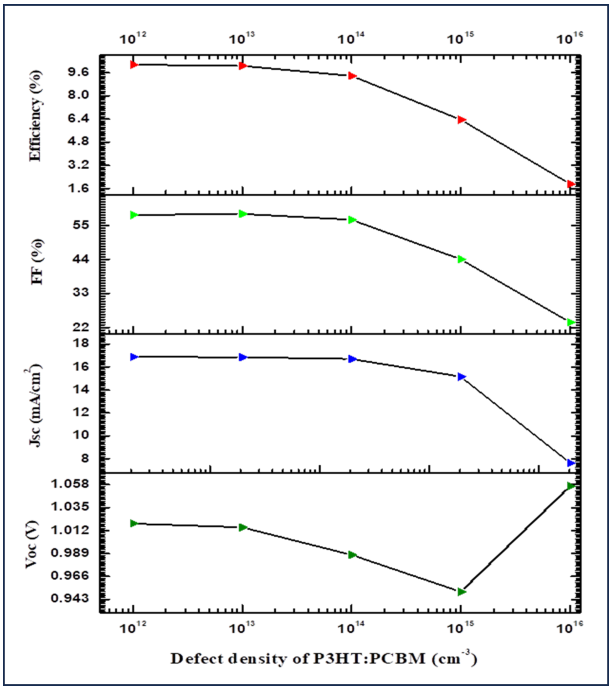


FIGURE 5.13: Influence of variation of device output parameters with varying defect density of P3HT:PCBM on device structure II.

5.2.1.3 Influence of Defect Density Variation in P3HT:PCBM on the Device Performance of Structures I and II

Fig. 5.12 and Fig. 5.13 shows the influence of varying defect density of the active layer on device output parameters in device structure I and device structure II.

The effect of varying defect density of active layer on the output performance of device structure I and device structure II were studied by varying the defect density values of the active layer from 10^{12} cm^{-3} to 10^{16} cm^{-3}. For device structure I, V_{oc} of 1.1803 V was obtained at 1×10^{12} cm^{-3}, J_{sc} of 15.136 mA/cm^2 was attained at 1×10^{12} cm^{-3}, FF of 55.21% was achieved at 1×10^{12} cm^{-3}, and efficiency of 9.77% was achieved at 10^{12} cm^{-3}.

For device structure I, as the defect density increased, a gradual decline in the device output parameters was observed. This demonstrates how an increase in the defect density of the active layer (P3HT:PCBM) can negatively impact the device's performance. The increase in defect density leads to a gradual decline in device performance due to increased charge carrier recombination and recombination-induced carrier loss.

In the case of device structure II, V_{oc} of 1.0191 V was attained at 10^{12} cm^{-3}, J_{sc} of 16.885 mA/cm^2 was achieved at 10^{12} cm^{-3}, FF of 58.93% was attained for 10^{12} cm^{-3}, and efficiency of 10.14% was obtained for 10^{12} cm^{-3} as shown in Fig. 5.13. As the defect density of active layer increased, the device output parameters gradually decreased. We have considered a low defect density for our research, which appears to be a challenging endeavor in practical applications.

The performance of both device structures seemed to decline as the defect density increased. Till 10^{15} cm^{-3}, a gradual decline was seen for device structure II but an abrupt change in V_{oc} was seen for device structure II showing 10^{15} cm^{-3} is the maximum limit of defect density that can be given to the structure.

Defect density in the P3HT:PCBM blend, particularly at interfaces like the buffer layer/active layer, can act as recombination centers for photogenerated charge carriers. This means that instead of being extracted as current, these charges recombine, reducing the photocurrent and overall efficiency. Defects can also act as traps for charge carriers, essentially holding them in place for a short period before they are recombined. This trapping effect can slow down charge transport, leading to a reduction in the FF and overall performance. Defects at interfaces, such as between the P3HT:PCBM blend and electrodes/buffer layers, are particularly crucial. These defects can impede charge extraction and collection, thereby significantly impacting the device's performance.

As the defect density increased, the efficiency of the SC typically decreased because the defects hinder both the generation and collection of charge carriers. Researchers are actively working on strategies to minimize defect densities in P3HT:PCBM SCs. This includes optimizing the morphology of the blend, using buffer layers to improve interface quality, and employing techniques like surface passivation to reduce the density of trap states. Defects in P3HT:PCBM can arise from various sources, including imperfections in the polymer chains, incomplete mixing of P3HT and PCBM and impurities at the interfaces.

5.2.2 Numerical Investigation of Active Layer BHJOSC with Graphene as HTL, ZnO and TiO_2 as ETLs

The design, simulation, and analysis of two configurations, ITO/graphene/P3HT:PCBM/ZnO/Al (Structure III) and ITO/graphene/P3HT:PCBM/TiO_2/Al (Structure IV), were carried out. Graphene serves as the HTL, while ZnO and TiO_2 serves as ETLs in structure III and structure IV respectively. The influence of varying thickness, electron mobility, hole mobility and defect density of P3HT:PCBM on the device output parameters of device structure III and device structure IV were also studied, analyzed and plotted.

ZnO is chosen as an ETL in structure III, due to its advantageous electronic properties, chemical stability, ease of low temperature synthesis and solution processability. These characteristics collectively facilitate faster and more efficient electron extraction, reduced recombination losses and enhanced overall efficiency. TiO_2 was chosen as an ETL in structure IV. It is an excellent ETL material for P3HT:PCBM BHJOSCs due to its combination of high electron mobility, stability, optical transparency, and favorable energy level alignment. It plays a crucial role in improving the performance and lifetime of the SCs.

5.2.2.1 Influence of Thickness Variation of Active Layer on the Device Performance of Structures III and IV

Figs. 5.14 to 5.17 show the influence of varying thickness of active layer on device output parameters in structure III and structure IV. A broader V_{oc} graph was obtained for structure III, as the thickness of P3HT:PCBM was increased. V_{oc} appeared more sensitive to thickness, which leads to an inference that sharper drop after optimal value often requires more careful surface treatment to suppress trap assisted recombination.

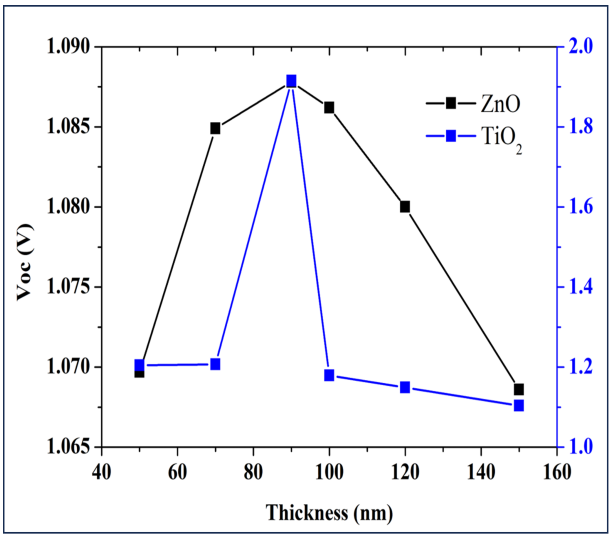


FIGURE 5.14: Influence of variation of V_{oc} with varying thickness of P3HT:PCBM on device structures III and IV.

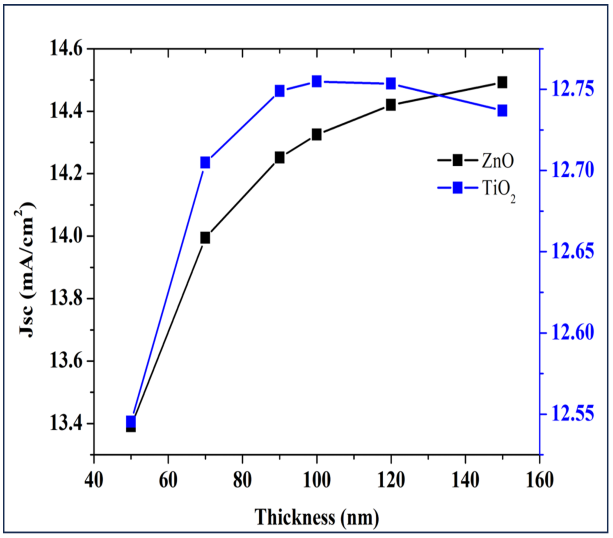


FIGURE 5.15: Influence of variation of J_{sc} with varying thickness of P3HT:PCBM on device structures III and IV.

ZnO generally offers better C_B alignment with many of the acceptors. ZnO provides higher mobility than TiO_2 better with thinner active layers.

When TiO_2 was used as the ETL, more trap states were created, especially in thicker films. As shown in the plot, device structure IV was more sensitive to thickness, hence a sharper drop after 90 nm was observed. V_{oc} is directly affected by quasi-fermi level splitting, which might be reduced by recombination at ETL interface. As the thickness of active layer is increased from 50 to 150 nm, the V_{oc} first increased to 1.0875 V at 90 nm for device structure III and 1.9 V at 90 nm for the device structure IV, then dropped. J_{sc}

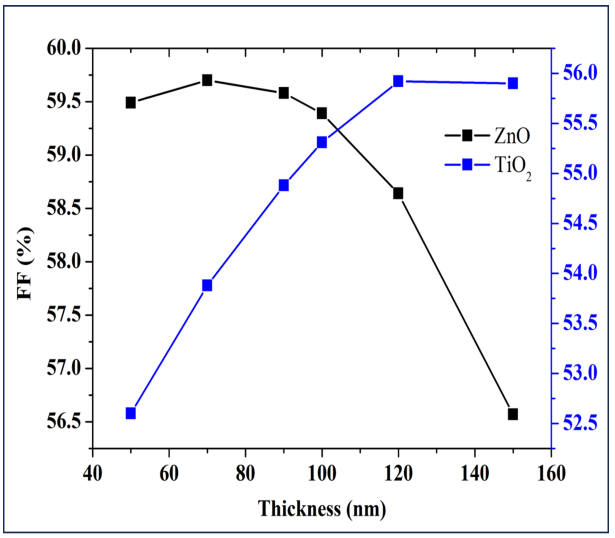


FIGURE 5.16: Influence of variation of FF with varying thickness of P3HT:PCBM on device structures III and IV.

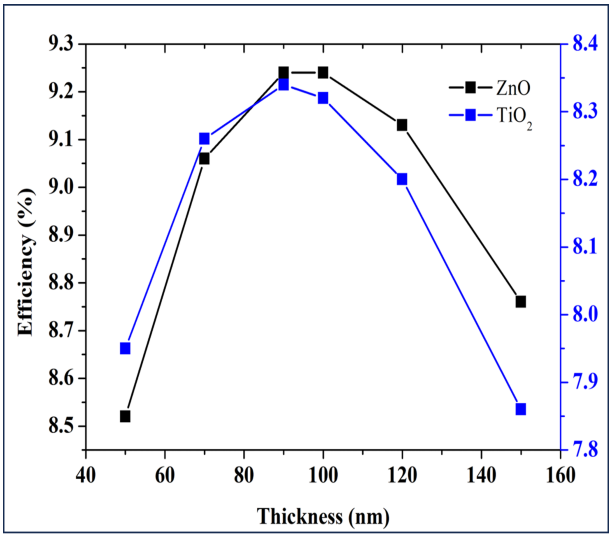


FIGURE 5.17: Influence of variation of efficiency with varying thickness of P3HT:PCBM on device structures III and IV.

increased to a maximum value of 12.78 mA/cm^2 at 100 nm and 14.5 mA/cm^2 at 150 nm for device structures III and IV. FF increased to 59.8% at 70 nm and 55.9% at 125 nm for device structures III and IV. Whereas efficiency reached 9.25% at 90 nm and 8.35% at 90 nm for device structures III and IV.

At optimum thickness (in the range of 80 to 100 nm), the thickness of active layer is thick enough to fully cover and isolate the active layer from the electrode (reducing shunting). This range of thickness is thin enough to allow fast electron extraction and

minimize recombination. Below and above this range pinholes or poor surface uniformity occurs.

Direct interaction between the active layer and the electrode may result in increased recombination and a diminished built-in potential. If the layer is excessively thick, R_s escalates, which impedes electron extraction. A thicker active layer establishes a longer pathway for electrons, thereby amplifying the risk of recombination. A thicker active layer can cause potential light reflection or parasitic absorption, which diminishes the photon flux reaching the active layer.

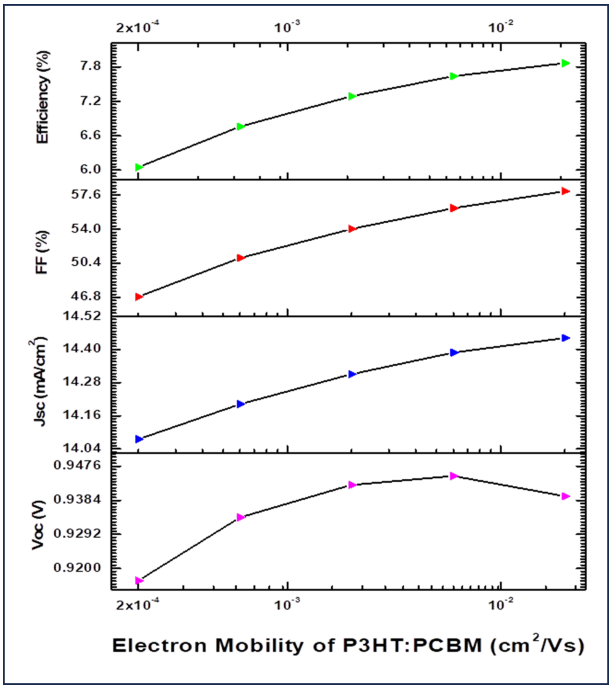


FIGURE 5.18: Influence of varying electron mobility of P3HT:PCBM on the device performance of structure III.

5.2.2.2 Influence of Electron Mobility and Hole Mobility Variation in Active Layer on the Device Performance of Structures III and IV

Fig. 5.18 and Fig. 5.19 displays the influence of varying electron and hole mobility of the active layer on device structure III. The electron mobility and hole mobility of the active layer was varied from 2 × 10^{-4} to 2× 10^{-2} cm^2/Vs. A V_{oc} of 0.9450 V for electron mobility of 6 × 10^{-3} cm^2/Vs, J_{sc} of 14.442 mA/cm^2, FF of 58.01%, and efficiency of 7.87% were obtained for electron mobility of 2× 10^{-2} cm^2/Vs. Hole mobility of active layer was varied from 2 × 10^{-4} to 2× 10^{-2} cm^2/Vs. Highest V_{oc} of 0.9414 V was obtained for 6

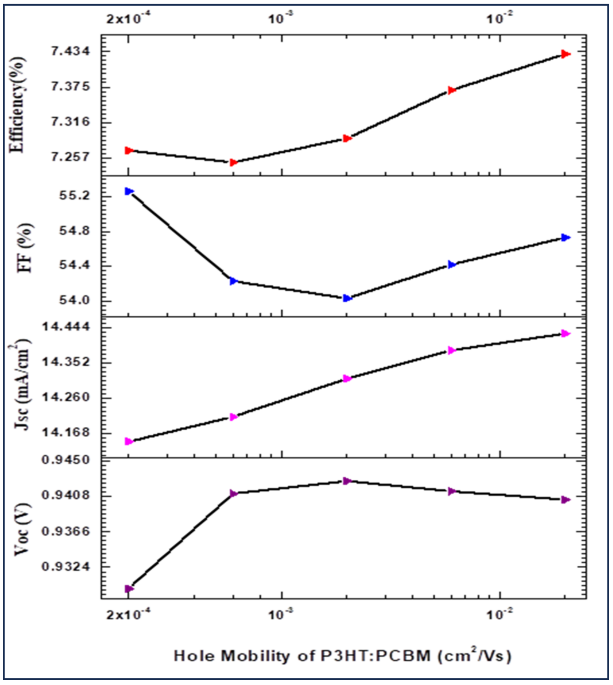


FIGURE 5.19: Influence of varying hole mobility of P3HT:PCBM on the device performance of structure III.

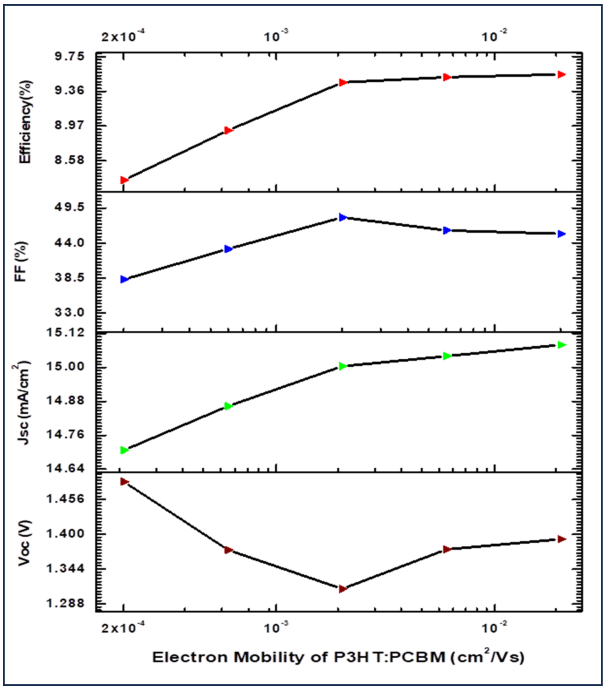


FIGURE 5.20: Influence of varying electron mobility of P3HT:PCBM on the device performance of structure IV.

$\times$ 10^{-3} cm^2/Vs. Highest J_{sc} of 14.429 mA/cm^2, highest FF of 55.30%, and efficiency of 7.43% were obtained for 2 $\times$ 10^{-2} cm^2/Vs.

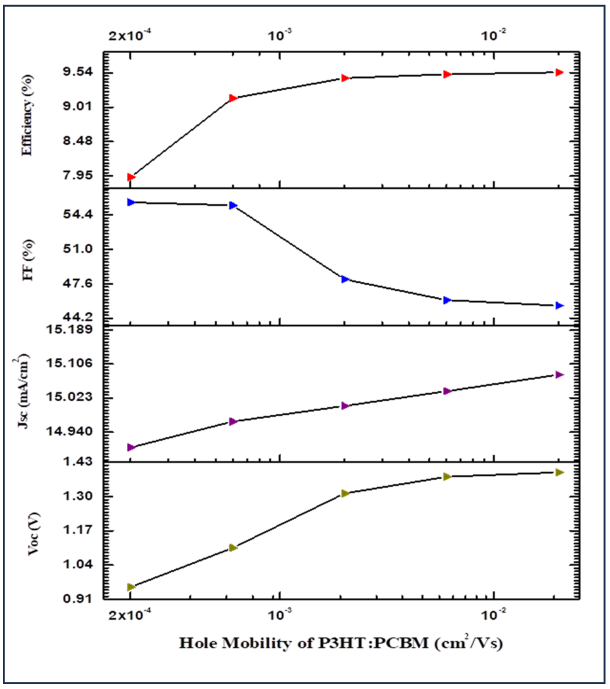


FIGURE 5.21: Influence of varying hole mobility of P3HT:PCBM on the device performance of structure IV.

Fig. 5.20 and Fig. 5.21 illustrate the impact of electron mobility and hole mobility of the active layer on the performance of device structure IV. Electron mobility and hole mobility of the active layer were varied from 2×10^{-4} to 2×10^{-2} cm^2/Vs. A V_{oc} of 1.4845 V for electron mobility of 2×10^{-4} cm^2/Vs, J_{sc} of 15.081 mA/cm^2 for 2×10^{-2} cm^2/Vs, FF of 48.04% for 2×10^{-3} cm^2/Vs, and efficiency of 9.55% were obtained for electron mobility of 2×10^{-2} cm^2/Vs for device structure IV.

Highest V_{oc} of 1.3922 V was obtained for hole mobility of 2×10^{-2} cm^2/Vs. Highest J_{sc} of 15.081 mA/cm^2 and highest FF of 55.64% were obtained for hole mobility of 2×10^{-4} cm^2/Vs. Maximum efficiency of 9.55% was obtained for hole mobility of 2×10^{-2} cm^2/Vs.

To achieve higher efficiencies in BHJOSCs, it is necessary to collect a maximum number of generated charge carriers. Indeed, the improvement of charge carriers mobility may be considered as one of the ways to increase the charge carriers collection. Maintaining a balanced mobility of the active layer is the most important factor to be considered in the working of an SC.

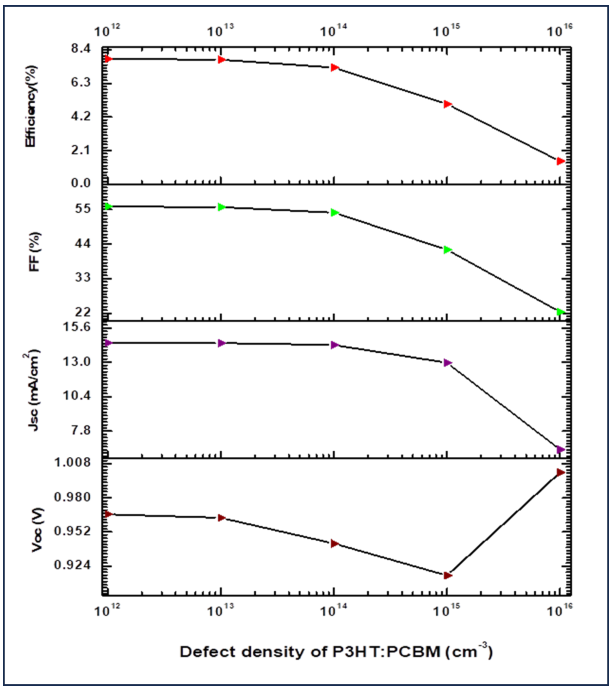


FIGURE 5.22: Influence of varying defect density of P3HT:PCBM on the device performance of structure III.

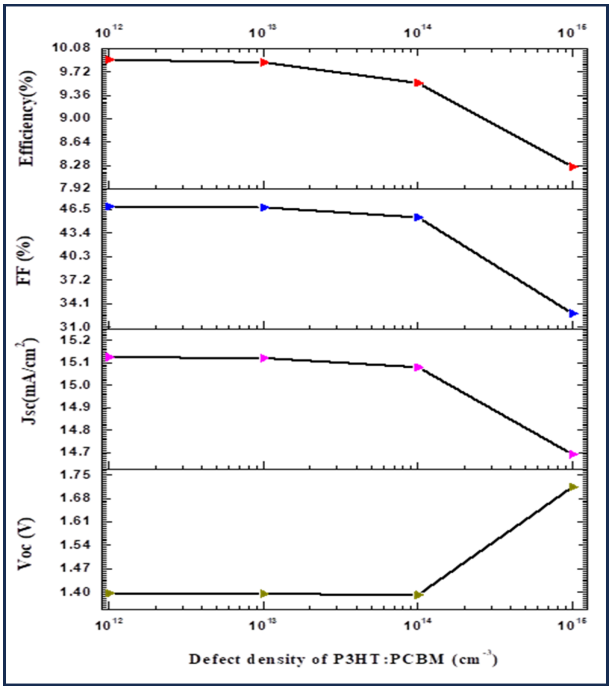


FIGURE 5.23: Influence of varying defect density of P3HT:PCBM on the device performance of structure IV.

5.2.2.3 Influence of Defect Density Variation in Active Layer on the Device Performance of Structures III and IV

Fig. 5.22 and Fig. 5.23 plots the influence of varying defect density of the active layer on the device structures III and IV. After the simulation study of structure III, a gradual decrease is observed in the device output parameters. Maximum V_{oc} of 0.9666 V, J_{sc} of 14.474 mA/cm^2, FF of 55.95%, and efficiency of 7.83% were achieved for 10^{12} cm^{-3}. After the simulation study of structure IV, a surprising output was recorded with highest V_{oc} 1.7143 V for 10^{15} cm^{-3}. J_{sc} of 15.125 mA/cm^2 for 10^{12} cm^{-3}, FF of 46.86% for 10^{12} cm^{-3}, and efficiency of 9.91% were obtained for 10^{12} cm^{-3}.

After 10^{15} cm^{-3}, V_{oc} increased in both structures, which is considered an abrupt behaviour. Consequently, a defect density of 10^{12} cm^{-3} is regarded as optimal for the active layer of device structure III and IV.

5.3 Numerical Investigation of P3HT:PCBM BHJOSC with GO as HTL, Diverse ETLs and Different Cathode Materials

In this study, an extensive numerical investigation on P3HT:PCBM BHJOSC with GO as HTL, diverse ETLs and different cathodes were carried out. The device structure ITO/GO/P3HT:PCBM/Al fabricated by Lee et al. was simulated using SCAPS-1D for standardization of the software. The structure was optimized on the basis of input factors such as thickness, defect density, electron mobility, hole mobility, interface defect density, and operating temperature.

Later, various device combinations are simulated with diverse ETLs and different cathodes. ETLs namely N,N'-Bis(N,N-dimethylpropan-1-amine oxide)peryle ne-3,4,9,10-tetracarboxylic diimide (PDINO), PFN-Br, ZnO, lithium fluoride (LiF)[342], indium gallium zinc oxide (IGZO), C_{60}, PCBM, titanium dioxide:graphene composite (TiO_2:gr) and nitrogen doped graphene (n-graphene) and different cathodes including aluminium (Al), calcium (Ca) and silver (Ag) were introduced. From these studies the best device configuration was found.

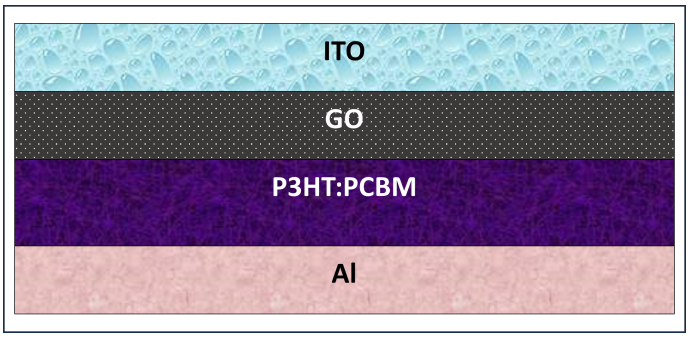


FIGURE 5.24: Device structure used in the experimental study of ITO/-GO/P3HT:PCBM/Al [336].

TABLE 5.3: Input parameters of P3HT:PCBM and GO used for the simulation study of ITO/GO/P3HT:PCBM/Al.

Parameters	P3HT:PCBM	GO
Thickness (d) (nm)	100 [336]	35[336]
Band gap (E_g) (eV)	1.27 [338]	2.48 [343]
Electron affinity (χ) (eV)	3.7 [338]	2.3 [343]
Dielectric permittivity (ε_r)	3.5 [339]	10 [343]
Conduction band density (C_B) (cm^{-3})	7.8×10^{19} [340]	1.8×10^{18} [343]
Valence band density (V_B) (cm^{-3})	7.8×10^{19} [340]	2.2×10^{18} [343]
Thermal velocity of electrons (V_e) (cm/s)	1×10^{7} [340]	1×10^{7} [343]
Thermal velocity of holes (V_h) (cm/s)	1×10^{7} [340]	1×10^{7} [343]
Electron mobility (μ_e) (cm^2/Vs)	2×10^{-3} [340]	2.6×10^{1} [343]
Hole mobility (μ_h) (cm^2/Vs)	2×10^{-3} [340]	1.23×10^{2} [343]
Doping concentration of donor (N_D) (cm^{-3})	0 [339]	0 [343]
Doping concentration of acceptor (N_A) (cm^{-3})	0 [339]	1×10^{18} [343]
Defect density (N_t) (cm^{-3})	6.847×10^{15}	1.9×10^{14} [343]

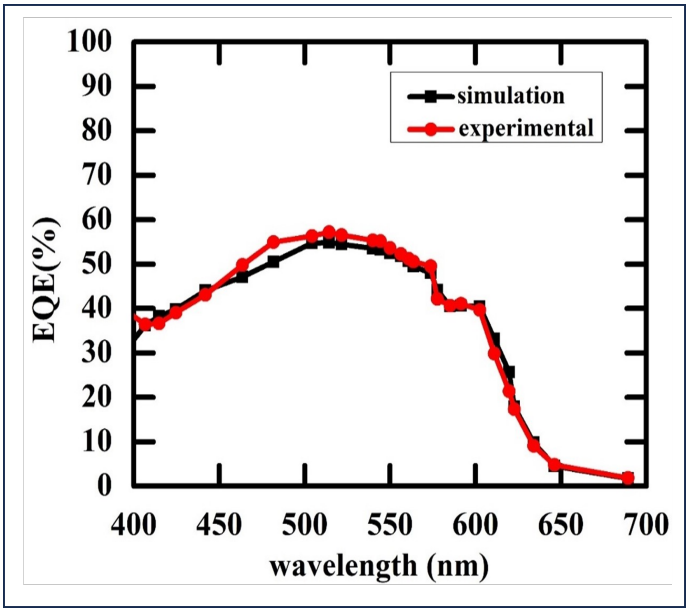


FIGURE 5.25: Matching EQE graph.

TABLE 5.4: Matched output parameters of experimental and simulation study.

	V_{oc} (V)	J_{sc} (mA/cm^2)	FF (%)	Efficiency (%)
Experimental [336]	0.57	6.94	41.2	1.63
Simulation	0.5329	7.6325	40.88	1.66

5.3.1 Standardization

A definite requirement for software validation is standardization (with an experimental work with device structure ITO/GO/P3HT:PCBM/Al) [336]. The device structure used for standardization is shown in Fig. 5.24. Table 5.3 lists the input parameters of P3HT:PCBM (active layer) and GO (HTL) used for the standardization. The following input parameters were chosen as default value from the SCAPS-1D software. The simulation was run at 300 K operating temperature under AM 1.5 G light with an intensity of 100 mW/cm^2. Capture cross-section, electron and hole thermal velocities for all layers were set to 1×10^{-15} cm^2 and 1×10^7 cm/s respectively. Furthermore, the capture cross-section for the HTL/active layer interface, and active layer/ETL interface were chosen as 1×10^{-15} cm^2. The characteristic energy value for a defect with a neutral Gaussian distribution was set to 0.1 eV. The energy level with respect to the reference (eV) was kept constant for all layers at 0.6 eV.

Standardization includes matching the EQE graph and output parameters. Fig. 5.25 shows the matching EQE graph. Table 5.4 gives the matching output parameters (experimental results and simulated results).

Later, we introduced diverse ETLs and different cathodes, and carried on with the simulation study.

5.3.2 Optimization

Influence of electrical parameters such as thickness, defect density, electron mobility and hole mobility of active layer and HTL were studied. The effect of interface defect density, operating temperature, R_s and R_{sh} were also investigated and finally, the device was optimized.

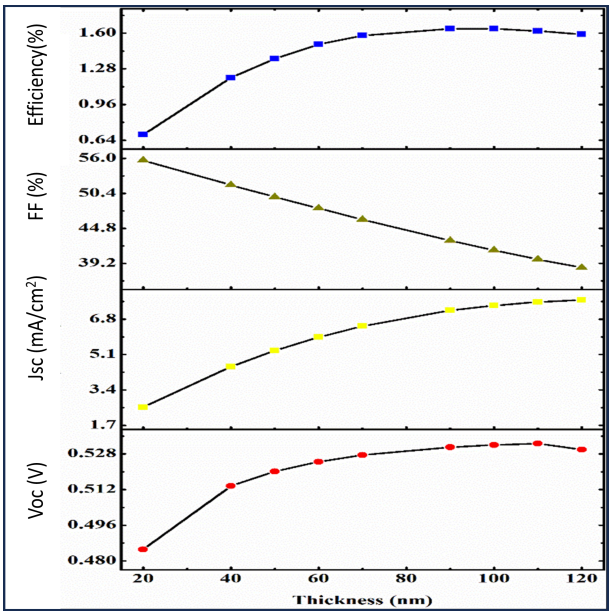


FIGURE 5.26: Influence of varying active layer thickness on device output parameters.

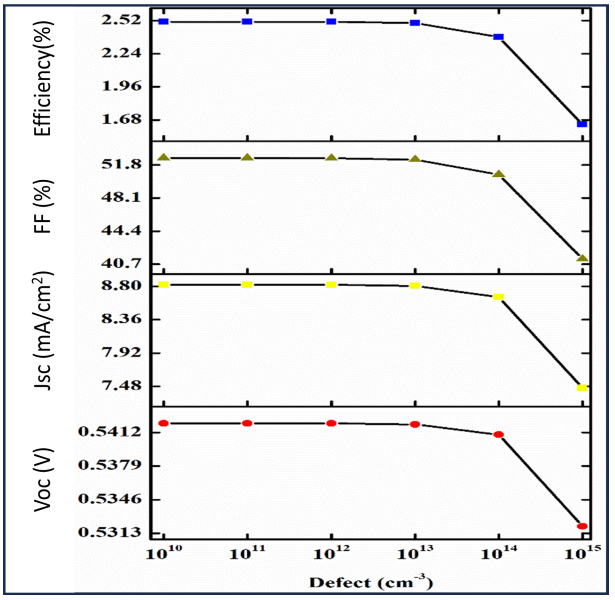


FIGURE 5.27: Influence of varying active layer defect density on device output parameters.

5.3.2.1 Influence of Varying Input Parameters of Active Layer on Device Output Performance

Thickness of active layer is a crucial parameter in the performance of BHJOSC. The effect on output parameters was studied as shown in Fig. 5.26. The thickness of the photoactive material was varied from 20 to 120 nm. As the thickness of the active material

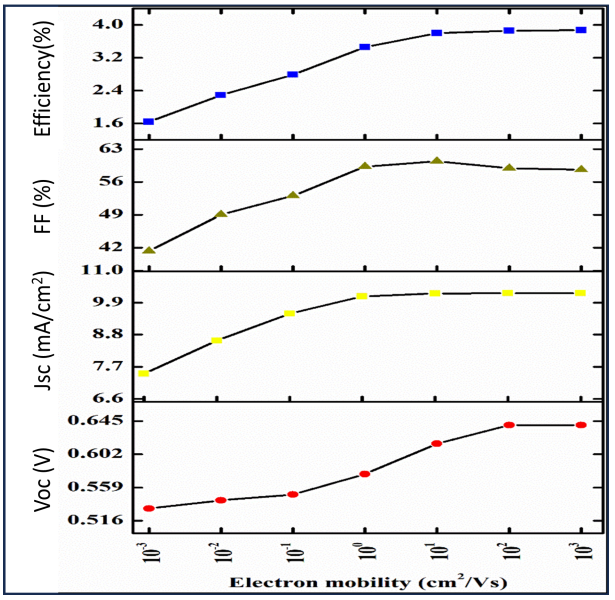


FIGURE 5.28: Influence of varying active layer electron mobility on device output parameters.

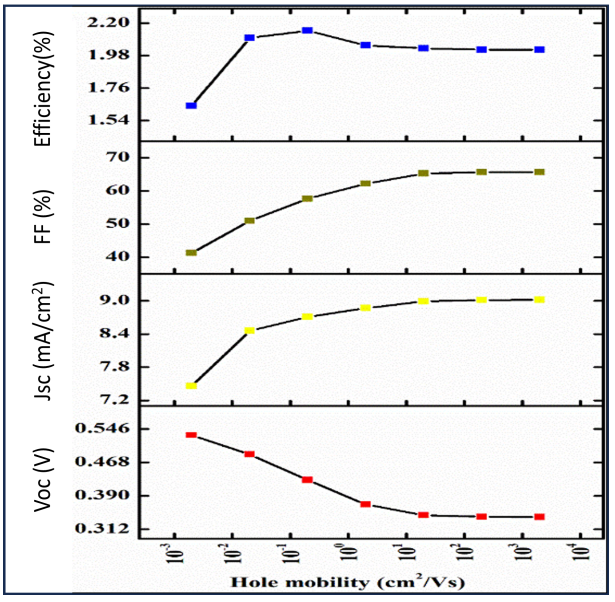


FIGURE 5.29: Influence of varying active layer hole mobility on device output parameters.

increased V_{oc} improved to 0.5333 V, J_{sc} increased to 7.63565 mA/cm^2, and efficiency reached a maximum value of 1.81% at 100 nm which then decreased slightly.

Fig. 5.27 illustrates the impact of defect density on device performance. As the defect density increased from 10^{10} to 10^{15} cm^{-3}, the V*oc* dropped to 0.5320 V, J*sc* declined to 7.46 mA/cm^2, FF decreased to 41.29%, and the efficiency dropped to 1.66%. This relation

between defect density and device performance is attributed to an increased recombination rate resulting from the rise in defect density.

Fig. 5.28 and Fig. 5.29 illustrates the impact of electron mobility and hole mobility on the output parameters of the device. The electron mobility ranges from 2×10^{-3} cm^2/Vs to 2×10^3 cm^2/Vs. With an increase in electron mobility, the V_{oc} increased to 0.643 V, J_{sc} increased to 10.456 mA/cm^2, and FF increased to 59.16%. A notably improved efficiency of 3.9% was achieved at 2×10^3 cm^2/Vs.

As the hole mobility is increased from 2×10^{-3} cm^2/Vs to 2×10^3 cm^2/Vs, V_{oc} decreased to 0.3397 V at 2×10^3 cm^2/Vs, J_{sc} increased to 8.99 mA/cm^2 at 2×10^3 cm^2/Vs, FF improved to 64.01% at 2×10^3 cm^2/Vs, and efficiency acquired a maximum value of 2.10% at 2×10^{-1} cm^2/Vs. The rise in material conductivity is affirmed by the increase in mobility. The equilibrium of mobilities should be maintained, as an uneven charge transport may occur if the mobility of electrons is reduced.

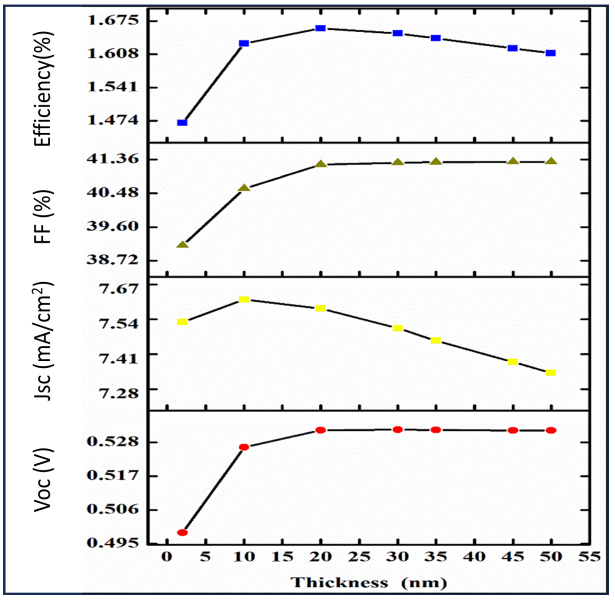


FIGURE 5.30: Influence of varying HTL thickness on device output parameters.

5.3.2.2 Influence of Various Parameters of HTL

The impact of HTL thickness on device performance is illustrated in Fig. 5.30. As the HTL thickness increased from 2 to 50 nm, the highest V_{oc} of 0.5320 V was achieved at 20 nm, an improved J_{sc} of 7.613 mA/cm^2 was observed at 10 nm, a better FF of 41.30% was attained at 20 nm, and a maximum efficiency of 1.66% occurred at 20 nm. The observed

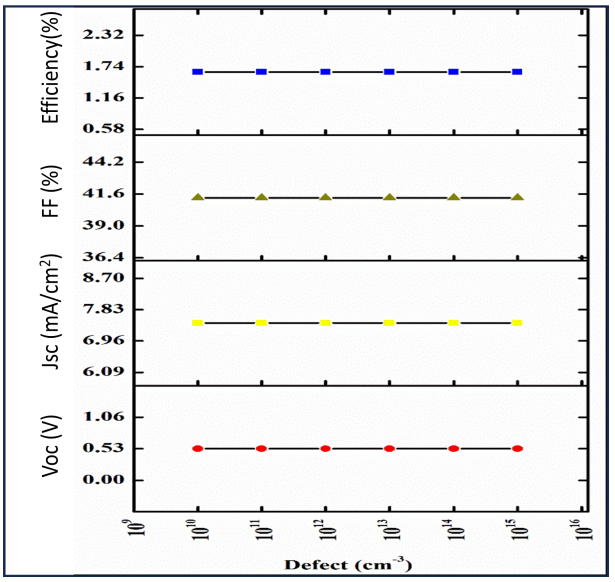


FIGURE 5.31: Influence of varying HTL defect density on device output parameters.

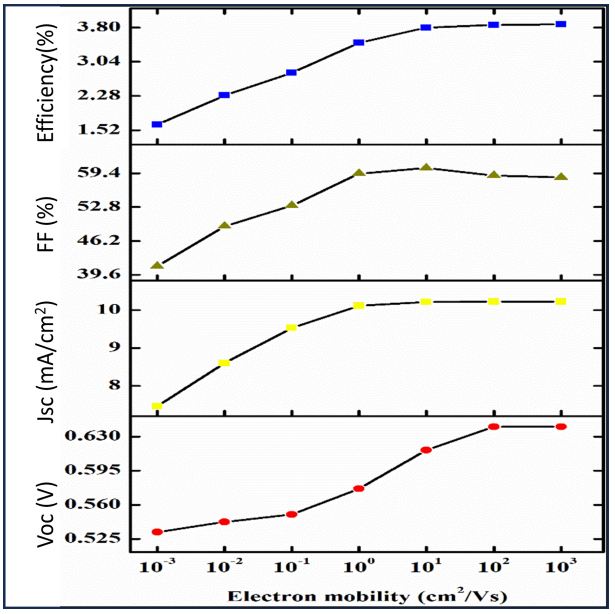


FIGURE 5.32: Influence of varying HTL electron mobility on device output parameters.

variation is due to the trade-off between efficient hole extraction and transport resistance. An HTL thickness of 20 nm provides optimal charge collection with reduced recombination, whereas excessively thick HTLs increase resistance and hinder carrier transport, resulting in lower device performance.

As the defect density of GO was varied from 10^{10} to 10^{15} cm^{-3}, as shown in Fig. 5.31, the values for V_{oc}, J_{sc}, FF and efficiency remained constant at 0.5329 V, 7.6326 mA/cm^2,

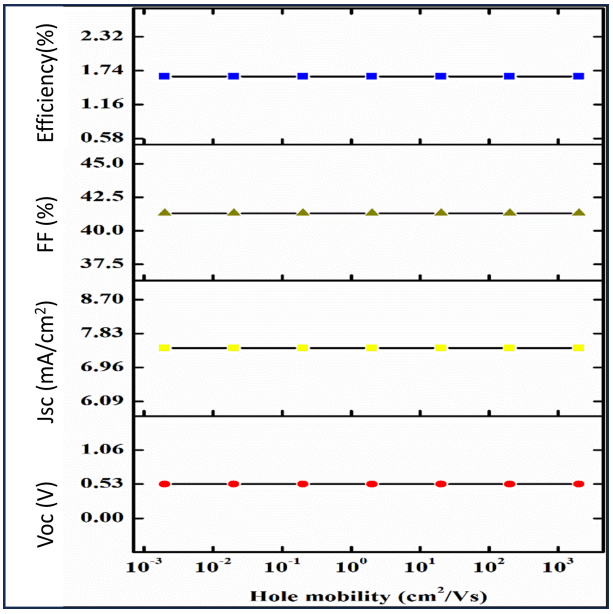


FIGURE 5.33: Influence of varying HTL hole mobility on device output parameters.

40.88% and 1.66% respectively. This indicates that the defect density of GO has minimal impact on the performance of the device.

The plot showing influence of varying electron mobility of GO layer on device performance is given in Fig. 5.32. Improved V_{oc} of 0.655 V, J_{sc} of 10.2 mA/cm^2, FF of 60.1%, and efficiency of 3.9% were obtained for the increasing electron mobility. As shown in Fig. 5.33 V_{oc}, J_{sc}, FF, and efficiency remained constant as hole mobility of GO changes from 2.6×10^{-3} to 2.6×10^{3} cm^2/Vs. The constant output parameters obtained were 0.5329 V, 7.6326 mA/cm^2, 40.88 %, and 1.66% respectively. The improvement in device performance with increasing electron mobility of GO is attributed to enhanced charge transport and reduced recombination losses. Conversely, varying the hole mobility has little effect on the output parameters, indicating that hole transport through GO is not the limiting factor in the device performance.

5.3.2.3 Influence of Varying Interface Defect Density, Operating Temperature, Series Resistance and Shunt Resistance

The interface defined in the device structure ITO/GO/P3HT:PCBM/Al is HTL/active layer interface (GO/P3HT:PCBM interface). Fig. 5.34 depicts the variation of device parameters with respect to change in interface defect density values. The simulation was done by varying the defect density of interface from 10^{10} to 10^{15} cm^{-2}. As the interface

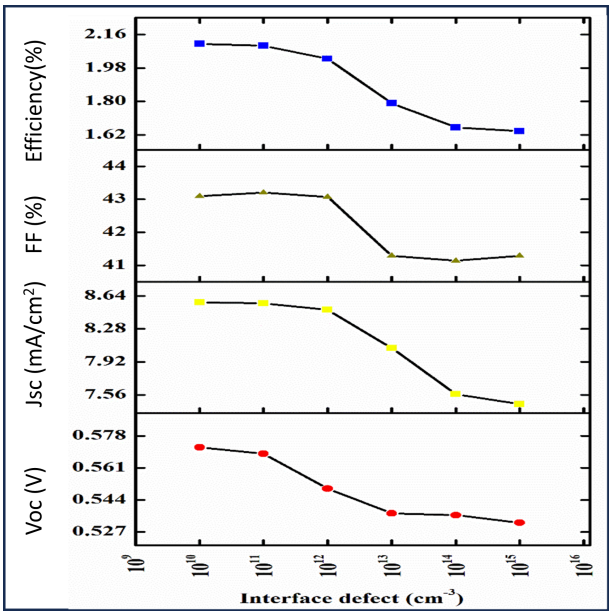


FIGURE 5.34: Influence of varying interface defect density on device output parameters.

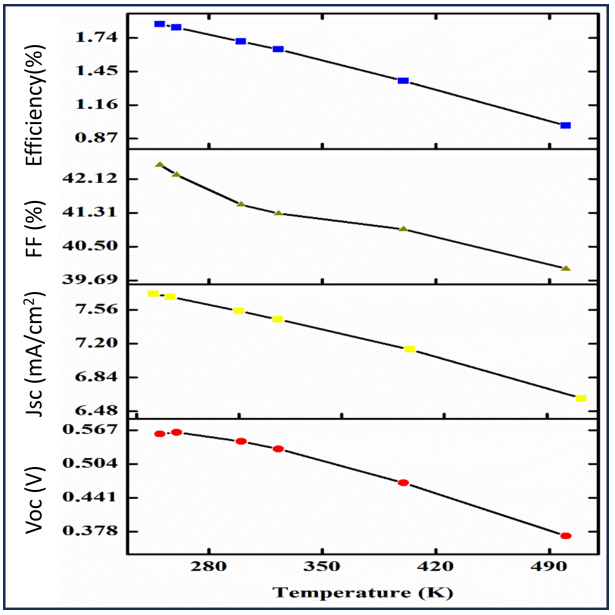


FIGURE 5.35: Influence of varying operating temperature on device output parameters.

defect density was increased, V_{oc}, J_{sc}, FF, and efficiency decreased. V_{oc} decreased to 0.536 V, J_{sc} decreased to 7.57 mA/cm^2, FF reduced to 41.14%, and efficiency declined to 1.64%. Increased interface defects introduce additional recombination centers, thereby reducing charge collection and device performance.

The device performance was examined while varying the operating temperature between 250 K and 500 K, as shown in Fig. 5.35. As temperature increased, V_{oc} decreased

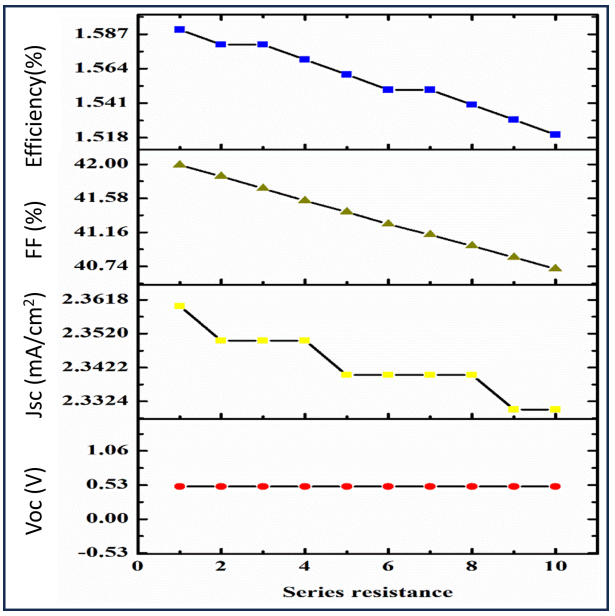


FIGURE 5.36: Influence of varying series resistance on device output parameters.

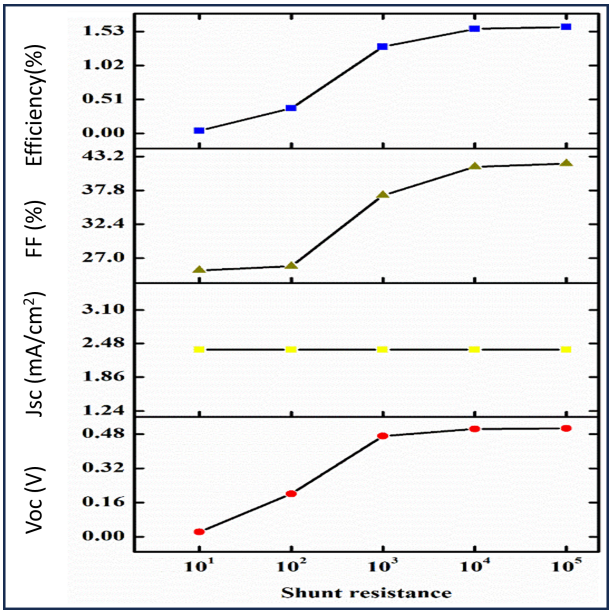


FIGURE 5.37: Influence of varying shunt resistance on device output parameters.

to 0.37 V, J_{sc} declined to 6.62 mA/cm^2, FF diminished to 39.97%, and efficiency dropped to 0.98%. The performance of the device was severely impacted by the operating temperature, which resulted in a slow decline in efficiency. This could be caused by an increase in R_s, which raises the recombination rate. As the temperature is increased, V_{oc} diminished to 0.37 V, J_{sc} dropped to 6.62 mA/cm^2, FF decreased to 39.97%, and the efficiency dropped to 0.98%. Higher temperatures enhance carrier recombination and reduce the

built-in potential, leading to lower PV performance.

The variation of PV characteristics with varying R_s and R_{sh} respectively, is represented in Fig. 5.36 and Fig. 5.37. When the R_s was increased from 1 to 10 Ohm, V_{oc} remained 0.5320 V, J_{sc} declined to 2.33 mA/cm^2, FF decreased to 40.71% and efficiency reduced to 1.52%. As the R_{sh} was increased from 10 to 100000 Ohm, V_{oc} increased to 0.532 V, while J_{sc} remained constant at 2.365 mA/cm^2, FF increased to 42.08%, and the efficiency improved to 1.6%. Higher Rs hinders charge transport, whereas higher Rsh suppresses leakage currents, resulting in improved device characteristics.

The device structure ITO/GO/P3HT:PCBM/Al was optimized and we attained improved V_{oc} of 0.6237 V, J_{sc} of 8.92765 mA/cm^2, FF of 77.6%, and efficiency of 4.32%.

5.3.3 Study of ITO/GO/P3HT:PCBM/ETL/Al with Diverse ETLs and Different Cathodes

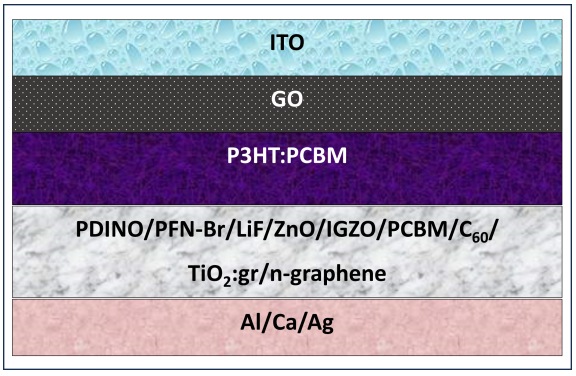


FIGURE 5.38: Device design used for the simulation study.

Simulation study of BHJOSC with P3HT:PCBM as active layer with ITO as anode, GO as HTL with different metal electrodes (Al, Ca and Ag) and diverse ETLs (PDINO, PFN-Br, LiF, ZnO, IGZO, PCBM, C_{60}, TiO_2:gr, and n-graphene). The ETL plays a vital role in enhancing the performance of BHJOSC. Introducing ETLs will in fact increase the device performance by improving the charge carrier transport.

Fig. 5.38 illustrates the designed device structure employed in the simulation study. Fig. 5.39 illustrates the energy band diagram of the layers utilized for the research. Tables 5.5 to 5.7 lists the input parameters of active layer, HTL and ETLs utilized in the simulation study.

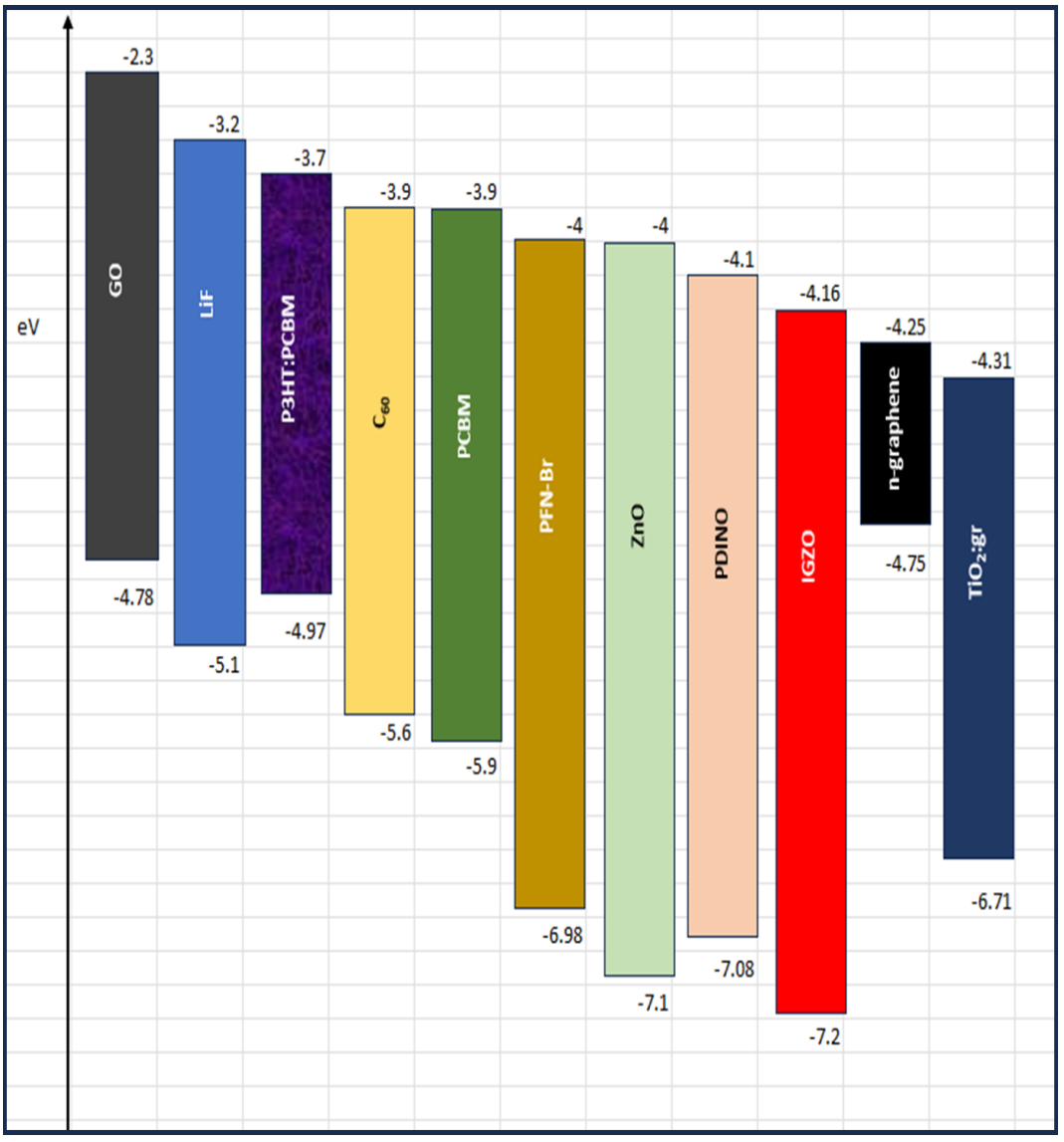


FIGURE 5.39: Energy band diagram of layers used in the simulation study of the device structure ITO/GO/P3HT:PCBM/ETL/Al.

The following input parameters were chosen as default value from the SCAPS-1D software. The simulation was run at 300 K operating temperature under AM 1.5 G light with an intensity of 100 mW/cm^2. Capture cross-section, electron and hole thermal velocities for all layers were set to 1×10^{-15} cm^2 and 1×10^7 cm/s respectively. Furthermore, the capture cross-section for the HTL/active layer interface, and active layer/ETL interface were chosen as 1×10^{-15} cm^2. The characteristic energy value for a defect with a neutral Gaussian distribution was set to 0.1 eV. The energy level with respect to the reference (eV) was kept constant for all layers at 0.6 eV.

Table 5.8 summarizes the output parameters achieved for different device configurations.

An enhanced V_{oc} of 0.9277 V was achieved for the device employing PFN-Br as the ETL and Al as the cathode. Device with LiF as ETL and Ca as cathode gives maximum J_{sc} of 11.498525 mA/cm^2. Highest FF of 81.73% was achieved for the device with IGZO as ETL and Ca as cathode. An efficiency of 8.00% was attained with the device configuration utilizing LiF as the ETL and Ca as the cathode.

TABLE 5.5: Input parameters of the active layer (P3HT:PCBM) and HTL (GO) used for the simulation of ITO/GO/P3HT:PCBM/Al.

Parameters	P3HT:PCBM	GO
Thickness (d) (nm)	100 [336]	35 [336]
Band gap (E_g) (eV)	1.27 [338]	2.48 [343]
Electron affinity (χ) (eV)	3.7 [338]	2.3 [343]
Dielectric permittivity (ε_r)	3.5 [339]	10 [343]
Conduction band density (C_B) (cm^{-3})	7.8×10^{19} [340]	1.8×10^{18} [343]
Valence band density (V_B) (cm^{-3})	7.8×10^{19} [340]	2.2×10^{18} [343]
Thermal velocity of electrons (V_e) (cm/s)	1×10^7 [340]	1×10^7 [343]
Thermal velocity of holes (V_h) (cm/s)	1×10^7 [340]	1×10^7 [343]
Electron mobility (μ_e) (cm^2/Vs)	2×10^{-3} [340]	2.6×10^1 [343]
Hole mobility (μ_h) (cm^2/Vs)	2×10^{-3} [340]	1.23×10^2 [343]
Doping concentration of donor (N_D) (cm^{-3})	0 [339]	0 [343]
Doping concentration of acceptor (N_A) (cm^{-3})	0 [339]	1×10^{18} [343]
Defect density (N_t) (cm^{-3})	6.847×10^{15}	1.9×10^{14} [343]

TABLE 5.6: Input material parameters used for ETLs-PDINO, PFN-Br, LiF, and ZnO.

Parameter	PDINO	PFN-Br	LiF	ZnO
Thickness (d) (nm)	5 [344]	5 [341]	20 [345]	20 [346]
Band gap (E_g) (eV)	2.98 [344]	2.98 [341]	1.9 [342]	3.1 [347]
Electron affinity (χ) (eV)	4.1 [344]	4.0 [341]	3.2 [342, 345, 348]	4.0 [349]
Dielectric constant (ε_r)	5 [344]	5 [341]	9.1 [346]	9 [350]
Conduction band density (C_B) (cm^{-3})	1×10^{19} [344]	1×10^{19} [341]	1×10^{20} [342, 351]	2×10^{18} [341]
Valence band density (V_B) (cm^{-3})	1×10^{19} [344]	1×10^{18} [341]	1×10^{20} [342, 351]	1.8×10^{19} [341]
Thermal velocity of electrons (V_e) (cm/s)	1×10^7 [344]	1×10^7 [341]	1×10^7 [342, 351]	1×10^7 [341]
Thermal velocity of holes (V_h) (cm/s)	1×10^7 [344]	1×10^7 [341]	1×10^7 [342, 351]	1×10^7 [341]
Electron mobility (μ_e) (cm^2/Vs)	2×10^{-6} [344]	2×10^{-6} [341]	1 [342, 351]	1×10^2 [341]
Hole mobility (μ_h) (cm^2/Vs)	1×10^{-3} [344]	1×10^{-4} [341]	1 [342, 351]	2.5×10^2 [341]
Doping concentration of donor (N_D) (cm^{-3})	2×10^{21} [344]	9×10^{18} [341]	1×10^{18}	1×10^{18} [341]
Doping concentration of acceptor (N_A) (cm^{-3})	0 [344]	0 [341]	0	0 [341]
Defect density (N_t) (cm^{-3})	1×10^9 [344]	1×10^{14} [341]	1×10^9 [351, 342]	1×10^{14} [341]

TABLE 5.7: Input parameters of ETLs-IGZO, PCBM, C_{60}, TiO_2:gr, and n-graphene.

Parameter	IGZO	PCBM	C_{60}	TiO_2:gr	n-graphene
Thickness (d) (nm)	5 [341]	5 [341]	5 [341]	50 [352]	33.4 [353]
Band gap (E_g) (eV)	3.05 [341]	2 [341]	1.7 [341]	2.4 [352]	0.5 [353]
Electron affinity (χ) (eV)	4.16 [341]	3.9 [341]	3.9 [341]	4.31 [352]	4.8 [353]
Dielectric constant (ε_r)	10 [341]	3.9 [341]	4.2 [341]	7.8 [352]	10 [353]
Conduction band density (C_B) (cm^{-3})	1×10^{19} [341]	1×10^{19} [341]	1×10^{19} [341]	1×10^{19} [352]	3×10^{19} [353]
Valence band density (V_B) (cm^{-3})	1×10^{19} [341]	1×10^{19} [341]	1×10^{19} [341]	1×10^{19} [352]	3×10^{19} [353]
Thermal velocity of electrons (V_e) (cm/s)	1×10^7 [341]	1×10^7 [341]	1×10^7 [341]	1×10^7 [352]	1×10^7 [353]
Thermal velocity of holes (V_h) (cm/s)	1×10^7 [341]	1×10^7 [341]	1×10^7 [341]	1×10^7 [352]	1×10^7[353]
Electron mobility (μ_e) (cm^2/Vs)	15 [341]	0.02 [341]	8×10^{-2} [341]	350 [352]	10 [353]
Hole mobility (μ_h) (cm^2/Vs)	0.1 [341]	0.02 [341]	3.5×10^{-3} [341]	350 [352]	1×10^5 [353]
Doping concentration of donor (N_D) (cm^{-3})	1×10^{19} [341]	1×10^{19} [341]	1×10^{19} [341]	5×10^{18} [352]	1×10^{26} [353]
Doping concentration of acceptor (N_A) (cm^{-3})	0 [341]	0 [341]	0 [341]	0 [352]	0 [353]
Defect density (N_t) (cm^{-3})	1×10^{19} [341]	1×10^{19} [341]	1×10^{19} [341]	1×10^{14} [352]	1×10^{14} [353]

The comparison shows that device with Ca as cathode showed better device performance while incorporating BHJOSC with GO as HTL. This can be attributed to the well

TABLE 5.8: Output parameters of various device configurations simulated using GO as HTL, diverse ETLs and different cathodes.

Cathode	ETL	V_{oc} (V)	J_{sc} (mA/cm^2)	FF (%)	Efficiency (%)
Aluminium	PDINO	0.9255	10.816248	76.29	7.63
Aluminium	PFN-Br	0.9277	11.4186	58.02	6.15
Aluminium	LiF	0.4298	10.31244	76.88	6.01
Aluminium	ZnO	0.9088	10.413318	77.43	7.33
Aluminium	IGZO	0.7161	10.442410	83.63	6.25
Aluminium	PCBM	0.8196	10.555798	76.74	6.64
Aluminium	C_{60}	0.8207	10.651364	76.62	6.70
Aluminium	TiO_2:gr	0.6104	10.434697	81.73	5.21
Aluminium	n-graphene	0.3679	10.428822	74.44	2.86
Calcium	PDINO	0.9523	10.2493	75.85	7.40
Calcium	PFN-Br	0.8490	11.2198	81.73	7.79
Calcium	LiF	0.8517	11.498525	81.73	8.00
Calcium	ZnO	0.9186	8.868	77.58	6.32
Calcium	IGZO	0.7456	10.435529	84.29	6.56
Calcium	PCBM	0.9213	10.565869	76.55	7.45
Calcium	C_{60}	0.9229	10.663121	76.44	7.52
Calcium	TiO_2:gr	0.6104	10.434699	81.73	5.21
Calcium	n-graphene	0.3679	10.428695	74.44	2.86
Silver	PDINO	0.8908	9.68514	72.34	6.24
Silver	PFN-Br	0.5766	10.05635	63.83	3.70
Silver	LiF	0.2919	10.19363	67.48	2.01
Silver	ZnO	0.8497	9.69244	79.38	6.54
Silver	IGZO	0.5961	10.438554	81.26	5.06
Silver	PCBM	0.8303	10.428956	64.99	5.65
Silver	C_{60}	0.8463	10.535471	73.20	6.53
Silver	TiO_2:gr	0.6104	10.434179	81.73	5.21
Silver	n-gr	0.3667	10.428614	74.41	2.85

matching energy band alignment with that of GO, since Ca (2.9 eV) has a lower work function compared to other cathodes. Our simulation study clearly shows enhanced efficiency (greater than 6.00%) for most of the device configurations studied. The obtained results compare favorably with several reported P3HT:PCBM-based BHJOSCs employing conventional HTLs such as PEDOT:PSS, where efficiencies typically lie in the range of 3–5% under similar device configurations. Previous experimental and simulation studies involving graphene-based interfacial layers have primarily focused on graphene or GO as standalone transport layers, with limited systematic investigations involving the combined optimization of GO-based HTLs, diverse ETLs, and multiple cathode materials in P3HT:PCBM BHJOSCs. The enhanced performance observed for the GO/LiF/Ca configuration highlights the importance of energy level engineering and electrode selection. The novelty of the present work lies in the comprehensive numerical investigation of GO as an alternative HTL, together with a comparative evaluation of different ETLs and cathodes, leading to the identification of an optimized device architecture with substantially improved performance and potential for enhanced device stability.

While several experimental and simulation studies have reported the use of graphene-based interfacial layers in P3HT:PCBM BHJOSCs, systematic investigations involving rGO as the HTL combined with a comparative analysis of multiple ETLs, cathodes, and device parameters remain limited. The novelty of the present work lies in the comprehensive optimization of rGO-based BHJOSCs through extensive parameter tuning and device engineering, leading to improved performance and providing deeper insights into the role of rGO as a stable and efficient HTL for P3HT:PCBM BHJOSCs.

5.4 Numerical Investigation of P3HT:PCBM BHJOSC with rGO as HTL, Diverse ETLs and Cathode Materials

An extensive numerical simulation of ITO/rGO/P3HT:PCBM/Al is done here. The influence of electrical parameters such as thickness, defect density, electron mobility and hole mobility of active layer and HTL were studied. The effect of interface defect density, operating temperature, R_s, and R_{sh} was also investigated. Finally the device was optimized using the optimum input parameters. Later, by incorporation of diverse ETLs and different cathodes, enhancement in efficiency was attained and the results were analyzed.

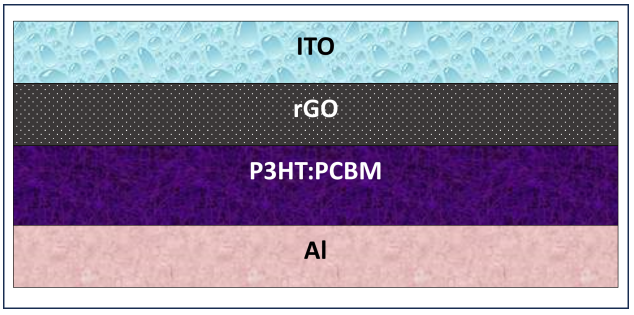


FIGURE 5.40: The device structure used for the experimental study of ITO/rGO/P3HT:PCBM/Al [336].

TABLE 5.9: Input material parameters of P3HT:PCBM and rGO.

Parameter	P3HT:PCBM	rGO
Thickness (d) (nm)	100 [336]	35 [336]
Band gap (E_g) (eV)	1.27 [338]	1.5 [354]
Electron affinity (χ) (eV)	3.7 [338]	4.8 [355]
Dielectric constant (ε_r)	3.5 [339]	13.3 [356]
Conduction band density (C_B) (cm^{-3})	7.8×10^{19} [340]	1×10^{19} [337]
Valence band density (V_B) (cm^{-3})	7.8×10^{19} [340]	1×10^{19} [337]
Thermal velocity of electrons (cm/s)	1×10^{7} [340]	1×10^{7}
Thermal velocity of holes (cm/s)	1×10^{7} [340]	1×10^{7}
Electron mobility (μ_e) (cm^2/Vs)	2×10^{-3}	320 [357]
Hole mobility (μ_h) (cm^2/Vs)	2×10^{-3}	320 [357]
Doping concentration of donor (N_D) (cm^{-3})	0 [339]	0
Doping concentration of acceptor (N_A) (cm^{-3})	0 [339]	1×10^{18}
Defect density (N_t) (cm^{-3})	6.847×10^{15}	1×10^{9}

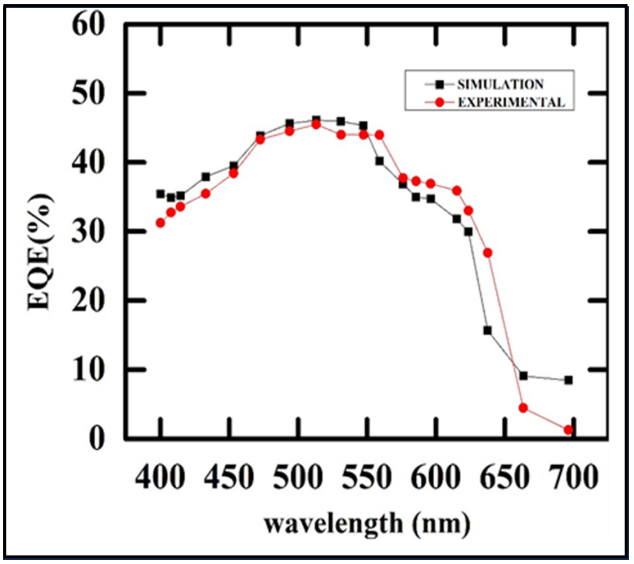


FIGURE 5.41: Matched EQE graph for the device structure ITO/rGO/P3HT:PCBM/Al.

TABLE 5.10: Matching experimental and simulation results.

	V_{oc} (V)	J_{sc} (mA/cm^2)	FF (%)	Efficiency (%)
Experimental	0.38	5.37	31.2	0.65
Simulation	0.3945	5.78	28.41	0.65

5.4.1 Standardization

Primarily standardization of the software using the experimentally reported device structure ITO/rGO/P3HT:PCBM/Al [336] was done. Fig. 5.40 illustrates experimental device structure used for standardization. Table 5.9 lists the input parameters of P3HT:PCBM and rGO used for the standardization.

The following input parameters were chosen as default value from the SCAPS-1D software. The simulation was run at 300 K operating temperature under AM 1.5G light with an intensity of 100 mW/cm^2. Capture cross-section, electron and hole thermal velocities for all layers were set to 1×10^{-15} cm^2 and 1×10^7 cm/s respectively. Furthermore, the capture cross-section for the HTL/active layer interface, and active layer/ETL interface was chosen as 1×10^{-15} cm^2. The characteristic energy value for a defect with a neutral Gaussian distribution was set to 0.1 eV. The energy level with respect to the reference (eV) was kept constant for all layers at 0.6 eV.

Fig. 5.41 matched EQE graph of ITO/rGO/P3HT:PCBM/Al [336] and Table 5.10 lists the matched experimental and simulation output parameters.

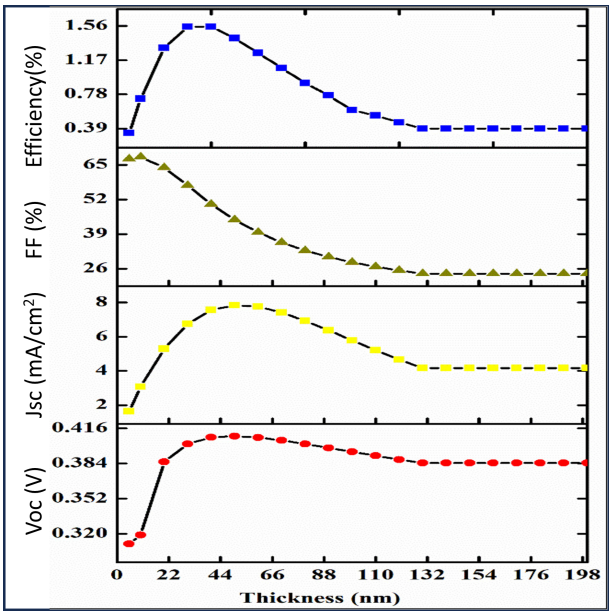


FIGURE 5.42: Variation of device output parameters vs active layer thickness.

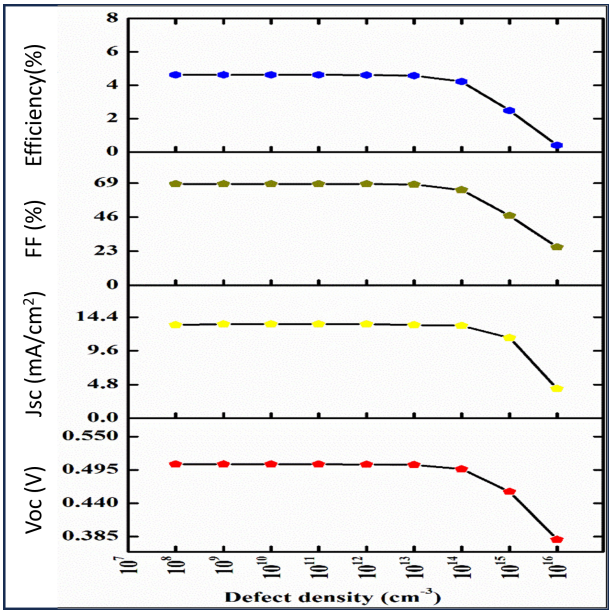


FIGURE 5.43: Variation of device output parameters vs active layer defect density.

5.4.2 Optimization

Optimization of the device structure ITO/rGO/P3HT:PCBM/Al on the basis of varying input parameters including thickness, electron mobility, hole mobility, defect density, interface defect density and temperature is done. The influence of varying thickness, electron mobility, hole mobility and defect density, of the active layer were studied. The

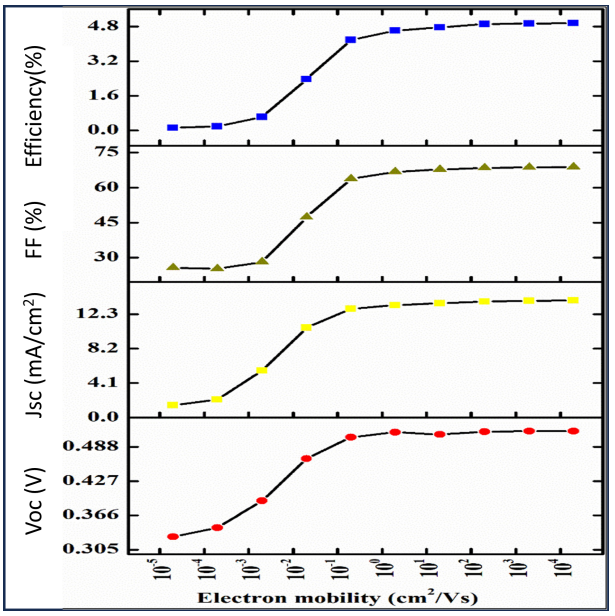


FIGURE 5.44: Variation of device output parameters vs active layer electron mobility.

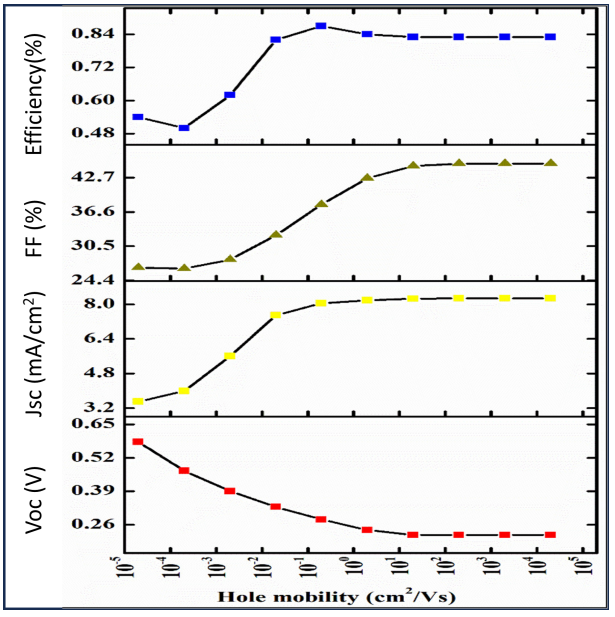


FIGURE 5.45: Variation of device output parameters vs active layer hole mobility.

impact of varying thickness, electron mobility, hole mobility, and defect density of HTL were examined. Later, the effect of changing interface defect density, R_s, R_{sh}, and operating temperature were studied.

5.4.2.1 Influence of Varying Input Parameters of Active Layer on the Device Performance

The impact of varying the active layer thickness on the V_{oc}, J_{sc}, FF, and efficiency were investigated and shown in Fig. 5.42. Thickness of the active layer was varied from the range of 5 to 200 nm, and the associated effect on device output parameters was analyzed. V_{oc} increased upto 0.4089 V as the thickness approached 50 nm, then subsequently dropped. J_{sc} reached 7.840 mA/cm^2 at 50 nm and thereafter dropped. Maximum FF of 67.16% was achieved at 5 nm, and a maximum efficiency of 1.55% was attained at 50 nm.

It seems that as the thickness increased, there is a noticeable increase in the surface area of the active layer. Increasing the thickness upto a certain point is crucial for achieving optimal device performance, as it improves the absorption of photons and the generation of e-h pairs. However, once the thickness surpasses the ideal value, the efficiency starts to decrease. This can be attributed to the fact that, beyond a certain thickness limit (the optimum value), the charge carriers have to travel a longer distance to reach the corresponding electrodes. Consequently, an increase in thickness above the optimum value significantly raises the likelihood of charge carrier recombination. This ultimately leads to a decline in the device's output parameters after reaching the optimum thickness value.

As shown in Fig. 5.43, as the defect density of the active layer was increased from 10^8 to 10^{16} cm^{-3}, V_{oc} decreased to 0.38 V, J_{sc} decreased to 4.196 mA/cm^2, FF decreased to 25.8%, and efficiency decreased to 0.41%.

For the purpose of device optimization, the effects of changing the active layer thickness and defect density on the V_{oc}, J_{sc}, FF, and efficiency were examined. We changed the active layer's thickness from 5 to 200 nm, and we examined the impact this had on the device's performance by holding all other variables constant during the simulations.

Fig. 5.44 and Fig. 5.45 display the influence of electron and hole mobility of active layer. As the electron mobility was increased to 2×10^4 cm^2/Vs, efficiency increased upto 4.95%. Higher charge mobility is necessary to reduce the charge recombination as well as promote the charge collection.

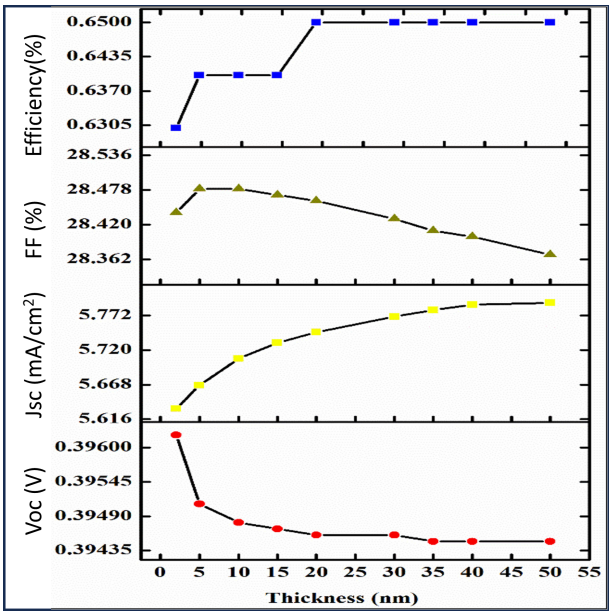


FIGURE 5.46: Variation of device output parameters vs thickness of HTL.

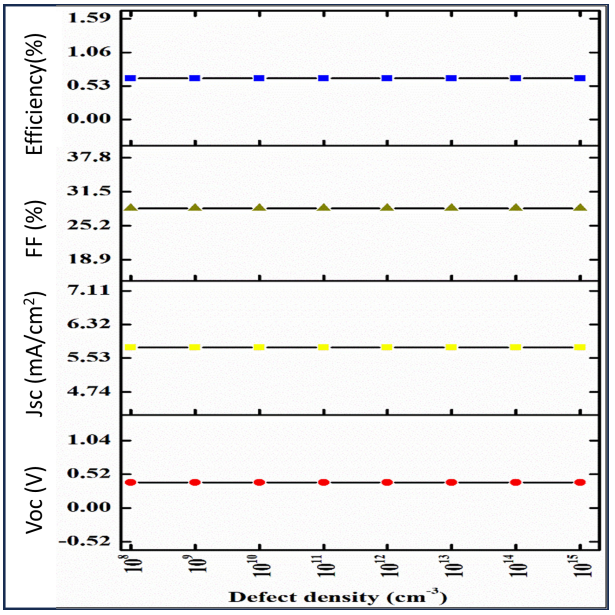


FIGURE 5.47: Variation of device output parameters vs defect density of HTL.

5.4.2.2 Influence of Varying Input Parameters of rGO (HTL) on the Device Performance

The effect of variation of electrical properties of HTL on device performance is discussed in this section. As shown in Fig. 5.46, as the thickness of rGO was varied, V_{oc} decreased gradually, giving maximum of 0.3962 V at 2 nm. But J_{sc} first increased to 5.791

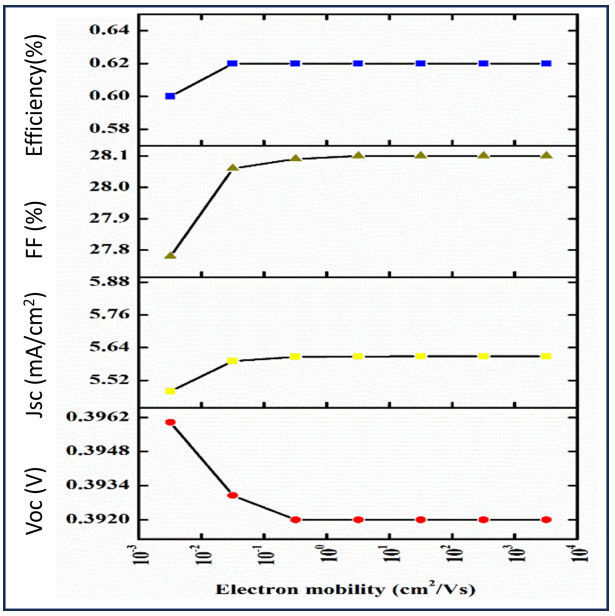


FIGURE 5.48: Variation of device output parameters vs electron mobility of HTL.

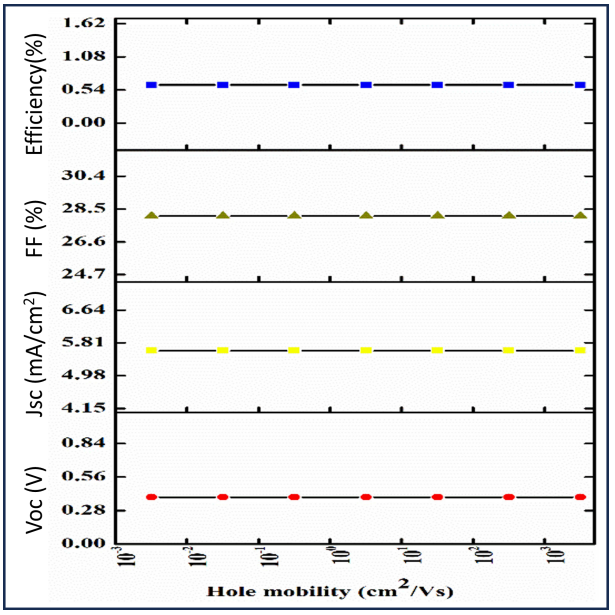


FIGURE 5.49: Variation of device output parameters vs hole mobility of HTL.

mA/cm^2 at 50 nm after which it declined. FF reached a maximum of of 28.48% at 5 nm and then decreased. Efficiency reached a maximum of 0.65% at 20 nm and then remained constant. If the HTL is too thin, it might lead to incomplete hole collection, resulting in lower current and reduced efficiency. On the other hand, if the HTL is too thick, it could impede charge transport, leading to similar performance issues. The thickness of the HTL can affect the ease with which holes can travel through the layer and reach the anode.

As the defect density of the rGO was increased from 10^8 to 10^{16} cm^{-3} the device output parameters remained constant as shown in Fig. 5.47.

The effect of varying electron and hole mobilities on device performance are shown in Fig. 5.48 and Fig. 5.49. As the electron mobility of rGO was varied, at an electron mobility of $3.2 \times 10^1 cm^2/Vs$, V_{oc} reached 0.39 V, J_{sc} reached 5.608 mA/cm^2, then remained constant. FF reached 28.10%, and efficiency reached 0.62%. As the hole mobility of rGO increased the V_{oc}, J_{sc}, FF, and efficiency remained constant at 0.532 V, 5.6493 mA/cm^2, 27.89% and 0.67%.

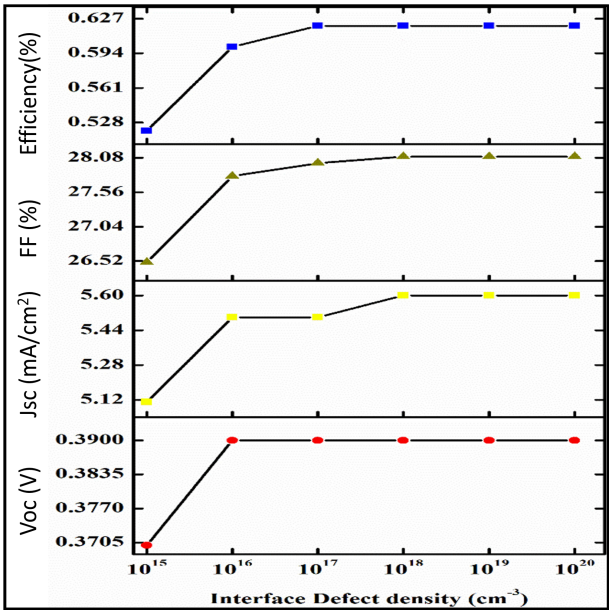


FIGURE 5.50: Variation of device output parameters vs interface defect density.

5.4.2.3 Influence of Varying Interface Defect Density, Series Resistance, Shunt Resistance and Operating Temperature on the Device Performance

The influence of varying interface defect density on the device performance is illustrated in Fig. 5.50. V_{oc}, J_{sc}, FF, and efficiency increased to 0.39 V, 5.60 mA/cm^2, 28.1% and 0.62% respectively, when the interface defect density increased from 10^{14} to 10^{20} cm^{-2}. At 1×10^{17} cm^{-2}, efficiency reached 0.62%. The improvement in performance suggests that moderate interface defects may enhance interfacial charge transfer and electric field-assisted carrier separation in the device.

Fig. 5.51 and Fig. 5.52 represents the variation of output parameters with varying R_s and R_{sh}, correspondingly. As the R_s is increased from 1 to 10 Ohm, V_{oc} remained

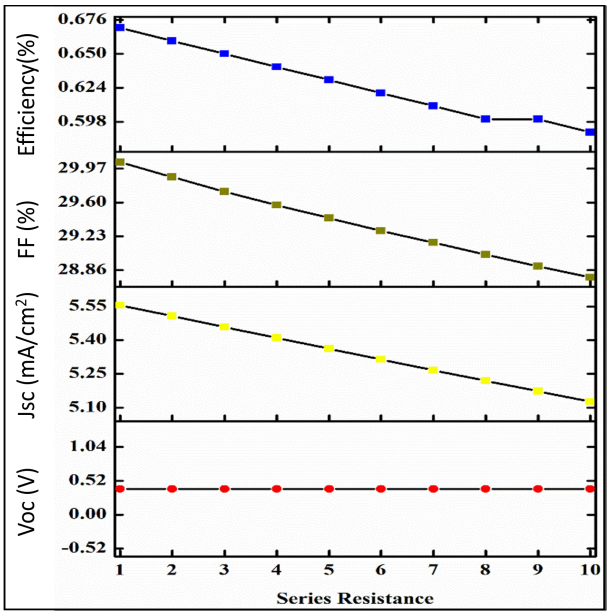


FIGURE 5.51: Variation of device output parameters vs series resistance.

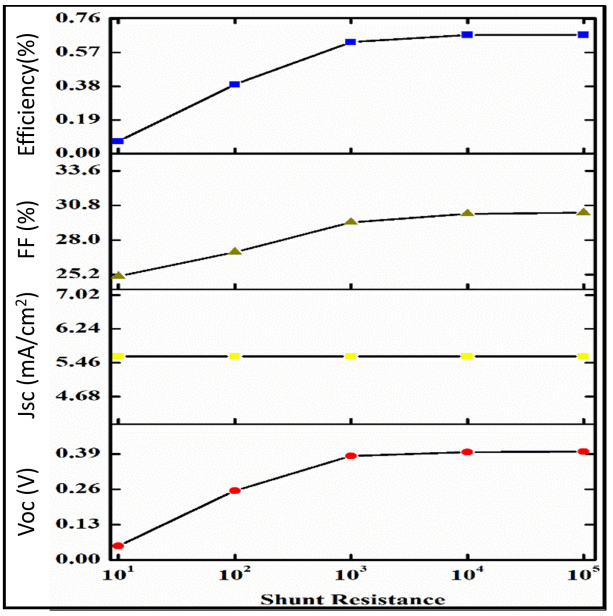


FIGURE 5.52: Variation of device output parameters vs shunt resistance.

constant as 0.3989 V, J_{sc} decreased to 5.126154 mA /cm^2, FF declines to 28.78%, and efficiency decreased to 0.59%. As the R_{sh} increased from 10 to 100000 Ohm, V_{oc} increased to 0.3987 V, J_{sc} remained 5.604581 mA/cm^2, FF increased to 30.20%, and efficiency increased to 0.67%. The R_{sh} has no effect on the short circuit current, while the V_{oc}, FF, and efficiency seemed to increase. Higher R_s limits charge extraction, whereas higher R_{sh} suppresses leakage currents and recombination losses, resulting in improved FF and

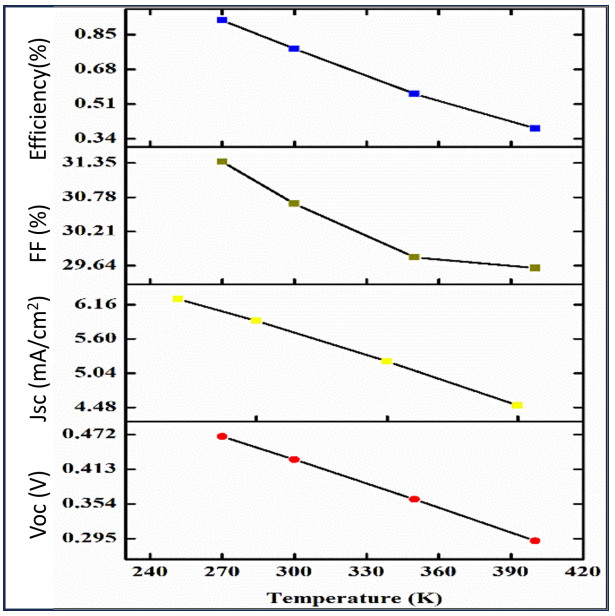


FIGURE 5.53: Variation of device output parameters vs operating temperature.

efficiency.

Fig. 5.53 illustrates how the device's output parameters were observed to be adversely affected by temperature variation. V_{oc}, J_{sc}, FF, and efficiency reduced to 0.29 V, 4.51 mA/cm^2, 29.63% and 0.42% respectively, as it approached 400 K. The decline in performance at elevated temperatures could be mainly due to increased carrier recombination and reduced built-in potential across the device.

ITO/rGO/P3HT:PCBM/Al was optimized and achieved enhanced V_{oc} of 0.7130 V, J_{sc} of 11.704530 mA/cm^2, FF of 79.73%, and efficiency of 6.65%. The enhanced performance of the optimized device could be attributed to improved charge transport, reduced recombination losses, and favorable energy level alignment between the device layers.

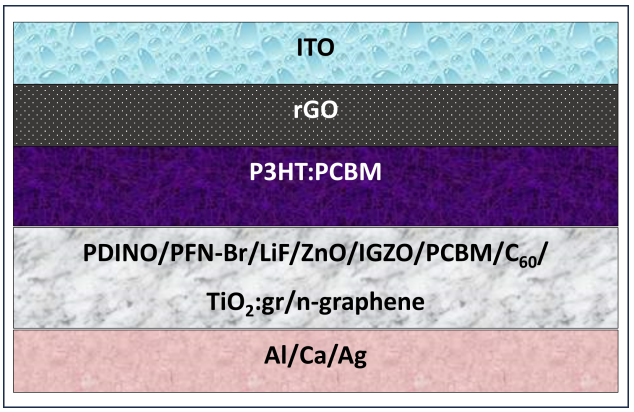


FIGURE 5.54: Schematic illustration of the device structure of ITO/r-GO/P3HT:PCBM/ETL/cathode.

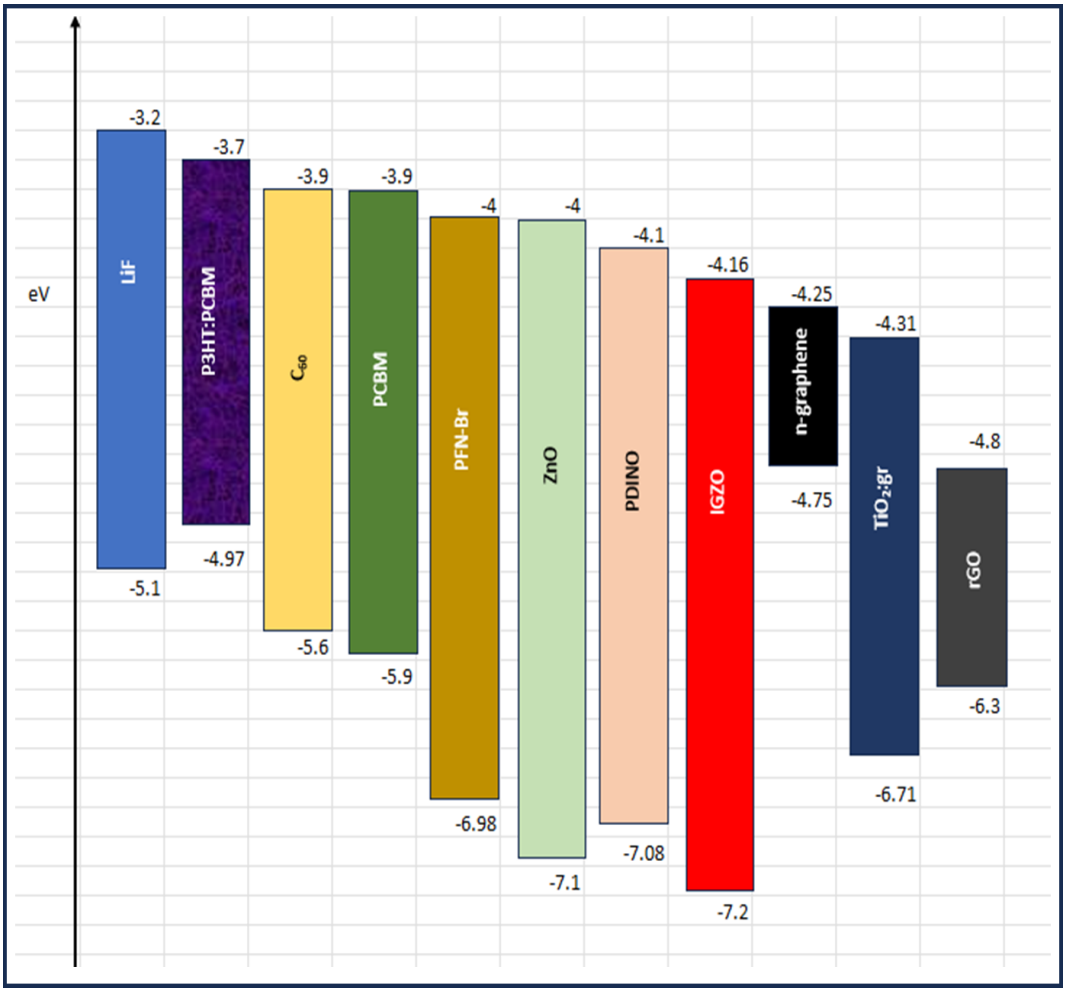


FIGURE 5.55: Schematic illustration of the energy band diagram of materials used for the simulation study of ITO/rGO/P3HT:PCBM/ETL/cathode.

TABLE 5.11: Input material parameters of P3HT:PCBM and rGO.

Parameter	P3HT:PCBM	rGO
Thickness (d) (nm)	100 [336]	35 [336]
Band gap (E_g) (eV)	1.27 [338]	1.5 [354]
Electron affinity (χ) (eV)	3.7 [338]	4.8 [355]
Dielectric constant (ε_r)	3.5 [339]	13.3 [356]
Conduction band density (C_B) (cm^{-3})	7.8×10^{19} [340]	1×10^{19} [337]
Valence band density (V_B) (cm^{-3})	7.8×10^{19} [340]	1×10^{19} [337]
Thermal velocity of electrons (cm/s)	1×10^{7} [340]	1×10^{7}
Thermal velocity of holes (cm/s)	1×10^{7} [340]	1×10^{7}
Electron mobility (μ_e) (cm^2/Vs)	2×10^{-3}	320 [357]
Hole mobility (μ_h) (cm^2/Vs)	2×10^{-3}	320 [357]
Doping concentration of donor (N_D) (cm^{-3})	0 [339]	0
Doping concentration of acceptor (N_A) (cm^{-3})	0 [339]	1×10^{18}
Defect density (N_t) (cm^{-3})	6.847×10^{15}	1×10^{9}

TABLE 5.12: Input parameters used for the ETLs-PDINO, PFN-Br, LiF, and ZnO.

Parameter	PDINO	PFN-Br	LiF	ZnO
Thickness (d) (nm)	5 [344]	5 [341]	20 [345]	20 [346]
Band gap (E_g) (eV)	2.98 [344]	2.98 [341]	1.9 [342]	3.1 [347]
Electron affinity (χ) (eV)	4.1 [344]	4.0 [341]	3.2 [342, 345]	4.0 [349]
Dielectric constant (ε_r)	5 [344]	5 [341]	9.1 [346]	9 [350]
Conduction band density (C_B) (cm^{-3})	1×10^{19} [344]	1×10^{19} [341]	1×10^{20} [342, 351]	2×10^{18} [341]
Valence band density (V_B) (cm^{-3})	1×10^{19} [344]	1×10^{18} [341]	1×10^{20} [342, 351]	1.8×10^{19} [341]
Thermal velocity of electrons (V_e) (cm/s)	1×10^{7} [344]	1×10^{7} [341]	1×10^{7} [342, 351]	1×10^{7} [341]
Thermal velocity of holes (V_h) (cm/s)	1×10^{7} [344]	1×10^{7} [341]	1×10^{7} [342, 351]	1×10^{7} [341]
Electron mobility (μ_e) (cm^2/Vs)	2×10^{-6} [344]	2×10^{-6} [341]	1 [342, 351]	1×10^{2} [341]
Hole mobility (μ_h) (cm^2/Vs)	1×10^{-3} [344]	1×10^{-4} [341]	1 [342, 351]	2.5×10^{2} [341]
Doping concentration of donor (N_D) (cm^{-3})	2×10^{21} [344]	9×10^{18} [341]	1×10^{18}	1×10^{18} [341]
Doping concentration of acceptor (N_A) (cm^{-3})	0 [344]	0 [341]	0	0 [341]
Defect density (N_t) (cm^{-3})	1×10^{9} [344]	1×10^{14} [341]	1×10^{9} [342, 351]	1×10^{14} [341]

TABLE 5.13: Input parameters of ETLs-IGZO, PCBM, C_{60}, TiO_2:gr, and n-graphene.

Parameter	IGZO	PCBM	C_{60}	TiO_2:gr	n-graphene
Thickness (d) (nm)	5 [341]	5 [341]	5 [341]	50 [352]	33.4 [353]
Band gap (E_g) (eV)	3.05 [341]	2 [341]	1.7 [341]	2.4 [352]	0.5 [353]
Electron affinity (χ) (eV)	4.16 [341]	3.9 [341]	3.9 [341]	4.31 [352]	4.8 [353]
Dielectric constant (ε_r)	10 [341]	3.9 [341]	4.2 [341]	7.8 [352]	10 [353]
Conduction band density (C_B) (cm^{-3})	1×10^{19} [341]	1×10^{19} [341]	1×10^{19} [341]	1×10^{19} [352]	3×10^{19} [353]
Valence band density (V_B) (cm^{-3})	1×10^{19} [341]	1×10^{19} [341]	1×10^{19} [341]	1×10^{19} [352]	3×10^{19} [353]
Thermal velocity of electrons (V_e) (cm/s)	1×10^{7} [341]	1×10^{7} [341]	1×10^{7} [341]	1×10^{7} [352]	1×10^{7} [353]
Thermal velocity of holes (V_h) (cm/s)	1×10^{7} [341]	1×10^{7} [341]	1×10^{7} [341]	1×10^{7} [352]	1×10^{7} [353]
Electron mobility (μ_e) (cm^2/Vs)	15 [341]	0.02 [341]	8×10^{-2} [341]	350 [352]	10 [353]
Hole mobility (μ_h) (cm^2/Vs)	0.1 [341]	0.02 [341]	3.5×10^{-3} [341]	350 [352]	1×10^{5} [353]
Doping concentration of donor (N_D) (cm^{-3})	1×10^{19} [341]	1×10^{19} [341]	1×10^{19} [341]	5×10^{18} [352]	1×10^{26} [353]
Doping concentration of acceptor (N_A) (cm^{-3})	0 [341]	0 [341]	0 [341]	0 [352]	0 [353]
Defect density (N_t) (cm^{-3})	1×10^{19} [341]	1×10^{19} [341]	1×10^{19} [341]	1×10^{14} [352]	1×10^{14} [353]

5.4.3 Study of ITO/rGO/P3HT:PCBM/ETL/ Metal Electrode with Diverse ETLs and Different Metal Electrodes

Fig. 5.54 shows designed device structure used for the study of ITO/rGO/P3HT:PCBM /ETL/metal electrode. Fig. 5.55 illustrates the energy band diagram of the layers used in the simulation study. Tables 5.11-5.13 lists the input parameters of the active layer, HTL and ETL layers used for the study. To maintain consistency with existing literature and ensure baseline reliability, the remaining parameters were kept at the default values configured within SCAPS-1D, a convention frequently used in similar simulation studies.

These default values were chosen by researchers in existing simulation studies. Operating temperature was set at 300 K under AM 1.5 G light with an intensity of 100 mW/cm^2. Capture cross-section, electron and hole thermal velocities for all layers were set to 1 $\times$ 10^{-15} cm^2 and 1 $\times$ 10^7 cm/s respectively. Furthermore, the capture cross-section for the HTL/active layer interface, and active layer/ETL interface were chosen as 1 $\times$ 10^{-15} cm^2. The characteristic energy value for a defect with a neutral Gaussian distribution was set to 0.1 eV. The energy level with respect to the reference (eV) was kept constant for all layers at 0.6 eV. Table 5.14 gives the device output parameters of the various configurations studied.

TABLE 5.14: Device output parameters attained for different configurations.

Metal	ETL	V_{oc} (V)	J_{sc} (mA/cm^2)	FF (%)	Efficiency (%)
Aluminium	PDINO	0.7309	11.84	81.07	7.02
Aluminium	PFN-Br	0.7271	12.04	71.39	6.25
Aluminium	LiF	0.577	12.5	68.92	4.97
Aluminium	ZnO	0.7309	11.83	81.08	7.01
Aluminium	IGZO	0.7309	11.77	81.08	6.97
Aluminium	PCBM	0.731	11.74	76.73	6.59
Aluminium	C_{60}	0.731	11.76	79.69	6.85
Aluminium	TiO_2:graphene	0.7311	11.75	80.71	6.93
Aluminium	n-graphene	0.5189	11.49	70.54	4.21
Calcium	PDINO	0.731	11.88	81.1	7.04
Calcium	PFN-Br	0.7324	12.27	79.21	7.12
Calcium	LiF	0.7909	26.61	56.99	12.00
Calcium	ZnO	0.731	11.87	81.1	7.04
Calcium	IGZO	0.7309	11.77554	81.11	6.98
Calcium	PCBM	0.7309	11.77595	81.11	6.98
Calcium	C60	0.7309	11.77854	81.12	6.98
Calcium	TiO_2:graphene	0.7311	11.74356	80.71	6.93
Silver	n-graphene	0.5207	11.49409	70.46	4.22
Silver	PDINO	0.7308	11.81524	76.87	6.64
Silver	PFN-Br	0.6252	11.98285	61.65	4.62
Silver	LiF	0.4271	12.28191	64.77	3.4
Silver	ZnO	0.7308	11.77807	81.06	6.98
Silver	IGZO	0.7312	11.73301	80.51	6.91
Silver	PCBM	0.7307	11.69365	59.69	5.1
Silver	C60	0.7631	11.8055	59.89	5.4
Silver	TiO_2:graphene	0.7311	11.74356	80.71	6.93
Silver	n-graphene	0.4506	11.4938	72.44	3.75

5.5 Comparison of P3HT:PCBM based BHJOSCs with Efficiency Exceeding 10%

Initially P3HT:PCBM BHJOSCs reported efficiencies of approximately 3-4%, which were subsequently improved to around 5-6% through advances in solvent engineering, thermal annealing, morphology control, and interface engineering [360, 361, 362]. Recent

experimental studies generally report efficiencies below 6%, whereas numerical simulation studies employing SCAPS-1D and GPVDM have predicted efficiencies exceeding 10% through optimization of device architecture, transport layers, and material parameters [363, 364]. In the present work, the optimized device structure ITO/rGO/P3HT:PCBM/LiF/Ca achieved a maximum simulated efficiency of 12.00%, demonstrating the potential of graphene derivative as a promising HTL in fullerene based BHJOSCs. Recent reviews also conclude that efficiencies beyond 10% are achievable through appropriate device and interface engineering [365].

5.6 Conclusion

The design and simulation of P3HT:PCBM BHJOSCs with higher efficiency, using graphene derivatives as HTL were successfully carried out. Graphene, GO and rGO were the graphene derivatives used as best HTLs in our studies.

Initially, the design and simulation of P3HT:PCBM BHJ OSCs with the device configuration ITO/graphene/P3HT:PCBM/ETL/Al were carried out, using diverse ETLs including PDINO, PFN-Br, ZnO, and TiO_2 were carried out. The key conclusion drawn from this work is that the device configuration ITO/graphene/P3HT:PCBM/PDINO/Al exhibited the best device performance.

Further, simulation of ITO/GO/P3HT:PCBM/ETL/metal electrodes was performed. In this study standardization of the software was done using the experimental device structure ITO/GO/P3HT:PCBM/Al. Optimization of this device structure was done and attained V_{oc} of 0.6237 V, J_{sc} of 8.92765 mA/cm^2, FF of 77.6%, and efficiency of 4.32%. Later, we introduced diverse ETLs and different cathodes, after which ITO/GO/P3HT:PCBM/LiF/Ca showed enhanced performance with V_{oc} of 0.8517 V, J_{sc} of 11.498525 mA/cm^2, FF of 81.73%, and efficiency of 8.00%.

Lastly, simulation and numerical investigation of ITO/rGO/P3HT: PCBM/ETL/Al was carried out. Standardization was done using the device structure ITO/rGO/P3HT: PCBM/Al and was optimized, which exhibited V_{oc} of 0.7130 V, J_{sc} of 11.704530 mA/cm^2, FF of 79.73%, and efficiency of 6.65%. Later, diverse ETLs and cathodes were introduced and various configurations were studied in which ITO/rGO/P3HT:PCBM/LiF/Ca attained best device performance with V_{oc} of 0.7909 V, J_{sc} of 26.61 mA/cm^2, FF of 56.99%, and efficiency of 12.00%.

Chapter 6

Numerical Investigation of PBDB-T:NCBDT BHJOSCs with Diverse Graphene HTLs and Different ETLs

This chapter details extensive numerical simulation study of PBDB-T:NCBDT BHJOSCs with diverse HTLs and ETLs. NCBDT, an SM-NFA with tunable band gap is used for the study. The transition from FAs to NFAs is of great interest lately in the field of BHJOSCs. Graphene derivatives including graphene, GO, rGO and p type doped graphene (P-graphene) were used as HTLs. Diverse ETLs comprising PDINO, PFN-Br, ZnO, LiF, PCBM, IGZO, TiO_2 and TiO_2:gr were used for the study.

Non-Fullerene acceptors (NFAs) are emerging as a significant area of research in the development of BHJOSCs. In contrast to the widely used FAs, the optical properties and electronic energy levels of NFAs can be readily tuned. NFA based OSCs also exhibit good thermal stability and photochemical stability, as well as longer device lifetimes, than their FA based counterparts. Historically, the performance of NFA OSCs has lagged behind that of fullerene based devices. However, recent developments have led to a rapid increase in the efficiencies of NFA based OSCs, demonstrating the viability of using NFAs to replace FAs in next-generation, high-performance OSCs. This chapter presents a research study on PBDB-T:NCBDT NFA-based BHJOSCs.

6.1 PBDB-T:NCBDT BHJOSCs

PBDB-T:NCBDT is a blend active material, where NCBDT is a low band gap SM-NFAs. SM-NFAs have acceptor-donor-acceptor (A-D-A) backbone architecture, which plays a crucial role in the field of NFA-OSCs due to their effective light harvesting abilities in the visible to NIR region [344]. The A-D-A structured SM-NFAs exhibit a distinctive characteristic that, their energy levels can be easily tuned by modifying the chemical structures of central donor unit (D) and/or end acceptor groups (A). Using these strategies, many high-performance low band gap SM-NFAs have been reported following the introduction of the fused-ring based ITIC [344].

In this study, PBDB-T:NCBDT is used as the active layer. PBDB-T is a conjugated polymer with a repeating unit structure consisting of a benzodithiophene (BDT) and thiophene core. It is a common donor material in polymer SCs [366, 367]. The structure is represented by a chain of BDT and thiophene units, making it a suitable candidate for efficient charge transport in OSCs. The BDT and thiophene rings are linked together, forming a conjugated backbone that allows for efficient electron and hole transport [366, 367]. PBDB-T's high HOMO and relatively high LUMO form a favorable energy cascade with NCBDT, enabling efficient exciton separation, fast charge transfer, and low energy loss in BHJOSCs. Fig. 6.1 illustrates the chemical structures of PBDB-T and NCBDT. A low band gap SM-NFA NCBDT consists of 4,8-dioctylbenzo[1,2-b:4,5-b']dithiophene (BDT)-based fused-ring (CBDT) as the central unit (D) and the fluorinated 2-(2,3-dihydro-3-oxo-1H-inden-1-ylidene)propanedinitrile (F-INCN) as the end groups (A).

NCBDT exhibits upshifted HOMO energy level mainly due to the additional octyl on the D unit and downshifted LUMO energy level due to the fluorination of A unit. NCBDT

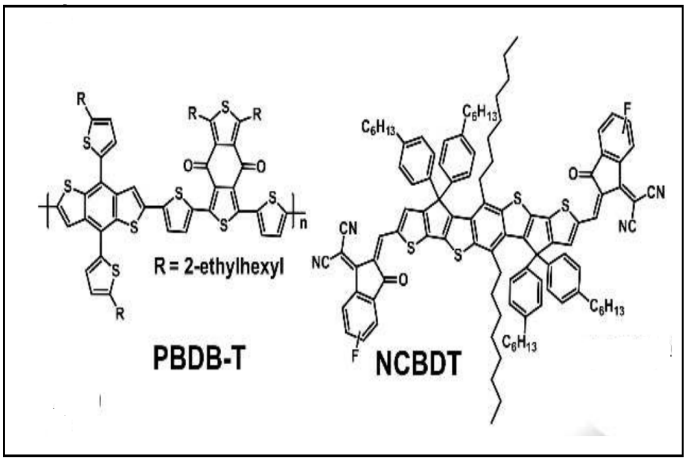


FIGURE 6.1: PBDB-T and NCBDT.

has a low optical band gap which extends the absorption range toward NIR region down to 860 nm. These distinct properties of the active layer blend have made us to select this particular material. [344, 368, 369, 370].

While numerous studies have been conducted using PBDB-T as the donor material and various NFAs, particularly focusing on BHJOSC work with PBDB-T:ITIC, only limited research has been carried out on simulation studies of PBDB-T:NCBDT BHJOSCs.

Herein, we choose a non-functionalized or undoped NCBDT as the acceptor, since its band gap is tunable and can be reduced from 1.65 to 1.47 eV compared to ITIC, making it a more suitable acceptor for BHJOSC. This property of the acceptor can lead to an increase in efficiency [368]. A PBDB-T:NCBDT NFA based BHJOSC was fabricated in 2018 with the configuration ITO/PEDOT:PSS/PBDB-T:NCBDT/PDINO/Al achieving an efficiency of 12% [369] with ITO as anode, PEDOT:PSS as HTL, PDINO as ETL and Al as cathode.

Subsequently, chlorination of NCBDT improved the efficiency up to 14% [370]. ITO/PEDOT:PSS/PBDB-T:NCBDT/PDINO/Al was reported later in the same year, via sequential deposition method and attained 10.19% [368]. In 2021, an NFA BHJOSC using PBDBT-2F:mNCBDT-4Cl as absorber layers was fabricated and attained efficiency of 12.56% [371].

Although experimental and simulation studies of PBDB-T:NCBDT-based NFA BHJOSCs with GO as the HTL have been reported, a comprehensive simulation study of PBDB-T:NCBDT NFA-based BHJOSCs with four different graphene derivatives as HTLs and

various ETLs, including graphene derivative composite-based ETLs, has not yet been reported.

6.2 Numerical Investigation of PBDB-T:NCBDT BHJOSC with Diverse Graphene HTLs and ETLs

A simulation study of PBDB-T:NCBDT BHJOSC with graphene derivatives as HTLs and diverse ETLs is presented and analyzed in this section. HTLs used are graphene, GO, rGO and p-graphene, while the ETLs used are PDINO, PFN-Br, ZnO, IGZO, PCBM, TiO_2 and TiO_2:gr.

The study begins with standardization of the simulation software, followed by the design, simulation and analysis of different device configurations employing the aforementioned HTLs and ETLs. Among these, the most efficient device configuration was identified and optimized based on several input parameters of the device.

The effects of various factors were systematically examined including the thickness of active layer, HTL and ETL and defect density of active layer, HTL and ETL. The influence of electron mobility of ETL and hole mobility of HTL were studied. Furthermore, the influence of operating temperature and interface defects were also examined.

6.2.1 Standardization

Standardization is a prerequisite for simulation studies, especially for OPVs. In this study, standardization was done using the device configuration investigated experimentally by Zhang et al. [368].

For the standardization purpose, the output J-V parameters, J-V graph and the EQE graph were simulated and analyzed. The device structure used for standardization is illustrated in Fig. 6.2. Table 6.1 lists the numerical input parameters of active layer, HTL and ETL used for the standardization. Numerical parameters listed in Table 6.1 were taken from previously reported works of BHJOSCs.

The remaining input parameters taken were default input parameters provided by SCAPS-1D and these default parameters were also used by other researchers in their simulation studies. The simulation was run at 300 K operating temperature under AM 1.5 G light with an intensity of 100 mW/cm^2. Capture cross-section, electron and hole thermal

velocities for all layers were set to 1×10^{-15} cm^2 and 1×10^7 cm/s respectively. Furthermore, the capture cross-section for the HTL/active layer interface, and active layer/ETL interface were chosen as 1×10^{-15} cm^2. The characteristic energy value for a defect with a neutral Gaussian distribution was set to 0.1 eV. The energy level with respect to the reference (eV) was kept constant for all layers at 0.6 eV.

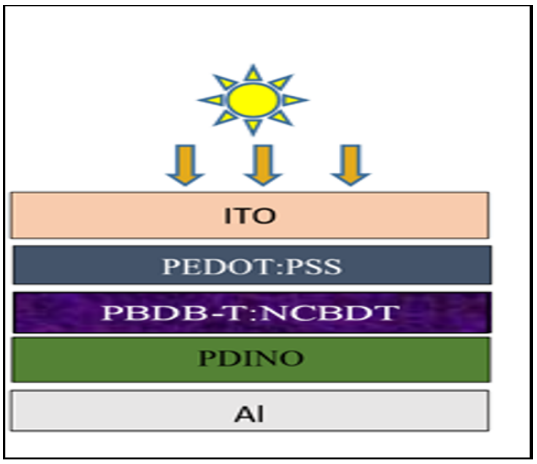


FIGURE 6.2: Figure illustrating the experimental device structure-ITO/PEDOT:PSS/PBDB-T:NCBDT/ PDINO/Al [368].

TABLE 6.1: Input parameters of PBDB-T:NCBDT, PEDOT:PSS and PDINO for the simulation of ITO/PEDOT:PSS/PBDB-T:NCBDT/PDINO/Al.

Parameter	PBDB-T:NCBDT	PEDOT:PSS	PDINO [341]
Thickness (d) (nm)	100 [344]	30 [341]	5 [341]
Band gap (E_g) (eV)	1.38 [344]	3.4 [341]	2.98 [341]
Electron affinity (χ) (eV)	3.98 [344]	3.2 [341]	4.1 [341]
Dielectric permittivity (ε_r)	3.65 [344]	3 [341]	3.1 [341]
Conduction band density (C_B) (cm^{-3})	1×10^{19} [344]	1×10^{22} [341]	2×10^{18} [341]
Valence band density (V_B) (cm^{-3})	1×10^{19} [344]	1×10^{22} [341]	1×10^{19} [341]
Electron mobility (μ_e) (cm^2/Vs)	8.8×10^{-5} [344]	4.5×10^{-3} [341]	2×10^{-6} [341]
Hole mobility (μ_h) (cm^2/Vs)	9.2×10^{-5} [344]	9.9×10^{-5} [341]	1×10^{-3} [341]
Doping concentration of acceptor (N_A) (cm^{-3})	0	1×10^{21} [341]	0 [341]
Doping concentration of donor (N_D) (cm^{-3})	0	0	2.0×10^{11} [341]
Defect density (N_t) (cm^{-3})	5×10^{11} [344]	1×10^{9} [341]	1.0×10^{14} [341]

Fig. 6.3 illustrates the J-V characteristics of experimental and simulation investigations align. Fig. 6.4 illustrates the EQE characteristics of experimental and simulation investigations align.

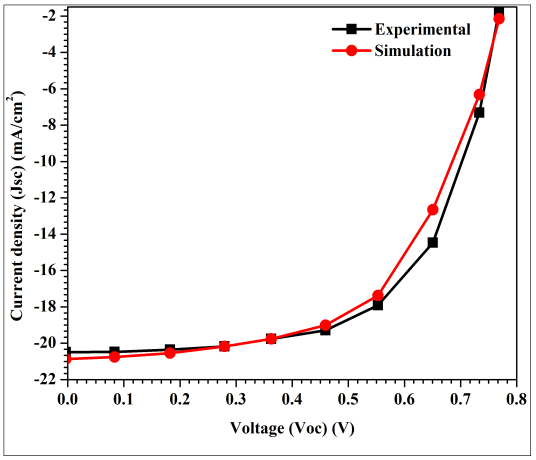


FIGURE 6.3: Matching simulation and experimental J-V graph of ITO/PEDOT:PSS/PBDB-T:NCBDT/PDINO/Al.

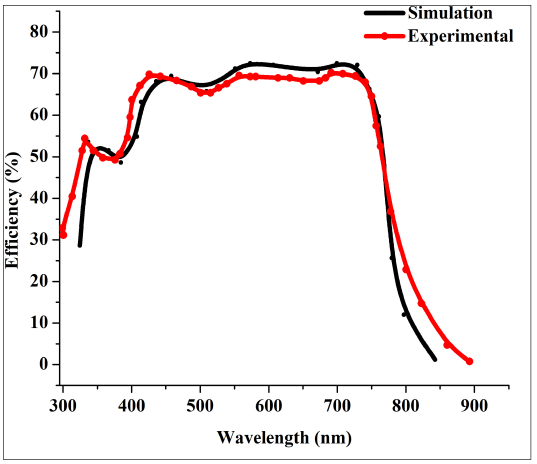


FIGURE 6.4: Matching simulation and experimental EQE graph of ITO/PEDOT:PSS/PBDB-T:NCBDT/ PDINO/Al.

TABLE 6.2: Comparison of simulated output with experimental result of ITO/PEDOT:PSS/PBDB-T:NCBDT/ PDINO/Al.

Parameters	Experimental [368]	Simulated
V_{oc} (V)	0.824	0.80403
J_{sc} (mA/cm^2)	19.45	20.610
FF (%)	62.9	60.43
Efficiency (%)	10.04	10.02

Table 6.2 gives the matched experimental and simulation output parameters. The close agreement between the experimentally measured and simulated results confirms that the parameters used for layers of the cell were close to those of the real device, thus validating the software.

6.2.2 Study of ITO/HTL/PBDB-T:NCBDT/ETL/Al with Graphene Derivative HTLs and Diverse ETLs

Following the standardization of the device, graphene derivative HTLs comprising of graphene, GO, rGO and p-graphene were introduced. Subsequently, diverse ETLs such as PDINO, ZnO, IGZO, TiO_2, TiO_2:gr (20%) and TiO_2:gr (10%) were incorporated for comparative analysis. The standardized device structure uses PEDOT:PSS as HTL, PDINO as ETL, ITO (4.5 eV) [336] as anode and Al (4.2 eV) [336] as cathode. Whereas in the structure that is to be simulated, a study on varying ITO workfunction from 4.5 to 4.8 eV using diverse ETLs and different graphene derivatives as HTLs is done, which makes the study unique.

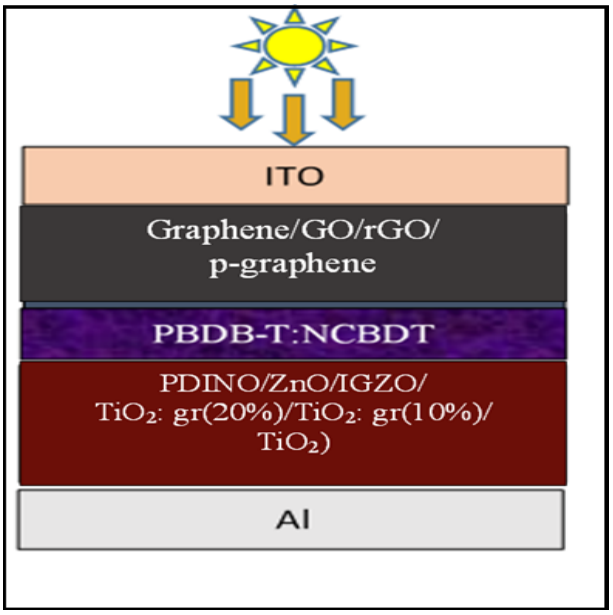


FIGURE 6.5: Device structure for the simulation of ITO/HTLs/PBDB-T:NCBDT/ ETLs/Al

Fig. 6.5 illustrates the device structure designed for the simulation study. Fig. 6.6 presents the energy band diagram of the layers used in the study. The energy band diagram is illustrated using the HOMO-LUMO levels of each layers obtained from band gap and electron affinity values. Table 6.3 lists the input parameters of PBDB-T:NCBDT and various HTLs used for the study. Table 6.4 lists the input parameters of ETLs used for the study. To maintain consistency with existing literature and ensure baseline reliability, the remaining parameters were kept at the default values configured within SCAPS-1D, a convention frequently used in similar simulation studies. Operating temperature was set at 300 K under AM 1.5 G light with an intensity of 100 mW/cm^2. Capture cross-section,

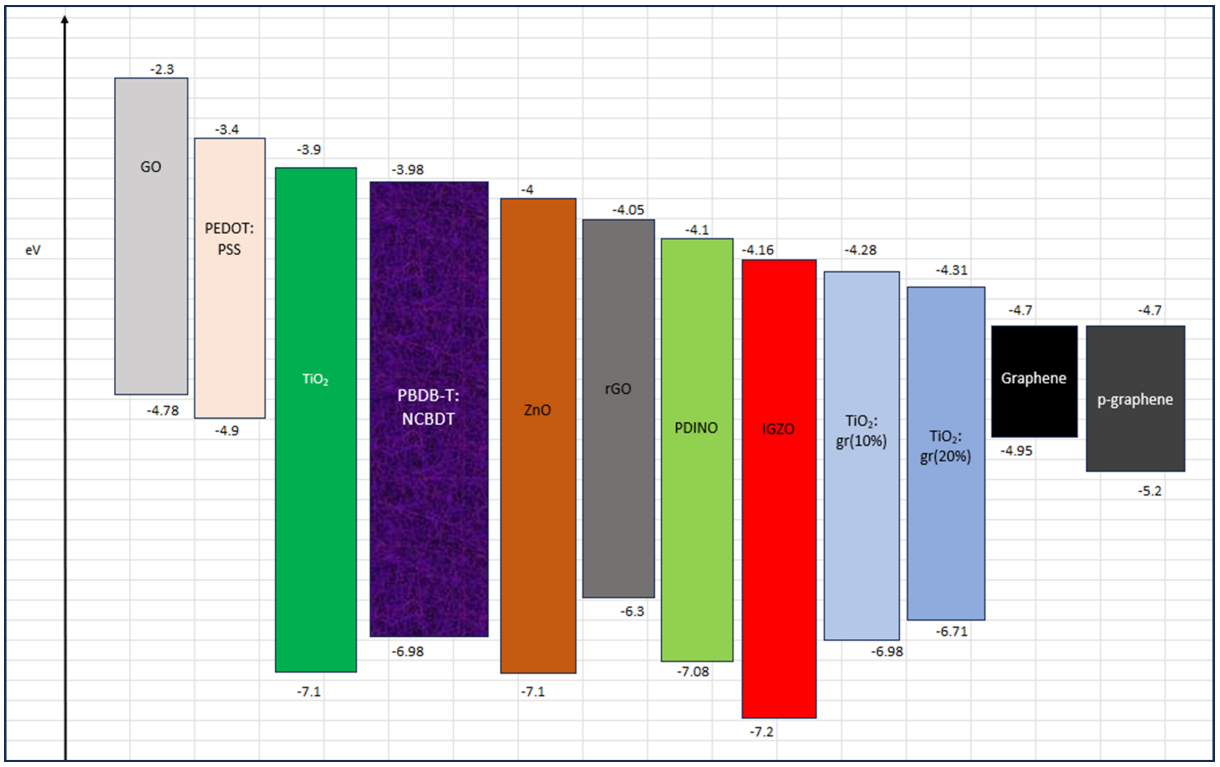


FIGURE 6.6: Energy band diagram of layers used for the simulation of ITO/HTLs/PBDB-T:NCBDT/ETLs/Al

electron and hole thermal velocities for all layers were set to 1×10^{-15} cm^2 and 1×10^7 cm/s respectively. Furthermore, the capture cross-section for the HTL/active layer interface, and active layer/ETL interface were chosen as 1×10^{-15} cm^2. The characteristic energy value for a defect with a neutral Gaussian distribution was set to 0.1 eV. The energy level with respect to the reference (eV) was kept constant for all layers at 0.6 eV.

TABLE 6.3: Input parameters of PBDB-T:NCBDT and various HTLs.

Parameter	PBDB-T:NCBDT	Graphene	GO	rGO	p-graphene	PEDOT:PSS
Thickness (d) (nm)	100 [344]	20 [337]	35 [336]	35 [336]	33 [372]	30 [341]
Band gap (E_g) (eV)	1.38 [344]	0.25 [337]	2.48 [343]	1.5 [354]	0.5 [372]	3.4 [341]
Electron affinity (χ) (eV)	3.98 [344]	4.7 [337]	2.3 [343]	4.4/4.8 [373]	4.7 [372]	3.2 [341]
Dielectric permittivity (ε_r)	3.65 [344]	13 [337]	10 [343]	13.3 [356]	7.1 [372]	3 [341]
Conduction band density (C_B) (cm^{-3})	1×10^{19} [344]	2×10^{20} [337]	1.8×10^{18} [343]	1×10^{19} [374]	3×10^{19} [372]	1×10^{22} [341]
Valence band density (V_B) (cm^{-3})	1×10^{19} [344]	1.8×10^{20} [337]	2.2×10^{18} [343]	1×10^{22} [374]	3×10^{19} [372]	1×10^{22} [341]
Electron mobility (μ_e) (cm^2/Vs)	8.8×10^{-5} [368]	1×10^{4} [337]	2.6×10^{1} [343]	3.2×10^{2} [357]	1.0×10^{1} [372]	4.5×10^{-3} [341]
Hole mobility (μ_h) (cm^2/Vs)	9.2×10^{-5} [368]	1×10^{1} [337]	1.23×10^{2} [343]	3.2×10^{2} [357]	1×10^{5} [372]	9.9×10^{-5} [341]
Doping concentration of acceptor (N_A) (cm^{-3})	0	1.0×10^{15}	1.0×10^{18} [337]	1.0×10^{18} [343]	1.0×10^{15} [372]	1×10^{21} [341]
Doping concentration of donor (N_D) (cm^{-3})	0	0	0	0	0	0
Defect density (N_t) (cm^{-3})	5×10^{11} [344]	1.9×10^{9} [337]	1.9×10^{9} [343]	1.9×10^{9}	1.9×10^{9} [372]	1×10^{9} [341]

Table 6.5 gives the photovoltaic output parameters of device configurations using different HTL and ETL combinations. Efficiency attained for device structures with different HTLs are as follows: PEDOT:PSS-10.01%, graphene-10.71%, GO-9.65%, rGO-12.26%,

TABLE 6.4: Input parameters of the various ETLs used for the simulation study.

Parameters	PDINO	ZnO	IGZO	TiO_2	TiO_2:gr(20%)	TiO_2:gr(10%)
Thickness (d) (nm)	5 [341]	20	5 [341]	5 [341]	50 [352]	50 [352]
Band gap (E_g) (eV)	2.98 [341]	3.1 [347]	3.05 [341]	3.2 [341]	2.4 [352]	2.7 [352]
Electron affinity (χ) (eV)	4.1 [341]	4 [375]	4.16 [341]	3.9 [341]	4.31 [352]	4.28 [352]
Dielectric permittivity (ε_r)	5 [341]	9 [350]	10 [341]	9 [341]	7.8 [352]	7.5 [352]
Conduction band density (C_B) (cm^{-3})	1×10^{19} [341]	2×10^{18} [350]	1×10^{19} [341]	1×10^{19} [341]	1×10^{19} [352]	1×10^{19} [352]
Valence band density (V_B) (cm^{-3})	1×10^{19} [341]	1.8×10^{19} [350]	1×10^{19} [341]	1×10^{19} [341]	1×10^{19} [352]	1×10^{19} [352]
Electron mobility (μ_e) (cm^2/Vs)	2×10^{-6} [341]	1×10^{2} [341]	15 [341]	20 [341]	350 [352]	125 [352]
Hole mobility (μ_h) (cm^2/Vs)	1×10^{-3} [341]	2.5×10^{2} [341]	0.1 [341]	10 [341]	350 [352]	125 [352]
Doping concentration of acceptor (N_A) (cm^{-3})	0	0	0	0	0	0
Doping concentration of donor (N_D) (cm^{-3})	2.0×10^{11}	1×10^{18}	1×10^{18} [341]	1×10^{18} [341]	5.0×10^{18} [352]	5.0×10^{18} [352]
Defect density (N_t) (cm^{-3})	1.0×10^{14} [341]	1.0×10^{14} [350]	1.0×10^{19} [341]	1.0×10^{14}	1.0×10^{14} [352]	1.0×10^{14} [352]

TABLE 6.5: Photovoltaic parameters of devices using different HTL and ETL combinations.

HTL	ETL	V_{oc} (V)	J_{sc} (mA/cm^2)	FF (%)	Efficiency (%)
PEDOT:PSS	PDINO	0.8041	20.5731	60.48	10.01
PEDOT:PSS	ZnO	0.7831	20.3115	57.57	9.16
PEDOT:PSS	IGZO	0.6716	19.8288	50.58	6.19
PEDOT:PSS	TiO_2:gr(20%)	0.5307	19.4801	46.98	4.69
PEDOT:PSS	TiO_2:gr(10%)	0.5427	19.6168	48.16	5.13
PEDOT:PSS	TiO_2	0.5251	19.6171	47.70	5.00
Graphene	PDINO	0.7913	22.3706	60.5	10.71
Graphene	ZnO	0.79	22.0989	57.97	9.78
Graphene	IGZO	0.6004	21.6095	50.14	6.54
Graphene	TiO_2:gr(20%)	0.5731	21.706	50.55	6.68
Graphene	TiO_2:gr(10%)	0.5286	21.3844	47.57	5.38
Graphene	TiO_2	0.5328	21.8159	48.55	5.63
GO	PDINO	0.719	22.8303	58.76	9.65
GO	ZnO	0.6933	22.3363	55.12	8.54
GO	IGZO	0.5266	21.714	46.88	5.37
GO	TiO_2:gr(20%)	0.4217	21.1044	42.44	3.78
GO	TiO_2:gr(10%)	0.4622	20.4226	44.51	4.20
GO	TiO_2	0.4508	20.2213	43.13	3.94
rGO	PDINO	0.8048	23.1354	65.68	12.26
rGO	ZnO	0.7828	22.9071	62.12	11.13
rGO	IGZO	0.6636	22.559	56.48	8.46
rGO	TiO_2:gr(20%)	0.6731	22.6997	55.77	8.73
rGO	TiO_2:gr(10%)	0.6715	22.6988	55.77	8.73
rGO	TiO_2	0.6731	19.3614	53.37	6.95
p-graphene	PDINO	0.8100	22.0788	58.30	10.95
p-graphene	ZnO	0.8094	21.8153	56.75	10.02
p-graphene	TiO_2:gr(20%)	0.7457	21.7218	53.23	8.62
p-graphene	TiO_2:gr(10%)	0.7457	21.7214	53.23	8.62
p-graphene	TiO_2	0.6508	18.1173	46.98	5.54

and p-type doped graphene-10.95%. The lowest efficiency was observed for the configuration ITO/GO/PBDB-T:NCBDT/TiO_2:gr(20%)/Al, while the the highest efficiency was attained for the configuration ITO/rGO/PBDB-T:NCBDT/PDINO/Al.

From the simulation studies, rGO appears to be the most advantageous option for HTL. According to the literature, rGO's band gap and electrical properties can be finely tuned across a broad spectrum while still preserving its unique characteristics, unlike other graphene forms. The HTL rGO can be tailored to meet the specific requirements of the given task.

The band gap hierarchy for graphene derivatives can be arranged as follows: graphene < p-graphene < rGO < GO. Among all the ETLs studied, PDINO consistently demonstrated the highest efficiency with all HTL combinations.

The configuration ITO/rGO/PBDB-T:NCBDT/PDINO/Al was further optimized with respect to varying work function (from 4.5 to 4.8 eV) and by adjusting the input parameters of the layers. Optimization was conducted by adjusting the thickness of the active layer, HTL and ETL, as well as the defect density of the active layer, HTL, and ETL.

Additionally, parameters like hole mobility of HTL, electron mobility of ETL, acceptor density of HTL, and donor density of ETL, interface defect densities of interface I and interface II, R_s and R_{sh} were optimized. The impact of operating temperature on the device performance was also examined.

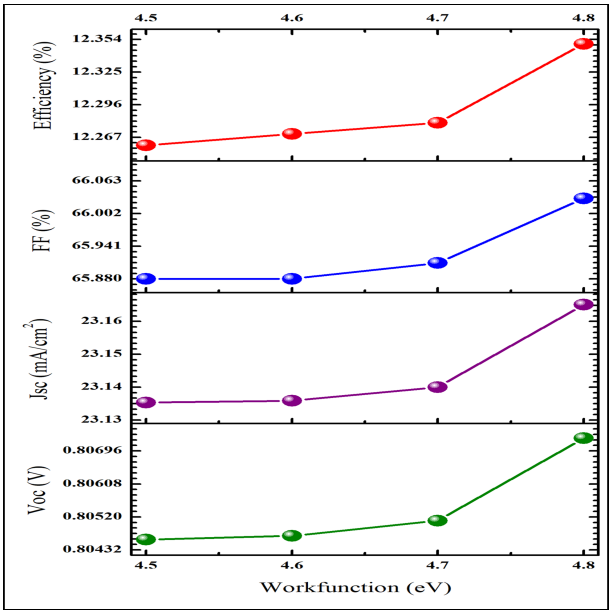


FIGURE 6.7: Effect of varying ITO work function on device performance

6.2.3 Optimization

6.2.3.1 Influence of Varying Work Function of ITO

After the simulation studies were carried out, the configuration with the highest efficiency was identified as ITO/rGO/PBDB-T:NCBDT/PDINO/Al. Furthermore, the work

function of ITO was varied (ranging from 4.5 to 4.8 eV) and studied for ITO/rGO/PBDB-T:NCBDT/PDINO/Al and an increase in all the device output parameters were observed. Fig. 6.7 shows the variation in device output parameters with increasing work function.

As the work function of ITO was increased from 4.5 to 4.8 eV, V_{oc} increased to 0.8073 V, J_{sc} increased to 23.165 mA/cm^2, FF improved to 66.03% and efficiency enhanced to 12.35%. The device performed better when the work function was increased, due to effective charge carrier injection. Better charge transport and fewer recombination losses might be the cause for higher device efficiency.

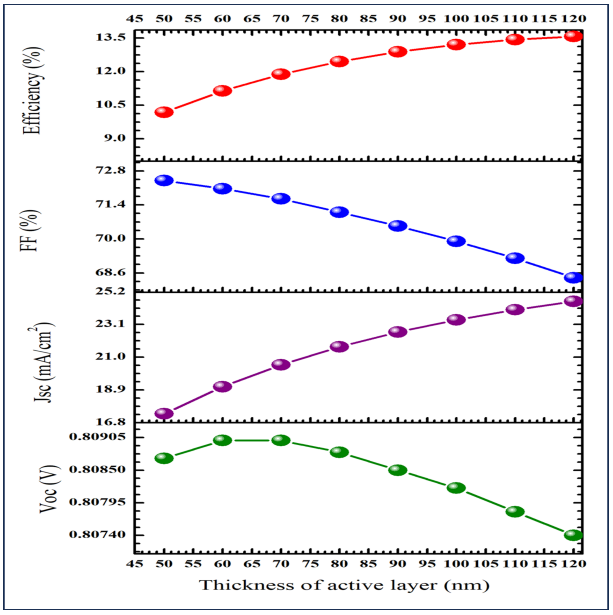


FIGURE 6.8: Effect of active layer thickness on device performance.

6.2.3.2 Influence of Thickness of Active Layer

The influence of varying thickness of the active layer on device output parameters was studied and is given in Fig. 6.8. As the thickness of active layer was increased from 50 to 120 nm, V_{oc} first increased to 0.8090 V at 70 nm, then declined to 0.8074 V, V_{oc} depends on the dark saturation current, which decreased at higher thickness. J_{sc} gradually increased to 24.588753 mA/cm^2, which could be due to effective transport of generated charges to the electrodes. FF decreased to 68.40%, which can be attributed to increased resistance to charge carrier movement. Efficiency increased from 10.18% at 50 nm to 13.58% at 120 nm, making 120 nm the optimum thickness for best efficiency. As the thickness of the active layer increased, the light absorption increased, thus generation of more excitons occured.

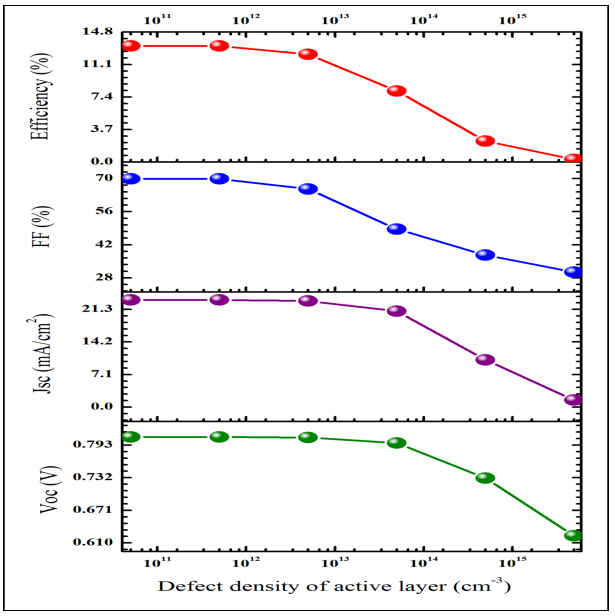


FIGURE 6.9: Effect of active layer defect density on device performance.

6.2.3.3 Influence of Defect Density of Active Layer

Fig. 6.9 exhibits the effect of defect density of active layer on device performance. It is evident from the plot that as the defect density of the active layer was increased from 5×10^{10} to 5×10^{15} cm^{-3}, the device performance deteriorated, reducing all the device output parameters. V_{oc} decreased from 0.8082 to 0.6235 V, J_{sc} declined from 23.387114 to 1.55314 mA/cm^2, FF declined from 69.90% to 30.38% and lowered efficiency from 13.32% to 0.29%. Increasing the defect density has an adverse effect on the device's output parameters. A higher defect density can lead to a higher recombination rate, which in turn affects the overall output performance.

6.2.3.4 Influence of Thickness of HTL

Influence of varying HTL thickness on the device performance is shown in Fig. 6.10. The thickness of HTL was varied from 5 to 20 nm. The V_{oc} increased to 0.8082 V, J_{sc} increased to 23.387114 mA/cm^2, FF increased to 69.90% and efficiency improved to 13.21%. Increasing the thickness of the HTL could improve device performance by enhancing hole transport and reducing recombination losses.

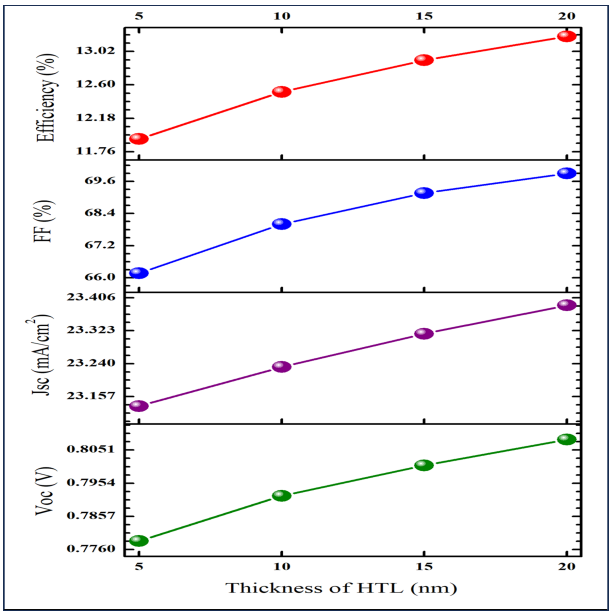


FIGURE 6.10: Effect of HTL thickness on device performance.

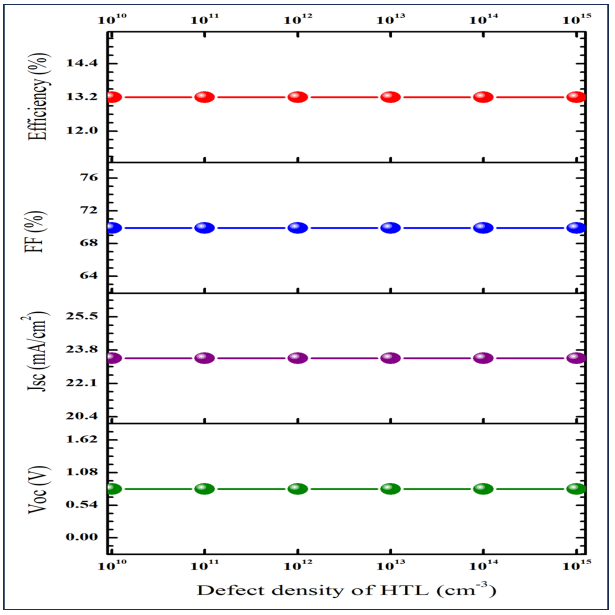


FIGURE 6.11: Effect of HTL defect density on device performance.

6.2.3.5 Influence of Defect Density of HTL

Fig. 6.11 shows the effect of varying defect density of HTL on the device performance. It is observed that as the defect density of HTL was varied from 1×10^{10} to 1×10^{15} cm^{-3}, no significant changes were observed, suggesting that variations in defect density of HTL does not affect the device performance significantly. Properties similar to graphene, such

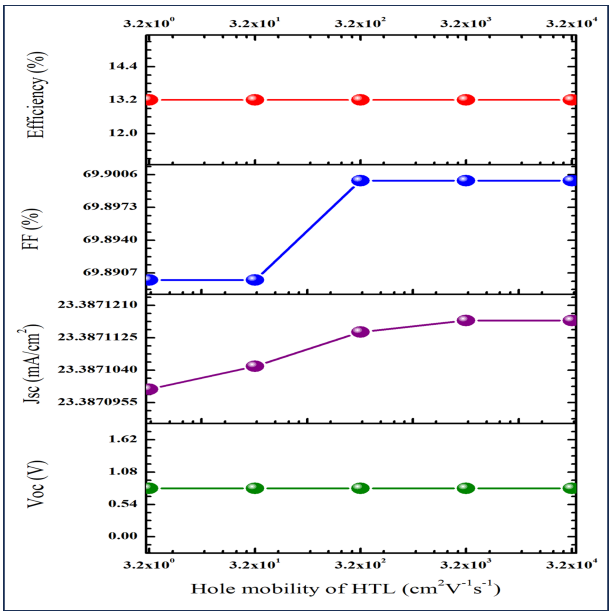


FIGURE 6.12: Effect of HTL hole mobility on device performance.

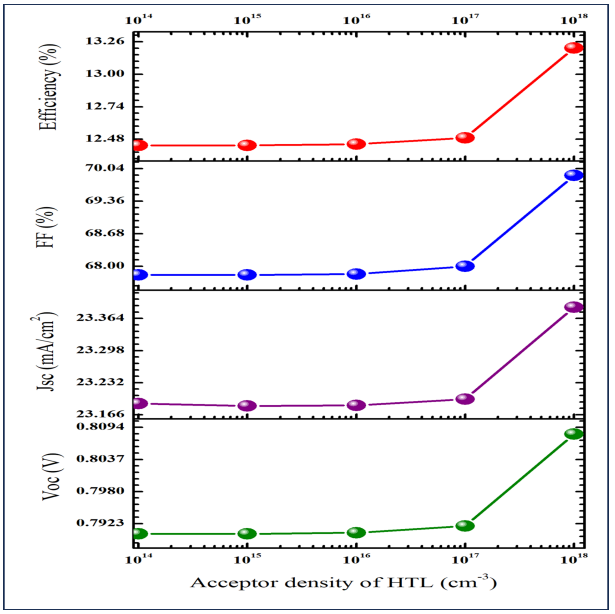


FIGURE 6.13: Effect of HTL acceptor density on device performance.

as high mobility and high electrical conductivity is exhibited by rGO. This high mobility and electrical conductivity might be shadowing the effect of defect density on the output performance of the device.

6.2.3.6 Influence of Hole Mobility of HTL

Fig. 6.12 shows the effect of varying hole mobility of the HTL. The hole mobility was varied from a range of 3.2 to 3.2 $\times$ 10^4 cm^2/Vs. As the mobility was increased, no change was observed in V_{oc}, but J_{sc} increased to 23.387117 mA/cm^2. The FF improved to 69.90% at 3.2 $\times$ 10^2 cm^2/Vs and then remained constant, whereas efficiency remained constant at 13.21%.

6.2.3.7 Influence of Acceptor Density of HTL

Fig. 6.13 plots the impact of raising the acceptor density of HTL. It shows an uplift in device output parameters. As the acceptor density was increased from 1 $\times$ 10^{14} to 1 $\times$ 10^{18} cm^{-3}, V_{oc} increased to 0.8082 V, J_{sc} increased to 23.387114 mA/cm^2, FF increased to 69.90% and efficiency increased to 13.21% making 1 $\times$ 10^{18} cm^{-3} the best value for acceptor density. This could improve the efficiency of hole injection from the organic active layer into the HTL which can be attributed to the improvement in device output parameters.

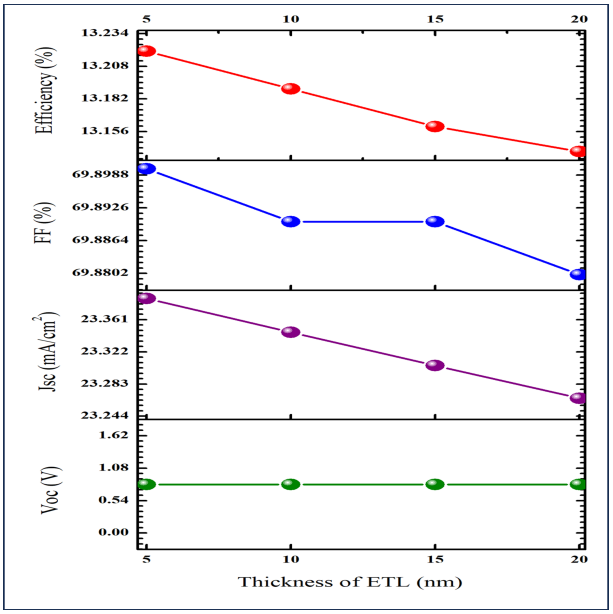


FIGURE 6.14: Effect of ETL thickness on device performance.

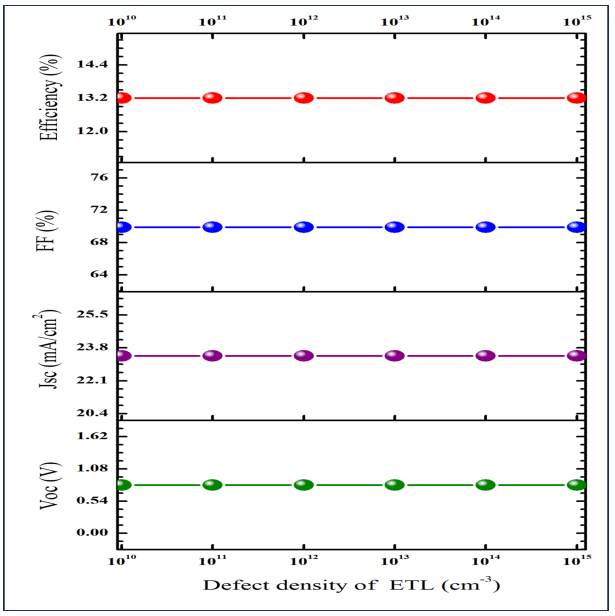


FIGURE 6.15: Effect of ETL defect density on device performance.

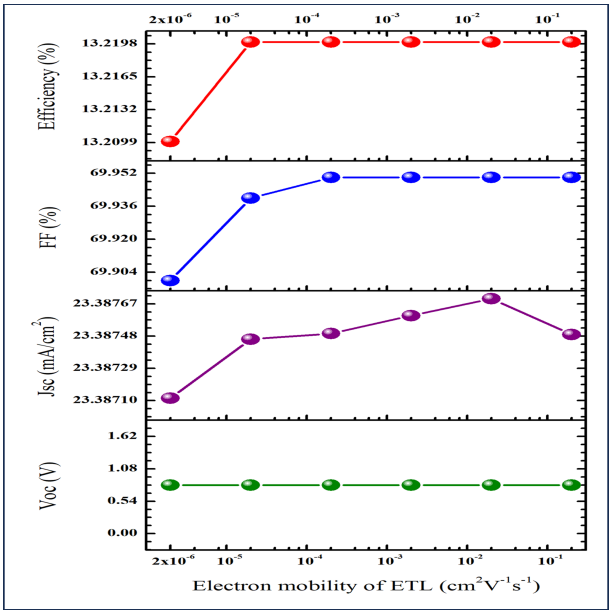


FIGURE 6.16: Effect of ETL electron mobility on device performance.

6.2.3.8 Influence of Thickness of ETL

The influence of varying thickness of ETL is shown in Fig. 6.14. As the thickness was varied from 5 to 20 nm, V_{oc} remained unchanged as 0.758 V, J_{sc} decreased to 23.265777 mA/cm^2, FF reduced to 69.88% and efficiency lowered to 13.14%. A thicker ETL increased the distance over which electrons must travel from the active layer to the electrode. This

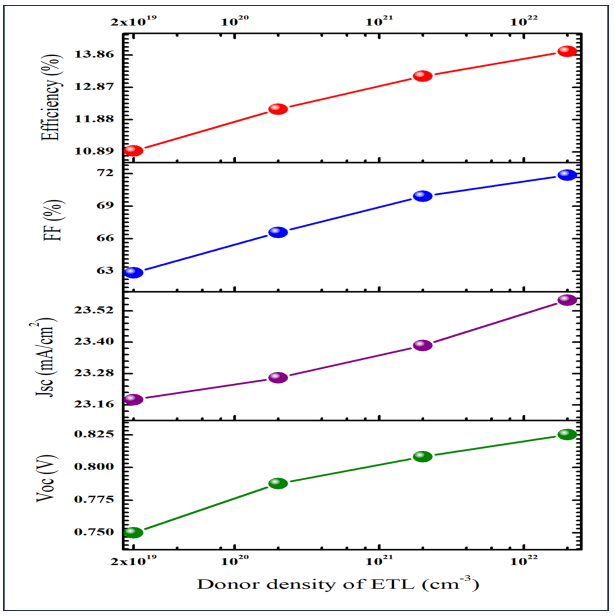


FIGURE 6.17: Effect of ETL donor density on device performance.

extended pathway can result in higher R_s, thus leading to lower current density and reduced device efficiency.

6.2.3.9 Influence of Defect Density of ETL

The influence of defect density of ETL on device output performance is shown in Fig. 6.15. As the defect density of ETL was varied from 1×10^{10} to 1×10^{15} cm^{-3}, no significant changes occurred in the device performance. The defects were not active in terms of charge trapping or recombination.

6.2.3.10 Influence of Electron Mobility of ETL

The influence of electron mobility of ETL is given in Fig. 6.16. As the electron mobility was increased from 2×10^{-6} to 2×10^{-1} cm^2/Vs, V_{oc} remained unchanged, J_{sc} increased to 23.387490 mA/cm^2 at 2×10^{-2} cm^2/Vs and then declined, FF increased to 69.95% at 2×10^{-4} cm^2/Vs and then remained unvaried and efficiency improved to 13.22% at 2×10^{-5} cm^2/Vs and maintained a constant value thereafter. Increased electron mobility facilitates efficient electron transport and collection at the cathode. Reduced carrier transit time decreases recombination losses, thereby improving J_{sc}, FF, and efficiency.

6.2.3.11 Influence of Donor Density of ETL

Fig. 6.17 gives the influence of donor density of ETL on the device performance. Higher electron mobility in ETL improves the electron transport of electrons from the active layer to the electrode, thus improving the device performance to a certain extent. As the donor density was increased from 2×10^{19} to 2×10^{22} cm^{-3}, an improvement in Voc to 0.8252 V, an increase in Jsc to 23.56143 mA/cm^2, an increase in FF to 71.84%, and an improvement in efficiency to 13.97% were attained. Increasing donor concentration might improve ETL conductivity and electron transport. Enhanced charge extraction might reduce carrier accumulation and recombination losses, thereby improving overall device performance.

6.2.4 Influence of Varying Interface Defect Densities, Series Resistance, Shunt Resistance and Operating Temperature

6.2.4.1 Influence of Varying Defect Densities of Interface I and interface II

The influence of varying interface defect densities of interface I (rGO/PBDB-T:NCBDT) and interface II (PBDB-T:NCBDT/PDINO) are shown in Fig. 6.18 and Fig. 6.19 respectively.

As the interface defect I was varied from 1×10^9 to 1×10^{11} cm^{-2}, V_{oc} increased to 0.8905 V, J_{sc} decreased to 23.341190 mA/cm^2, FF reduced to 67.95% and efficiency increased to 14.12%.

As the interface II defect density was varied from 1×10^9 to 1×10^{11} cm^{-2}, the V_{oc} decreased to 0.8076 V, J_{sc} decreased to 23.350383 mA/cm^2, FF declined to 69.81% and efficiency dropped to 13.16%. These results indicate that an increase in defect density of interface I enhances the efficiency and V_{oc} whereas the J_{sc} and FF show a surprising effect on device performance. Increasing the defect density of interface II diminishes the device performance. The increase in defect density of interface II could possibly hinder the movement of electrons thus diminishing the overall device performance. This could be possibly due to formation of a poor interface.

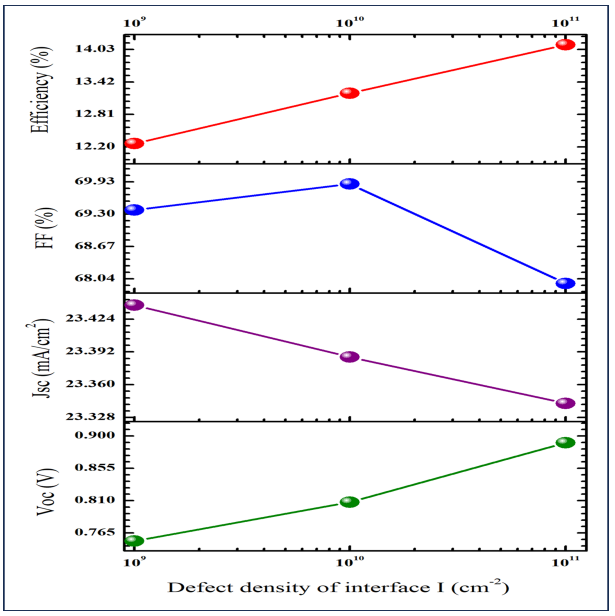


FIGURE 6.18: Effect of interface I defect density on device performance.

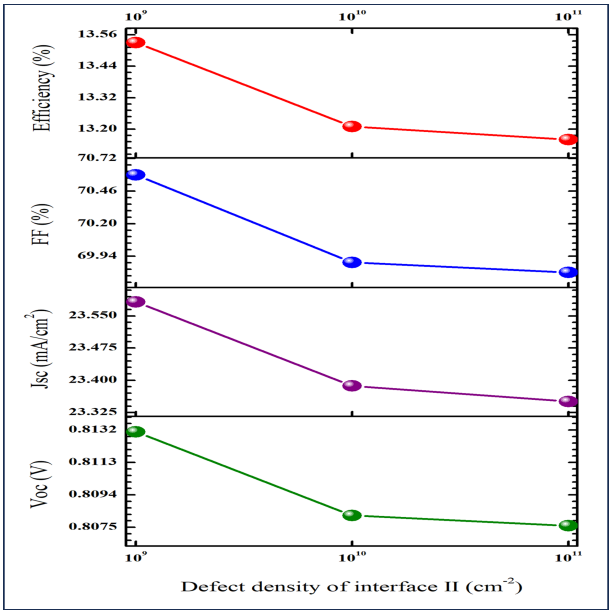


FIGURE 6.19: Effect of interface II defect density on device performance.

6.2.4.2 Influence of Series Resistance and Shunt Resistance

Fig. 6.20 and Fig. 6.21 shows the effect of R_s and R_{sh} on the device performance respectively. The R_s was varied from 1 to 10 ohm, and as shown in graph, V_{oc} remained unaffected, while J_{sc} gradually decreased to 23.188758 mA/cm^2, FF diminished from 67.69%

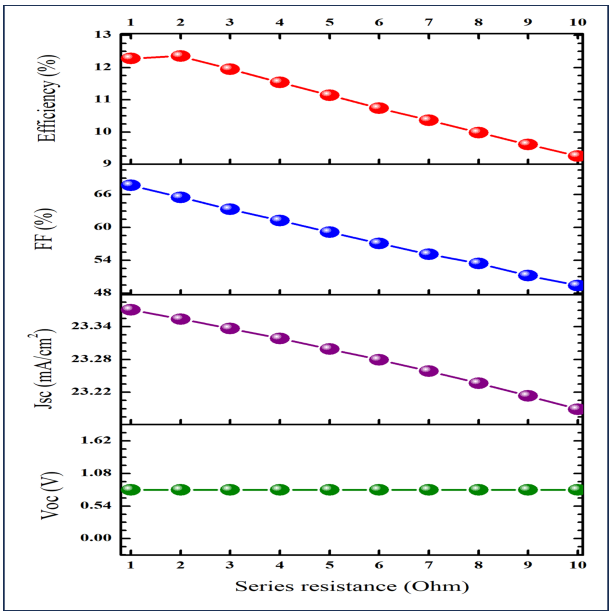


FIGURE 6.20: Effect of series resistance on device performance.

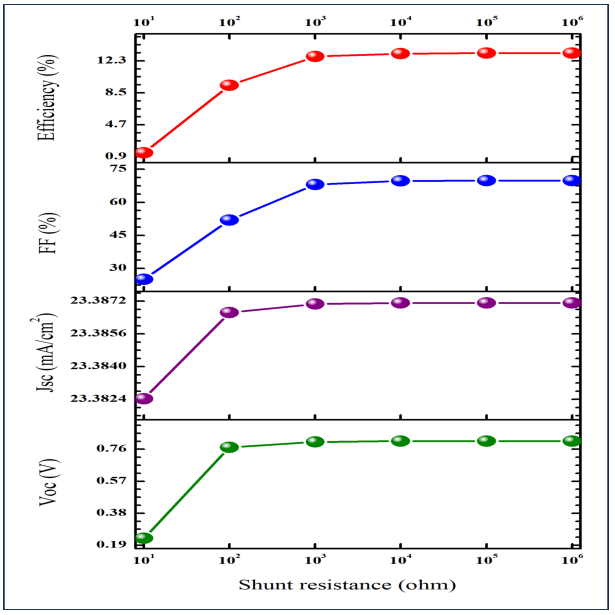


FIGURE 6.21: Effect of shunt resistance on device performance.

to 49.36% and efficiency decreased significantly from 12.28% to 9.25%. An increase in series resistance impedes carrier transport and could lead to power losses within the device. Consequently, FF and efficiency decreased significantly while J_{sc} slightly declined.

Meanwhile as the R_{sh} was increased from 10 to 10^6 Ohm, V_{oc} increased to 0.8082 V, J_{sc} improved to 23.3872 mA/cm^2, FF improved to 69.88% and efficiency improved to 13.21%. Higher shunt resistance minimizes leakage currents and suppresses parasitic

charge pathways. This could have improved overall device performance by ensuring that photogenerated carriers contribute effectively to the external current.

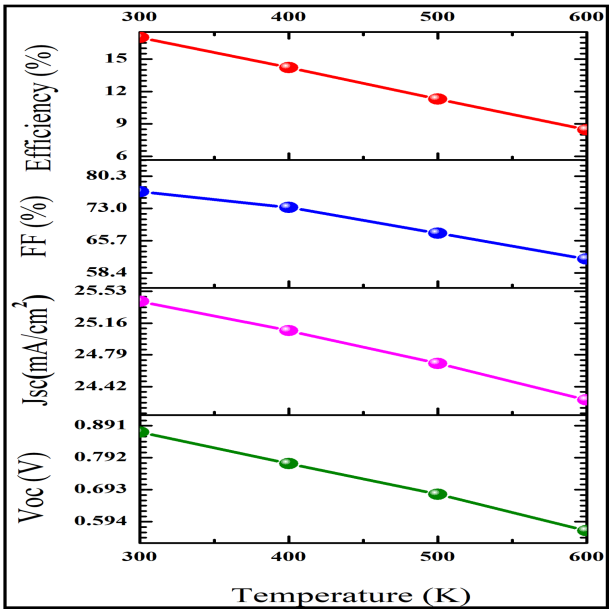


FIGURE 6.22: Effect of operating temperature on device performance.

6.2.4.3 Influence of Operating Temperature

The impact of operating temperature on the device performance was studied by varying the operating temperature from 300 to 600 K and is plotted in Fig. 6.22. As the operating temperature was increased, the device output parameters seemed to decline. The V_{oc} decreased to 0.5665 V, J_{sc} declined to 24.265707 mA/cm^2, FF decreased to 61.55% and efficiency reduced to 8.46%. The performance of SC is adversely affected by rising temperatures, mainly due to decreased V_{oc}, higher recombination losses, decreased efficiency and increased R_s.

Table 6.6 lists the optimized input parameters obtained for the device and The optimized input parameters selected for the final simulation are suitable for real-world applications, as they fall within physically realistic ranges commonly used in experimental studies of SCs. These parameter values are consistent with those reported in the literature for similar devices. Furthermore, the obtained output results are within the expected range for practical BHJOSC applications and show good agreement with previously reported experimental BHJOSC performance. Table 6.7 lists the optimized output parameters.

TABLE 6.6: Optimized device input parameters for ITO/rGO/PBDB-T:NCBDT/ PDINO/Al.

Layers	d (nm)	μ_e (cm^2/Vs)	μ_p (cm^2/Vs)	N_t (cm^{-3})	N_D (cm^{-3})	N_A (cm^{-3})
PBDB-T:NCBDT (Active layer)	100	-	-	1×10^{10}	-	-
rGO (HTL)	20	-	3.2×10^2	1×10^{10}	-	1×10^{18}
PDINO (ETL)	5	2×10^{-4}	-	1×10^{10}	1×10^{22}	-

TABLE 6.7: Optimized device output parameters for ITO/rGO/PBDB-T:NCBDT/PDINO/Al.

V_{oc} (V)	J_{sc} (mA/cm^2)	FF (%)	Efficiency (%)
0.8878	25.407228	77.45	17.47

6.3 Numerical Investigation of PBDB-T:NCBDT based BHJOSC with Double Layered HTLs and Diverse ETLs

A double HTL can create a cascade energy level alignment that facilitates efficient hole extraction from the active layer to the anode. The stepwise energy level matching reduces energy losses and minimizes interfacial barriers. Using a second HTL with appropriate energy band alignment and morphology can act as a blocking layer for electrons, thereby reducing charge recombination at the anode interface.

Double HTLs allow fine tuning of work function alignment between the active layer and the electrodes. Some single layer HTLs (like PEDOT:PSS) are acidic and hygroscopic, which degrades the active layer and electrode over time. A second HTL can protect the device from moisture and chemical degradation, improving operational and shelf life stability.

In this study, we introduce an innovative double-layered HTL based BHJOSC by integrating GO/MoS_2 as supplimentary HTLs alongside PEDOT:PSS. The double layer HTL enhances the performance of the BHJOSCs structured as ITO/PEDOT:PSS/GO or MoS_2/PBDB-T:NCBDT/PDINO/Al. To date, there has been no documented research on a double HTL BHJOSC utilizing the SM-NFA NCBDT.

This additional HTL is positioned between the photoactive layer and PEDOT: PSS, and various configurations has been simulated.

A comprehensive simulation analysis involving multiple ETLs including N,N'-Bis(N,N-dimethylpropan-1-ami ne oxide)perylene-3,4,9,10-te tracarboxylic diimide (PDINO), PFN-Br, indium gallium zinc oxide (IGZO)) and C_{60} has yielded improved efficiency for the proposed configuration. This has been optimized to achieve a notable efficiency.

GO is ideal for BHJOSCs and its promising placement in BHJOSCs has been disussed in Chapter 3. MoS_2 offers superior conductivity, hole mobility and stability, improving charge transport and reducing recombination in OSCs [300, 376]. MoS_2 has a lower band gap (1.3 eV) compared to that of GO (2.48 eV) and exhibit favourable valence band alignment with active layer, facilitating efficient hole extraction and transport. It is chemically stable and less prone to degradation under environmental conditions (e.g., oxygen and moisture) compared to GO, making it more reliable for long-term device performance. It offers reasonably high hole mobility of 150 cm^2/Vs compared to GO (123 cm^2/Vs), enhancing the efficiency of charge transport. Its flexibility and consistent performance makes it a strong candidate for flexible devices.

Both materials offer advantages in terms of availability, cost and light absorption, driving ongoing research to fully explore their potential as HTLs. Fig. 6.23 shows the device structure used for the simulation study and Fig. 6.24 displays the energy band alignment of the layers utilized in the simulation study.

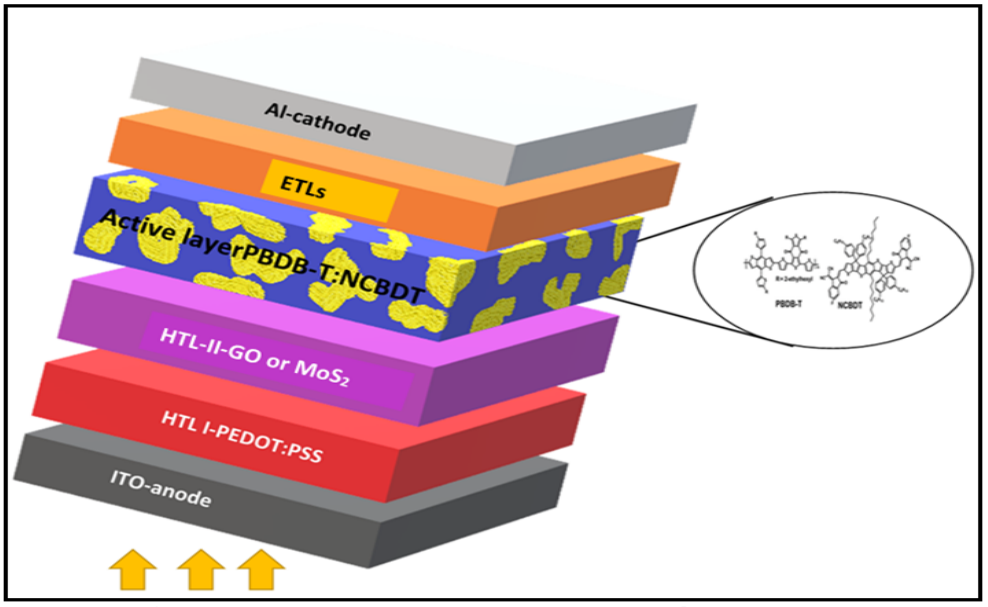


FIGURE 6.23: Device structure used for the simulation study of ITO/HTL-I/HTL-II/PBDB-T:NCBDT/ETL/Al.

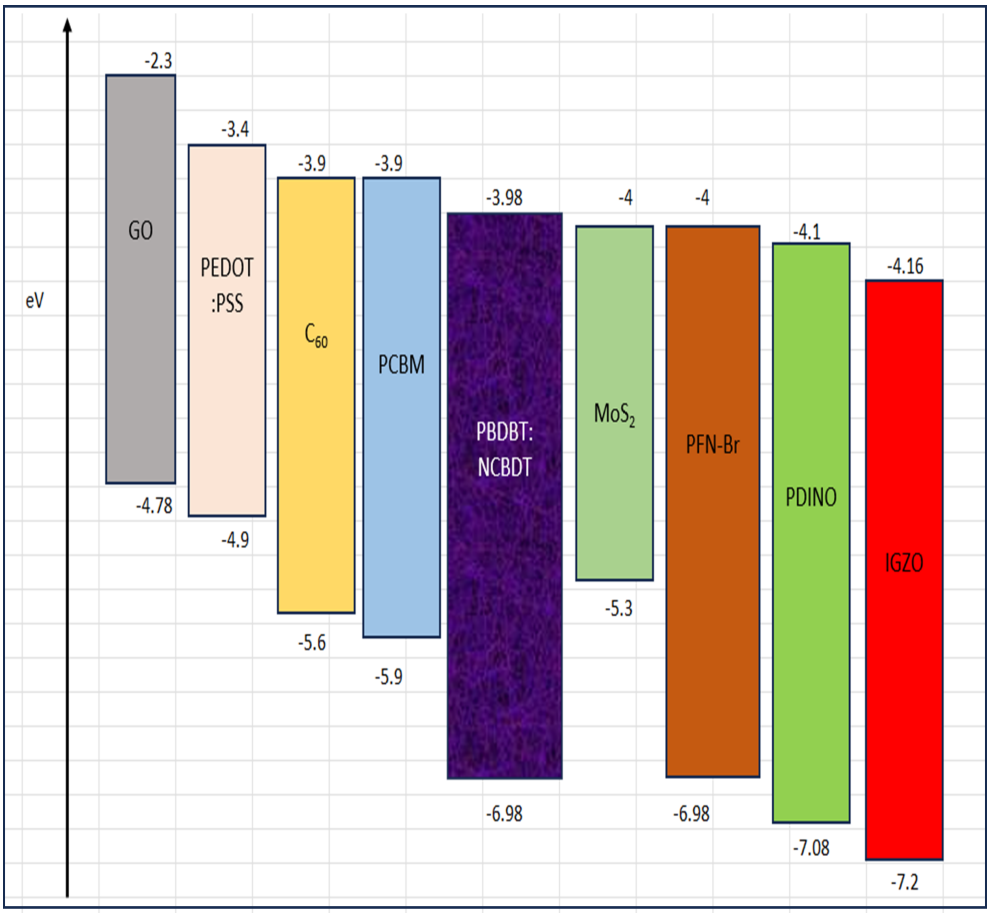


FIGURE 6.24: Energy band diagram of the layers used in the simulation study of ITO/HTL-I/HTL-II/PBDB-T:NCBDT/ETL/Al.

Table 6.8 lists the input parameters of active layer and HTLs used for the simulation study. Tables 6.9 lists the input parameters of ETLs used for the simulation study.

TABLE 6.8: Input parameters for PEDOT:PSS, MoS_2, GO, and PBDB-T:NCBDT for the simulation study.

Parameter	PEDOT:PSS	MoS_2	GO	PBDB-T:NCBDT
Thickness (d) (nm)	30 [341]	30 [377]	35 [336]	100 [344]
Band gap (E_g) (eV)	1.5 [341]	1.3 [377]	2.48 [343]	1.38 [344]
Electron affinity (χ) (eV)	3.4 [341]	4 [377]	2.3 [343]	3.91 [344]
Dielectric permittivity (ε_r)	3[341]	4 [377]	10 [343]	3.65 [344]
Conduction band density (C_B) (cm^{-3})	1×10^{22} [341]	0.75×10^{18} [377]	1.8×10^{18} [343]	1×10^{19} [344]
Valence band density (V_B) (cm^{-3})	1×10^{22} [341]	0.18×10^{19} [377]	2.2×10^{18} [343]	1×10^{19} [344]
Electron mobility (μ_e) (cm^2/Vs)	4.5×10^{-3} [341]	100 [377]	26 [343]	8.8×10^{-5} [368]
Hole mobility (μ_h) (cm^2/Vs)	9.9×10^{-5} [341]	150 [377]	123 [343]	9.2×10^{-5} [368]
Shallow donor density (N_D) (cm^{-3})	0 [341]	0	0 [343]	0 [344]
Shallow acceptor density (N_A) (cm^{-3})	1×10^{21} [341]	1×10^{15} [377]	1×10^{18} [343]	0
Defect density (N_t) (cm^{-3})	1×10^{9} [341]	1×10^{10} [377]	1.9×10^{9} [343]	5×10^{10} [344]

The device output parameters obtained after the simulation study of the device structure ITO/HTL-I/HTL-II/PBDB-T:NCBDT/ETL/Al are given in the Table 6.10.

TABLE 6.9: Input parameters of ETLs used for the simulation study.

Parameter	PDINO	PFN-Br	IGZO	PCBM	C_{60}
Thickness (d) (nm)	5 [341]	5 [378]	5[341]	5 [341]	5 [341]
Band gap (E_g) (eV)	2.98 [341]	2.98 [378]	3.05 [341]	2 [341]	1.7 [341]
Electron affinity (χ) (eV)	4.1 [341]	4 [378]	4.16 [341]	3.9 [341]	3.9 [341]
Dielectric permittivity (ε_r)	5 [341]	5 [378]	10 [341]	3.9 [341]	4.2 [341]
Conduction band density (C_B) (cm^{-3})	1×10^{19} [341]	1×10^{19} [378]	1×10^{19} [341]	1×10^{19} [341]	1×10^{19} [341]
Valence band density (V_B) (cm^{-3})	1×10^{19} [341]	1×10^{19} [378]	1×10^{19} [341]	1×10^{19} [341]	1×10^{19} [341]
Electron mobility (μ_e) (cm^2/Vs)	2×10^{-6} [341]	2×10^{-6} [378]	15 [341]	0.02 [341]	8×10^{-2} [341]
Hole mobility (μ_h)(cm^2/Vs)	1×10^{-3} [341]	1×10^{-4} [378]	0.1 [341]	0.02 [341]	3.5×10^{-3} [341]
Shallow acceptor density (N_A) (cm^{-3})	0 [341]	0 [378]	0 [341]	0 [341]	0 [341]
Shallow donor density (N_D) (cm^{-3})	2×10^{21} [341]	9×10^{18} [378]	1×10^{18} [341]	1×10^{10} [341]	1×10^{15} [341]
Defect density (N_t) (cm^{-3})	1×10^{14} [341]	1×10^{9} [378]	1×10^{19} [341]	1×10^{9} [341]	1×10^{9} [341]

TABLE 6.10: Output parameters of device configurations with double HTLs after the simulation study of ITO/HTL-I/HTL-II/PBDB-T:NCBDT/ETL/Al

HTL-I	HTL-II	ETL	V_{oc} (V)	J_{sc} (mA/cm^2)	FF (%)	Efficiency (%)
PEDOT:PSS	MoS_2	PDINO	1.5544	21.109005	41.21	13.52
PEDOT:PSS	MoS_2	PFN-Br	1.1898	20.687564	48.22	11.87
PEDOT:PSS	MoS_2	IGZO	1.0638	20.636257	46.98	10.31
PEDOT:PSS	MoS_2	PCBM	1.3065	20.537569	39.57	10.62
PEDOT:PSS	MoS_2	C60	1.1510	20.546545	44.65	10.56
PEDOT:PSS	GO	PDINO	1.1214	21.949934	53.34	13.13
PEDOT:PSS	GO	PFN-Br	0.9463	21.632381	55.60	11.38
PEDOT:PSS	GO	IGZO	0.8984	21.754957	52.28	10.22
PEDOT:PSS	GO	PCBM	1.1497	21.639909	45.53	11.30
PEDOT:PSS	GO	C_{60}	0.9410	21.644457	51.95	10.58

ITO/PEDOT:PSS/MoS_2/PBDB-T:NCBDT/PDINO/Al exhibited best performance with V_{oc} of 1.5544 V, J_{sc} of 21.109005 mA/cm^2, FF of 41.21%, and efficiency of 13.52%.

6.3.1 Optimization

6.3.1.1 Influence of Varying Input Parameters of PBDB-T:NCBDT (Active Layer)

The influence of varying thickness and defect density of the active layer on the device output parameters V_{oc}, J_{sc}, FF and efficiency are displayed as contour plots as shown in Figs. 6.25 to 6.28. The x-axis represents the active layer thickness, while the y-axis represents the active layer defect density. The figures illustrate the simultaneous influence of varying both thickness and defect density on the device output parameters. The thickness was varied from 50 to 150 nm and defect density was varied from 5×10^{11} to 5×10^{13} cm^{-3}. A maximum efficiency of 13.56% was attained.

The influence of varying electron mobility and hole mobility of the active layer on the device output parameters V_{oc}, J_{sc}, FF and efficiency are displayed as contour plots

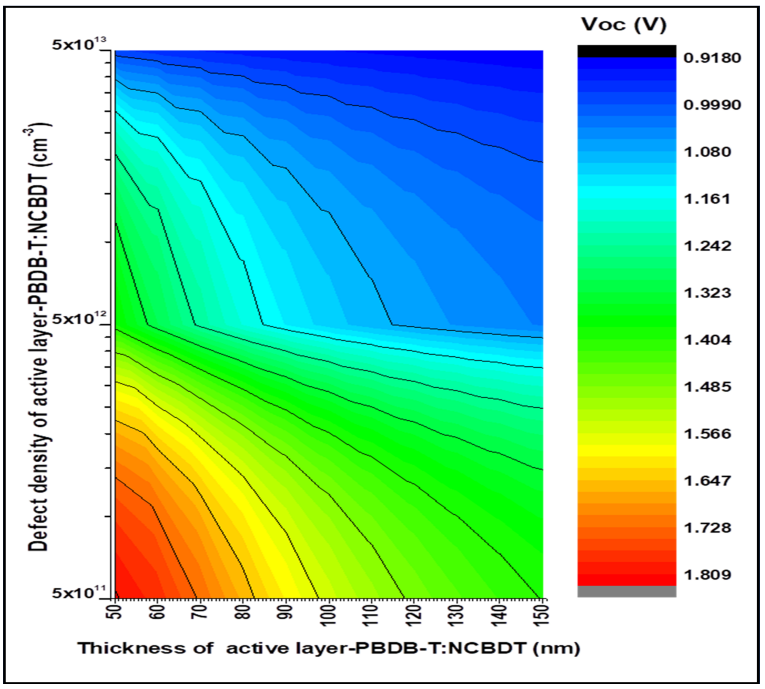


FIGURE 6.25: Effect of thickness and defect density of active layer on V_{oc}.

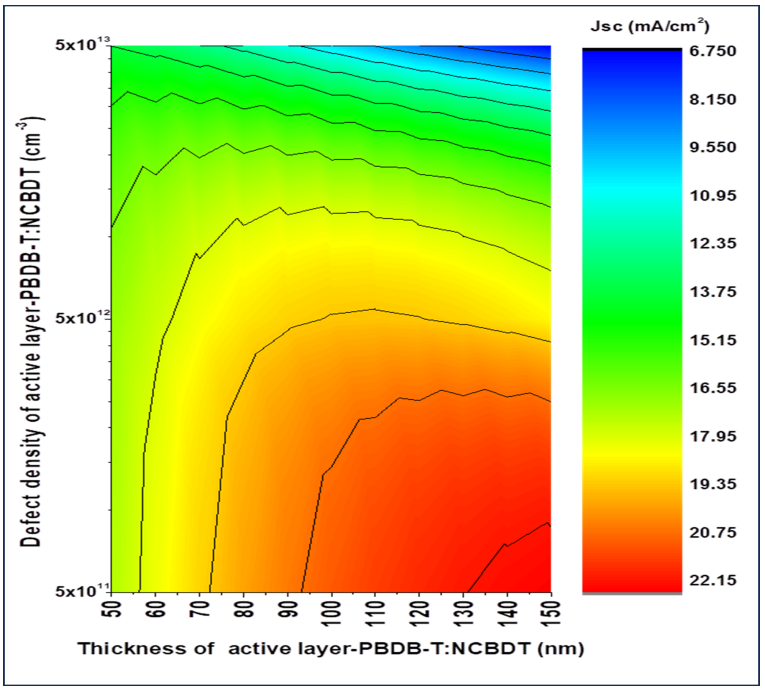


FIGURE 6.26: Effect of thickness and defect density of active layer on J_{sc}.

as shown in Figs. 6.29 to 6.32. The x-axis represents the active layer electron mobility, while the y-axis represents the active layer hole mobility. The figures illustrate the simultaneous influence of varying both electron mobility and hole mobility on the device output

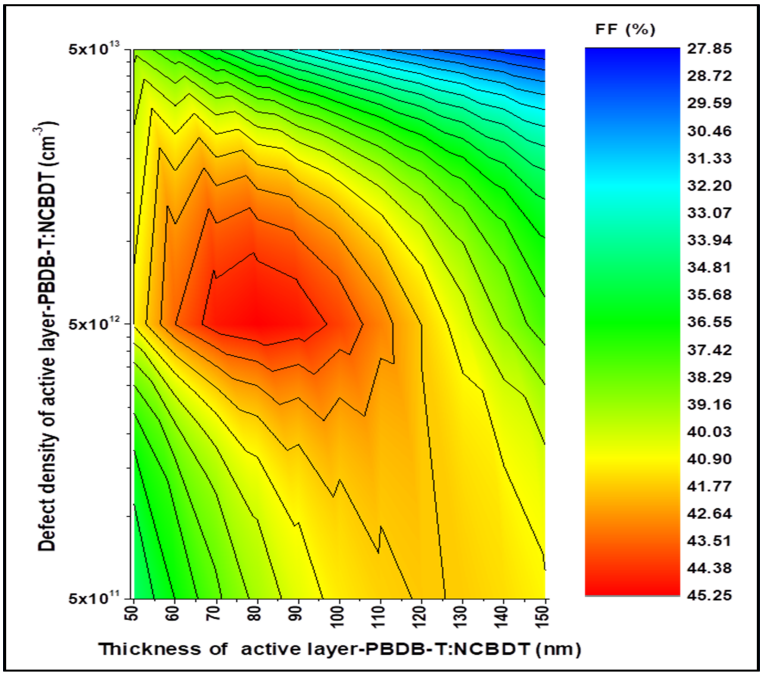


FIGURE 6.27: Effect of thickness and defect density of active layer on FF.

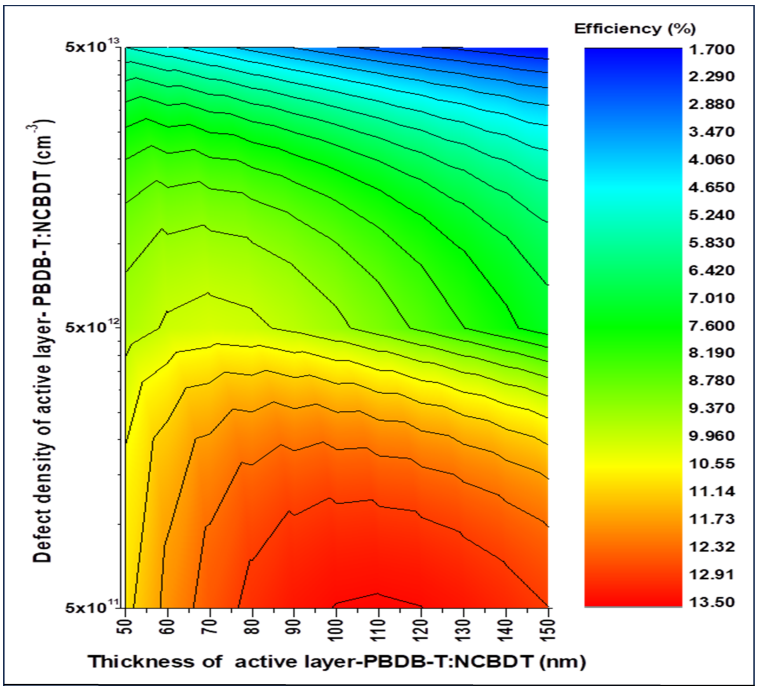


FIGURE 6.28: Effect of thickness and defect density of active layer on efficiency.

parameters. The electron mobility was varied from 8.8×10^{-1} to 8.8×10^{-5} cm^2/Vs. The hole mobility was varied from 9.2×10^{-1} to 9.2×10^{-5} cm^2/Vs. A maximum efficiency of 17.88% was attained.

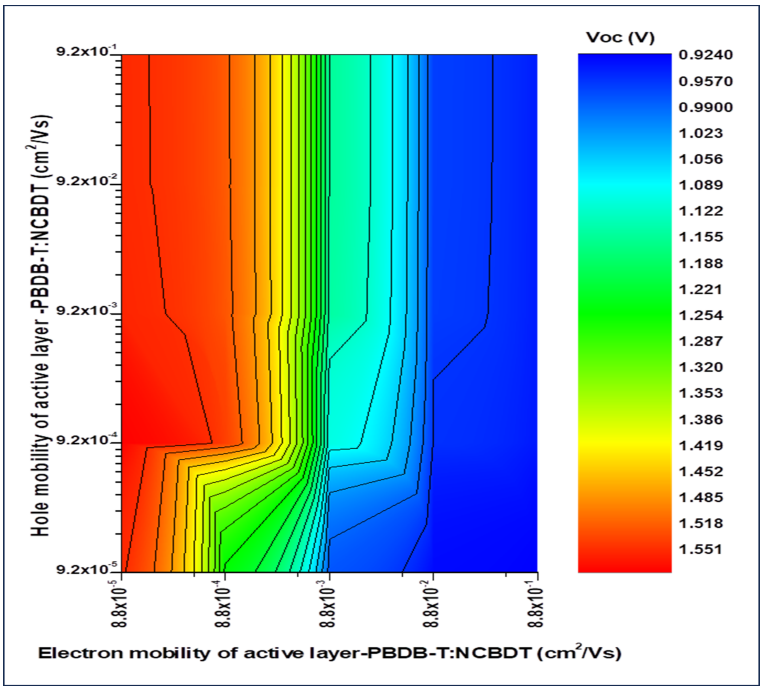


FIGURE 6.29: Effect of electron mobility and hole mobility of active layer on V_{oc}.

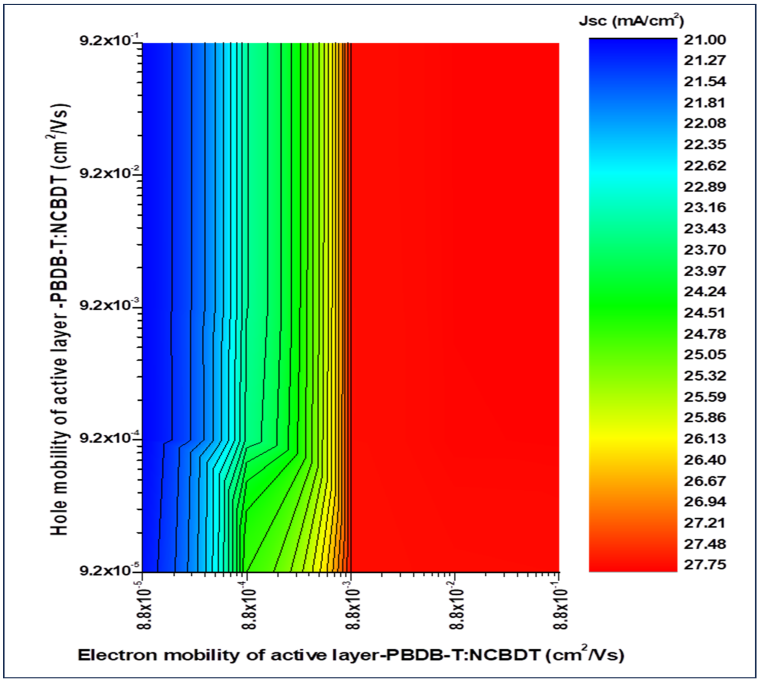


FIGURE 6.30: Effect of electron mobility and hole mobility of active layer on J_{sc}.

These contour maps demonstrate the importance of balanced charge transport. The contour plots show that V_{oc} was relatively high when electron and hole mobilities are balanced. As μ_e and μ_h increase, carriers are extracted faster, causing J_{sc} to rise. The FF

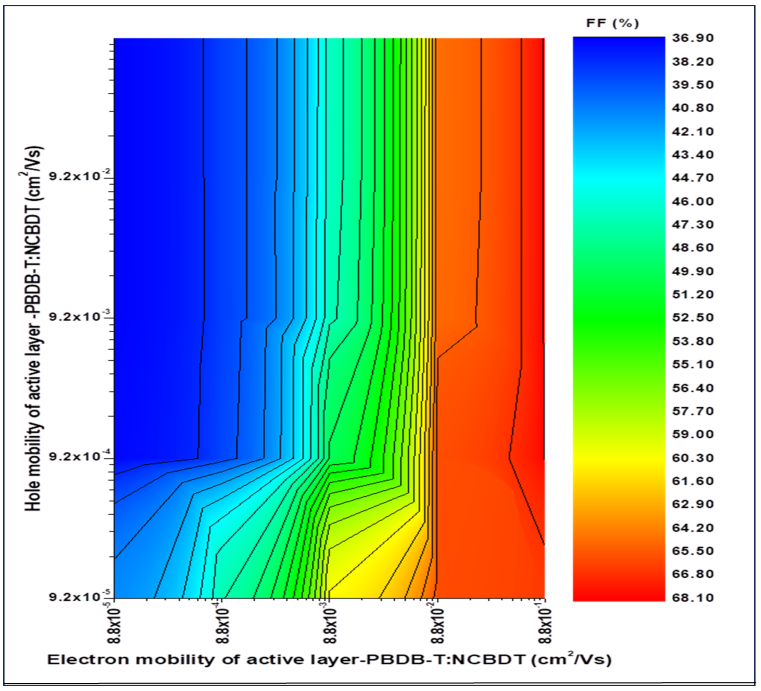


FIGURE 6.31: Effect of electron mobility and hole mobility of active layer on FF.

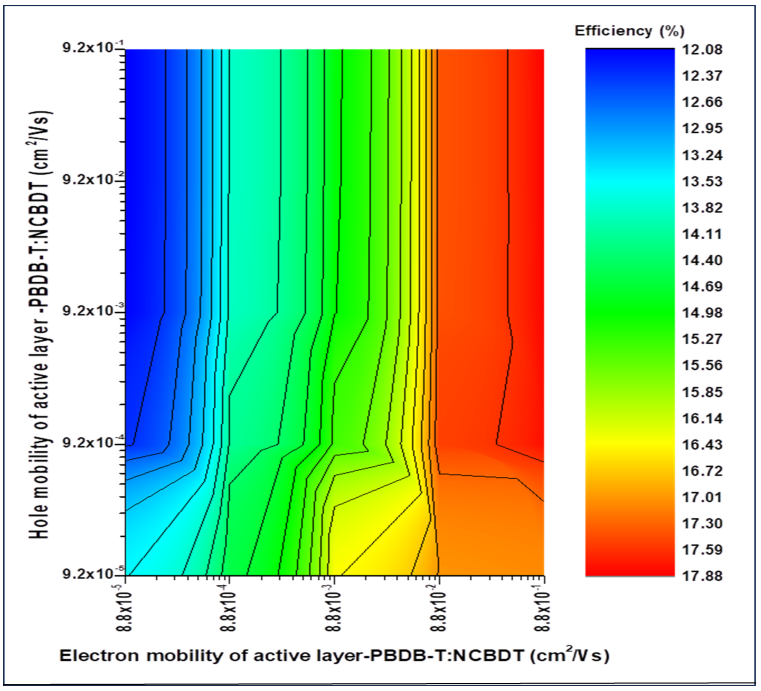


FIGURE 6.32: Effect of electron mobility and hole mobility of active layer on efficiency.

contour shows a strong dependence on mobility balance. This is why the contour exhibits maximum FF near the region where $\mu_e \approx \mu_h$. Efficiency reaches its maximum (17.88%) when electron and hole mobilities are balanced. The device performance is enhanced when,

electron and hole mobilities in the active layer are balanced. This balance ensures efficient charge extraction, minimizes recombination, maintains a stable internal electric field, and enhances overall device performance.

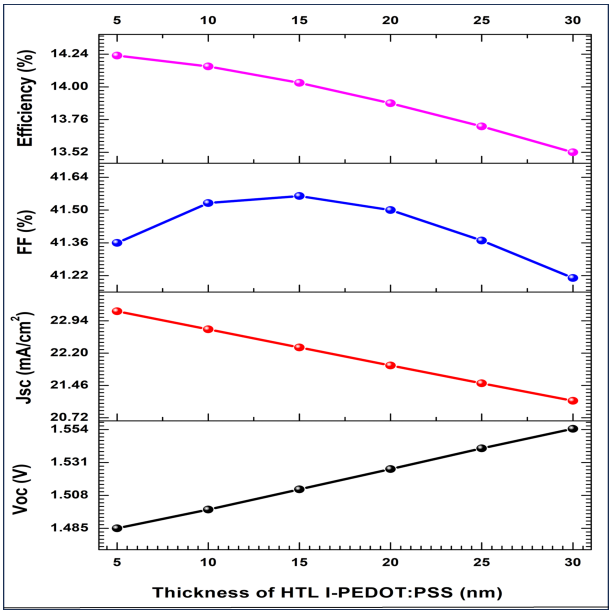


FIGURE 6.33: Influence of varying thickness of HTL-I (PEDOT:PSS) on the device output parameters.

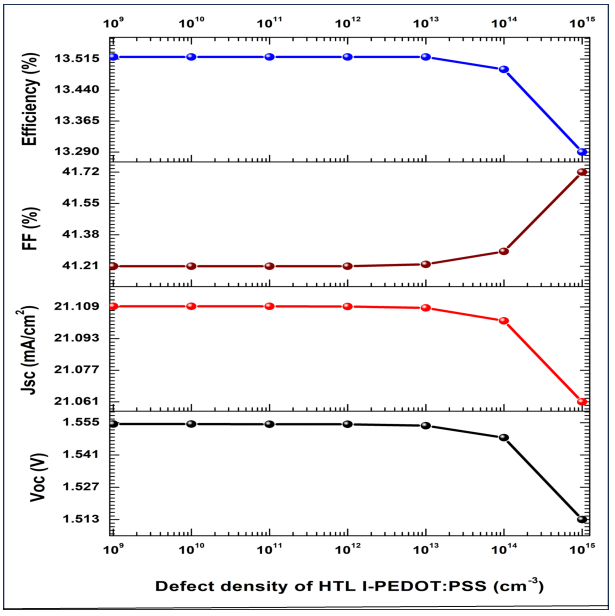


FIGURE 6.34: Influence of varying defect density of HTL-I (PEDOT:PSS) on the device output parameters.

The influence of varying thickness of HTL-I on the device performance is shown in Fig. 6.33. As the thickness was increased from 5 to 30 nm V_{oc} increased from 1.4849 to 1.5544

V, J_{sc} decreased from 23.160377 to 21.109005 mA/cm^2, FF first increased to 41.56% at 15 nm, then decreased to 41.21% and efficiency decreased from 14.23% to 13.52%.

The influence of varying defect density of HTL-I on device performance is depicted in Fig. 6.34. As the defect density was increased from 1 × 10^9 to 1 × 10^{15} cm^{-3}, V_{oc} decreased from 1.5544 to 1.5130 V at 1 × 10^{15} cm^{-3}, J_{sc} decreased from 21.109004 to 21.060695 mA/cm^2 at 1 × 10^{15} cm^{-3}, FF increased from 41.21% to 41.72% at 1 × 10^{15} cm^{-3} and efficiency initially remained constant at 13.52% and then decreased to 13.29% at 1 × 10^{15} cm^{-3}.

Increasing defect density in the PEDOT:PSS layer of NFA based BHJOSCs can have multiple negative effects on device performance [379, 380]. These include reduced hole transport, increased charge recombination, poor interface quality between layers, and potential morphological issues within the active layer [379, 380].

As a result, the overall efficiency and stability of the SCs decline. Optimizing the PEDOT:PSS layer, including reducing its defect density, is essential for improving the performance of the NFA based BHJOSCs.

6.3.1.2 Influence of Varying Input Parameters of MoS_2 (HTL-II)

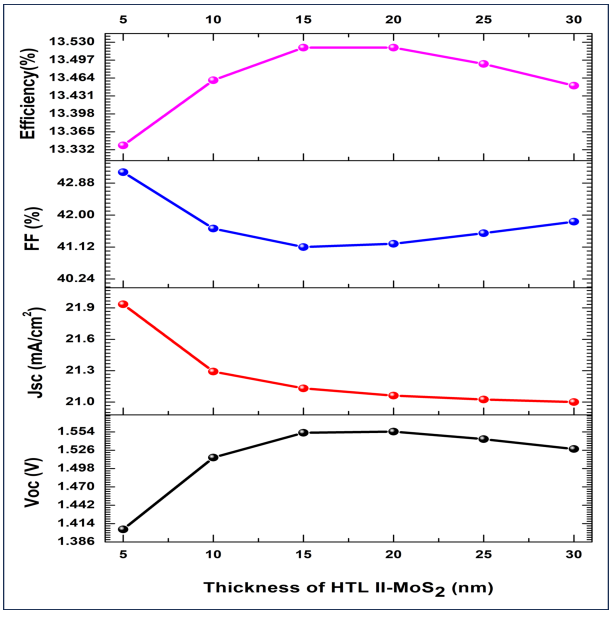


FIGURE 6.35: Influence of varying thickness of HTL-II (MoS_2) on the device output parameters

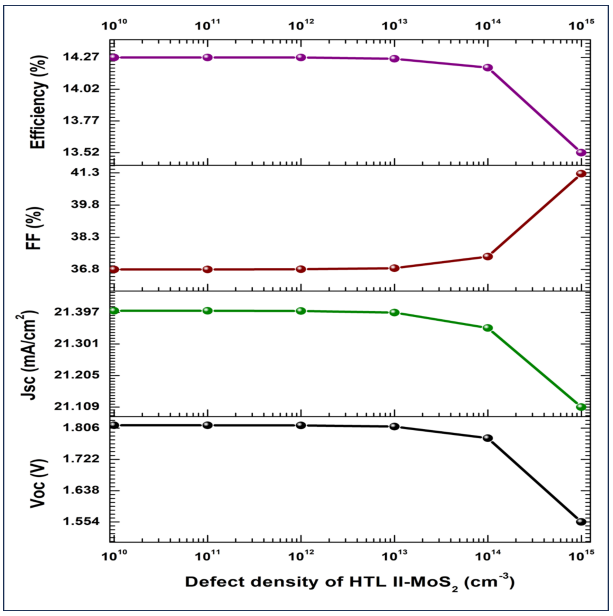


FIGURE 6.36: Influence of varying defect density of HTL-II (MoS_2) on the device output parameters.

The influence of varying thickness of HTL-II on the device performance is depicted in Fig. 6.35. As the thickness of HTL-II was varied from 5 to 30 nm the V_{oc} increased from 1.4052 to 1.5279 V at 15 nm, then decreased. J_{sc} decreased from 21.981578 to 21.046976 mA/cm^2, FF decreased from 43.18% to 41.82% and efficiency increased from 13.34% to 13.53% at 15 nm and then decreased.

The influence of varying defect density of HTL-II on the device performance is shown in Fig. 6.36. As the defect density increased from 1×10^9 to 1×10^{15} cm^{-3}, the V_{oc} decreased from 1.8141 to 1.5544 V, J_{sc} decreased from 21.402129 to 21.109006 mA/cm^2, FF increased from 36.75% to 41.21% and efficiency decreased from 14.2% to 13.52%.

6.3.1.3 Influence of Varying Input Parameters of PDINO (ETL)

The influence of varying thickness of ETL-PDINO on the device output parameters is shown in Fig. 6.37. As the thickness was varied from 5 to 30 nm V_{oc} increased to 1.5654 V. J_{sc} increased to 21.3292378 mA/cm^2. FF surprisingly decreased to 41.09% and efficiency improved to 13.72%.

The influence of varying defect density of ETL is shown in Fig. 6.38. As the defect density of PDINO was increased from 1×10^9 to 1×10^{20} cm^{-3}, the V_{oc} declined to 1.5513

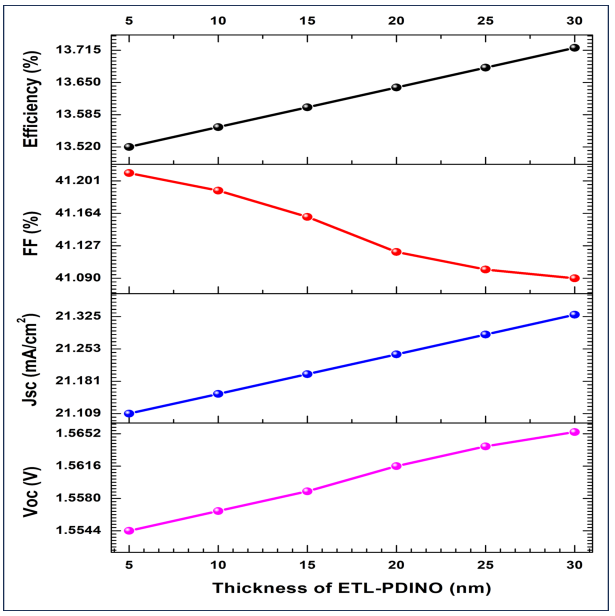


FIGURE 6.37: Influence of varying thickness of ETL (PDINO) on the device output parameters.

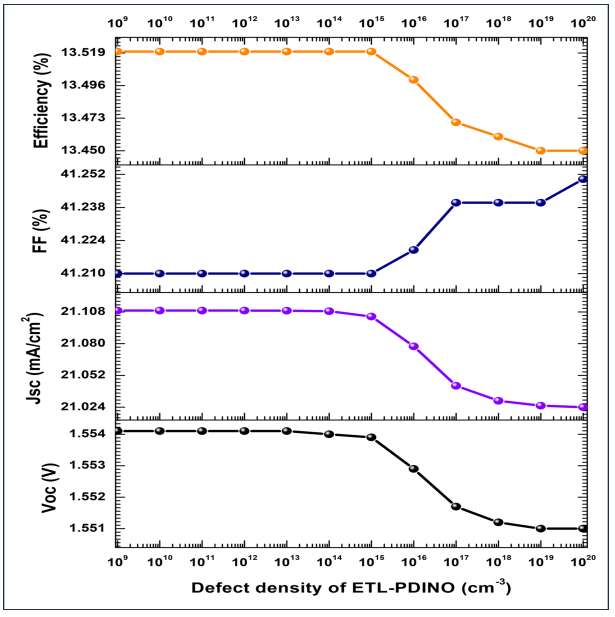


FIGURE 6.38: Influence of varying defect density of ETL (PDINO) on the device output parameters.

V, J_{sc} reduced to 21.023858 mA/cm^2, FF unexpectedly increased to 41.25% and efficiency decreased to 13.45%.

After extended simulation study the optimized thickness, defect density of active layer, HTL-I (PEDOT:PSS), HTL-II (MoS_2) and ETL (PDINO) is found. Best electron mobility

and hole mobility of the active layer (PBDB-T:NCBDT) is also found. Table 6.11 lists the optimized input parameters of the device studied. The optimized input parameters selected for the final simulation are suitable for real-world applications, as they fall within physically realistic ranges commonly used in experimental studies of SCs. These parameter values are consistent with those reported in the literature for similar devices. Furthermore, the obtained output results are within the expected range for practical BHJOSC applications and show good agreement with previously reported experimental BHJOSC performance.

TABLE 6.11: Optimized input parameters of the simulated device structure.

Parameters	PEDOT:PSS	MoS_2	PBDB-T:NCBDT	PDINO
Thickness (d) (nm)	5	20	110	30
Defect density (N_t) (cm^{-3})	1×10^{9}	1×10^{10}	5×10^{11}	1×10^{9}
Electron mobility (μ_e) (cm^2/Vs)	-	-	8.8×10^{-1}	-
Hole mobility (μ_h) (cm^2/Vs)	-	-	9.2×10^{-1}	-

From the results it is evident that the efficiency of the device has been improved. In the experimental study, the efficiency was about 10.04% which has been improved to 19.49% (an increase of 9.46%) by the incorporation of an additional HTL between the PEDOT:PSS HTL and active layer. MoS_2 surpasses GO as an HTL because of its better band alignment, stability, charge selectivity, and tunability, which makes it particularly advantageous in SCs where efficient hole transport and minimal losses are critical. However, the choice can depend on the specific device architecture and fabrication conditions. Table 6.12 lists the optimized output parameters of device.

TABLE 6.12: Optimized output parameters of the simulated device structure.

Parameters	V_{oc} (V)	J_{sc} (mA/cm^2)	FF (%)	Efficiency (%)
	1.3942	25.929526	53.92	19.49

6.4 Comparison of PBDB-T:NCBDT based BHJOSCs

Table 6.13 provides a comparison of previous works done on PBDB-T:NCBDT with our study. Our research is distinguished by its innovative approach, featuring a double HTL configuration with MoS_2 as the intermediate layer. From the comparison, it is evident that the newly designed and simulated double HTL structure of PBDB-T:NCBDT BHJOSC shows highly promising results and can be further investigated in the future.

TABLE 6.13: Comparison of previous works done on PBDB-T:NCBDT BHJOSCs with our study.

Parameters	Voc (V)	Jsc (mA/cm^2)	FF (%)	Efficiency (%)
(Experimental) [368]	0.872	12.91	61.3	6.91
(Experimental) [368]	0.873	8.39	44.47	3.28
(Experimental) [368]	0.824	19.45	62.9	10.04
(Experimental) [368]	0.847	18.64	64.6	10.19
(Experimental) [369]	0.8398	20.33	71.0	12.12
(Experimental) [370]	0.885	20.81	70.9	13.1
(Experimental) [370]	0.851	22.35	74.3	14.1
(Simulation) [381]	1.08	27.92	72.57	21.84
(Simulation) [382]	0.8878	25.407	77.45	17.47
(Simulation-This work)	1.3942	25.929526	53.92	19.49

6.5 Conclusion

We simulated PBDB-T:NCBDT BHJOSCs using various graphene derivatives (graphene, GO, rGO, p-graphene) as HTLs and different ETLs (PDINO, ZnO, IGZO, TiO_2, TiO_2:gr(20%), and TiO_2:gr (10%). The optimal ITO work function was 4.8 eV, achieving a 12.35% efficiency with rGO as the HTL, outperforming the typical 10.02%. After optimizing device parameters, an extensive analysis of different parameters, including thickness, defect density, mobilities, acceptor and donor densities, R_s and R_{sh} were done. We attained a V_{oc} of 0.8878 V, J_{sc} of 25.407228 mA/cm^2, FF of 77.45%, and an efficiency of 17.47%, while carefully considering all experimental conditions. Among graphene derivatives, rGO showed the best performance due to its tunable band gap and high dielectric permittivity. These findings suggest rGO as a promising HTL for PBDB-T:NCBDT BHJOSCs, though experimental validation is needed.

Simulation study of double HTL ITO/HTL-I/HTL-II/PBDB-T:NCBDT/ETL/Al, a double-decked HTL-based BHJOSC was carried out. MoS_2 was incorporated as an additional HTL due to its lower band gap and better band alignment with the active layer, as well as superior electron and hole mobility compared to GO. By adding MoS_2 between PEDOT:PSS and the active layer (ITO/PEDOT:PSS/MoS_2/PBDB-T:NCBDT/PDINO/Al), the device efficiency improved significantly, achieving a V_{oc} of 1.3942 V, J_{sc} of 25.929526 mA/cm^2, FF of 53.92%, and efficiency of 19.49%. This enhancement not only boosts the overall efficiency but also mitigates degradation caused by direct contact between PEDOT:PSS and the active layer.

Chapter 7

Numerical Investigation of PBDB-T:INTIC BHJOSC with Diverse Graphene Derivative HTLs and ETLs

This chapter explores the numerical simulation study of PBDB-T:INTIC BHJOSCs with the incorporation of diverse materials as interfacial layers. INTIC is an SM-NFA with its absorption range in the NIR region. First, we designed and simulated a simple yet unique device configuration ITO/PEDOT:PSS:rGO/PBDB-T:INTIC/n-graphene/Al and later, an extensive numerical simulation study of ITO/HTL/PBDB-T:INTIC/ETL/Al with graphene derivatives in both HTLs and ETLs, along with other diverse ETLs is carried out.

In this chapter, a numerical investigation of PBDB-T:INTIC BHJOSCs with graphene derivatives in the HTL and ETL is carried out. The NIR absorbing SM-NFA INTIC used for this study features a lower band gap than the widely used ITIC. Further, ITIC is a symmetric NFA, whereas INTIC is an asymmetric NFA, which makes it much simpler to synthesize, compared to ITIC [145, 383, 384, 382, 385].

Designing and simulation of ITO/PEDOT:PSS:rGO/PBDB-T:INTIC/n-graphene/Al is done in the initial study. Later, designing and simulation of ITO/HTL/PBDB-T:INTIC/ETL/Al is conducted in which graphene derivatives are used as both HTLs and ETLs, along with other diverse ETL materials.

7.1 PBDB-T:INTIC BHJOSC

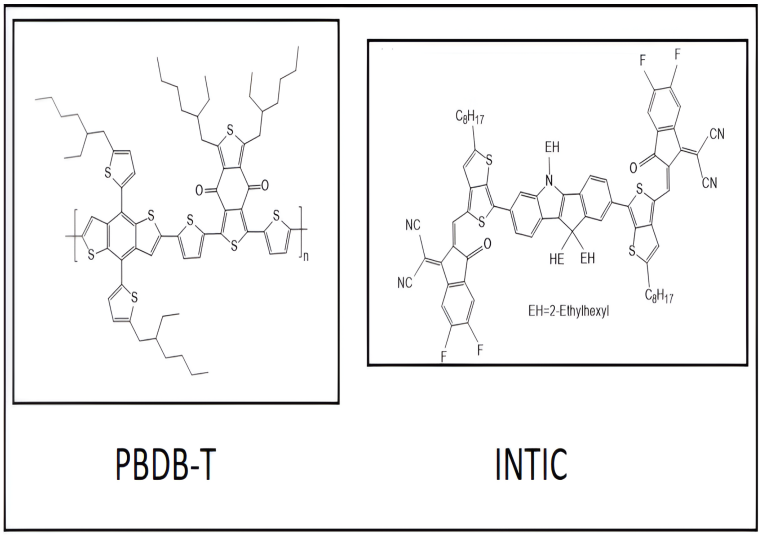


FIGURE 7.1: PBDB-T and INTIC.

Fig. 7.1 displays the chemical structures of PBDB-T and INTIC. The SM-NFA material 2,2'-((2Z,2'Z)-((6,6'-(5,10,10-tris(2-ethylhexyl)-5,10-dihydroindeno[1,2-b]indole-2,7-diyl)bis(2-octylthieno[3,4-b]thio-phene-6,4-diyl))bis(methanylylidene))bis(5,6-difluoro-3-oxo-2,3-dihydro-1H-indene-2,1-diylidene))dimalononitrile (INTIC) uses indeno[1,2-b]indole (IN) as the D cores [145]. IN was reported as not only having an extended π-system with a good electron donating capability deriving from its indole Nitrogen atom, but it can also be easily synthesized in one step from commercially available materials [145]. This means that INTIC is more easily synthesized compared to other NFAs.

The PBDB-T:INTIC blend shows promise in enhancing stability when compared to certain conventional BHJOSCs, a factor that is crucial for real world applications [383]. Furthermore, the absorption spectra of PBDB-T and INTIC are complementary, which broadens the range of light harvesting.

While limited research has been conducted on PBDB-T:INTIC BHJOSCs [145], a recent study by Zhang et al. explored the INTIC acceptor with different donors, achieving an efficiency of 11.08% using MoO_3 as the HTL, ZnO as the ETL, ITO as the anode and Ag as the cathode [145].

Additionally, a simulation study on graded bulk hetero-junction organic solar cell (GBHJOSC) with PBDB-T:INTIC as the active layer, PEDOT:PSS as the HTL, PDINO as the ETL, ITO as the anode and Al as the cathode achieved an efficiency of 12.49% [344].

7.2 Numerical Investigation of PBDB-T:INTIC BHJOSC with PEDOT:PSS:rGO HTL and n-graphene ETL

This simulation study involves the numerical investigation of PBDB-T:INTIC BHJOSC with graphene derivative incorporated in both the HTL and ETL. Recently several approaches have been developed to improve the transport properties and work function of most commonly used HTL-PEDOT:PSS. The incorporation of rGO in PEDOT:PSS improves the device performance. PEDOT:PSS:rGO composite is used as the HTL and n-type doped graphene (n-graphene) is used as the ETL.

Fig. 7.2 illustrates the device structure of ITO/PEDOT:PSS:rGO/PBDB-T:INTIC/n-graphene/Al used for the simulation study. Fig. 7.3 illustrates the energy band diagram of the layers used in the study. The input parameters of HTL, active layer and ETL were taken from previous literature and is clearly listed in Table 7.1, whereas other conditional parameters provided were chosen from the default values provided in the software. These conditional parameters were chosen in existing simulation works in literature.

To maintain consistency with existing literature and ensure baseline reliability, the remaining parameters were kept at the default values configured within SCAPS-1D, a convention frequently used in similar simulation studies. The device modelling was performed at 300 K and make use of the AM 1.5G spectrum. The voltage range for scanning was set from 0 volts to 0.8 Volts. Capture cross-section, electron and hole thermal velocities

for all layers were set to 1×10^{-15} cm^2 and 1×10^{7} cm/s respectively. Furthermore, the capture cross-section for the HTL/active layer interface, and active layer/ETL interface were chosen as 1×10^{-15} cm^2. The characteristic energy value for a defect with a neutral Gaussian distribution was set to 0.1 eV. The energy level with respect to the reference (eV) was kept constant for all layers at 0.6 eV. The work functions of ITO and Al were chosen as 4.5 eV [336] and 4.2 eV [336], respectively.

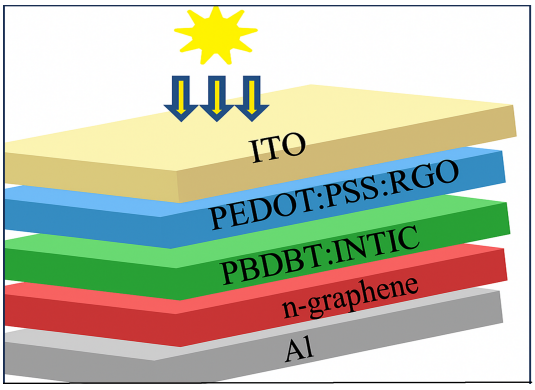


FIGURE 7.2: Device structure of ITO/PEDOT:PSS:rGO/PBDB-T:INTIC/n-graphene/Al.

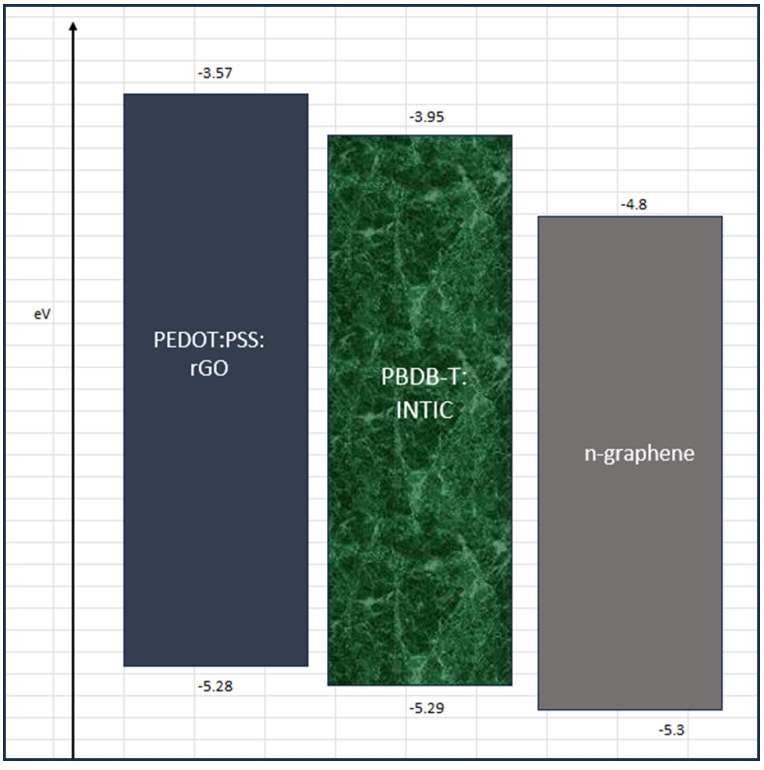


FIGURE 7.3: Energy band diagram of the layers used in the device structure-ITO/PEDOT:rGO/ PBDB-T:INTIC/n-graphene/Al.

TABLE 7.1: Input parameters for PEDOT:PSS:rGO, PBDBT:INTIC and n-graphene

Parameters	PEDOT:PSS:rGO	PBDBT:INTIC	n-graphene
Thickness (d) (nm)	50	100 [344]	33 [386]
Band gap (E_g) (eV)	1.71 [387]	1.34 [145, 344]	0.5 [386]
Electron affinity (χ) (eV)	3.57 [387]	3.95 [344]	4.8 [386]
Dielectric permittivity (ε_r)	3.5 [388]	3.65 [344]	7.8 [386]
Conduction band density (C_B) (cm^{-3})	1×10^{22}	1×10^{19}	3×10^{19} [386]
Valence band density (V_B) (cm^{-3})	1×10^{22}	1×10^{19}	3×10^{19} [386]
Electron thermal velocity (V_e) (cm/s)	1×10^{7}	1×10^{7}	1×10^{7} [386]
Hole thermal velocity (V_h) (cm/s)	1×10^{7}	1×10^{7}	1×10^{7} [386]
Electron mobility (μ_e) (cm^2/Vs)	43 [389]	6.02×10^{-3} [145]	1×10^{5} [386]
Hole mobility (μ_h) (cm^2/Vs)	43 [389]	7.72×10^{-3} [145]	1×10^{1} [386]
Doping concentration of acceptor (N_A) (cm^{-3})	1×10^{16} [389]	0	5×10^{16} [386]
Doping concentration of donor (N_D) (cm^{-3})	0	0	0
Defect density (N_t) (cm^{-3})	1×10^{14}	5×10^{11}	1×10^{14} [386]

7.2.1 Influence of Thickness of Active Layer

Fig. 7.4 shows the influence of thickness variation of the active layer on device output parameters. As the thickness of the active layer is varied from 50 to 110 nm, the V_{oc} decreased from 0.1106 to 0.0597 V. The J_{sc} decreased from 7.275278 to 6.592830 mA/cm^2. The FF reduced from 27.32 to 25.725% and the efficiency decreased from 0.22 to 0.10%. Increasing the active layer thickness increased the carrier transport distance, leading to greater recombination losses due to the relatively low carrier mobility of organic semiconductors. Consequently, charge collection efficiency decreased, resulting in lower device performance.

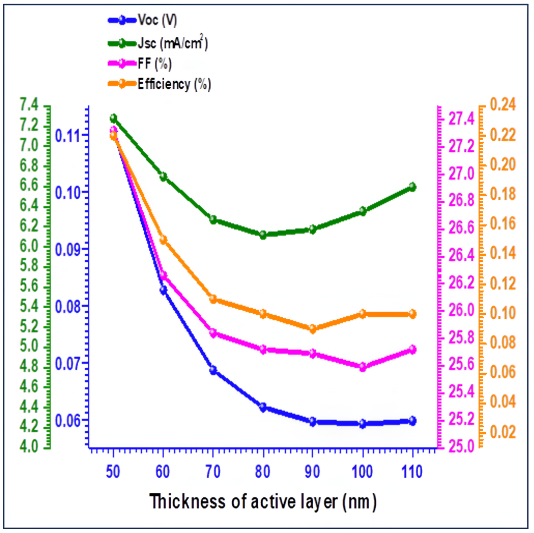


FIGURE 7.4: Influence of varying thickness of the active layer on the device output parameters

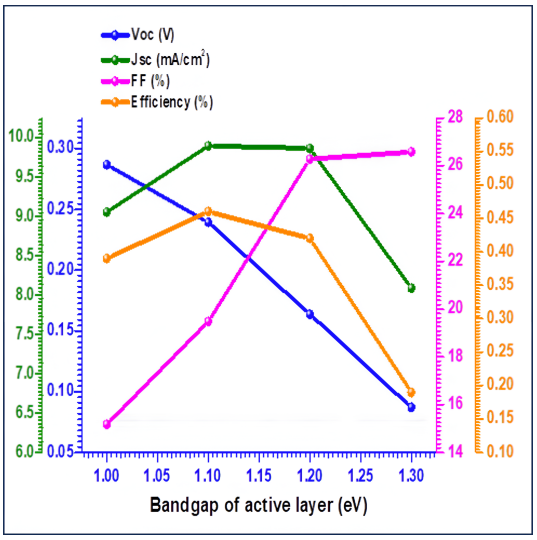


FIGURE 7.5: Influence of varying band gap of the active layer on the device output parameters

7.2.2 Influence of Band Gap of Active Layer

The impact of varying band gap of the active layer on the device performance is plotted in Fig. 7.5. As the band gap is varied from 1 to 1.3 eV, V_{oc} varied from 0.2866 to 0.0870 V. J_{sc} varied from 9.054339 to 8.086150 mA/cm^2. The FF increased from 15.18 to 26.58% and the efficiency varied from 0.39% to 0.19%. A larger band gap reduces the absorption of low-energy photons, thereby decreasing exciton generation and photocurrent. The reduction in photogenerated carriers outweighs any improvement in carrier transport, causing a decline in efficiency.

7.2.3 Influence of Electron Affinity of Active Layer

The influence of varying electron affinity of the active layer on device performance is shown in Fig. 7.6. As the electron affinity was changed from 3.95 to 4.5 eV, V_{oc} varied from 0.0546 to 0.3404 V, J_{sc} varied from 2.30596 to 6.273372 mA/cm^2. FF varied from 24.98 to 31.45% and the efficiency varied from 0.03 to 0.67%. Increasing electron affinity improves the energetic alignment between the active layer and ETL, facilitating electron extraction and reducing interfacial charge accumulation. This suppresses recombination losses and enhances PV performance.

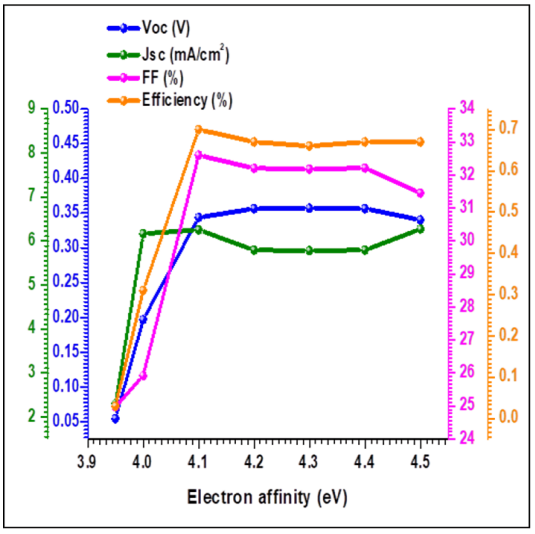


FIGURE 7.6: Influence of varying electron affinity of the active layer on the device output parameters.

7.3 Numerical Investigation of PBDB-T:INTIC BHJOSC with Diverse Graphene Derivative HTLs and Different ETLs

Recently, derivatives of graphene have attracted interest for their use as charge transport layers in SM-NFA based BHJOSCs, owing to their exceptional optical, electronic and mechanical properties. While few experimental and two simulation studies on PBDB-T:INTIC based BHJOSCs exist as mentioned in section 7.1, none have investigated the use of graphene derivatives as transport layers, particularly for HTLs and various ETLs.

In our present study, we focused on numerical simulation of SM-NFA based BHJOSC with PBDB-T:INTIC as the active layer, diverse graphene derivative HTLs and different ETLs. The software was first validated using an experimentally fabricated reference device with the structure ITO/PEDOT:PSS/PBDB-T:NCBDT/PDINO/Al [368], thereafter NCBDT was substituted with INTIC (a rarely researched SM-NFA).

PEDOT:PSS HTL used in this configuration is replaced with graphene derivatives such as graphene, p-graphene, GO, and rGO. Along with this, different combinations of device structure were studied with diverse ETLs that include PDINO, PFN-Br, IGZO, TiO_2:gr(20%), and TiO_2:gr(10%).

The absorption range of the active layer is crucial for the device performance. PBDB-T absorbs between 550 nm and 700 nm, while INTIC absorbs between 700 nm and 800

nm. The absorption ranges of the materials used for the ETL, such as PDINO, PFN-Br, IGZO and TiO_2:gr, are around 500 nm, 400 nm, 300 nm and 250-350 nm, respectively.

7.3.1 Standardization

Standardization is done using the device structure ITO/PEDOT:PSS/PBDB-T:NCBDT/ PDINO/Al [368], followed by numerical simulation study of BHJOSC with diverse HTLs and ETLs.

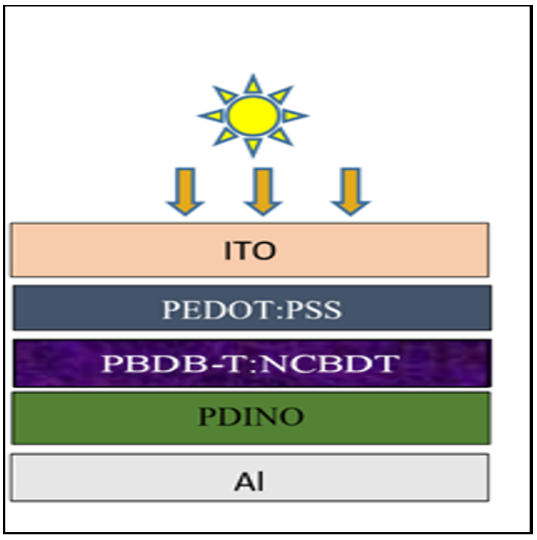


FIGURE 7.7: Device structure used for standardization [368].

TABLE 7.2: Input parameters of PBDB-T:NCBDT and PEDOT:PSS used for the simulation of ITO/PEDOT:PSS/PBDB-T:NCBDT/PDINO/Al.

Parameters	PEDOT:PSS	PBDB-T:NCBDT	PDINO
Thickness (d) (nm)	30 [341, 344, 390]	100 [344, 368]	5 [341, 368]
Band gap (E_g) (eV)	1.5 [341, 391]	1.38 [344, 368]	2.98 [341]
Electron affinity (χ) (eV)	3.4 [341, 392]	3.91 [344, 368, 369]	4.1 [341, 393]
Dielectric permittivity (ε_r)	3 [341, 394]	3.65 [344]	5 [341]
Conduction band density (C_B) (cm^{-3})	1×10^{22} [341]	1×10^{19} [344]	1×10^{19} [341]
Valence band density (V_B) (cm^{-3})	1×10^{22} [341]	1×10^{19} [344]	1×10^{19} [341]
Electron mobility (μ_e) (cm^2/Vs)	4.5×10^{-3} [341]	8.8×10^{-5} [344]	2×10^{-6} [341, 395]
Hole mobility (μ_h) (cm^2/Vs)	9.9×10^{-5} [341]	9.2×10^{-5} [344]	1×10^{-3} [341, 395]
Doping concentration of acceptor (N_A) (cm^{-3})	0 [341]	0 [344]	2×10^{21} [341]
Doping concentration of donor (N_D) (cm^{-3})	1×10^{21} [341]	0 [344]	0 [341]
Defect density (N_t) (cm^{-3})	1×10^{9} [341]	5×10^{11} [344]	$\times 10^{14}$ [341]

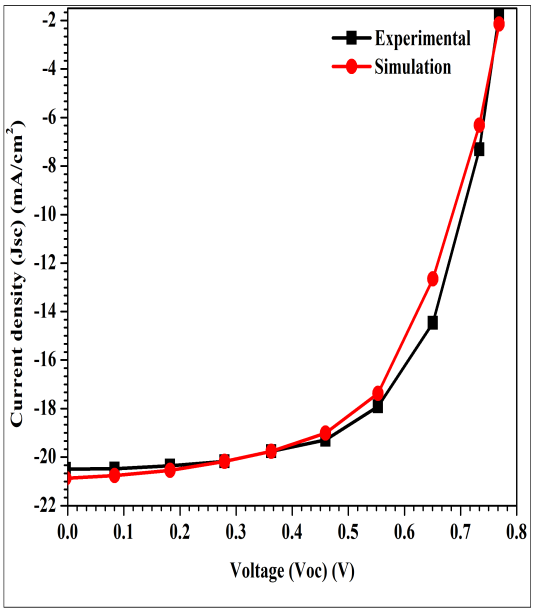


FIGURE 7.8: Matched J-V graph of experimental and simulation work of ITO/PEDOT:PSS/PBDB-T:NCBDT/PDINO/Al.

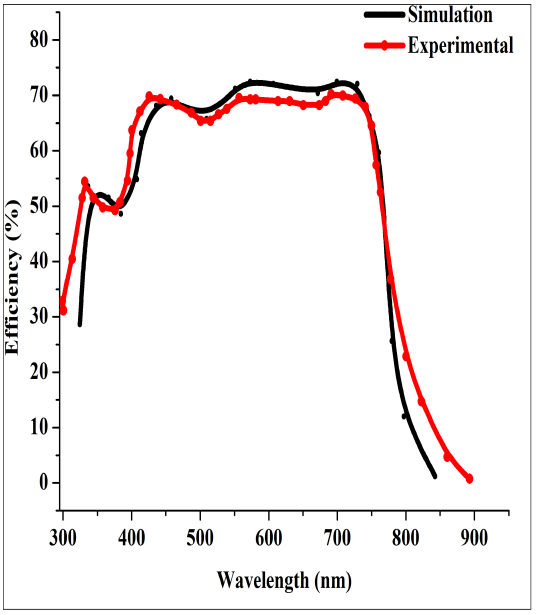


FIGURE 7.9: Matched EQE graph of experimental and simulated data of ITO/PEDOT:PSS/PBDB-T:NCBDT/PDINO/Al [368].

Fig. 7.7 displays the device structure used for standardization. Table 7.2 lists the input parameters of the active layer, HTL, and ETL used for standardization study.

To maintain consistency with existing literature and ensure baseline reliability, the

TABLE 7.3: Matching experimental and simulation output parameters.

Parameters	Experimental [368]	Simulated
V_{oc} (V)	0.82	0.80
J_{sc} (mA/cm^2)	19.45	20.61
FF (%)	62.90	60.43
Efficiency (%)	10.04	10.02

remaining parameters were kept at the default values configured within SCAPS-1D, a convention frequently used in similar simulation studies. The device modelling was performed at 300 K and make use of the AM 1.5 G spectrum. The voltage range for scanning was set from 0 volts to 0.8 Volts. Capture cross-section, electron and hole thermal velocities for all layers were set to 1×10^{-15} cm^2 and 1×10^7 cm/s respectively. Furthermore, the capture cross-section for the HTL/active layer interface, and active layer/ETL interface were chosen as 1×10^{-15} cm^2. The characteristic energy value for a defect with a neutral Gaussian distribution was set to 0.1 eV. The energy level with respect to the reference (eV) was kept constant for all layers at 0.6 eV. The work functions of ITO and Al were chosen as 4.5 eV [336] and 4.2 eV [336], respectively.

Fig. 7.8 and Fig. 7.9 exhibits matching J-V graph and matched EQE graph respectively. Table 7.3 lists the matching experimental and simulated device output parameters. The software is validated by the close match between the simulated and experimentally measured results, which demonstrates that the parameters used for the cell's layers are similar to those of the actual device.

7.3.2 Study of ITO/HTL/PBDB-T:INTIC/ETL/Al

Fig. 7.10 shows the device structure used for the simulation study. Fig. 7.11 illustrates energy band diagram of layers used in the simulation study. Table 7.4 lists the input parameters of the active layer and HTLs used for the simulation study. Table 7.5 lists the input parameters of ETLs used for the study.

Capture cross-section, electron and hole thermal velocities for all layers were set to 1×10^{-15} cm^2 and 1×10^7 cm/s respectively. Furthermore, the capture cross-section for the HTL/active layer interface, and active layer/ETL interface were chosen as 1×10^{-15} cm^2. The characteristic energy value for a defect with a neutral Gaussian distribution was set to 0.1 eV. The energy level with respect to the reference (eV) was kept constant for all layers at 0.6 eV. The operating temperature used for the simulation study was taken

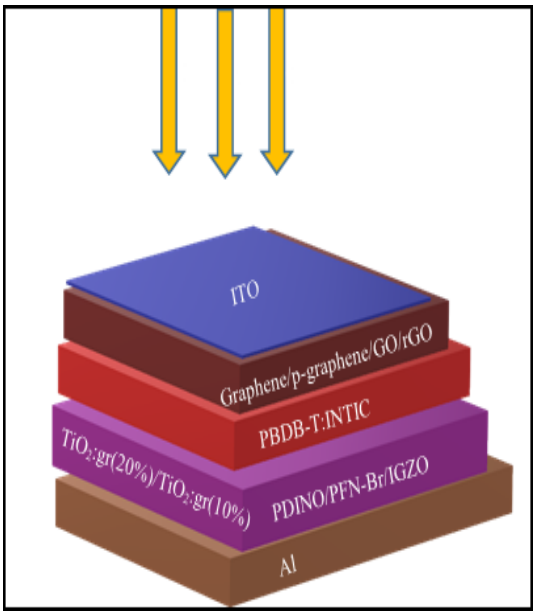


FIGURE 7.10: Device structure used for the simulation study of ITO/HTL/PBDB-T:INTIC/ETL/Al.

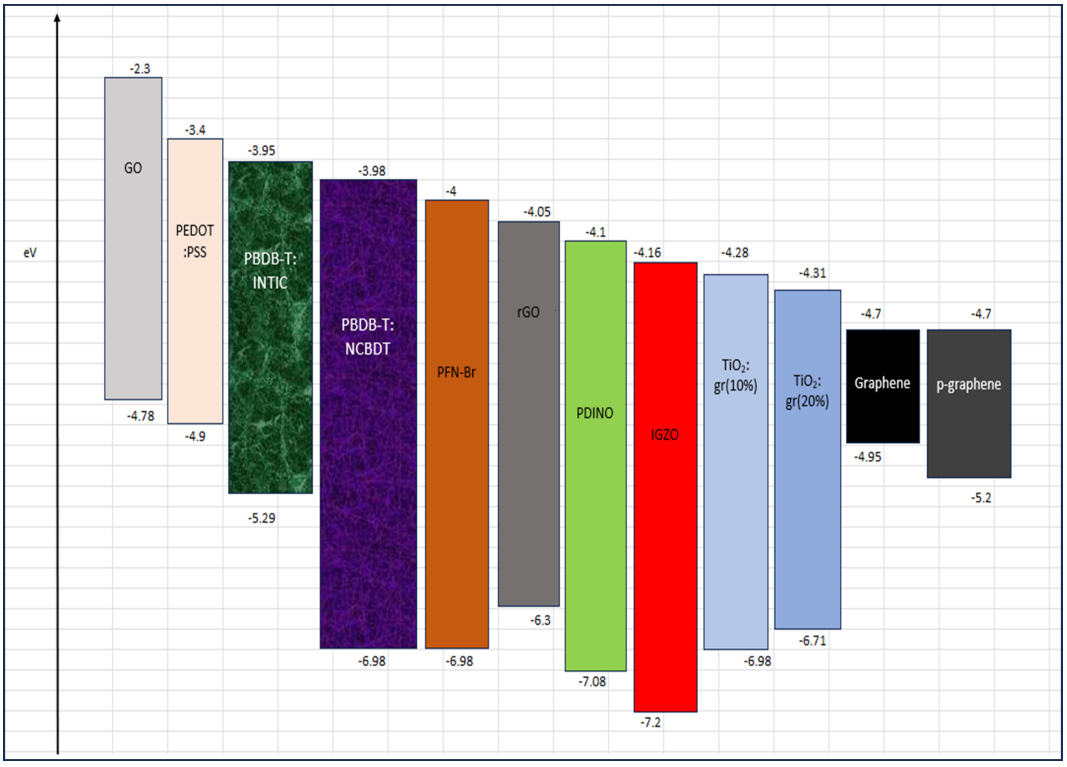


FIGURE 7.11: Energy band diagram of the layers used in the device structure used for the simulation study of ITO/HTL/PBDB-T:INTIC/ETL/Al.

to be 300 K. Simulation study was done under AM 1.5 G light with an intensity of 100 mW/cm^2.

TABLE 7.4: Input parameters of PBDB-T:INTIC and HTLs used for the simulation of ITO/HTL/PBDB-T:INTIC/ETL/Al.

Parameter	PBDB-T:INTIC	Graphene	p-graphene	GO	rGO
Thickness (d) (nm)	100 [344]	20 [337, 396]	33 [372]	35 [336]	35 [336]
Band gap (E_g) (eV)	1.34 [344, 145]	0.25 [337, 397, 398, 399]	0.5 [372]	2.48 [343, 400]	1.5/1.52 [354, 401]
Electron affinity (χ) (eV)	3.95 [344]	4.7 [337, 402, 403]	4.7 [372]	2.3 [343]	4.05 [401]
Dielectric permittivity (ε_r)	3.65 [344]	13 [337, 404, 405]	7.1[372]	10 [343, 406]	13.3 [356]
Conduction band density (C_B) (cm^{-3})	1×10^{19}	2×10^{20} [337]	3×10^{19} [372]	1.8×10^{18} [343]	1×10^{19} [374]
Valence band density (V_B) (cm^{-3})	1×10^{19}	1.8×10^{20} [337]	3×10^{19} [372]	2.2×10^{18} [343]	1×10^{22} [374]
Electron mobility (μ_e) (cm^2/Vs)	6.02×10^{-3} [145]	1×10^{4} [337]	1×10 [372]	2.6×10 [343, 407]	3.2×10^{2} [357]
Hole mobility (μ_h) (cm^2/Vs)	7.72×10^{-4} [145]	1×10 [337]	1×10^{5} [372]	1.23×10^{2} [343, 408]	3.2×10^{2} [357]
Doping concentration of acceptor (N_A) (cm^{-3})	0	0 [337]	0 [372]	0 [343]	0
Doping concentration of donor (N_D) (cm^{-3})	0 [382]	1×10^{15} [337]	1×10^{15} [372]	1×10^{18} [382]	1×10^{18}
Defect density (N_t) (cm^{-3})	5×10^{11}	1.9×10^{9} [337]	1.9×10^{9} [372]	1.9×10^{9}	1.9×10^{9}

TABLE 7.5: Input parameters of ETLs used for the simulation of ITO/HTL/PBDB-T:INTIC/ETL/Al.

Parameters	TiO_2:gr(20%)	TiO_2:gr(10%)	PDINO	PFN-Br	IGZO
Thickness (d) (nm)	50 [352]	50 [352]	5 [341, 368]	5 [378, 409, 410]	5 [341, 411]
Band gap (E_g) (eV)	2.4 [352]	2.7 [352]	2.98 [341]	2.98 [378, 412]	3.05 [341, 413]
Electron affinity (χ) (eV)	4.31 [352]	4.28 [352]	4.1 [341, 393]	4 [378]	4.16 [341, 414]
Dielectric permittivity (ε_r)	7.8 [352]	7.5 [352]	5 [341]	5 [378]	10 [341, 415]
Conduction band density (C_B) (cm^{-3})	1×10^{19} [352]	1×10^{19} [352]	1×10^{19} [341]	1×10^{19} [378]	1×10^{19} [341]
Valence band density (V_B) (cm^{-3})	1×10^{19} [352]	1×10^{19} [352]	1×10^{19} [341]	1×10^{19} [378]	1×10^{19} [341]
Electron mobility (μ_e) (cm^2/Vs)	350 [352]	125 [352]	2×10^{-6} [341, 395]	2×10^{-6} [378, 395]	15 [341, 416, 417]
Hole mobility (μ_h) (cm^2/Vs)	350 [352]	125 [352]	1×10^{-3} [341]	1×10^{-4} [378, 395]	0.1 [341, 416, 417]
Doping concentration of acceptor (N_A) (cm^{-3})	0 [352]	0 [352]	0 [341]	0 [378]	0 [341]
Doping concentration of donor (N_D) (cm^{-3})	5×10^{18} [352]	5×10^{18} [352]	2×10^{21} [341]	9×10^{18} [378]	1×10^{18} [341]
Defect density (N_t) (cm^{-3})	1×10^{14} [352]	1×10^{14} [352]	1×10^{14} [341]	1×10^{9} [378]	1×10^{19} [341]

TABLE 7.6: Device output parameters after the simulation study with graphene derivative HTLs and diverse ETLs.

HTL	ETL	V_{oc} (V)	J_{sc} (mA/cm^2)	FF (%)	Efficiency (%)
Graphene	PDINO	0.64	19.32	73.86	9.18
Graphene	PFN-Br	0.62	18.66	63.03	7.30
Graphene	IGZO	0.59	18.39	55.01	6.04
Graphene	TiO_2:gr(20%)	0.49	18.09	51.08	4.61
Graphene	TiO_2:gr(10%)	0.53	18.21	52.15	5.02
p-graphene	TiO_2:gr(20%)	0.53	17.92	51.30	4.92
p-graphene	TiO_2:gr(10%)	0.56	18.03	52.32	5.32
GO	PDINO	0.59	20.17	73.35	8.70
GO	PFN-Br	0.57	19.51	62.11	6.90
GO	IGZO	0.54	19.22	54.31	5.65
GO	TiO_2:gr(20%)	0.44	18.86	49.81	4.17
GO	TiO_2:gr(10%)	0.47	19.00	51.03	4.59
rGO	PDINO	0.67	19.90	80.78	10.74
rGO	PFN-Br	0.65	19.32	68.00	8.49
rGO	IGZO	0.61	19.16	57.75	6.74

Based on the simulation study, the best configuration was found to be ITO/rGO/PBDB-T:INTIC/PDINO/Al, with V_{oc} of 0.67 V, J_{sc} of 19.90 mA/cm^2, FF of 80.78% and efficiency of 10.74%.

Table 7.6 lists the device output parameters obtained for different device configurations. The simulation results clearly show that rGO with intermediate band gap (1.5 eV) gives best output parameters. Our investigation evidently shows that among all the ETLs used, PDINO demonstrates the highest efficiency with all HTL combinations.

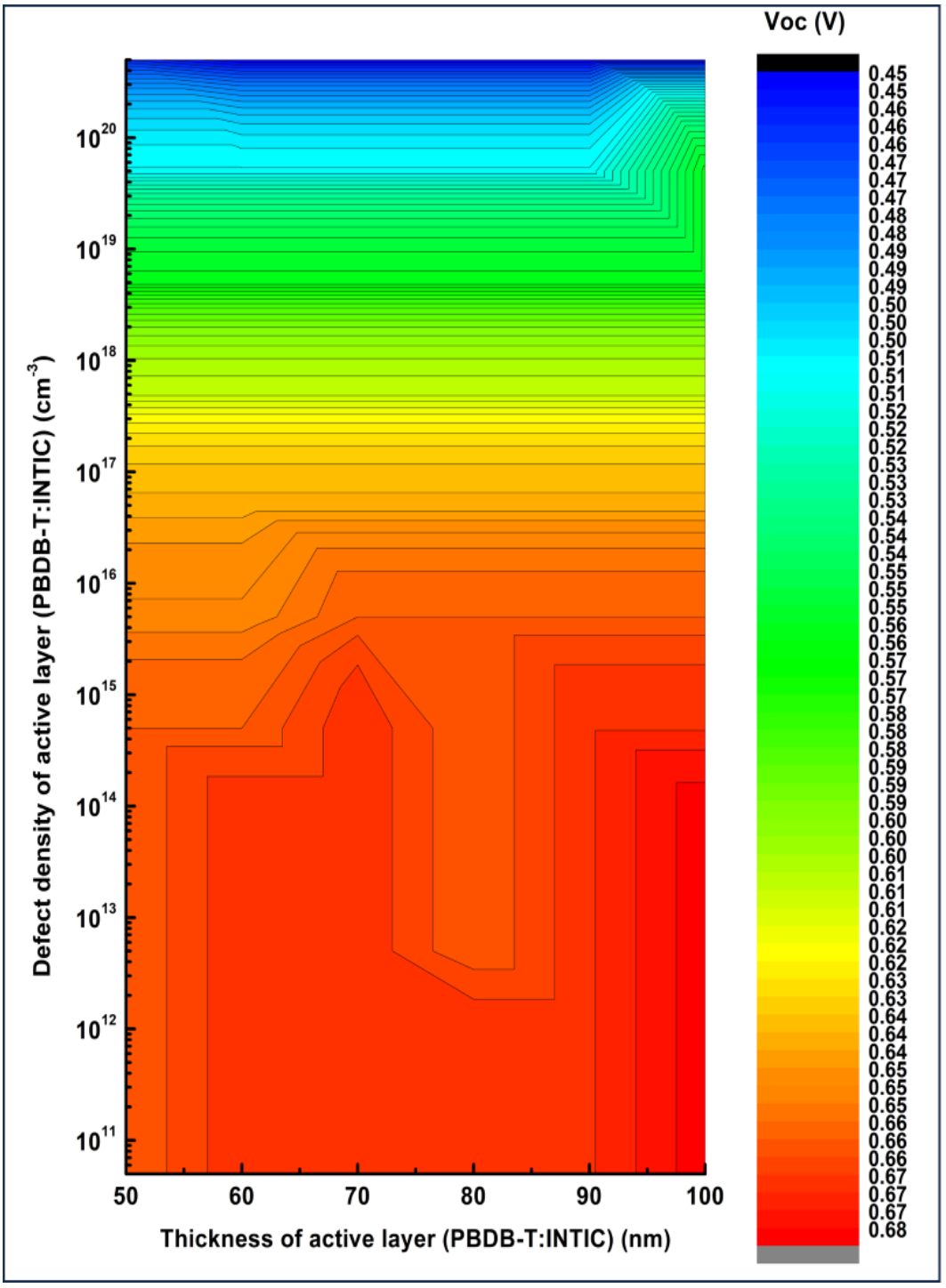


FIGURE 7.12: Influence of thickness and defect density variation of active layer on V_{oc} of the device.

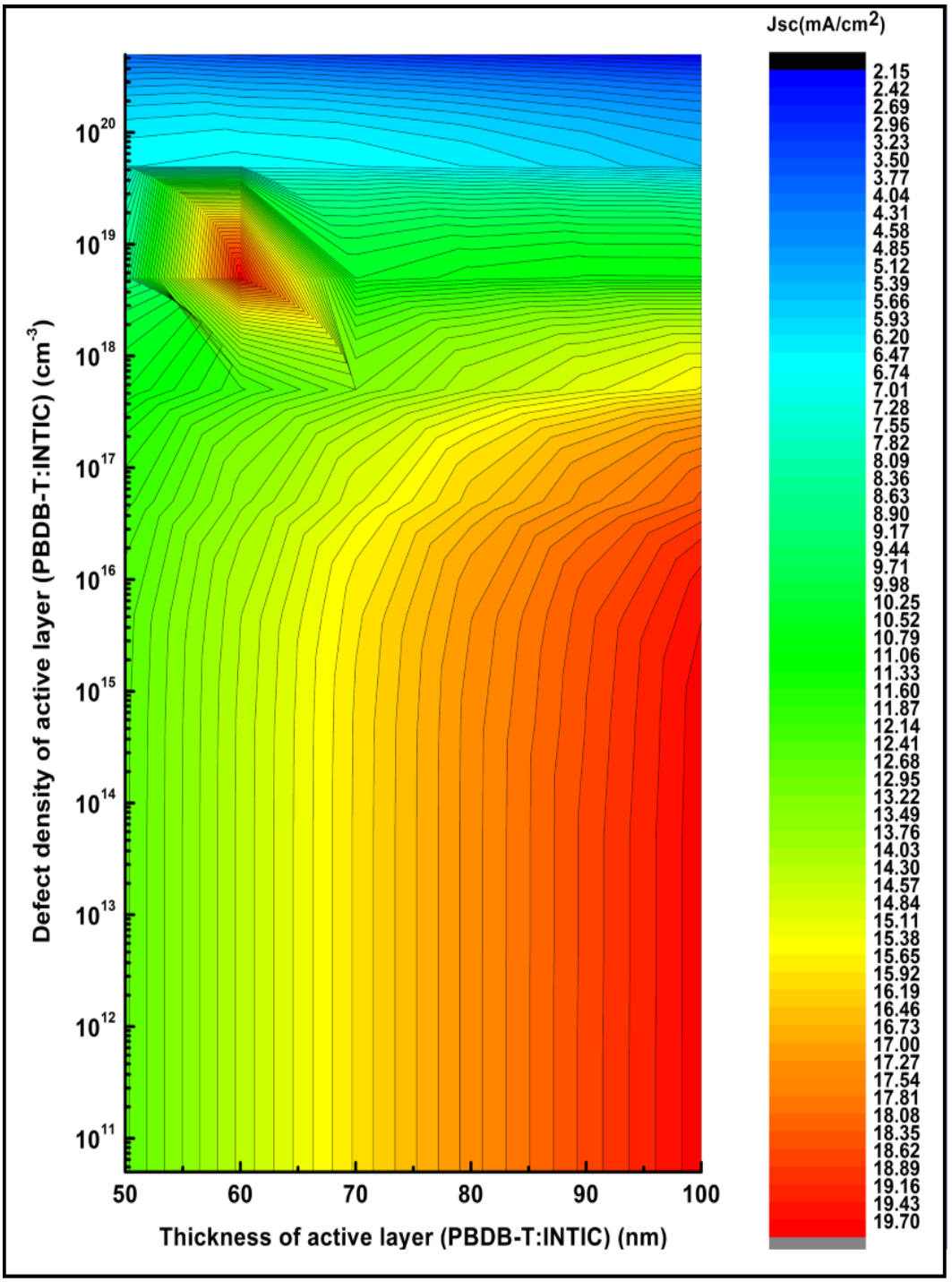


FIGURE 7.13: Influence of thickness and defect density variation of active layer on J_{sc} of the device.

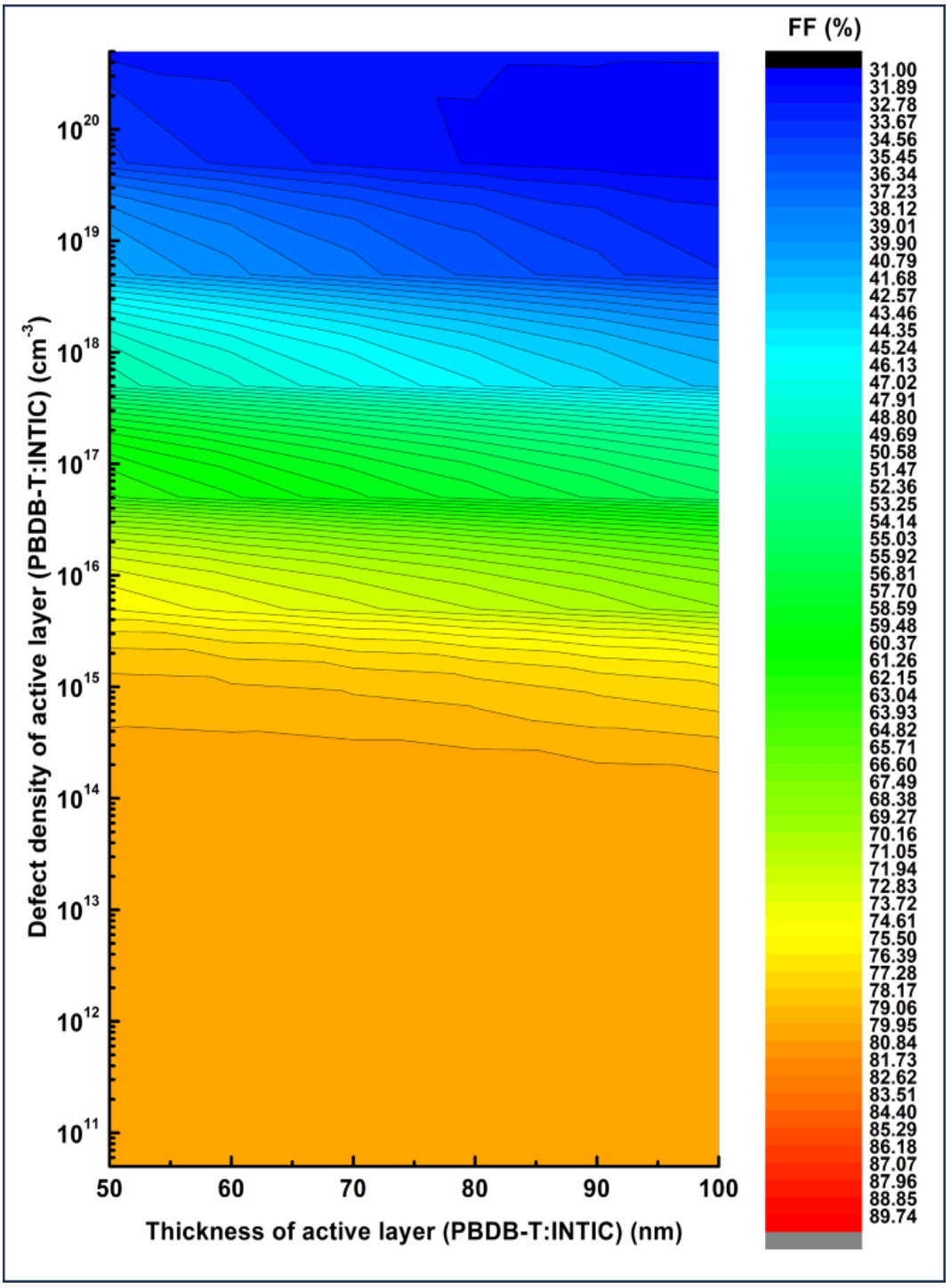


FIGURE 7.14: Influence of thickness and defect density variation of active layer on FF of the device.

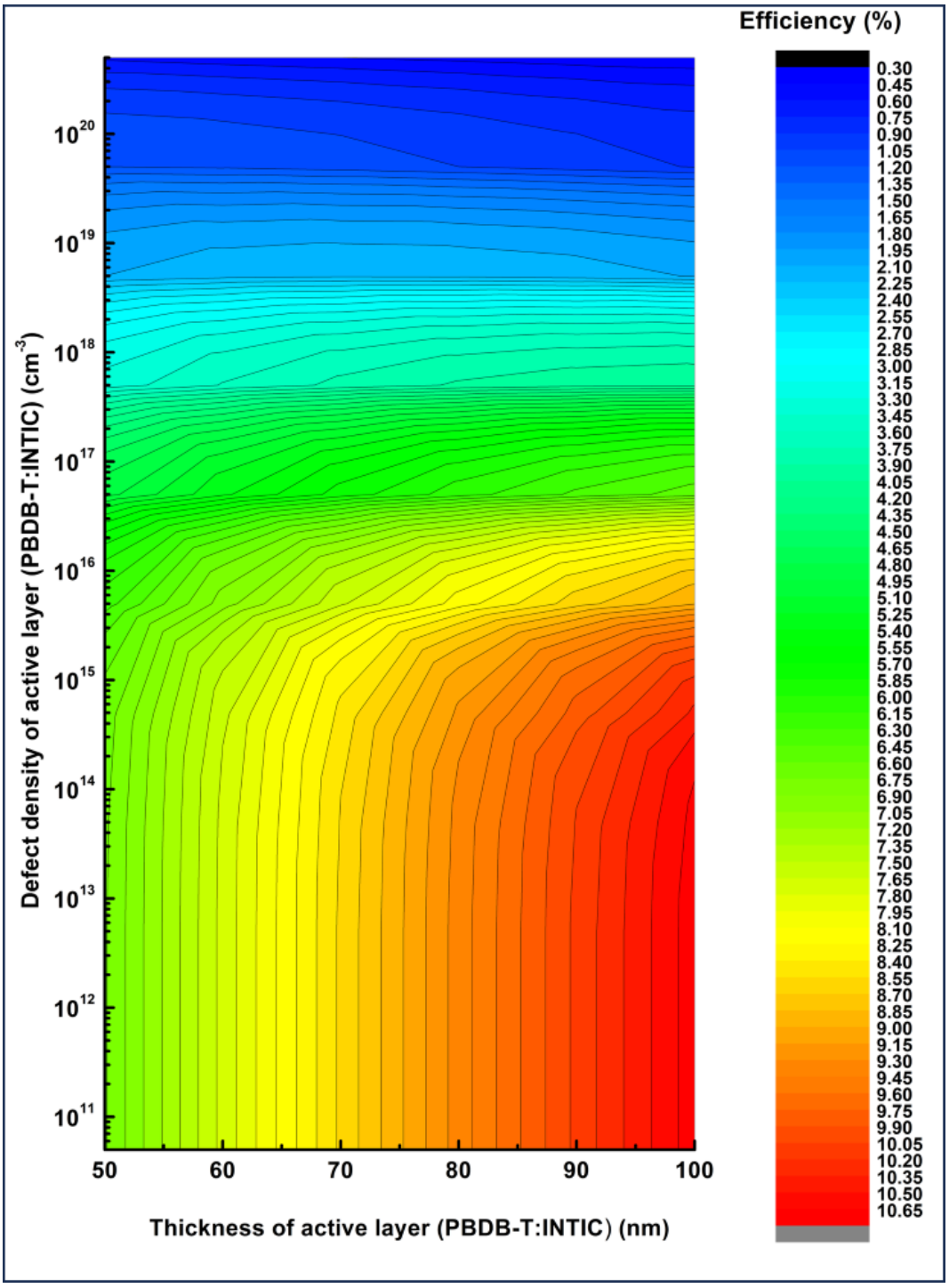


FIGURE 7.15: Influence of thickness and defect density variation of active layer on efficiency of the device.

7.3.3 Optimization of ITO/rGO/PBDB-T:INTIC/PDINO/Al

The best device structure is optimized with respect to the input parameters of the layers. It is conducted by studying the influence of thickness of the active layer, HTL and ETL, as well as the defect density of the active layer, HTL, and ETL.

7.3.3.1 Influence of Thickness and Defect Density Variation of Active Layer

Figs. 7.12 to 7.15 display the contour plots showing the effect of variation of thickness and defect density of absorber layer on V_{oc}, J_{sc}, FF, and efficiency of the device respectively. The x-axis represents the thickness and y-axis represents defect density respectively. Simultaneous influence of these two factors is analyzed using the contour plots. The thickness of the absorber layer was varied from 50 to 100 nm, and for each thickness, the defect density was varied from 5×10^{10} to 5×10^{20} cm^{-3}. A maximum efficiency of 10.74% was attained.

In NFA based BHJ OSCs, the active layer thickness significantly impacts the device performance. While thicker layers enhance light absorption and exciton generation, they also increase challenges in charge transport and recombination losses. Typically an optimal thickness of around 100 nm could be considered as optimal for NFA based BHJOSC and device engineering have enabled thicker layers but a higher absorber thickness leads to declination in device performance.

In BHJ OSCs with similar active materials, a higher defect density in the active layer increased recombination losses, reduces charge transport and lowers charge collection efficiency, ultimately diminishing device performance. Minimizing defects is essential for increasing efficiency which seems to be a tedious task while fabricating these SCs. As the defect density of the active layer increased, it becomes much difficult for the charge carriers to move through the layers and reach the respective electrodes. Controlling of the active layer morphology is very crucial, particularly in reducing defects, which include traps that could lead to more recombination losses.

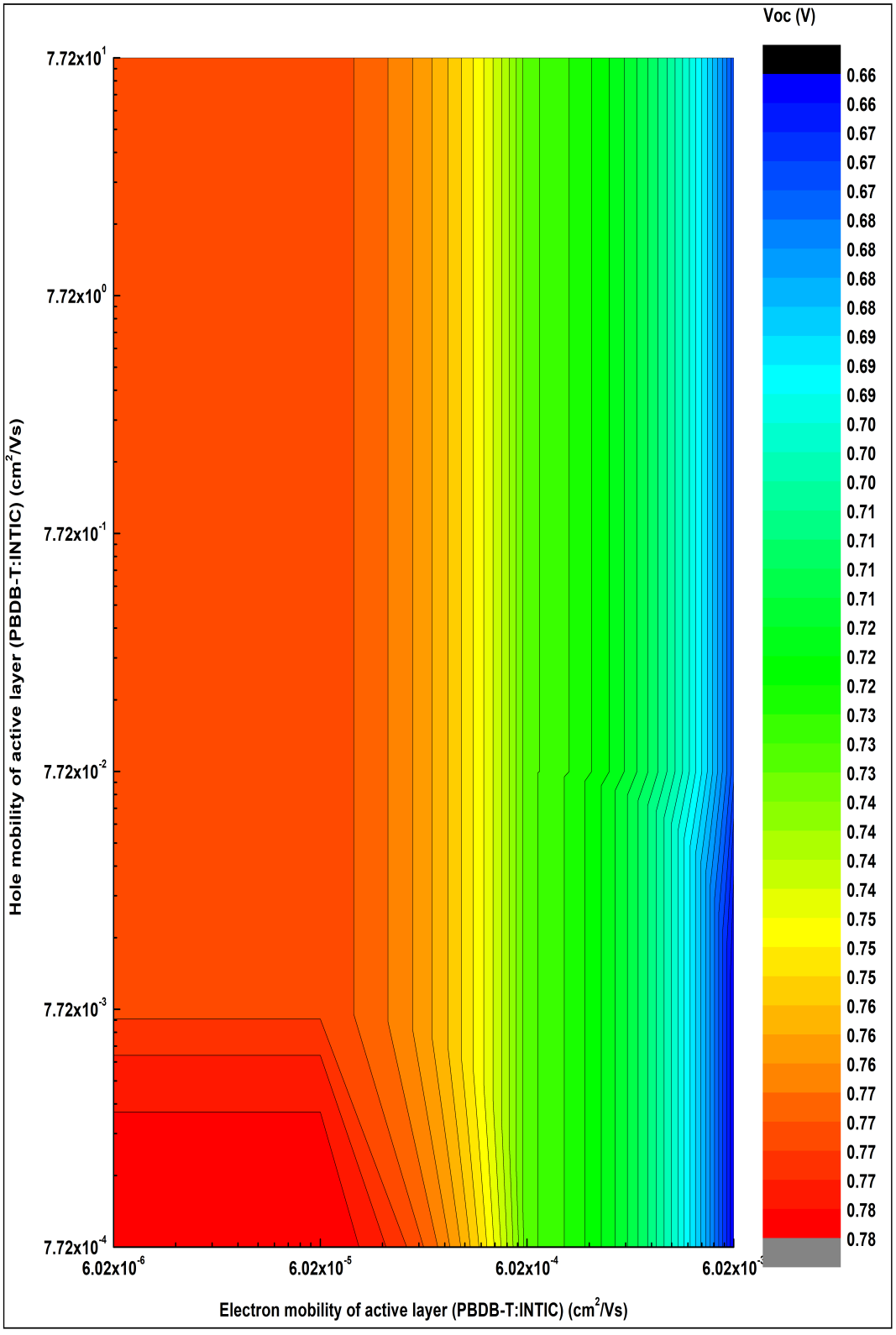


FIGURE 7.16: Influence of varying electron and hole mobilities of active layer on V_{oc}.

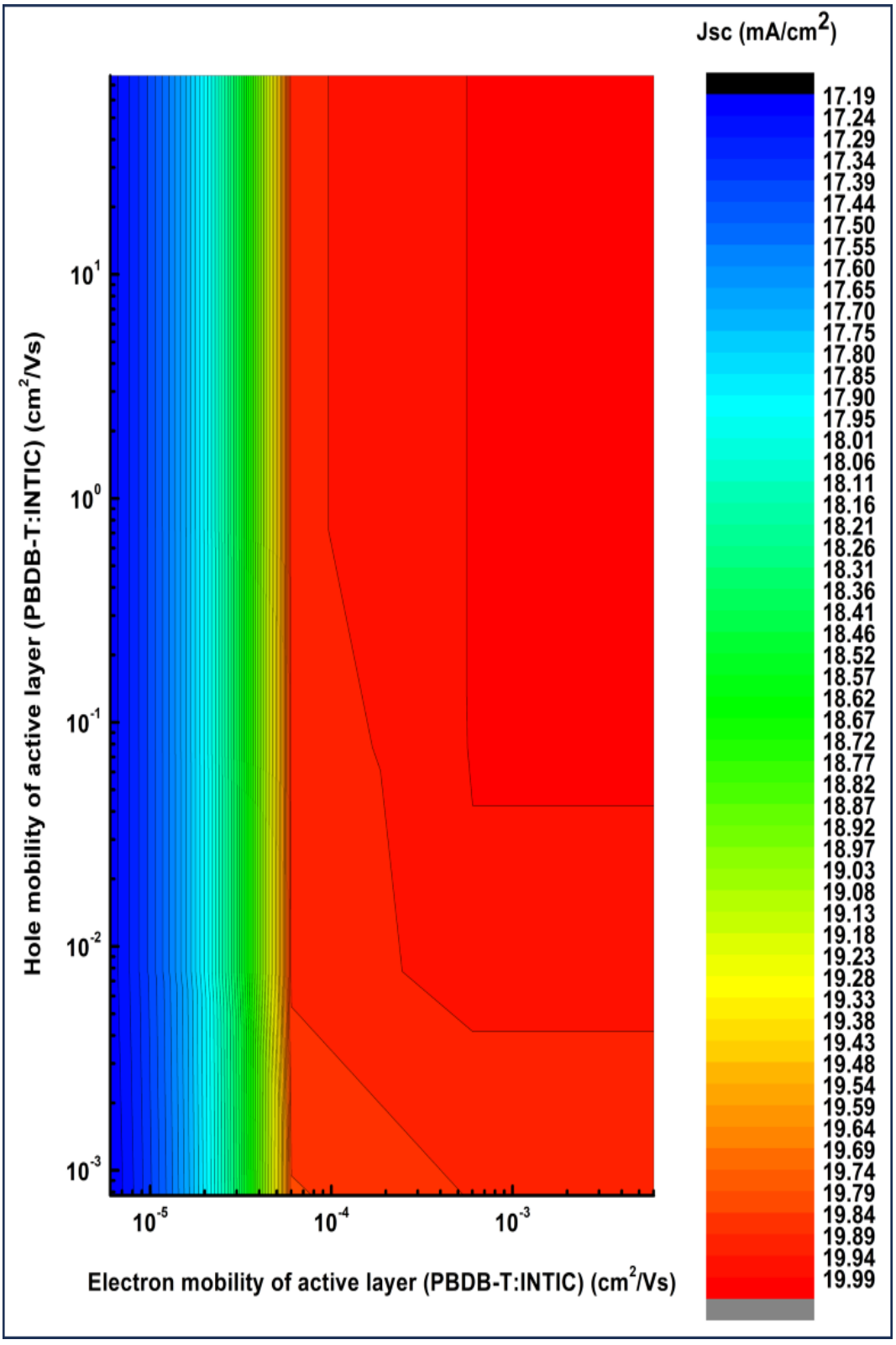


FIGURE 7.17: Influence of varying electron and hole mobilities of active layer on J_{sc}.

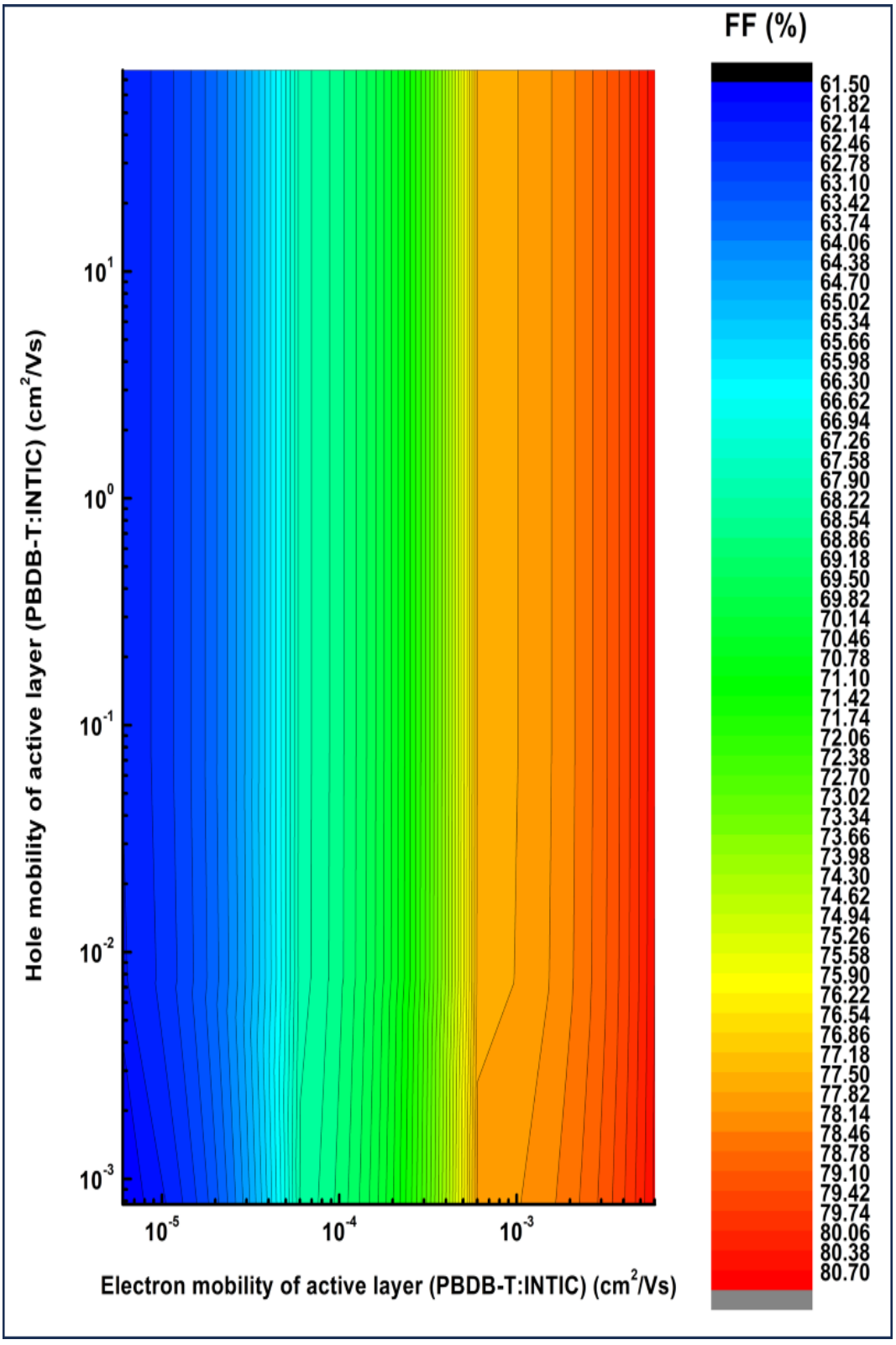


FIGURE 7.18: Influence of varying electron and hole mobilities of active layer on FF.

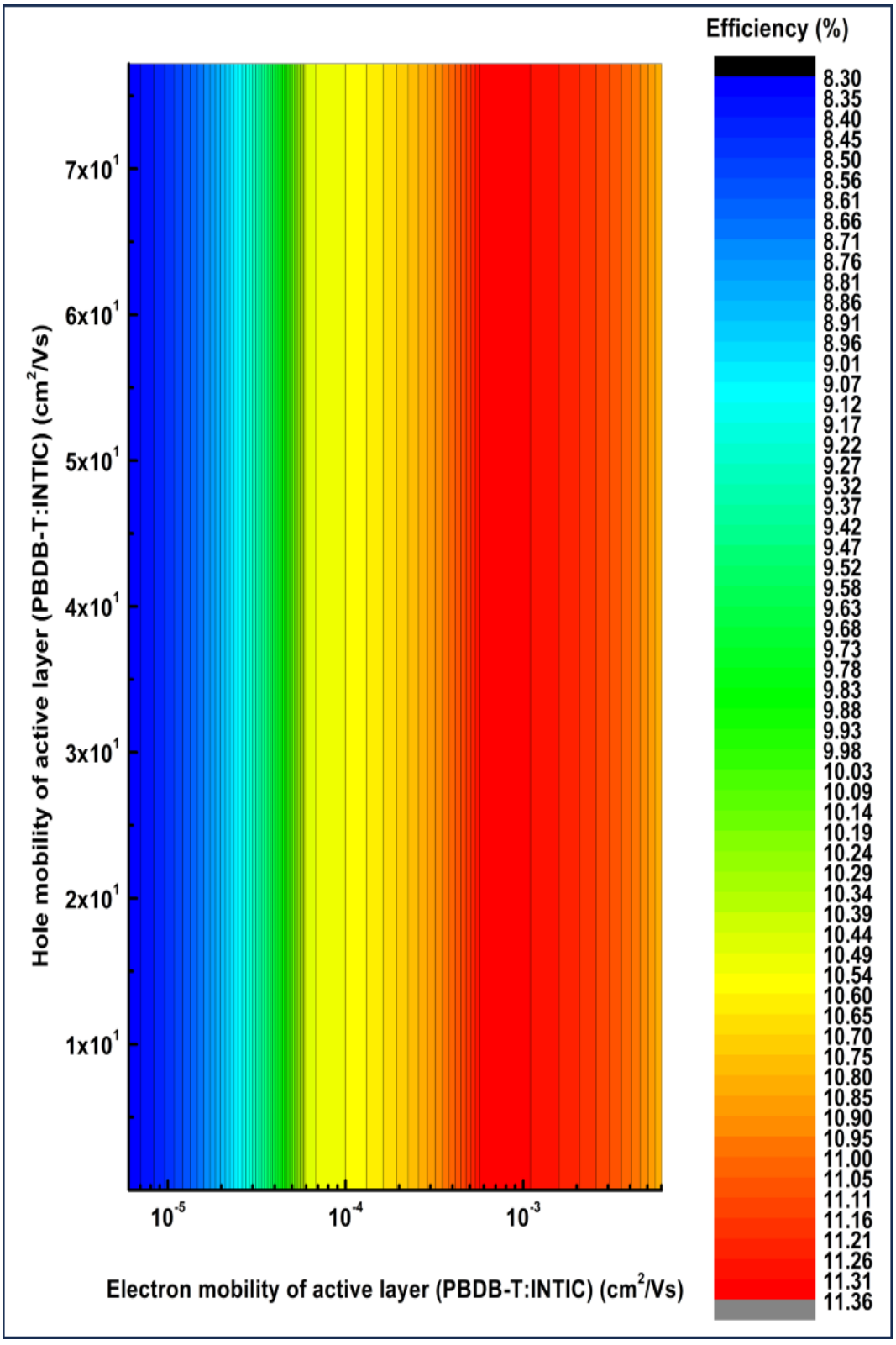


FIGURE 7.19: Influence of varying electron and hole mobilities of active layer on efficiency.

7.3.3.2 Influence of Varying Electron and Hole Mobility Variation of Active Layer

Higher electron mobility causes increased charge carrier encounters that leads to more frequent recombination of electrons and holes particularly at interfaces. Figs. 7.16 to 7.19 display contour plots that show the variation of V_{oc}, J_{sc}, FF and efficiency with varying electron and hole mobility of the active layer, where x-axis represents electron mobility and y-axis represents hole mobility. Simultaneous influence of these two factors is analyzed using the contour plots. It reduces the number of charges that can be collected at electrode. Collection of charges at electrodes in high mobility materials may have unfavourable energy levels that can create barriers for charge extraction reducing V_{oc}.

The electron mobility was varied from 6.02×10^{-3} to 6.02×10^{-6} cm^2/Vs and hole mobility was varied from 7.72×10^{-4} to 7.72×10 cm^2/Vs. A maximum efficiency of 11.36% was attained. In BHJOSC, balanced electron and hole mobility values favour smooth performance of the device.

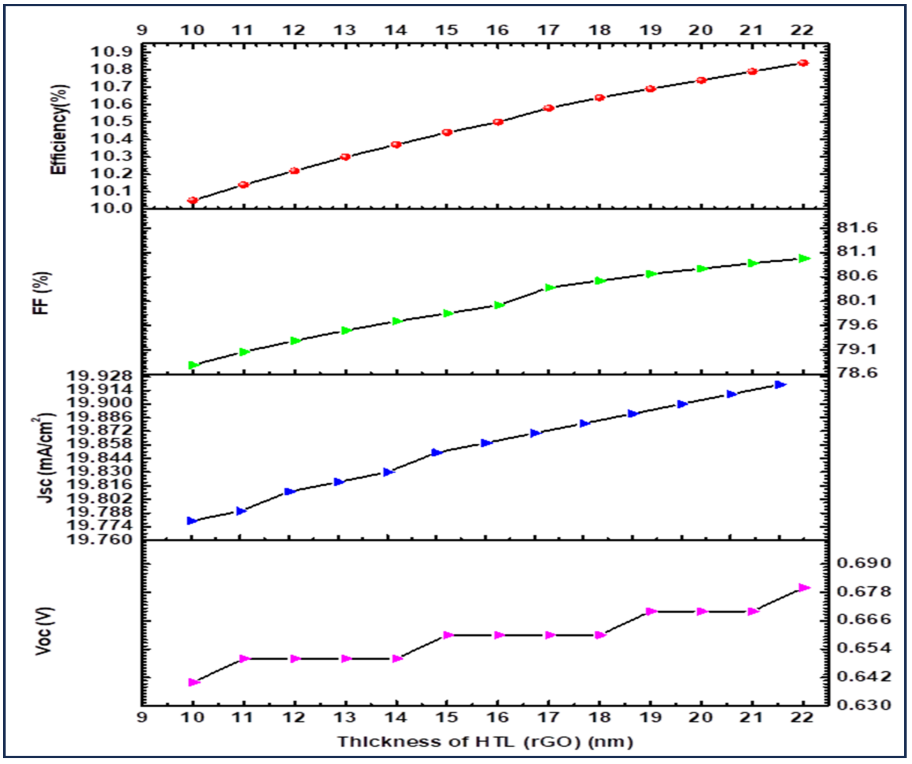


FIGURE 7.20: Influence of varying thickness of HTL on the device output parameters.

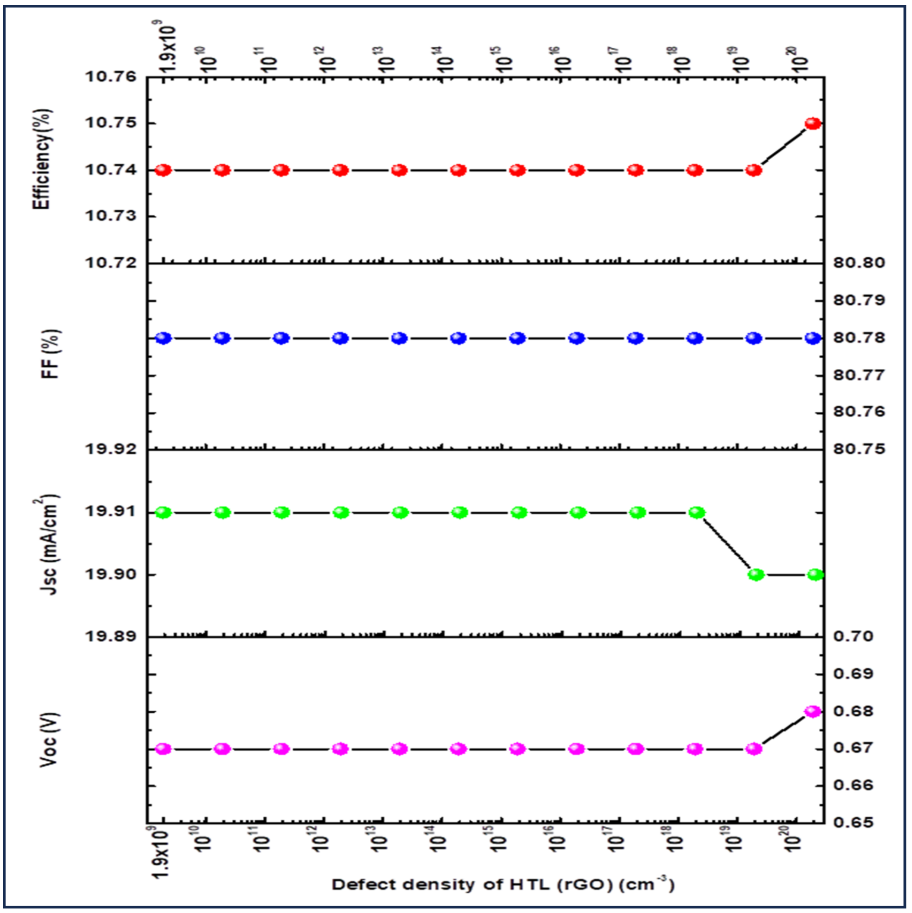


FIGURE 7.21: Influence of varying defect density of HTL on the device output parameters.

7.3.3.3 Influence of Varying Thickness and Defect Density of HTL

Fig. 7.20 shows the influence of varying thickness on the device performance and Fig. 7.21 shows the influence of varying defect density on the device performance.

The thickness of HTL was varied from 10 to 22 nm. As the thickness was increased V_{oc} of 0.6781 V, J_{sc} of 19.92 mA/cm^2, FF of 80.99%, and efficiency of 10.84% was achieved.

The HTL used in this device configuration is rGO, which is considered to be one of the best alternative for PEDOT:PSS as HTL. The energy band of rGO is well-aligned with that of the active layer chosen. Better hole transport from the active layer to the anode may be made possible using thicker HTL, which may reduce interface charge carrier recombination losses. Increasing the thickness of the HTL may help smoothening of the interface between the active layer and the HTL and lessen the impact of defects. The efficiency of the device may increase with a thicker HTL, as it acts as a buffer, improving energy level alignment and potentially lowering the barrier height for hole injection.

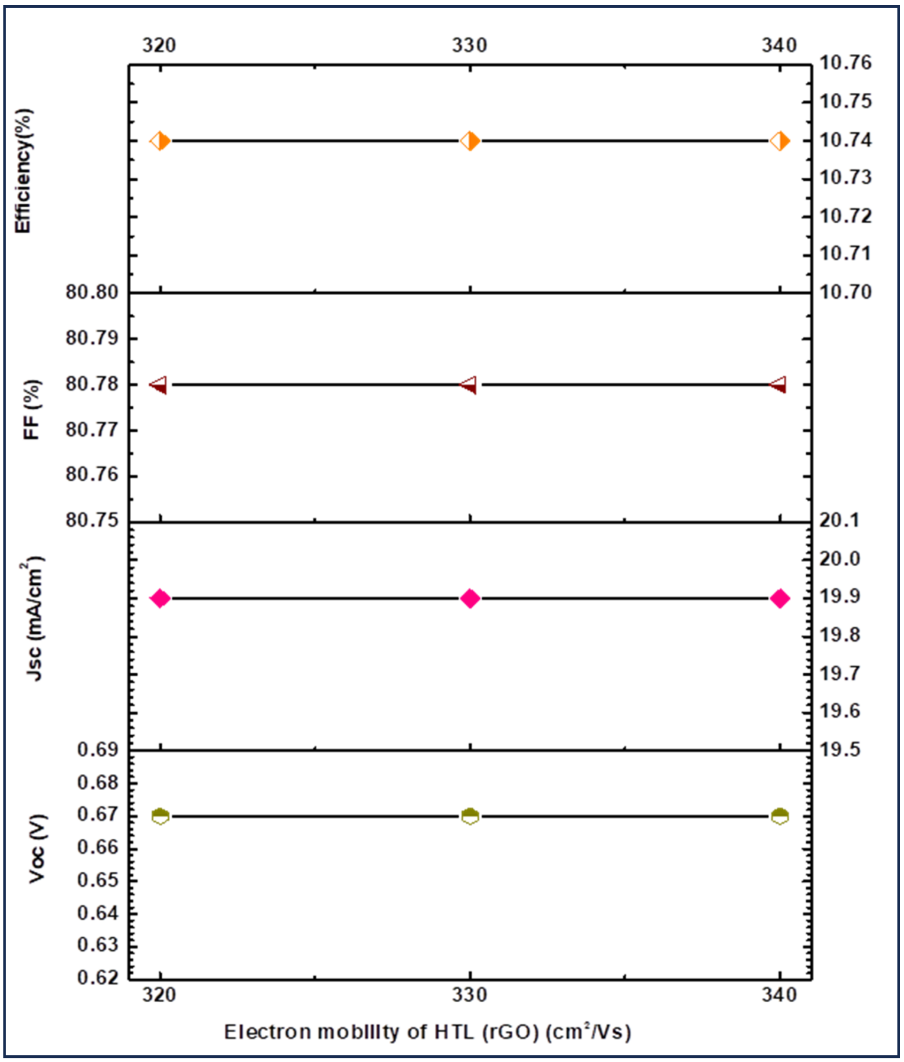


FIGURE 7.22: Influence of varying electron mobility of HTL on the device output parameters.

The variation in defect density of rGO from 1.9×10^9 to 1.9×10^{20} cm^{-3} was analyzed. V_{oc} remain constant at 0.67 V. J_{sc} decreased to 19.903 mA/cm^2, FF remained constant at 80.78% whereas, efficiency remained constant and surprisingly at 1.9×10^{20} cm^{-3} efficiency increased to 10.75%. Among all the HTLs used in the study, rGO was found to be the best HTL.

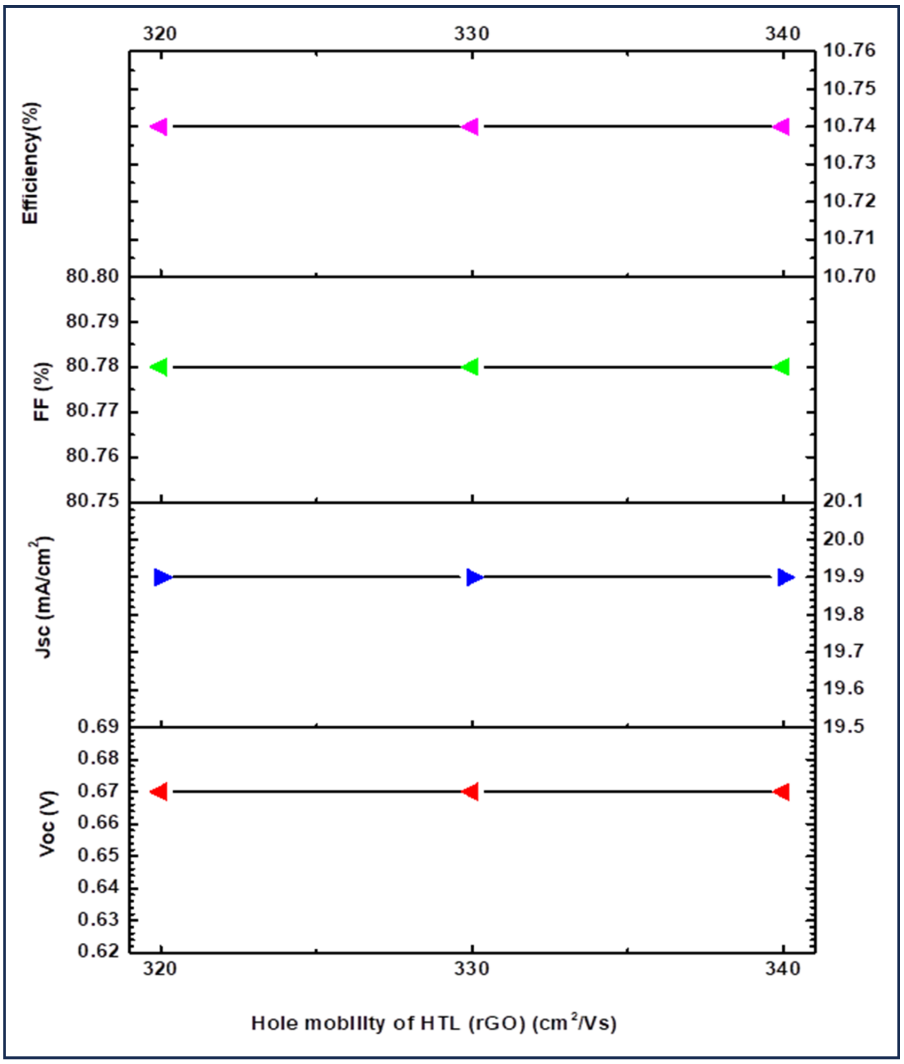


FIGURE 7.23: Influence of varying hole mobility of HTL on the device output parameters.

7.3.3.4 Influence of Varying Electron and Hole Mobilities of HTL

Fig. 7.22 and Fig. 7.23 displays the influence of variation of electron mobility and hole mobility of HTL on the device performance respectively.

The mobilities were varied from 3.2 $\times$ 10^2 to 3.4 $\times$ 10^2 cm^2/Vs. No significant changes were observed in the device performance. As both electron and hole mobilities were increased, V_{oc}, J_{sc}, FF and efficiency remained constant at 0.67 V, 19.90 mA/cm^2, 80.78% and 10.74% respectively. Mobilities of 3.2 $\times$ 10^2 cm^2/Vs is considered as a record high mobility attained for rGO.

7.3.3.5 Influence of Varying Thickness and Defect Density of ETL

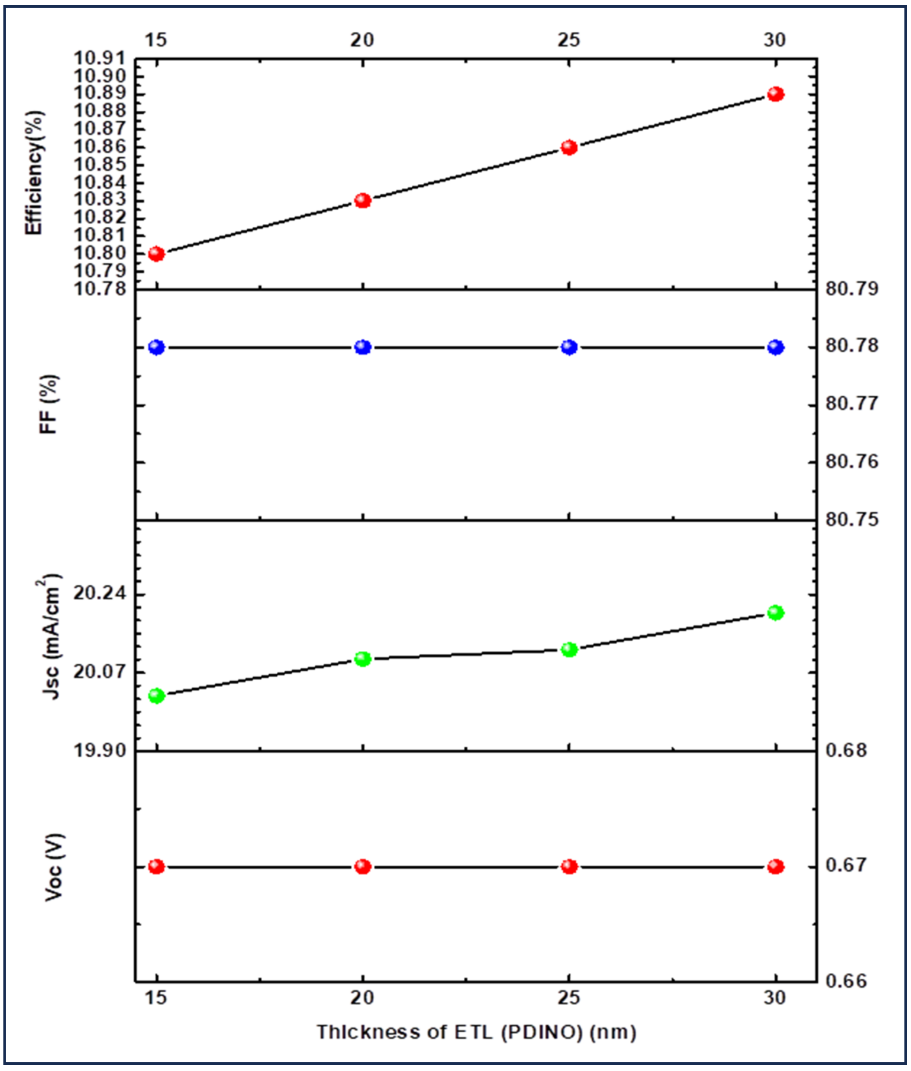


FIGURE 7.24: Influence of varying thickness of ETL on the device output parameters.

Fig. 7.24 and Fig. 7.25 displays the influence of varying thickness and defect density of ETL on the device performance respectively. The thickness of ETL was varied from 15 to 30 nm. The V_{oc} seemed to remain constant at 0.67 V, J_{sc} reaches 20.18 mA/cm^2, FF remained constant at 80.78% and efficiency reached 10.89%. A thicker ETL can facilitate better transport of electrons from the active layer to the cathode, reducing resistive losses and enhancing overall current flow. V_{oc} remained constant at 0.67 V, J_{sc} decreased to 19.80 mA/cm^2, FF surprisingly increased to 80.79% and efficiency decreased to 10.69%.

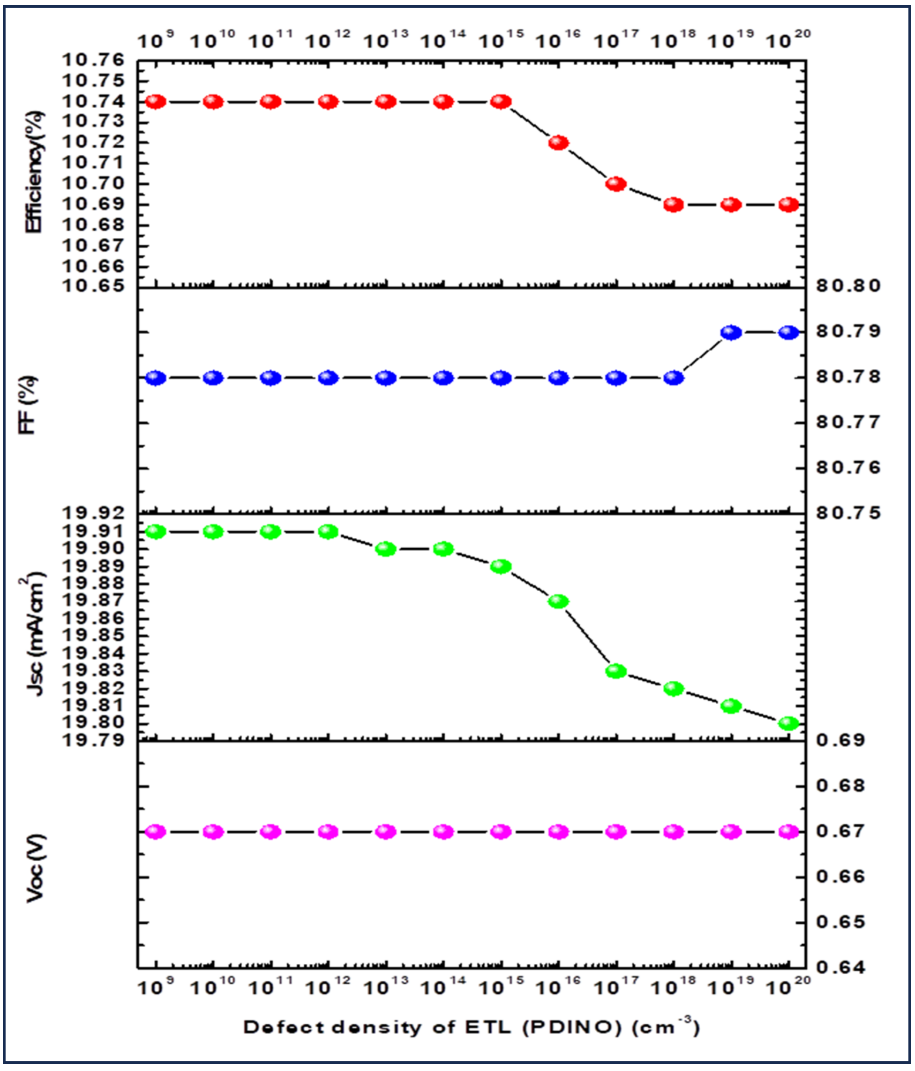


FIGURE 7.25: Influence of varying defect density of ETL on the device output parameters.

7.3.3.6 Influence of Varying Electron and Hole Mobilities of ETL

Fig. 7.26 and Fig. 7.27 displays the influence of varying electron and hole mobilities of ETL on the device performance respectively.

As the electron mobility was varied from 2×10^{-6} to 2.3×10^{-6} cm^2/Vs the V_{oc} and J_{sc} remained constant at 0.67 V and 19.90 mA/cm^2 respectively. Whereas, FF increased from 80.78% to 80.79% and efficiency remained constant at 10.74%. Furthermore, when the hole mobility was varied from 1×10^{-3} to 1.3×10^{-3} cm^2/Vs, V_{oc}, J_{sc}, FF and efficiency remained constant at 0.67 V, 19.90 mA/cm^2, 80.78% and 10.74%.

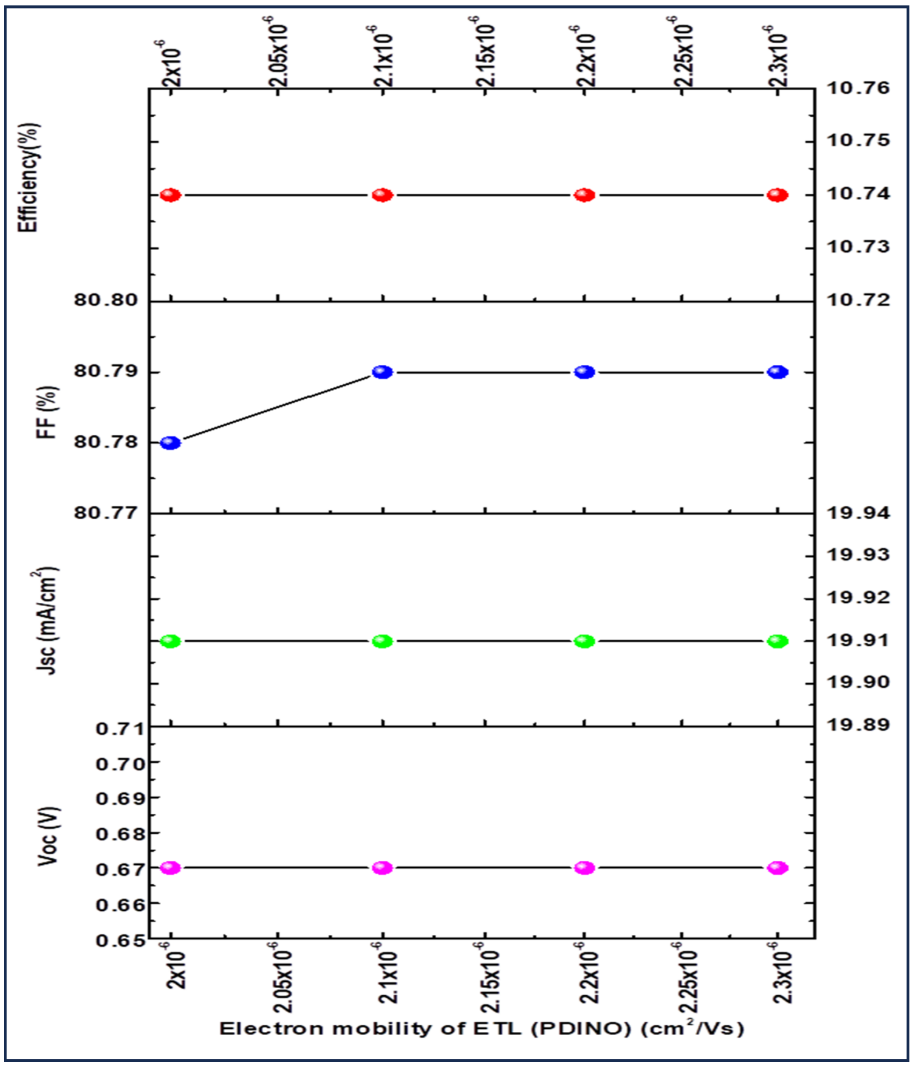


FIGURE 7.26: Influence of varying electron mobility of ETL on the device output parameters.

7.3.3.7 Influence of Varying Doping Densities of HTL and ETL

Figs. 7.28 to 7.31 display contour plots showing the influence of varying doping densities of HTL and ETL on V_{oc}, J_{sc}, FF and efficiency respectively. Acceptor density is marked on the x-axis and donor density is marked on the y-axis. Simultaneous influence of these two factors is analyzed using the contour plots. The acceptor doping density (N_A) and the donor doping density (N_D) of both HTL and ETL were varied and the change in device performance, were analyzed and studied. The N_A was varied from 1×10^{15} to 1×10^{18} cm^{-3} and the N_D was varied from 1×10^{20} to 1×10^{22} cm^{-3}. Highest efficiency of 10.74% was obtained.

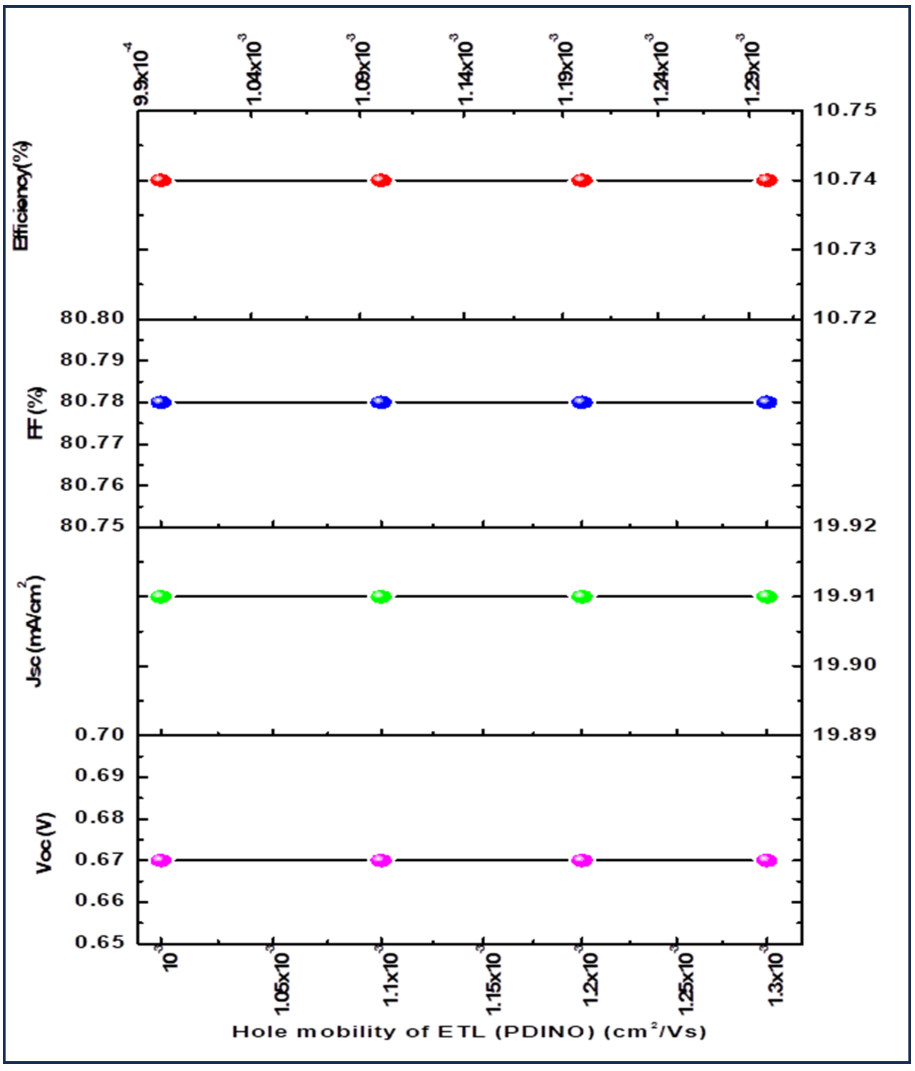


FIGURE 7.27: Influence of varying hole mobility of ETL on the device output parameters.

A similar trend in improving device performance by increasing the doping densities is observed in NFA based BHJOSC. The conductivity is enhanced by the higher density, which permits greater current flow and increased device efficiency. Doping introduces impurities that create additional energy states, thereby reducing the material's overall resistivity. However, it is important to balance doping levels since too much doping can result in defects that may impair performance.

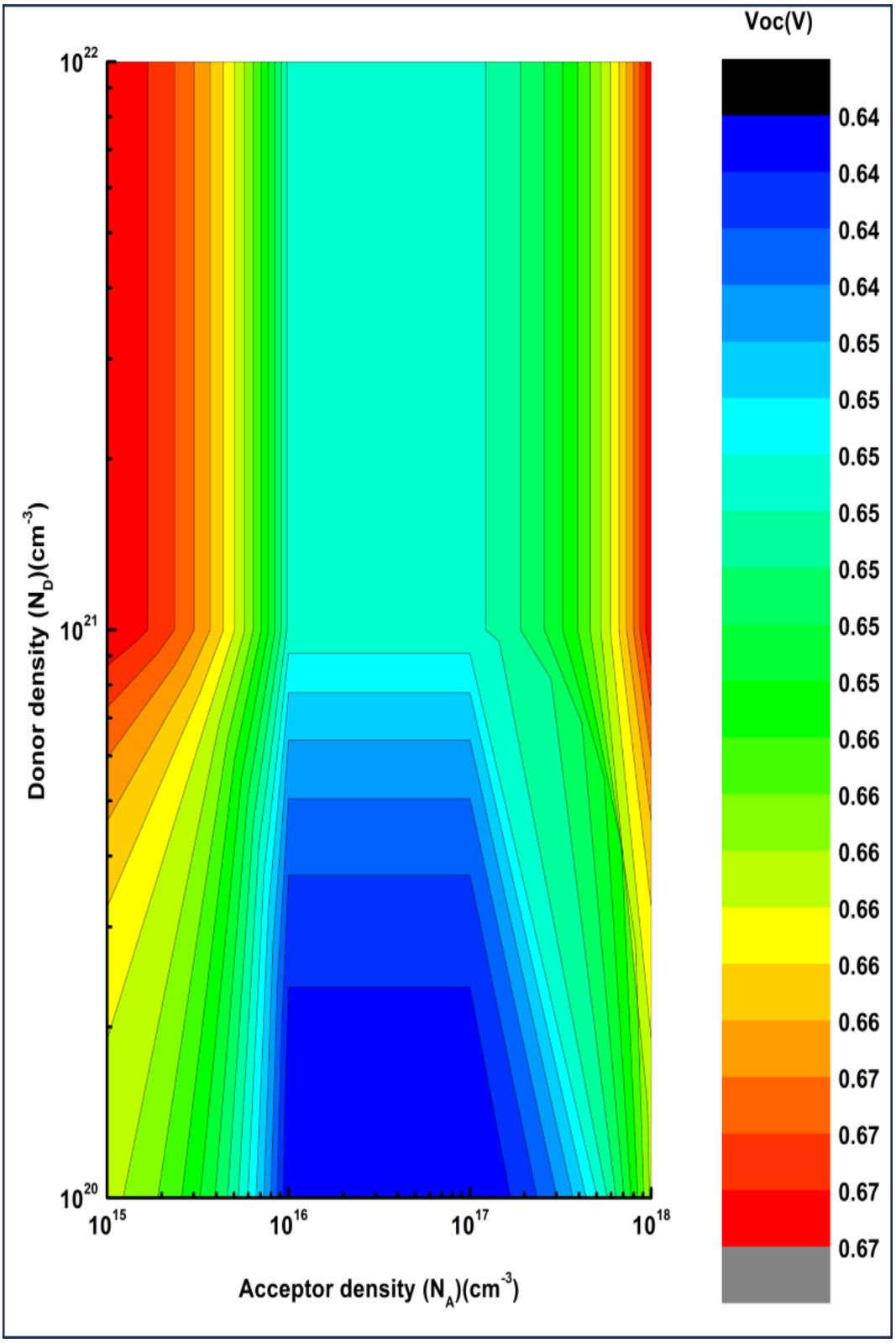


FIGURE 7.28: Influence of varying doping density of HTL and ETL on V_{oc}.

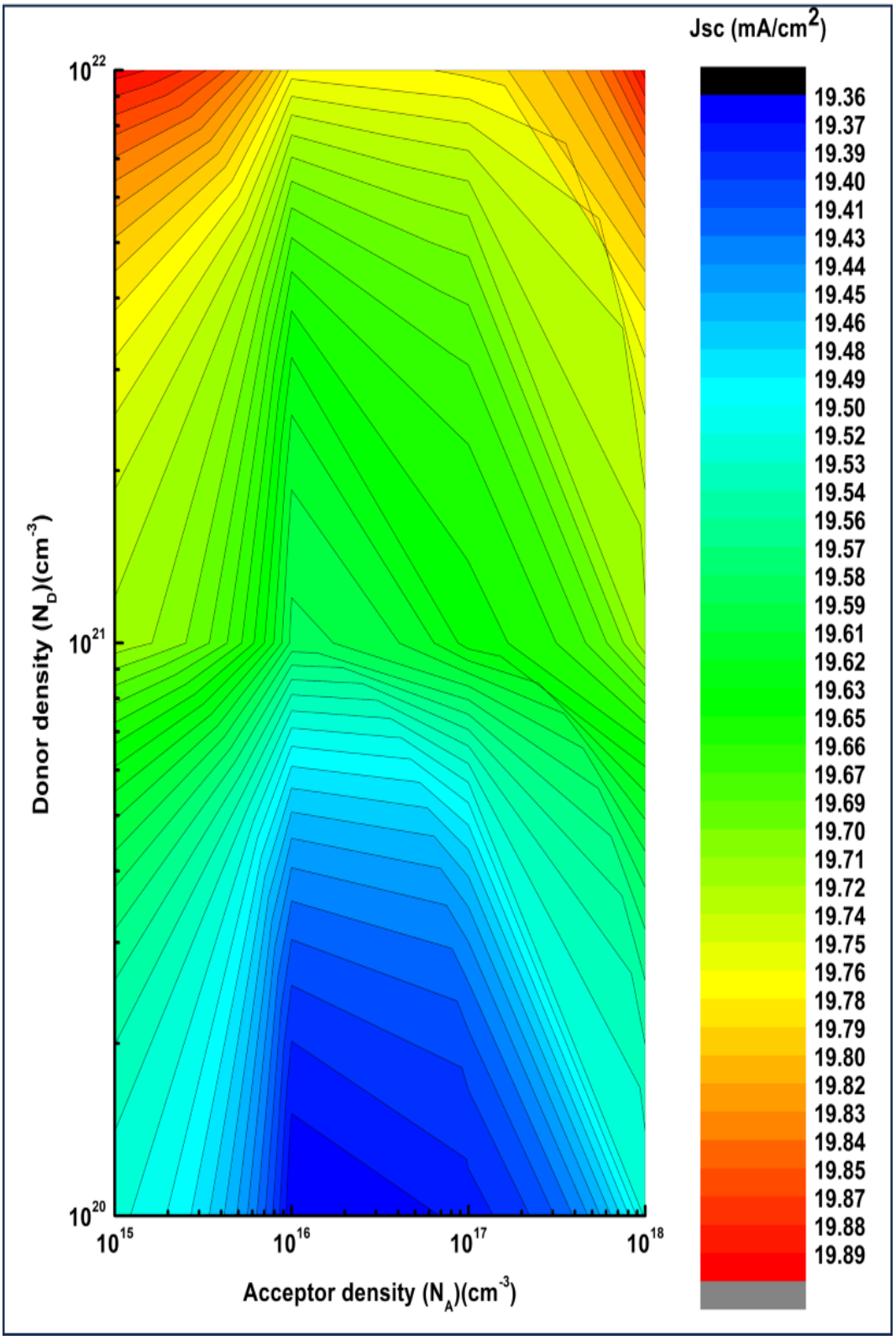


FIGURE 7.29: Influence of varying doping density of HTL and ETL on J_{sc}.

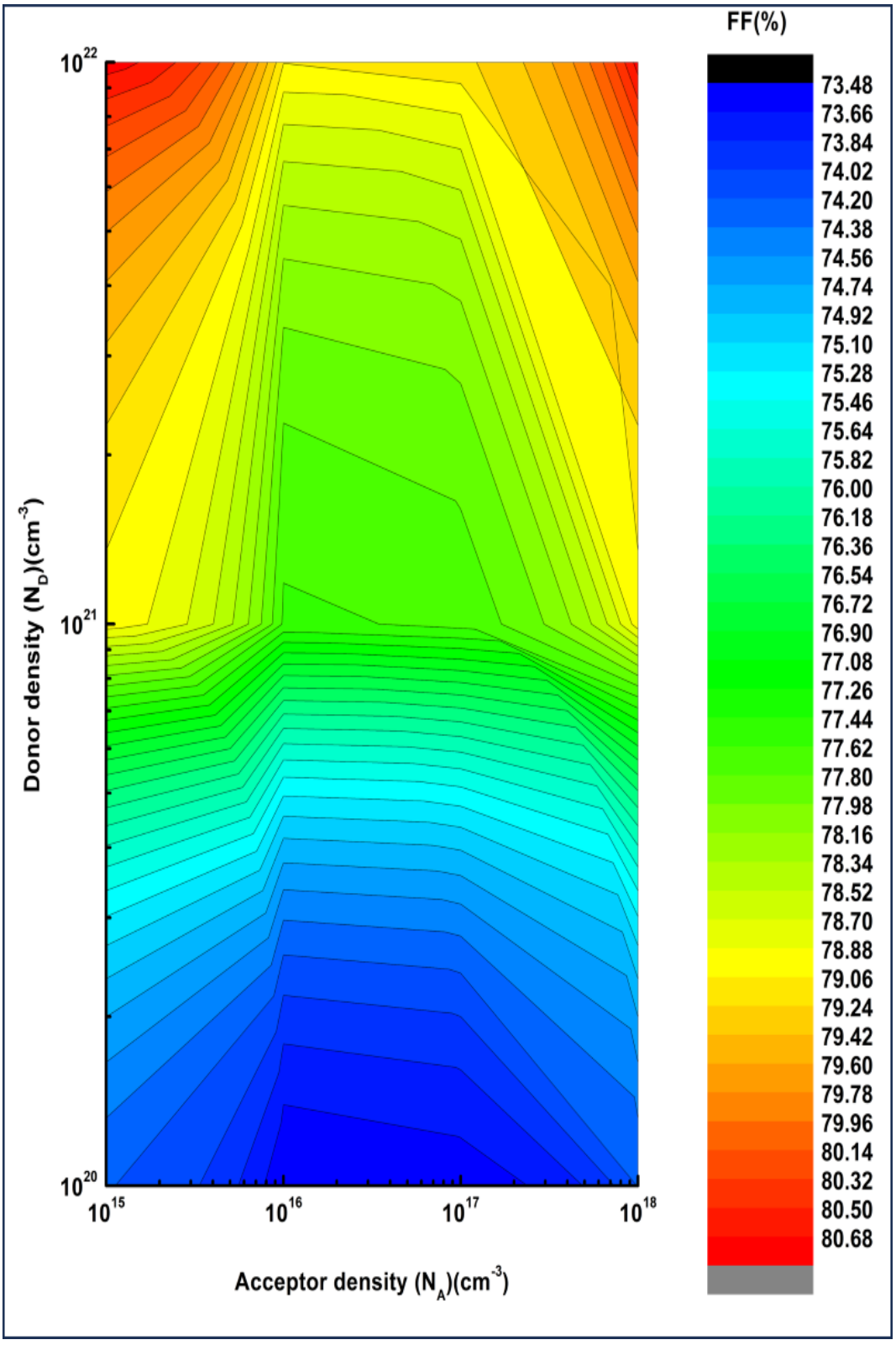


FIGURE 7.30: Influence of varying doping density of HTL and ETL on FF.

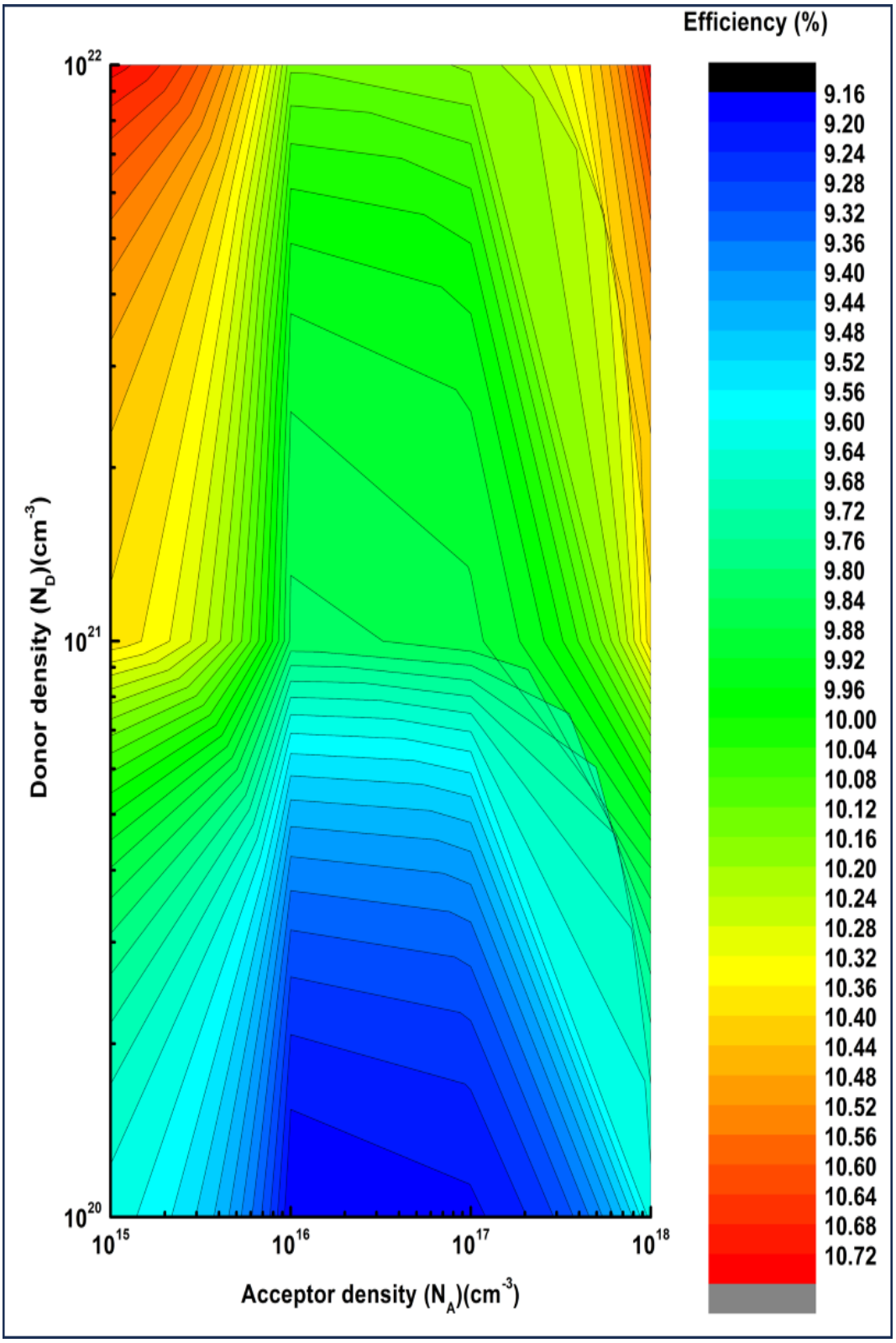


FIGURE 7.31: Influence of varying doping density of HTL and ETL on efficiency.

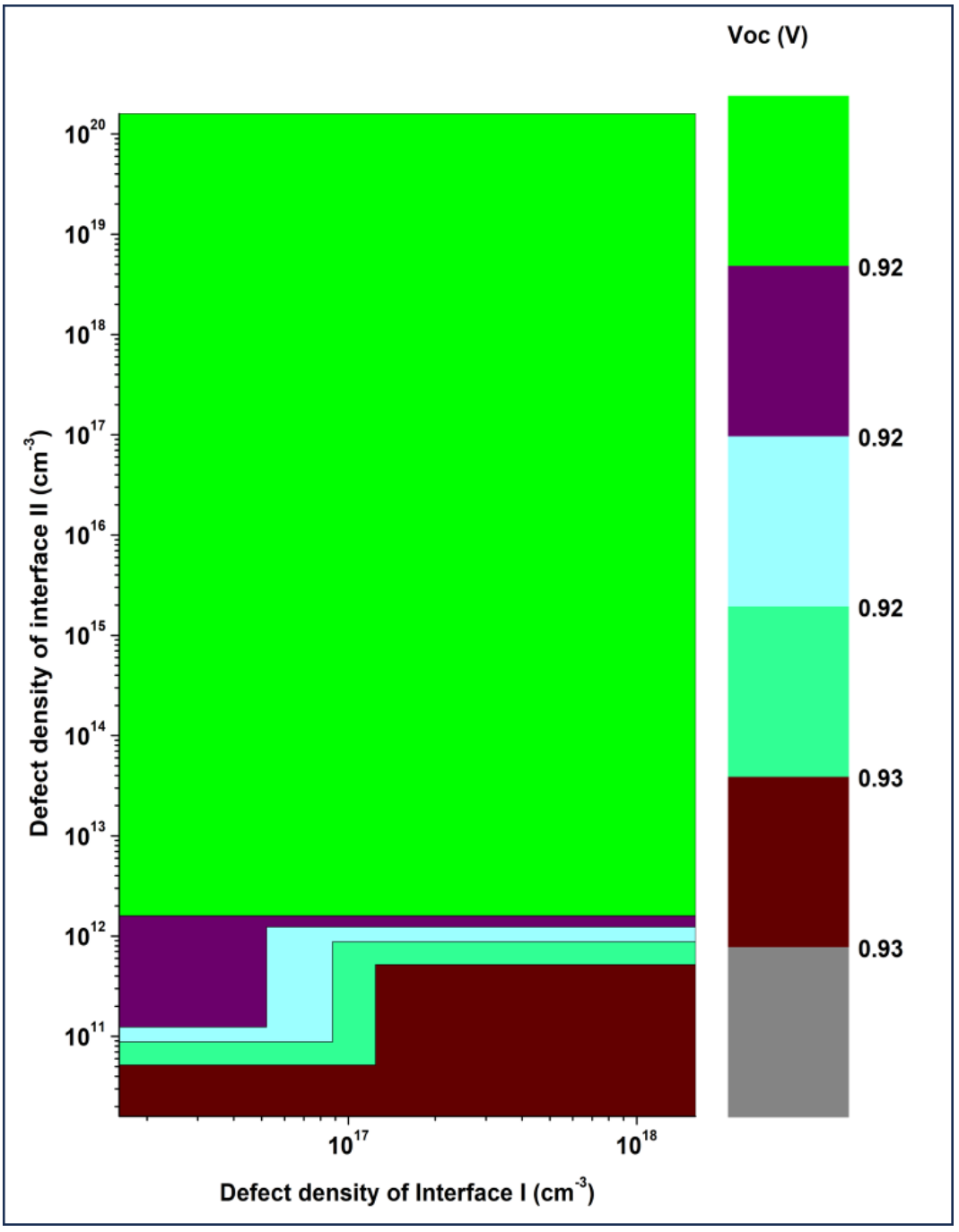


FIGURE 7.32: Influence of varying defect densities of interface I and II on V_{oc}.

7.3.3.8 Influence of Varying Interface Defects on the Device Performance

The interface defect I comprises of rGO/PBDB-T:INTIC and interface II comprises of PBDB-T:INTIC/PDINO. Figs. 7.32 to 7.35 display contour plots showing the influence of varying interface defects (I and II) on device output parameters V_{oc}, J_{sc}, FF, and efficiency

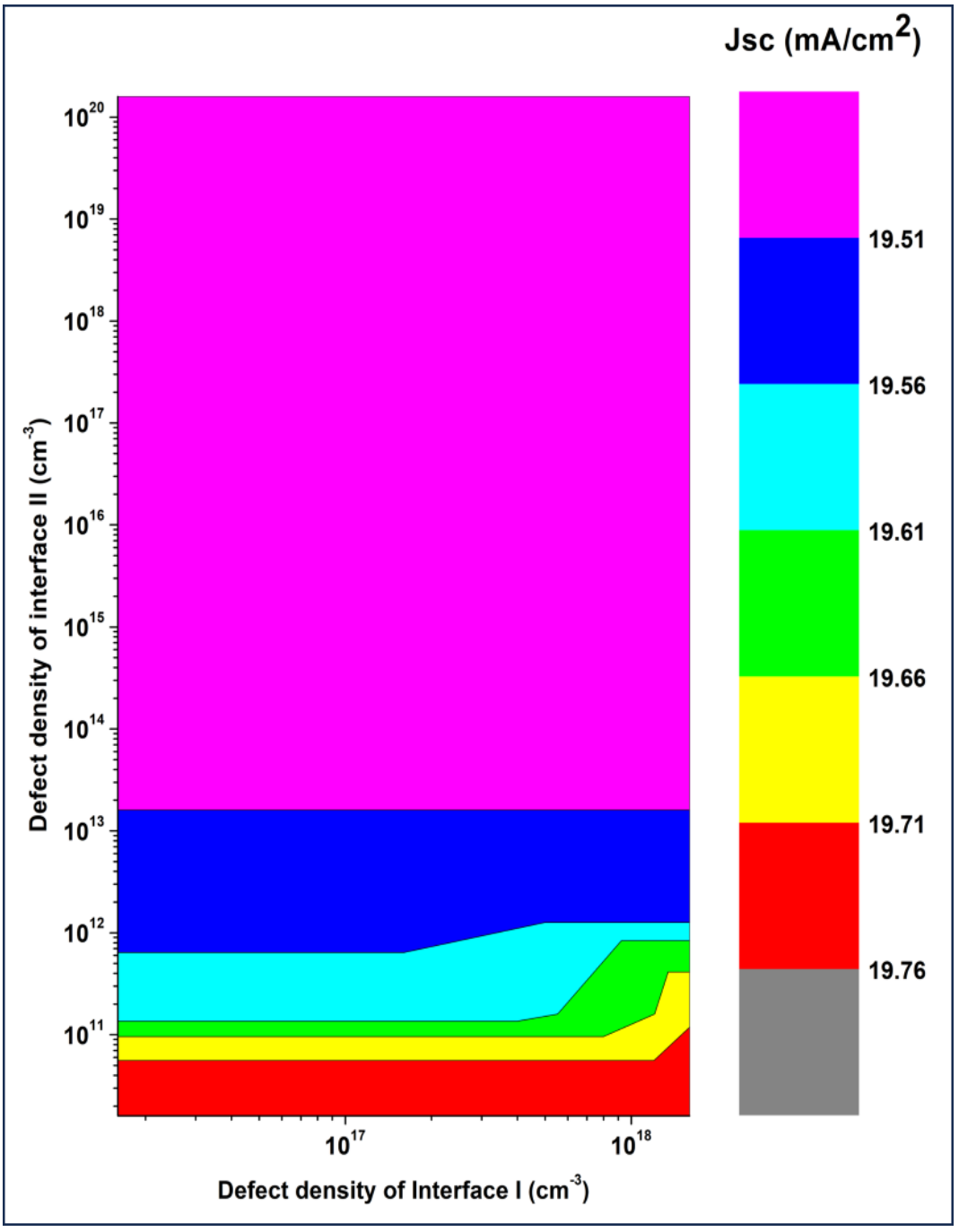


FIGURE 7.33: Influence of varying defect densities of interface I and II on J_{sc}.

respectively, in which x-axis represents defect density of interface I and y-axis represents defect density of interface II. Simultaneous influence of these two factors is analyzed using the contour plots. The interface I defect density was varied from 1.6×10^{16} to 1.6×10^{18} cm^{-2}. The interface II defect density was varied from 1.6×10^{10} to 1.6×10^{20} cm^{-2}. Highest efficiency of 12.86% was obtained.

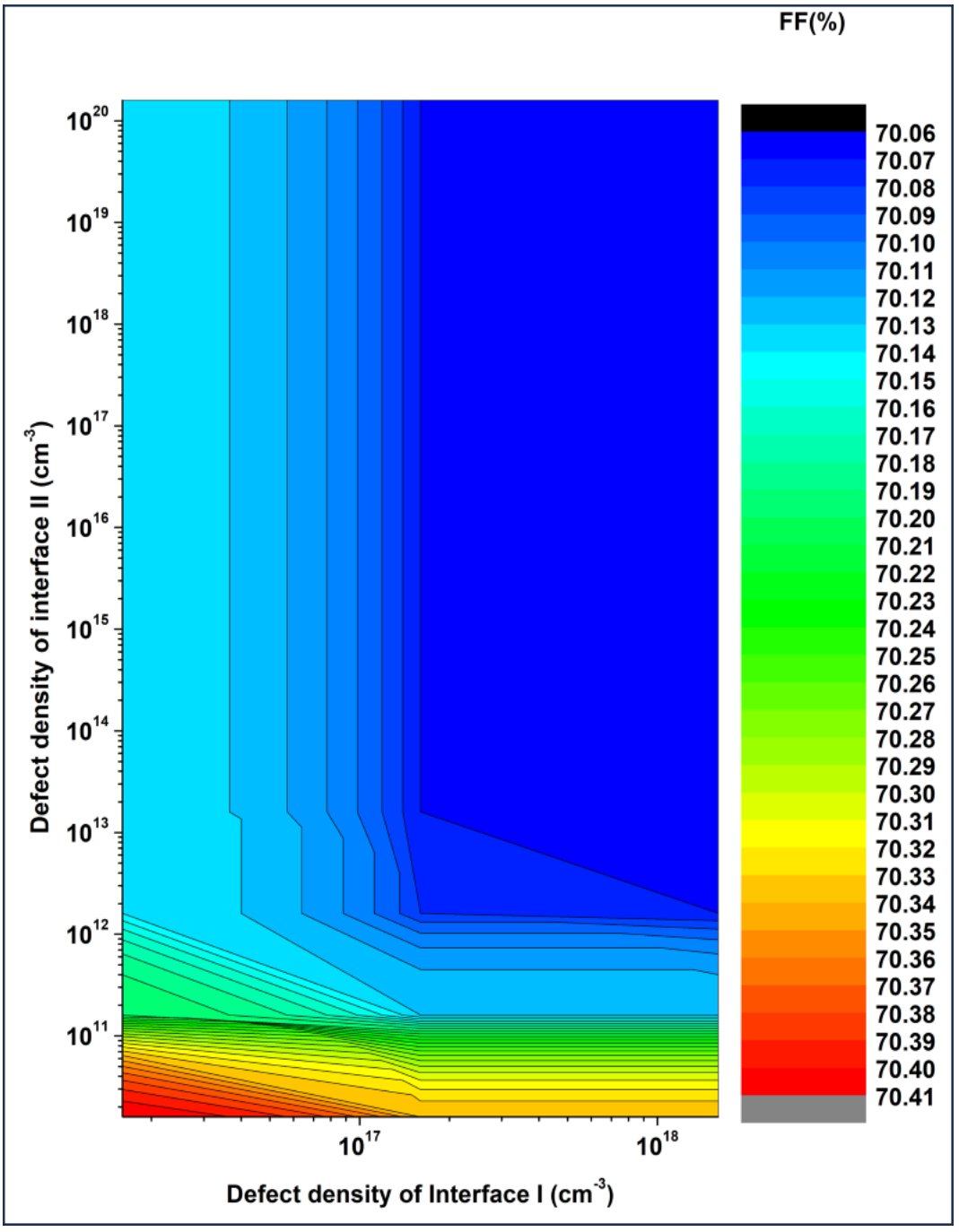


FIGURE 7.34: Influence of varying defect densities of interface I and II on FF.

Increased energy losses can result from defects that introduce states that trap carriers or produce sub band gap states. As a result V_{oc} and total efficiency decreased as a result. Reducing interface layer defect density will improve the device performance in OSCs.

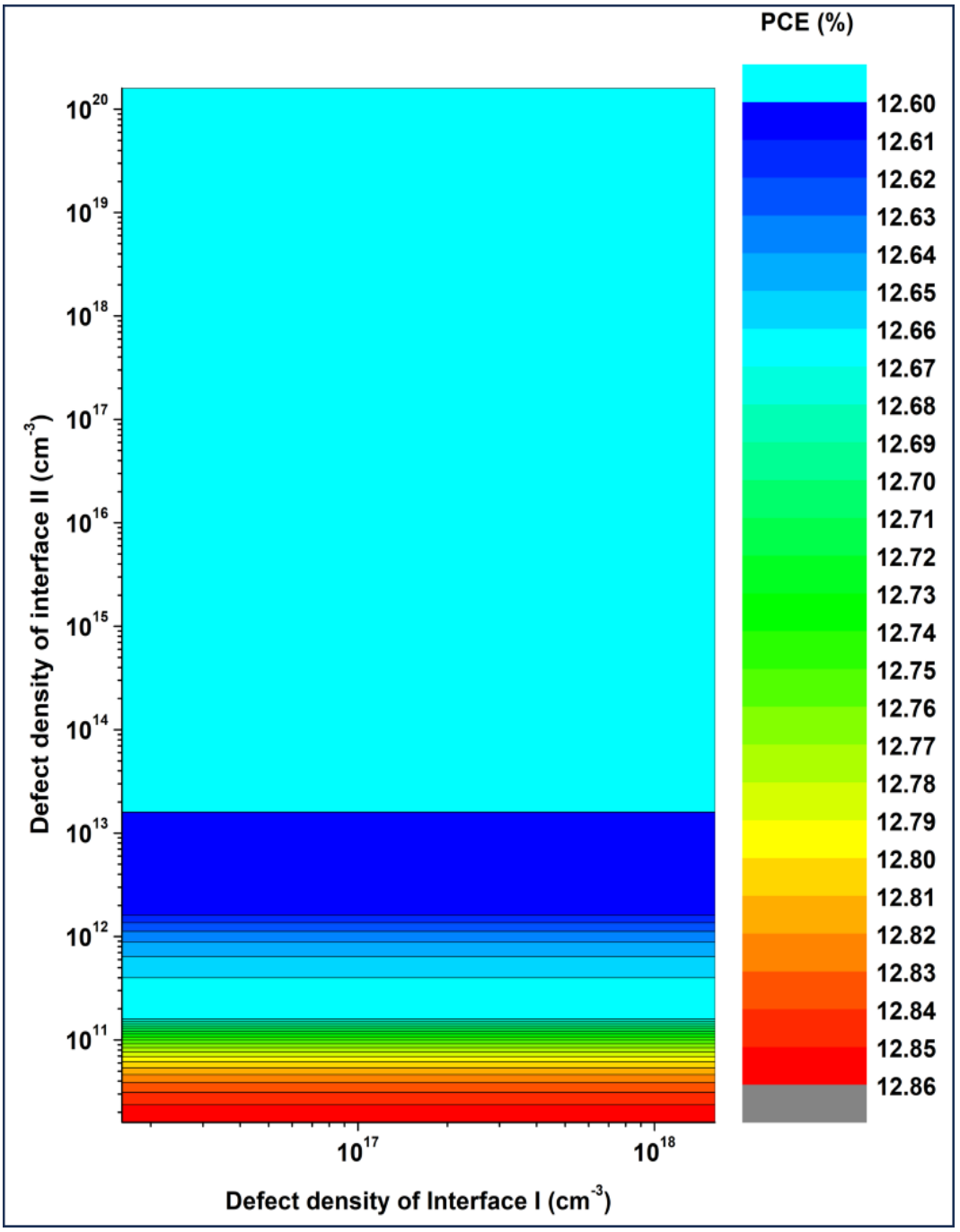


FIGURE 7.35: Influence of varying defect densities of interface I and II on efficiency.

Interface defects may act as sites for charge carriers (electrons and holes) to recombine and may produce energy barriers, that prevents motion of charge carriers. Overall efficiency declines when carriers have these defects because they are prone to recombine rather than contribute to current generation.

This may reduce current production by blocking the movement of electrons and holes to their respective electrodes. Reduced charge mobility can result from interface defects that disrupt the ordered structure of the organic materials. As carriers struggle to reach the electrodes, poor transport characteristics lead to decreased efficiency.

Optimised input and output parameters of the device structure is listed in Table 7.7 and Table 7.8 respectively. The optimized input parameters selected for the final simulation are suitable for real-world applications, as they fall within physically realistic ranges commonly used in experimental studies of SCs. These parameter values are consistent with those reported in the literature for similar devices. Furthermore, the obtained output results are within the expected range for practical BHJOSC applications and show good agreement with previously reported experimental BHJOSC performance.

TABLE 7.7: Optimized input parameters of the device structure simulated.

Layers	Thickness (d) (nm)	Defect density (N_t) (cm^{-3})	Electron mobility (μ_e) (cm^2/Vs)	Hole mobility (μ_h) (cm^2/Vs)
PBDB-T:INTIC (Active layer)	100	5×10^{10}	6.02×10^{-4}	7.72×10^{-4}
rGO (HTL)	22	1.9×10^{9}	3.2×10^{2}	3.2×10^{2}
PDINO (ETL)	30	1×10^{9}	2.3×10^{-6}	1×10^{-3}

TABLE 7.8: Optimized output parameters of the simulated device structure.

V_{oc} (V)	J_{sc} (mA/cm^2)	FF (%)	Efficiency (%)
0.73	19.97	76.95	11.22

Optimization of this device structure is done and V_{oc} of 0.73 V, J_{sc} of 19.97 mA/cm^2, FF of 76.95% and efficiency of 11.22% is obtained.

7.4 Comparison of Device Performance of PBDB-T:INTIC BHJOSCs

PBDB-T:INTIC is a rarely studied SM-NFA based BHJOSC, making our investigation unique, and the incorporation of graphene derivatives in its interfacial layers adds further novelty, as no experimental or simulation studies on such devices have been reported to date. Table 7.9 compares our findings with previously reported studies on PBDB-T:INTIC BHJOSCs. Comparing the studies listed in the table, our simulated device achieves performance closely comparable to the experimental work, while the use of rGO as the hole transport layer results in a better overall device configuration.

TABLE 7.9: Comparison table of PBDB-T:INTIC NFABHJOSCs.

Experimental/simulation	Active layer	HTL	ETL	Cathode	Anode	V_{oc} (V)	J_{sc} (mA/cm^2)	FF (%)	Efficiency (%)	Reference
Experimental	PBDB-T:INTIC	MoO_3	ZnO	Ag	ITO	0.847	19.42	67.89	11.08	[145]
Simulation	PBDB-T:INTIC	PEDOT:PSS	PDINO	Al	ITO	0.798	19.88	78.68	12.49	[344]
Simulation (Our work)	PBDB-T:INTIC	PEDOT:PSS:rGO	n-graphene	Al	ITO	0.561	20.882	54.58	6.39	[382]
Simulation (This work)	PBDB-T:INTIC	rGO	PDINO	Al	ITO	0.73	19.97	76.95	11.22	[385]

7.5 Conclusion

We performed a simulation study of a unique SM-NFA-based BHJOSC with the structure ITO/PEDOT:PSS:rGO/PBDB-T:INTIC/n-graphene/Al, investigating the impact of input parameters like thickness, band gap, and electron affinity of the active layer. The study highlights the use of PEDOT:PSS:rGO composite as the HTL and n-graphene as the ETL achieving, V_{oc} of 0.5609 V, J_{sc} of 20.882272 mA/cm^2 and FF of 54.58% and an efficiency of 6.39%. The optimal parameters for the active layer were 100 nm thickness, 1.1 eV band gap, 3.95 eV electron affinity, and a defect density of 1×10^{10} cm^{-3}. Additionally, we explored a novel device structure, ITO/HTL/PBDB-T:INTIC/ETL/Al, using graphene derivatives as HTLs and ETLs to enhance performance and stability, considering factors like layer thickness, defect density, and charge mobilities.

We investigated the performance of ITO/HTL/PBDB-T:INTIC/ETL/Al novel device structure using graphene derivatives as HTLs and various ETLs. This study introduces a structure with graphene derivatives to enhance performance and stability, considering factors like layer thickness, defect density charge mobilities, doping densities and interface defect densities. After optimization, the ITO/rGO/PBDB-T:INTIC/PDINO/Al configuration achieved a V*oc* of 0.73 V, J*sc* of 19.97 mA/cm^2, FF of 76.95%, and efficiency of 11.22%. INTIC's lower band gap and strong NIR absorption improve charge generation, and rGO proves superior to PEDOT:PSS as an HTL due to its tunable properties, making it the ideal choice for NFA-based BHJOSCs.

Chapter 8

Conclusion

This chapter summarizes our extensive research study done on BHJOSCs. The major inferences acquired from the studies are discussed. The significant results attained from the simulation studies on P3HT:PCBM BHJOSCs, PBDB-T:NCBDT BHJOSCs, and PBDB-T:INTIC BHJOSCs with diverse HTLs and ETLs are highlighted.

The research study focusses on designing and simulating highly efficient BHJOSCs using SCAPS-1D. Aiming to improve device stability, charge transport, and efficiency. Graphene derivatives based interfacial layers are incorporated into these device structures and simulation studies are conducted. Numerical investigation of these BHJOSCs with diverse ETLs are carried out. Furthermore, the influence of varying input parameters of each layer on device performance are analyzed.

8.1 Major Inferences

Numerical simulation studies of BHJOSCs with FA and NFA materials are conducted in our study. P3HT:PCBM based BHJOSCs, PBDB-T:NCBDT based BHJOSCs, and PBDB-T:INTIC based BHJOSCs were numerically designed, simulated, and analysed.

P3HT:PCBM, an FA material based BHJOSC, is the most extensively studied active layer in BHJOSCs. However, its unavoidable drawbacks have urged researchers to shift toward NFA material based BHJOSCs. PBDB-T:NCBDT, an SM-NFA based BHJOSC is regarded as a superior and desirable option compared to the FAs (P3HT:PCBM). NCBDT is an SM-NFA material with very limited experimental and simulation studies available.

Another emerging material, PBDB-T:INTIC is a BHJ blend that we have used as a photoactive material for our numerical investigations. INTIC is also, an SM-NFA whose band gap is tunable and its absorption range extends into the NIR region. NFA based BHJOSCs can be considered a superior option compared to FA based BHJOSCs, since improved device performance is attained for NFA based BHJOSCs.

Improving the performance and stability of BHJOSCs has been a primary focus since the early years of research. Incorporation of interfacial layers in the BHJOSCs improves charge flow and eventually enhances device performance. The state of the art HTL-PEDOT: PSS has been introduced for so long in BHJOSCs. However, its demerits - namely, hygroscopicity and acidic nature have been constant issues affecting the stability of BHJOSCs. Hence, graphene derivatives have been introduced as alternative HTLs. Pure graphene, GO, rGO, p-graphene and PEDOT:PSS:rGO composite are used as HTLs.

Key Findings

P3HT:PCBM BHJOSCs

- After extensive numerical simulation studies done on P3HT:PCBM BHJOSCs with graphene, GO and rGO as HTL, with diverse ETLs and different cathodes, V_{oc} of 0.7909 V, J_{sc} of 26.61 mA/cm^2, FF of 56.99%, and highest efficiency of 12.00% were achieved for the configuration ITO/rGO/P3HT:PCBM/LiF/Ca, where ITO was used as anode, rGO as the HTL, LiF as the ETL and Ca as the cathode.

PBDB-T:NCBDT BHJOSCs

- Simulation studies of PBDB-T:NCBDT with graphene derivatives (graphene, GO, rGO and p-graphene) as HTLs and diverse ETLs yielded promisisng results. After optimization of the novel device configuration ITO/rGO/PBDB-T:NCBDT/PDINO/Al, V_{oc} of 0.8878 V, J_{sc} of 25.407228 mA/cm^2, FF of 77.45%, and peak efficiency of 17.47% were attained where, ITO was used as the anode, rGO as the HTL, PDINO as the ETL and Al as the cathode.
- Among the studies carried out on PBDB-T:NCBDT BHJOSC, a V_{oc} of 1.3942 V, J_{sc} of 25.929526 mA/cm^2, FF of 53.92%, and enhanced efficiency of 19.49% were achieved for the novel double HTL configuration ITO/PEDOT:PSS/MoS_2/PBDB-T:NCBDT/PDINO/Al in which PEDOT:PSS and MoS_2 are the two HTLs used. ITO was used as anode, PDINO as the ETL and Al as the cathode.

PBDB-T:INTIC BHJOSCs

- A simulation study of PBDB-T:INTIC BHJOSC with ITO as the anode, PEDOT:PSS:rGO composite as the HTL, n-graphene as the ETL, and Al as the cathode exhibited a V_{oc} of 0.5609 V, J_{sc} of 20.882272 mA/cm^2, FF of 54.58%, and a maximum efficiency of 6.39%.
- Extensive numerical simulation studies of PBDB-T:INTIC BHJOSC, with diverse HTLs and ETLs show a V_{oc} of 0.73 V, J_{sc} of 19.97 mA/cm^2, FF of 76.95%, and efficiency of 11.22% for the device structure ITO/rGO/PBDB-T:INTIC/PDINO/Al with ITO as anode, rGO as HTL, PDINO as ETL and Al as cathode.

All these studies consistently demonstrate that rGO is a superior HTL among all the graphene derivatives, that can be incorporated into BHJOSCs as interfacial layers. Additionally, the graphene derivative GO, is at cutting-edge research in BHJOSCs and is given considerable preference in ongoing studies. The findings also reveal that PDINO acts as an effective and suitable ETL in BHJOSCs.

It is evident from the results and analysis that, graphene derivatives can be successfully incorporated as interfacial layers (both HTLs and ETLs), cementing its inevitable role in the advancement of BHJOSCs.

8.1.1 Limitations and Future Directions

The present work is primarily based on SCAPS-1D simulations and therefore inherits the limitations of one-dimensional device modelling. The simulations do not explicitly account for nanoscale D-A morphology, excitonic processes, energetic disorder, charge-transfer states, or environmental degradation phenomena that strongly influence the performance and stability of practical BHJOSCs. Furthermore, the predicted device performance depends on the accuracy of the material parameters employed in the simulations. Consequently, the obtained results should be regarded as theoretical design guidelines that require experimental validation.

Despite these limitations, the present study identifies several high-performance BHJOSC architectures with strong potential for practical realization.

- ITO/rGO/P3HT/LiF/Ca (12.00%)
- ITO/rGO/PBDB-T/PDINO/Al (17.47%)
- ITO/PEDOT/MoS_2/PBDB-T/PDINO/Al (19.49%)
- ITO/rGO/PBDB-T/PDINO/Al (11.22%)

Among the investigated devices, the optimized configurations listed above exhibited superior PV performance and therefore represent promising candidates for experimental fabrication. Particular emphasis should be placed on validating the use of rGO as a replacement for conventional PEDOT:PSS HTLs and investigating the effectiveness of PDINO as an ETL in non-fullerene BHJOSCs.

Future experimental studies should focus on developing high-quality graphene-derivative interfacial layers with controlled thickness, conductivity, work function, and surface morphology to achieve efficient charge extraction and minimize interfacial recombination. Detailed characterization using structural, optical, and electrical techniques should be carried out to correlate film morphology, interface quality, and charge transport with device performance. In addition, long-term operational, thermal, and environmental stability studies are essential to evaluate the practical viability of the proposed architectures. Further investigations on scalable fabrication techniques, flexible substrates, tandem device integration, and environmentally benign processing methods would facilitate the translation of the present simulation results into high-efficiency, stable, and commercially viable BHJOSCs.

Chapter 9

Recommendations and Scope for Future Work

Recommendations for future research studies are provided in this chapter, grounded in the outcomes of the studies carried out.

9.1 Recommendations for Future Work

The present study has demonstrated the promising role of graphene and graphene derivatives, as transport layers in BHJOSCs and has achieved efficiency improvements with optimized device architectures. However, there are several areas to explore in this research.

- **Experimental validation of simulated device**
  The present study focuses on numerical simulations. Future studies can be carried out on fabrication and characterisation of the proposed device configurations to confirm their real-world applicability.

- **Learning underlying mechanisms**
  The underlying mechanisms of FA and NFA based BHJOSCs can be examined and analysed using these simulation techniques. The influence of varying interior parameters of the layers on the device performance can be studied.

- **Analysis on degradation and stability**
  Long-term stability and deterioration have been an unresolved issue in BHJOSCs. Future studies can execute systematic studies on the operational stability of devices employing graphene derivatives.

- **Exploring novel materials for interfacial layers and active layer**
  Further investigations on other NFAs with tunable band gaps and broader absorption spectra could unlock higher efficiencies and stability. Exploring the possibility of incorporation of more 2D materials as interfacial layers in BHJOSCs can be carried out.

Bibliography

[1] International Energy Agency (IEA), "World Energy Outlook 2023", 2023.

[2] S. Banales *et al.*, "Enabling the future of energy through digitalization," *IEEE Industry Applications Magazine*, 2020.

[3] L. Zuo *et al.*, "Renewable energy and digitalization: Future perspectives," *Renewable and Sustainable Energy Reviews*, 2025.

[4] W. Bingxin *et al.*, "Digitalization trends and impacts on global power systems," *Energy Reports*, 2025.

[5] D. Simion *et al.*, "Digitalization and its role in energy transition," *Energy and AI*, 2023.

[6] M. Mondejar *et al.*, "Digitalization for a sustainable energy future," *Renewable and Sustainable Energy Reviews*, 2021.

[7] Z. Ghasemian *et al.*, "An overview of the global energy sector: Trends and policy implications," *Energy Policy*, 2020.

[8] T. Kober *et al.*, "Global energy demand scenarios: Challenges and prospects," *Energy Strategy Reviews*, 2020.

[9] R. G. Newell *et al.*, "Global energy outlooks comparison: Modeling approaches and policy implications," *Energy Economics*, 2019.

[10] J. Cook *et al.*, "Trends in international energy use and policy," *International Journal of Energy Research*, 2021.

[11] J. J. Conti *et al.*, "International energy outlook 2016," *U.S. Energy Information Administration*, 2016.

[12] P.-R. Bauquis, "Reappraisal of global energy demand and supply perspectives," *Energy Policy*, 2001.

[13] D. I. Stern, "Energy transition and future global energy demand," *Nature Energy*, 2019.

[14] A. Yadav and S. S. Chandel, "Prospects and challenges of renewable energy in india: A review," *Renewable and Sustainable Energy Reviews*, vol. 81, pp. 1–11, 2019.

[15] A. K. Mishra and B. Behera, "Socio-economic impact of solar energy on rural development in india," *Energy Policy*, vol. 92, pp. 302–312, 2016.

[16] T. Hayat, J. Khan, A. Farooq, and N. U. Khan, "Solar energy: Potential and future prospects in pakistan," *Renewable and Sustainable Energy Reviews*, vol. 81, pp. 1129–1137, 2019.

[17] C. Greacen, "Photovoltaic systems for rural electrification in thailand: A case study," *Energy Policy*, vol. 19, no. 5, pp. 510–521, 1991.

[18] E. Aranovitch, "European solar market trends and opportunities," *Renewable Energy*, vol. 1, no. 2, pp. 137–145, 1990.

[19] A. Rogalski, Z. Bielecki, J. Mikolajczyk, and J. Wojtas, "Ultraviolet photodetectors: From photocathodes to low-dimensional solids," *Sensors*, May 2023.

[20] J. Haddock and J. Duffie, *Solar Energy: Principles of Thermal Collection and Storage*. McGraw-Hill, 1991.

[21] A. L. Dyer and B. C. Thompson, "Organic photovoltaics: Principles and techniques for nanostructure design," *Materials Today*, vol. 21, no. 6, pp. 566–578, 2018.

[22] J. A. Nelson, *The Physics of Solar Cells*. Properties of Semiconductor Materials, London: Imperial College Press, 1st edition, 384 pages. 2003.

[23] J. C. Bernede, "Organic photovoltaic cells: history, principle and techniques," *Journal of the Chilean Chemical Society*, vol. 53, no. 3, pp. 1549–1564, 2008.

[24] P. Würfel, "Photovoltaic principles and organic solar cells," *Chimia*, vol. 61, no. 12, pp. 770–770, 2007.

[25] H. J. El-Khozondar, R. J. El-Khozondar, R. Al Afif, and C. Pfeifer, "Modified solar cells with antireflection coatings," *International Journal of Thermofluids*, vol. 11, p. 100103, 2021.

[26] C. Ji, W. Liu, Y. Bao, X. Chen, G. Yang, B. Wei, F. Yang, and X. Wang, "Recent applications of antireflection coatings in solar cells," in *Photonics*,MDPI, vol. 9, p. 906, 2022.

[27] S. Calnan, "Applications of oxide coatings in photovoltaic devices," *Unspecified Journal or Preprint*, 2014.

[28] W. Shockley, "The theory of p-n junctions in semiconductors and p-n junction transistors," *Bell system technical journal*, vol. 28, no. 3, pp. 435–489, 1949.

[29] W. Barrik and M. S. Shur, "Depletion-region width of p–n junction under high forward-bias conditions," *Proc. IEE*, vol. 126, no. 5, pp. 409–414, 1979.

[30] D. Krambeck, "Characteristics of junction diodes." All About Circuits, 2016.

[31] W. Shockley and H. J. Queisser, "Detailed balance limit of efficiency of p–n junction solar cells," *Journal of Applied Physics*, vol. 32, no. 3, pp. 510–519, 1961.

[32] M. A. Green, "Solar cell fill factors: General graph and empirical expressions," *Solid-State Electronics*, vol. 24, pp. 788–789, 1981.

[33] S. Hubbard, "Recombination," *Photovoltaic Solar Energy: From Fundamentals to Applications*, pp. 39–46, 2016.

[34] X. Chen, *Surface Recombination in Metal Halide Perovskites*, World Scientific, ch. Chapter 2, pp. 61–79, 2022.

[35] A. E. Becquerel, "Mémoire sur les effets électriques produits sous l'influence des rayons solaires," *Comptes Rendus*, vol. 9, pp. 561–567, 1839.

[36] W. Smith, "Effect of light on selenium during the passage of an electric current," *Nature*, vol. 7, p. 303, 1873.

[37] A. Pochettino, "Sul fenomeno fotoelettrico nei composti organici," *Nuovo Cimento*, vol. 11, pp. 37–49, 1906.

[38] M. Volmer, "Über die photoelektrizität in verschiedenen stoffen," *Annalen der Physik*, vol. 346, no. 4, pp. 775–795, 1913.

[39] D. M. Chapin, C. S. Fuller, and G. L. Pearson, "A new silicon p-n junction photocell for converting solar radiation into electrical power," *Journal of Applied Physics*, vol. 25, no. 5, pp. 676–677, 1954.

[40] R. H. Bube, "Photoconductivity in organic materials," *Physical Review*, vol. 121, no. 3, pp. 745–755, 1961.

[41] G. A. Chamberlain, "Organic solar cells: A review," *Solar Cells*, vol. 8, no. 1, pp. 47–83, 1983.

[42] A. Goetzberger, C. Hebling, and H.-W. Schock, *Photovoltaic Materials, History, Status and Outlook*, Materials Science and Engineering: R: Reports, vol. 40, 2003.

[43] S. E. Shaheen, C. J. Brabec, F. Padinger, T. Fromherz, and N. S. Sariciftci, "2.5% efficient organic plastic solar cells," *Applied Physics Letters*, vol. 78, no. 6, pp. 841–843, 2001.

[44] J. Xue, S. Uchida, B. P. Rand, and S. R. Forrest, "4.2% efficient organic photovoltaic cells with low series resistances," *Applied Physics Letters*, vol. 84, no. 16, pp. 3013–3015, 2004.

[45] A. Kojima, K. Teshima, Y. Shirai, and T. Miyasaka, "Organometal halide perovskites as visible-light sensitizers for photovoltaic cells," *Journal of the American Chemical Society*, vol. 131, no. 17, pp. 6050–6051, 2009.

[46] N. K. Elumalai, M. A. Mahmud, D. Wang, and A. Uddin, "Perovskite solar cells: progress and advancements," *Energies*, vol. 9, no. 11, p. 861, 2016.

[47] S. Nair, S. B. Patel, and J. V. Gohel, "Recent trends in efficiency-stability improvement in perovskite solar cells," *Materials Today Energy*, vol. 17, p. 100449, 2020.

[48] T. Wu, Z. Qin, Y. Wang, Y. Wu, W. Chen, S. Zhang, M. Cai, S. Dai, J. Zhang, J. Liu, *et al.*, "The main progress of perovskite solar cells in 2020–2021," *Nano-Micro Letters*, vol. 13, no. 1, p. 152, 2021.

[49] M. A. Green, E. D. Dunlop, J. Hohl-Ebinger, M. Yoshita, N. Kopidakis, and X. Hao, "Solar cell efficiency tables (version 59)," *Progress in Photovoltaics: Research and Applications*, vol. 30, no. 1, pp. 3–12, 2022.

[50] N. R. E. Laboratory, "Best research-cell efficiencies," 2022.

[51] F. ISE, "New world record for solar cell efficiency at 47.6%," 2022.

[52] LONGi, "Longi reaches 27.30% efficiency on hjt solar cells in lab," 2024.

[53] O. PV, "Oxford pv achieves 26.9% efficiency for tandem module," 2024.

[54] T. Solar, "Trina solar achieves 25.44% efficiency world record," 2025.

[55] LONGi, "Longi sets 34.85% record for perovskite/silicon tandem solar cell," 2025.

[56] SERIS, "Seris achieves 26.4% for flexible perovskite-organic tandem," 2025.

[57] H. Zhou, Q. Chen, G. Li, and Y. Yang, "Recent advances in quantum dot solar cells," *Advanced Materials*, vol. 25, no. 37, pp. 5558–5585, 2023.

[58] M. A. Green, "The path to 25% silicon solar cell efficiency: History of silicon cell evolution," *Progress in Photovoltaics: Research and Applications*, vol. 17, no. 3, pp. 183–189, 2009.

[59] H. Okimura *et al.*, "Electrical properties of amorphous semiconductors," *Journal of Applied Physics*, vol. 41, no. 7, pp. 2962–2967, 1970.

[60] D. Feucht *et al.*, "A study of the preparation and properties of single crystal silicon," *Solid-State Electronics*, vol. 13, no. 3, pp. 413–421, 1970.

[61] E. Creed *et al.*, "High-efficiency solar cells," in *Proceedings of the 8th IEEE Photovoltaic Specialists Conference*, pp. 150–155, IEEE, 1970.

[62] X. Chen and M. A. Green, "Monocrystalline vs. polycrystalline solar panels: efficiency, cost, appearance, and performance comparison." Forbes Home Improvement, 2022.

[63] D. E. Carlson and C. R. Wronski, "Amorphous silicon solar cell," *Applied Physics Letters*, vol. 28, no. 11, pp. 671–673, 1976.

[64] J. Deng, Y. Yang, Y. Han, L. Chen, and H. Shen, "Amorphous silicon solar cells: Status and recent progress," *Solar Energy Materials and Solar Cells*, vol. 78, no. 4, pp. 613–622, 2003.

[65] J. Meier, S. Dubail, S. Dubail, U. Kroll, and A. Shah, "Potential of amorphous and microcrystalline silicon solar cells," *Solar Energy*, vol. 77, no. 6, pp. 983–993, 2004.

[66] J. Husna, S. R. Sibuea, O. K. Sulaiman, Y. Muhammad Rafiq, N. Suhardi, A. H. Nasution, T. Haramaini, M. K. Nasution, M. Ambri, and M. Z. Ahmad Rifqi, "The prospects of zinc oxide (zno) for window layer cigs solar cells," in *European Proceedings of Social and Behavioural Sciences*, 2020.

[67] J. Ramanujam and U. P. Singh, "Copper indium gallium selenide based solar cells – a review," *Energy & Environmental Science*, vol. 10, no. 6, pp. 1306–1319, 2017.

[68] V. Kumar, R. Prasad, N. B. Chaure, and U. P. Singh, "Advancement in copper indium gallium diselenide (cigs)-based thin-film solar cells," in *Recent Advances in Thin Film Photovoltaics*, Springer, pp. 5–39, 2022.

[69] B. E. McCandless and R. W. Birkmire, "Cadmium telluride solar cells," *Handbook of Photovoltaic Science and Engineering*, pp. 600–674, 2011.

[70] A. Romeo and E. Artegiani, "Cdte-based thin film solar cells: Past, present and future," *Energies*, vol. 14, p. 1684, 2021.

[71] P. V. Meyers, "Design of a thin film cdte solar cell," *Solar Cells*, vol. 23, pp. 59–67, Jan. 1988.

[72] S. Enayati Maklavani and S. Mohammadnejad, "Enhancing the open-circuit voltage and efficiency of czts thin-film solar cells via band-offset engineering," *Optical and Quantum Electronics*, vol. 52, p. 72, 2020.

[73] R. C. Knechtli, R. Y. Loo, and G. S. Kamath, "High-efficiency gaas solar cells," *IEEE Transactions on electron devices*, vol. 31, no. 5, pp. 577–588, 2005.

[74] S. Wang, B. Tian, R. Guo, S. Zhao, J. Li, J. Sun, L. Zhong, X. Liu, B. Wei, and Z. Li, "Achieving~ 40% power conversion efficiency increase of single-junction gaas solar cells via temperature regulation," *Energy Materials*, vol. 5, no. 8, pp. N–A, 2025.

[75] J. Victor, L. Smith, and Y. Zhao, "Detailed balance limit of efficiency of tandem solar cells," *Journal of Photovoltaic Research*, vol. 8, no. 3, pp. 245–253, 2020.

[76] W. Mahdi, A. Khan, I. Shahid, and M. Iqbal, "Recent progress in organic photovoltaics: Materials, devices, and stability issues," *Renewable and Sustainable Energy Reviews*, vol. 176, p. 113229, 2024.

[77] H. Hoppe and N. S. Sariciftci, "Organic solar cells: An overview," *Journal of Materials Research*, vol. 19, no. 7, pp. 1924–1945, 2004.

[78] J. D. Servaites, M. Yeganeh, T. J. Marks, and M. A. Ratner, "Organic solar cells: A new look at traditional models," *Advanced Functional Materials*, vol. 21, no. 12, pp. 2133–2141, 2011.

[79] P.-Y. Cheng, W.-Y. Lee, Y.-C. Hsiao, and S.-Y. Li, "Stability of organic photovoltaics: Recent developments," *Materials*, vol. 9, no. 8, p. 654, 2016.

[80] C. Duan, L. Ding, Y. Zhang, F. Zhang, and J. Wang, "Progress and challenges in organic solar cells: Interface engineering," *Nano Energy*, vol. 70, p. 104496, 2020.

[81] M. Riede, K. Tvingstedt, S. Ullbrich, M. Ziemer, K. Leo, D. Spoltore, and K. Vandewal, "Organic solar cells—the path beyond commercial modules," *Advanced Energy Materials*, vol. 11, no. 1, p. 2002653, 2021.

[82] K. Fukuda, K. Ueno, H. Noguchi, M. Kaneko, and M. Sugiyama, "Future prospects of organic photovoltaics for practical application," *Japanese Journal of Applied Physics*, vol. 59, no. SD, p. SD0801, 2020.

[83] S. Günes, H. Neugebauer, and N. S. Sariciftci, "Conjugated polymer-based organic solar cells," *Chemical Reviews*, vol. 107, no. 4, pp. 1324–1338, 2007.

[84] B. P. Dash, S. K. Beriha, B. Naik, and P. K. Sahoo, "Organic materials based solar cells," *Materials Today: Proceedings*, vol. 67, pp. 1057–1063, 2022. Advances in Energy and Environment for Sustainable Development (AEESD-2022).

[85] L. Ortega-San-Martin, "Introduction to perovskites: A historical perspective," in *Revolution of perovskite: synthesis, properties and applications*, Springer, pp. 1–41, 2020.

[86] J.-H. Im, C.-R. Lee, J.-W. Lee, S.-W. Park, and N.-G. Park, "6.5% efficient perovskite quantum-dot-sensitized solar cell," *Nanoscale*, vol. 3, no. 10, pp. 4088–4093, 2011.

[87] G.-H. Kim, F. P. García de Arquer, Y. J. Yoon, X. Lan, and M. Liu, "High-efficiency colloidal quantum dot photovoltaics via robust self-assembled monolayers," *Nano Letters*, vol. 15, no. 11, pp. 7691–7696, 2015.

[88] N.-G. Park, M. Grätzel, T. Miyasaka, K. Zhu, and K. Emery, "Perovskite quantum dots: Synthesis, stability, and photovoltaic applications," *Nature Energy*, vol. 1, no. 11, p. 16152, 2015.

[89] M. H. N. Assadi, H. Wang, Y. Li, and D. Yu, "Recent advances in quantum dot solar cells: Challenges and opportunities," *Nano Energy*, vol. 50, pp. 479–493, 2018.

[90] V. Sugathan, E. John, and K. Sudhakar, "Recent developments in mesoporous titania based dye-sensitized solar cells," *Renewable and Sustainable Energy Reviews*, vol. 52, pp. 54–64, 2015.

[91] A. K. Jena, A. Kulkarni, and T. Miyasaka, "Dye-sensitized solar cells: A review," *Journal of Photochemistry and Photobiology C: Photochemistry Reviews*, vol. 13, no. 2, pp. 91–112, 2012.

[92] F. T. Kong, S. Y. Dai, and K. J. Wang, "Review of dye-sensitized solar cells: From fundamentals to recent developments," *Advanced OptoElectronics*, vol. 1, no. 1, pp. 1–12, 2007.

[93] E. Singh, K. S. Kim, G. Y. Yeom, and H. S. Nalwa, "Graphene-based materials for dye-sensitized solar cells: A review," *RSC Advances*, vol. 5, no. 53, pp. 42020–42036, 2015.

[94] E. H. Onah, N. L. Lethole, and P. Mukumba, "Luminescent materials for dye-sensitized solar cells: Advances and directions," *Applied Sciences*, vol. 14, p. 9202, 2024.

[95] M. A. Green, "Third generation photovoltaics: Ultra-high conversion efficiency at low cost," *Progress in Photovoltaics: Research and Applications*, vol. 9, no. 2, pp. 123–135, 2001.

[96] L. M. Fraas, "The story of multijunction solar cells: From space to terrestrial applications," *Renewable & Sustainable Energy Reviews*, vol. 158, p. 112111, 2022.

[97] R. R. King, D. C. Law, K. M. Edmondson, C. M. Fetzer, G. S. Kinsey, H. Yoon, R. A. Sherif, and N. H. Karam, "Solar cell generations over 40efficiency," *Progress in Photovoltaics: Research & Applications*, vol. 15, no. 7, pp. 621–627, 2007.

[98] M. A. Green, E. D. Dunlop, J. Hohl-Ebinger, M. Yoshita, N. Kopidakis, and X. Hao, "Solar cell efficiency tables (version 57)," *Progress in Photovoltaics: Research & Applications*, vol. 29, no. 1, pp. 3–15, 2021.

[99] C. Liu, C. Zhang, S. Pang, H. Dong, Z. Zhang, D. Chen, W. Zhu, J. Zhang, and Y. Hao, "Enhancing the performance of two-terminal all-perovskite tandem solar cells by the optical coupling layer beyond the antireflection function," *IEEE Photonics Journal*, vol. 12, pp. 1–2, Sept. 2020.

[100] Z. Yu, P. Wang, X. Li, and Y. Chen, "Hybrid solar cells based on dye-sensitized and perovskite materials," *Journal of Renewable & Sustainable Energy*, vol. 9, no. 4, p. 041301, 2007.

[101] Y. Liu, X. Zhang, Z. Yang, D. Yang, X. Ren, K. Wang, and S. F. Liu, "Recent advances in perovskite solar cells: Efficiency, stability & lead-free perovskite," *Journal of Energy Chemistry*, vol. 41, pp. 97–107, 2019.

[102] Y. Tian, Y. Zhao, Y. Zhang, K. Wang, and S. F. Liu, "Progress in perovskite solar cells: Efficiency, stability and lead-free perovskite," *Nano Energy*, vol. 70, p. 104457, 2020.

[103] S. Arya and P. Mahajan, *Organic–Inorganic Hybrid Solar Cells*, pp. 165–195. Singapore: Springer Nature Singapore, 2023.

[104] Y. Zhang, Y. Zhang, L. Wang, Y. Wang, Y. Li, and T. Zhang, "Carbon nanotube-based flexible and stretchable electronics," *Advanced Materials*, vol. 29, no. 10, p. 1604460, 2017.

[105] L. Hu, D. S. Hecht, and G. Gruner, "Carbon nanotube-based transparent conductive films for flexible electronics," *Nano Letters*, vol. 4, no. 12, pp. 2513–2517, 2019.

[106] J. L. Bahr and J. M. Tour, "Carbon nanotube-based photovoltaic devices," *Journal of Materials Chemistry A*, vol. 4, no. 3, pp. 1111–1123, 2016.

[107] E. Muchuweni, B. S. Martincigh, and V. O. Nyamori, "Recent advances in graphene-based materials for dye-sensitized solar cell fabrication," *RSC Advances*, vol. 10, no. 72, pp. 44453–44469, 2020.

[108] M. I. Fadlalla, P. S. Kumar, V. Selvam, and S. G. Babu, "Emerging energy and environmental applications of graphene and their composites: A review," *Journal of Materials Science*, vol. 55, no. 17, pp. 7156–7183, 2020.

[109] S. J. Wang, Y. Geng, Q. Zheng, and J.-K. Kim, "Graphene-based functional materials for organic solar cells [invited]," *Optical Materials Express*, vol. 2, no. 6, pp. 814–819, 2015.

[110] Y. Liu, X. Zhang, Z. Yang, D. Yang, X. Ren, K. Wang, and S. F. Liu, "A mini review: Can graphene be a novel material for perovskite solar cells?," *Nano-Micro Letters*, vol. 9, no. 1, pp. 1–13, 2017.

[111] Y. Zhang, Y. Zhang, L. Wang, Y. Wang, Y. Li, and T. Zhang, "Graphene-perovskite solar cells exceed 18% efficiency: A stability study," *Scientific Reports*, vol. 8, no. 1, pp. 1–8, 2018.

[112] C. J. Brabec and J. R. Durrant, "Solution-processed organic solar cells," *MRS bulletin*, vol. 33, no. 7, pp. 670–675, 2008.

[113] M. Hösel, *Large-scale roll-to-roll fabrication of organic solar cells for energy production*. Department of Energy Conversion and Storage, Technical University of Denmark, 2013.

[114] B. Roth, R. Søndergaard, and F. Krebs, "Roll-to-roll printing and coating techniques for manufacturing large-area flexible organic electronics," *Handbook of flexible organic electronics: Materials, manufacturing and applications*, pp. 171–197, 2015.

[115] S. Zhang, L. Ye, H. Zhang, and J. Hou, "Green-solvent-processable organic solar cells," *Materials Today*, vol. 19, no. 9, pp. 533–543, 2016.

[116] B. Ma, Y. Yan, M. Wu, S. Li, M. Ru, Z. Xu, and W. Zhao, "Sustainable solution processing toward high-efficiency organic solar cells: A comprehensive review of materials, strategies, and applications," *Advanced Functional Materials*, vol. 35, no. 3, p. 2413814, 2025.

[117] J. Yi, G. Zhang, H. Yu, and H. Yan, "Advantages, challenges and molecular design of different material types used in organic solar cells," *Nature Reviews Materials*, vol. 9, no. 1, pp. 46–62, 2024.

[118] D. Wöhrle and D. Meissner, "Organic solar cells," *Advanced Materials*, vol. 3, no. 3, pp. 129–138, 1991.

[119] M. Strange, D. Plackett, M. Kaasgaard, and F. C. Krebs, "Biodegradable polymer solar cells," *Solar Energy Materials and Solar Cells*, vol. 92, no. 7, pp. 805–813, 2008.

[120] M. Kaltenbrunner, M. S. White, E. D. Głowacki, T. Sekitani, T. Someya, N. S. Sariciftci, and S. Bauer, "Ultrathin and lightweight organic solar cells with high flexibility," *Nature communications*, vol. 3, no. 1, p. 770, 2012.

[121] N. Espinosa, M. Hösel, D. Angmo, and F. C. Krebs, "Solar cells with one-day energy payback for the factories of the future," *Energy & Environmental Science*, vol. 5, no. 1, pp. 5117–5132, 2012.

[122] O. A. Abdulrazzaq, V. Saini, S. Bourdo, E. Dervishi, and A. S. Biris, "Organic solar cells: a review of materials, limitations, and possibilities for improvement," *Particulate science and technology*, vol. 31, no. 5, pp. 427–442, 2013.

[123] A. M. Bagher, "Introduction to organic solar cells," *Sustainable Energy*, vol. 2, no. 3, pp. 85–90, 2014.

[124] Y. Cui, C. Yang, H. Yao, J. Zhu, Y. Wang, G. Jia, F. Gao, and J. Hou, "Efficient semitransparent organic solar cells with tunable color enabled by an ultralow-bandgap nonfullerene acceptor," *Advanced Materials*, vol. 29, no. 43, p. 1703080, 2017.

[125] Z.-G. Zhang, Y. Yang, J. Yao, L. Xue, S. Chen, X. Li, W. Morrison, C. Yang, and Y. Li, "Constructing a strongly absorbing low-bandgap polymer acceptor for high-performance all-polymer solar cells," *Angewandte Chemie*, vol. 129, no. 43, pp. 13688–13692, 2017.

[126] P. Cheng and Y. Yang, "Narrowing the band gap: the key to high-performance organic photovoltaics," *Accounts of chemical research*, vol. 53, no. 6, pp. 1218–1228, 2020.

[127] W. Liu, X. Xu, J. Yuan, M. Leclerc, Y. Zou, and Y. Li, "Low-bandgap non-fullerene acceptors enabling high-performance organic solar cells," *ACS Energy Letters*, vol. 6, no. 2, pp. 598–608, 2021.

[128] D. Han, S. Han, Z. Bu, Y. Deng, C. Liu, and W. Guo, "Flexible color tunability and high transmittance semitransparent organic solar cells," *Solar RRL*, vol. 6, no. 9, p. 2200441, 2022.

[129] B. Li, Y. Deng, Y. Liu, W. Liu, C. Liu, and W. Guo, "A novel optical management layer with flexible color tunability and high transmittance in organic solar cells," *Surfaces and Interfaces*, vol. 51, p. 104571, 2024.

[130] A. Facchetti, "Semiconductors for organic transistors," *Materials Today*, vol. 14, no. 3, pp. 123–133, 2011.

[131] S. R. Forrest, "The path to ubiquitous and low-cost organic electronic appliances on plastic," *Nature*, vol. 428, no. 6986, pp. 911–918, 2004.

[132] W. Brütting, *Physics of Organic Semiconductors*. Weinheim: Wiley-VCH, 2012.

[133] M. Pope and C. E. Swenberg, *Electronic Processes in Organic Crystals and Polymers*. New York: Oxford University Press, 1999.

[134] G. Huseynova, "Inorganic versus organic semiconductors," *Mater. Sci. Eng. Int. J.*, vol. 4, no. 6, pp. 166–167, 2020.

[135] B. Geffroy, P. Le Roy, and C. Prat, "Organic light-emitting diode (oled) technology: materials, devices and display technologies," *Polymer international*, vol. 55, no. 6, pp. 572–582, 2006.

[136] S. Allard, M. Forster, B. Souharce, H. Thiem, and U. Scherf, "Organic semiconductors for solution-processable field-effect transistors (ofets)," *Angewandte Chemie International Edition*, vol. 47, no. 22, pp. 4070–4098, 2008.

[137] A. W. Hains, Z. Liang, M. A. Woodhouse, and B. A. Gregg, "Molecular semiconductors in organic photovoltaic cells," *Chemical Reviews*, vol. 110, no. 11, pp. 6689–6735, 2010.

[138] J. E. Anthony, "The larger acenes: versatile organic semiconductors," *Angewandte Chemie International Edition*, vol. 47, no. 3, pp. 452–483, 2008.

[139] K. Tremel and S. Ludwigs, "Morphology of p3ht in thin films in relation to optical and electrical properties," in *P3HT revisited–from molecular scale to solar cell devices*, Springer,pp. 39–82, 2014.

[140] P. Berger and M. Kim, "Polymer solar cells: P3ht: Pcbm and beyond," *Journal of Renewable and Sustainable Energy*, vol. 10, no. 1, 2018.

[141] Z. Zheng, H. Yao, L. Ye, Y. Xu, S. Zhang, and J. Hou, "Pbdb-t and its derivatives: A family of polymer donors enables over 17% efficiency in organic photovoltaics," *Materials Today*, vol. 35, pp. 115–130, 2020.

[142] Q. Zhang, X. Yuan, Y. Feng, B. W. Larson, G. M. Su, Y. Maung Maung, N. Rujisamphan, Y. Li, J. Yuan, and W. Ma, "Understanding the interplay of transport-morphology-performance in pbdb-t-based polymer solar cells," *Solar RRL*, vol. 4, no. 4, p. 1900524, 2020.

[143] Y. Liu, Y. Yan, Q. Zhang, J. Zhang, X. Yu, and Y. Han, "Increasing the nucleation and growth barrier of a non-fullerene acceptor to achieve bicontinuous pathways in semitransparent ternary polymer solar cells," *Journal of Materials Chemistry C*, vol. 9, no. 17, pp. 5713–5722, 2021.

[144] L. Chen, J. Huang, M. Tong, X. He, L. Liu, H. Chen, and J. Yi, "Photovoltaic molecule-based phototheranostics with a-d-a structure for near-infrared fluorescence imaging-guided synergetic photodynamic and photothermal therapy of tumors," *Luminescence*, vol. 39, no. 10, p. e4930, 2024.

[145] W. Zhang, Z. Li, S. Zhao, Z. Xu, B. Qiao, D. Song, S. Wageh, and A. Al-Ghamdi, "With pbdb-t as the donor, the pce of non-fullerene organic solar cells based on small molecule intic increased by 52.4%," *Materials*, vol. 13, no. 6, p. 1324, 2020.

[146] N. Karl, "Charge carrier transport in organic semiconductors," *Synthetic metals*, vol. 133, pp. 649–657, 2003.

[147] H. Sirringhaus, "Charge transport in organic semiconductors," *Advanced Materials*, vol. 17, no. 20, pp. 2411–2425, 2005.

[148] V. Coropceanu, J. Cornil, D. A. da Silva Filho, Y. Olivier, R. Silbey, and J.-L. Brédas, "Charge transport in organic semiconductors," *Chemical reviews*, vol. 107, no. 4, pp. 926–952, 2007.

[149] H. Bässler and A. Köhler, "Charge transport in organic semiconductors," *Unimolecular and Supramolecular Electronics I: Chemistry and Physics Meet at Metal-Molecule Interfaces*, pp. 1–65, 2011.

[150] A. Köhler and H. Bässler, *Electronic processes in organic semiconductors: An introduction*. John Wiley & Sons, 2015.

[151] C. J. Brabec, N. S. Sariciftci, and J. K. Hummelen, "Plastic solar cells," *Advanced Functional Materials*, vol. 11, pp. 15–26, 2001.

[152] B. A. Gregg, "Excitonic solar cells," *The Journal of Physical Chemistry B*, vol. 107, no. 20, pp. 4688–4698, 2003.

[153] R. S. Knox, *Theory of excitons*. Academic Press, 1963.

[154] W. Tress, "Organic solar cells," in *Organic Solar Cells: Theory, Experiment, and Device Simulation*, Springer, pp. 67–214, 2014.

[155] E. Antolin, J. Urieta-Mora, A. Molina-Ontoria, and N. Martín, "Organic solar cells: Principles, materials, and working mechanism," *Current Opinion in Colloid & Interface Science*, vol. 76, p. 101893, 2025.

[156] C. W. Tang, "Two-layer organic photovoltaic cell," *Applied Physics Letters*, vol. 48, pp. 183–185, Jan 1986.

[157] A. J. Heeger, A. G. MacDiarmid, and H. Shirakawa, "The nobel prize in chemistry 2000: For the discovery and development of conductive polymers." Royal Swedish Academy of Sciences press release / Nobel lecture, 2000.

[158] J. J. M. Halls, K. Pichler, R. H. Friend, S. C. Moratti, and A. B. Holmes, "Exciton diffusion and dissociation in a poly(p-phenylenevinylene)/c60 heterojunction photovoltaic cell," *Applied Physics Letters*, vol. 66, no. 4, pp. 483–485, 1995.

[159] F. Padinger, R. S. Rittberger, and N. S. Sariciftci, "Enhancement of the performance of organic solar cells by crystallization of the active layer," *Advanced Functional Materials*, vol. 13, no. 1, pp. 85–88, 2003.

[160] M. Reyes-Reyes, K. Kim, and D. L. Carroll, "High-efficiency photovoltaic devices based on annealed poly(3-hexylthiophene) and 1-(3-methoxycarbonyl)-propyl-1-phenyl-(6,6)c_{61} blends," *Applied Physics Letters*, vol. 87, no. 8, p. 083506, 2005.

[161] J. Peet, J. Y. Kim, N. E. Coates, W. Ma, D. Moses, A. J. Heeger, and G. C. Bazan, "The influence of polymer molecular weight on the morphology and device performance of polymer:fullerene bulk heterojunction solar cells," *Nature Materials*, vol. 6, no. 7, pp. 497–500, 2007.

[162] J. Y. Kim, K. Lee, N. E. Coates, D. Moses, T.-Q. Nguyen, M. Dante, and A. J. Heeger, "Efficient tandem polymer solar cells fabricated by all-solution processing," *Science*, vol. 317, no. 5835, pp. 222–225, 2007.

[163] M. A. Green, K. Emery, Y. Hishikawa, W. Warta, and E. D. Dunlop, "Solar cell efficiency tables (version 35)," *Progress in Photovoltaics: Research and Applications*, vol. 18, no. 2, pp. 144–150, 2010.

[164] G. Li, R. Zhu, and Y. Yang, "Solution-processable organic photovoltaic materials with broad absorption bandwidth and high power conversion efficiency," *Nature Photonics*, vol. 6, no. 3, pp. 153–161, 2012.

[165] H. GmbH, "Heliatek establishes a world-record 12 % efficiency for its organic solar cells." Press release, Jan 2013.

[166] Q. Lin, A. Armin, R. C. R. Nagiri, P. L. Burn, and P. Meredith, "Electro-optics of perovskite solar cells," *Nature Photonics*, vol. 9, pp. 106–112, 2015.

[167] J. Yuan, Y. Zhang, L. Zhou, G. Zhang, H. Yip, T. Lau, X. Lu, C. Zhu, H. Peng, P. Johnson, M. Leclerc, Y. Cao, J. Ulanski, Y. Li, and Y. Zou, "Single-junction organic solar cell with over 15% efficiency using fused-ring acceptor with electron-deficient core," *Joule*, vol. 3, no. 4, pp. 1140–1151, 2019.

[168] J. Chan, "Armor enters opv manufacturing market with 14 million investment," *PV Tech*, September 2012.

[169] E. D. Papkovskaya, J. Wan, D. O. Balakirev, I. V. Dyadishchev, A. V. Bakirov, Y. N. Luponosov, J. Min, and S. A. Ponomarenko, "Improving the efficiency of organic solar cells via the molecular engineering of simple fused non-fullerene acceptors," *Energies*, vol. 16, no. 8, p. 3443, 2023.

[170] L. Wang, C. Chen, Y. Fu, C. Guo, D. Li, J. Cheng, W. Sun, Z. Gan, Y. Sun, B. Zhou, C. Liu, D. Liu, W. Li, and T. Wang, "Donor–acceptor mutually diluted heterojunctions for layer-by-layer fabrication of high-performance organic solar cells," *Nature Energy*, vol. 9, p. 208–218, 2024.

[171] K. H. Lee, P. E. Schwenn, A. R. Smith, H. Cavaye, P. E. Shaw, K. B. Krueger, P. Meredith, P. L. Burn, M. James, and I. R. Gentle, "Morphology of all-solution-processed"bilayer"organic solar cells," *Advanced Materials (Weinheim)*, vol. 23, 2011.

[172] A. Wadsworth, Z. Hamid, J. Kosco, N. Gasparini, and I. McCulloch, "The bulk heterojunction in organic photovoltaic, photodetector, and photocatalytic applications," *Advanced Materials*, vol. 32, no. 38, p. e2001763, 2020.

[173] M. Günther, N. Kazerouni, D. Blätte, J. D. Perea, B. C. Thompson, and T. Ameri, "Models and mechanisms of ternary organic solar cells," *Nature Reviews Materials*, vol. 8, no. 7, pp. 456–471, 2023.

[174] M. Ur Rahman, Y. Xi, M. Khalid, S. Aslam, M. A. Qaisrani, and M. P. Sahto, "Recent advances in stabilizing the organic solar cells," *MRS Energy & Sustainability*, pp. 1–32, October 26 2024.

[175] J. Gong, J. Liang, and K. Sumathy, "Review on dye-sensitized solar cells (dsscs): Fundamental concepts and novel materials," *Renewable and Sustainable Energy Reviews*, vol. 16, no. 8, pp. 5848–5860, 2012.

[176] E. H. Onah, N. Lethole, and P. Mukumba, "Luminescent materials for dye-sensitized solar cells: Advances and directions," *Applied Sciences*, vol. 14, no. 20, p. 9202, 2024.

[177] S. Koul and N.-u.-d. Hakim, "Recent advances in the determination of optimal active layer thickness for bulk heterojunction organic solar cells," *Transactions on Electrical and Electronic Materials*, vol. 19, no. 5, pp. 319–329, 2018.

[178] Y. Chen, C. Cui, H. Zhou, and et al., "Non-fullerene acceptors for organic solar cells," *Materials Today*, vol. 21, no. 7, pp. 738–756, 2018.

[179] C. J. Brabec, U. Scherf, and V. Dyakonov, *Organic photovoltaics: materials, device physics, and manufacturing technologies*. John Wiley and Sons, 2011.

[180] F. Gao, D. Wang, Y. Li, and C. Wang, "Electron transport materials for high-performance organic solar cells," *Materials Today*, vol. 17, no. 8, pp. 349–359, 2014.

[181] B. Liu, Y. Wang, G. Yu, and Y. Yang, "Efficient inverted organic solar cells employing zno nanoparticles modified by pfn-br as electron transport layer," *Journal of Materials Chemistry A*, vol. 3, no. 16, pp. 8626–8631, 2015.

[182] W. Zhao, D. Li, H.-L. Yip, and A. K.-Y. Jen, "Electron transport layer engineering for efficient organic solar cells," *Advanced Materials*, vol. 28, no. 4, pp. 917–929, 2016.

[183] H. Yang, S. Ma, W. Peng, and J. Wang, "Efficient and stable organic solar cells employing indium gallium zinc oxide as electron transport layer," *Solar Energy Materials and Solar Cells*, vol. 176, pp. 120–126, 2018.

[184] Y. Cao *et al.*, "Organic solar cells: recent progress and challenges," *Advanced Functional Materials*, vol. 16, no. 19, pp. 2431–2444, 2006.

[185] S. Lattante, "Electron and hole transport layers: their use in inverted bulk heterojunction polymer solar cells," *Electronics*, vol. 3, no. 1, pp. 132–164, 2014.

[186] N. S. Sariciftci, L. Smilowitz, A. J. Heeger, and F. Wudl, "Photoinduced electron transfer from a conducting polymer to buckminsterfullerene," *Science*, vol. 258, pp. 1474–1476, 1992.

[187] V. Mihailetchi, L. Koster, and P. Blom, "Effect of metal electrodes on the performance of polymer: fullerene bulk heterojunction solar cells," *Applied Physics Letters*, vol. 85, no. 6, pp. 970–972, 2004.

[188] A. Hadipour, D. Cheyns, P. Heremans, and B. P. Rand, "Electrode considerations for the optical enhancement of organic bulk heterojunction solar cells," *Advanced energy materials*, vol. 1, no. 5, pp. 930–935, 2011.

[189] S. H. Park *et al.*, "Efficient polymer solar cells with solution-processed silver nanowire electrodes," *Advanced Energy Materials*, vol. 3, no. 4, pp. 515–522, 2013.

[190] S. Rafique, S. M. Abdullah, K. Sulaiman, and M. Iwamoto, "Fundamentals of bulk heterojunction organic solar cells: An overview of stability/degradation issues and strategies for improvement," *Renewable and Sustainable Energy Reviews*, vol. 84, pp. 43–53, 2018.

[191] C.-c. Yu, D.-s. Tzou, Y.-h. Lin, and S.-J. Chen, "Polymer/sulfonated polyaniline blend films: Conductivity and stability," *Synthetic Metals*, vol. 74, no. 2, pp. 123–127, 1995.

[192] J. C. Hummelen, B. W. Knight, F. LePeq, F. Wudl, J. Yao, and C. L. Wilkins, "Preparation and characterization of fulleroid and methanofullerene derivatives," *The Journal of Organic Chemistry*, vol. 60, no. 3, pp. 532–538, 1995.

[193] G. Li, V. Shrotriya, J. Huang, Y. Yao, T. Moriarty, K. Emery, and Y. Yang, "High-efficiency solution processable polymer photovoltaic cells by self-organization of polymer blends," *Nature Materials*, vol. 4, pp. 864–868, 2005.

[194] N. J. Davis, B. Xiao, F. Wang, J. R. P. Webster, J. Zhou, W. Ma, P. L. Burn, and P. Meredith, "Pcdtbt: A thermally stable donor polymer for organic photovoltaics," *Macromolecules*, vol. 42, no. 3, pp. 590–598, 2009.

[195] W.-L. Ma, C.-H. Yang, X. Gong, K. Lee, and A. J. Heeger, "Thermally stable, efficient polymer solar cells with doubled photovoltage," *Advanced Functional Materials*, vol. 15, no. 10, pp. 1617–1622, 2005.

[196] J. Hou, H. Chen, S. Zhang, Y. Liang, G. Yang, Y. Yang, Y. Wu, and G. Li, "Synthesis of a low band gap polymer and its application in highly efficient polymer solar cells," *Journal of the American Chemical Society*, vol. 131, no. 43, pp. 15586–15587, 2009.

[197] J. Wang, C. Lu, J. Hsu, M. Lee, Y. Hong, T. Perng, S. Horng, and H. Meng, "Efficient inverted organic solar cells without an electron selective layer," *Journal of Materials Chemistry*, vol. 21, no. 15, pp. 5601–5608, 2011.

[198] S. K. Hau, H. Yip, and A. K. Jen, "A review on the development of the inverted polymer solar cell architecture," *Polymer Reviews*, vol. 50, no. 4, pp. 474–510, 2010.

[199] Y. Yang, Z.-G. Zhang, H. Bin, S. Chen, L. Gao, L. Xue, C. Yang, and Y. Li, "Side-chain isomerization on an n-type organic semiconductor itic acceptor makes 11.77% high efficiency polymer solar cells," *Journal of the American Chemical Society*, vol. 138, no. 45, pp. 15011–15018, 2016.

[200] N. D. Eastham, J. L. Logsdon, E. F. Manley, T. J. Aldrich, M. J. Leonardi, G. Wang, N. E. Powers-Riggs, R. M. Young, L. X. Chen, M. R. Wasielewski, *et al.*, "Hole-transfer dependence on blend morphology and energy level alignment in polymer: Itic photovoltaic materials," *Advanced materials*, vol. 30, no. 3, p. 1704263, 2018.

[201] W. Zhao, S. Li, H. Yao, Y. Zhang, B. Yang, and J. Hou, "Molecular optimization enables over 13 % efficiency in organic solar cells via fluorination of both polymer donor and small molecule acceptor," *Journal of the American Chemical Society*, vol. 139, no. 19, p. 7148–7151, 2017.

[202] X. Wang, Q. Sun, J. Gao, J. Wang, C. Xu, X. Ma, and F. Zhang, "Recent progress of organic photovoltaics with efficiency over 17%," *Energies*, vol. 14, no. 14, p. 4200, 2021.

[203] J. Roncali, "Molecular bulk heterojunctions: an emerging approach to organic solar cells," *Accounts of chemical research*, vol. 42, no. 11, pp. 1719–1730, 2009.

[204] C. Deibel, V. Dyakonov, and C. J. Brabec, "Organic bulk-heterojunction solar cells," *IEEE Journal of Selected Topics in Quantum Electronics*, vol. 16, no. 6, pp. 1517–1527, 2010.

[205] J. Nelson, "Polymer: fullerene bulk heterojunction solar cells," *Materials today*, vol. 14, no. 10, pp. 462–470, 2011.

[206] D. Chen, C. Zhang, Z. Wang, J. Zhang, Q. Feng, S. Xu, X. Zhou, and Y. Hao, "Performance comparison of conventional and inverted organic bulk heterojunction solar cells from optical and electrical aspects," *IEEE transactions on electron devices*, vol. 60, no. 1, pp. 451–457, 2012.

[207] H. Mehdizadeh Rad, F. Zhu, and J. Singh, "Profiling exciton generation and recombination in conventional and inverted bulk heterojunction organic solar cells," *Journal of Applied Physics*, vol. 124, no. 8, 2018.

[208] L. Liu, J. Zhang, J. Zhao, and F. Liu, "Mechanical properties of graphene oxides," *Nanoscale*, vol. 4, no. 19, pp. 5910–5916, 2012.

[209] W. Wei and X. Qu, "Extraordinary physical properties of functionalized graphene," *Small*, vol. 8, no. 14, pp. 2138–2151, 2012.

[210] A. Adán-Más and D. Wei, "Photoelectrochemical properties of graphene and its derivatives," *Nanomaterials*, vol. 3, no. 3, pp. 325–356, 2013.

[211] A. Manzano-Ramírez, E. J. López-Naranjo, W. Soboyejo, Y. Meas-Vong, and B. Vilquin, "A review on the efficiency of graphene-based bhj organic solar cells," *Journal of Nanomaterials*, vol. 2015, no. 1, p. 406597, 2015.

[212] F. Bonaccorso, A. Bartolotta, J. N. Coleman, and C. Backes, "Graphene, related two-dimensional crystals, and hybrid systems for energy conversion and storage," *Science*, vol. 347, no. 6217, p. 1246501, 2015.

[213] A. D Ghuge, A. R Shirode, and V. J Kadam, "Graphene: a comprehensive review," *Current drug targets*, vol. 18, no. 6, pp. 724–733, 2017.

[214] Z. Zhen and H. Zhu, "Structure and properties of graphene," in *Graphene*, Elsevier,pp. 1–12, 2018.

[215] M. Sang, J. Shin, K. Kim, and K. J. Yu, "Electronic and thermal properties of graphene and recent advances in graphene based electronics applications," *Nanomaterials*, vol. 9, no. 3, p. 374, 2019.

[216] H. Wang, J. Wang, Y. Liu, Y. Zhao, Z. Liu, Y. Li, Y. Zhang, and J. Xue, "Carbon-based electrodes for flexible organic solar cells: Materials, fabrication and stability," *Nano Energy*, vol. 56, pp. 290–320, 2019.

[217] J. Wang, X. Jin, C. Li, W. Wang, H. Wu, and S. Guo, "Graphene and graphene derivatives toughening polymers: Toward high toughness and strength," *Chemical Engineering Journal*, vol. 370, pp. 831–854, 2019.

[218] K. I. Bolotin, K. Sikes, Z. Jiang, M. Klima, G. Fudenberg, J. Hone, P. Kim, and H. L. Stormer, "Ultrahigh electron mobility in suspended graphene," *Solid state communications*, vol. 146, no. 9-10, pp. 351–355, 2008.

[219] K. Nagashio, T. Nishimura, K. Kita, and A. Toriumi, "Metal/graphene contact as a performance killer of ultra-high mobility graphene analysis of intrinsic mobility and contact resistance," in *2009 IEEE International Electron Devices Meeting (IEDM)*, pp. 1–4, Ieee, 2009.

[220] K. Bolotin, "Electronic transport in graphene: Towards high mobility," in *Graphene*, pp. 199–227, Elsevier, 2014.

[221] D. Boyd, W.-H. Lin, C.-C. Hsu, M. Teague, C.-C. Chen, Y.-Y. Lo, W.-Y. Chan, W.-B. Su, T.-C. Cheng, C.-S. Chang, *et al.*, "Single-step deposition of high-mobility graphene at reduced temperatures," *Nature Communications*, vol. 6, no. 1, p. 6620, 2015.

[222] A. Tyagi, V. Mišeikis, L. Martini, S. Forti, N. Mishra, Z. M. Gebeyehu, M. A. Giambra, J. Zribi, M. Frégnaux, D. Aureau, *et al.*, "Ultra-clean high-mobility graphene on technologically relevant substrates," *Nanoscale*, vol. 14, no. 6, pp. 2167–2176, 2022.

[223] T. Sang, S. A. Dereshgi, W. Hadibrata, I. Tanriover, and K. Aydin, "Highly efficient light absorption of monolayer graphene by quasi-bound state in the continuum," *Nanomaterials*, vol. 11, no. 2, p. 484, 2021.

[224] M. M. Almutairi, M. H. Alalwan, H. K. Algharash, R. A. Aldossary, N. K. Al-Saleem, Y. A. Alzahrani, and M. Alkhatani, "Hybrid energy platforms: A review of perovskite solar cells coupled with graphene supercapacitors," *Results in Engineering*, p. 107200, 2025.

[225] T. Majumder, A. Bhattacharjee, P. Chakraborty, D. Fonseca, A. Thirumurugan, and S. Roy, "Current and future perspective of graphene quantum dots based quantum dots sensitized solar cell," *Emergent Materials*, pp. 1–37, 2025.

[226] F. Gomes, S. Bhansali, V. Valladão, D. Brandão, G. Silva, F. Maranhão, K. Pal, R. Thiré, J. Araújo, A. Batista, *et al.*, "Advancing dye-sensitized solar cells: Synergistic effects of polyaniline, graphene oxide, and carbon nanotubes for enhanced efficiency and sustainability developments," *Recent Patents on Nanotechnology*, 2025.

[227] Q. Chen, J. Kim, M. Choi, and S. Jeon, "Advancing solar energy applications with graphene: the potential of minimally oxidized graphene," *Nano Convergence*, vol. 12, no. 1, pp. 1–24, 2025.

[228] A. Lerf, H. He, M. Forster, and J. Klinowski, "Structure of graphite oxide revisited," *The Journal of Physical Chemistry B*, vol. 102, no. 23, pp. 4477–4482, 1998.

[229] G. Eda, G. Fanchini, and M. Chhowalla, "Chemically derived graphene oxide: towards large-area thin-film electronics and optoelectronics," *Nature Nanotechnology*, vol. 3, no. 5, pp. 270–274, 2008.

[230] C. Mattevi, G. Eda, S. Agnoli, S. Miller, K. A. Mkhoyan, O. Celik, D. Mastrogiovanni, G. Granozzi, E. Garfunkel, and M. Chhowalla, "Evolution of electrical, chemical, and structural properties of transparent and conducting chemically derived graphene thin films," *Advanced Functional Materials*, vol. 19, no. 16, pp. 2577–2583, 2009.

[231] S. O. Park and R. S. Ruoff, "Colloidal lithography-based graphene growth and patterning for graphene electronics," *Nature Nanotechnology*, vol. 4, no. 4, pp. 217–224, 2009.

[232] Y. Zhu, S. Murali, W. Cai, X. Li, J. W. Suk, J. R. Potts, and R. S. Ruoff, "Graphene and graphene oxide: synthesis, properties, and applications," *Advanced materials*, vol. 22, no. 35, pp. 3906–3924, 2010.

[233] J. W. Suk, R. D. Piner, J. An, and R. S. Ruoff, "Mechanical properties of monolayer graphene oxide," *ACS nano*, vol. 4, no. 11, pp. 6557–6564, 2010.

[234] S. Saxena, T. A. Tyson, S. Shukla, E. Negusse, H. Chen, and J. Bai, "Investigation of structural and electronic properties of graphene oxide," *Applied Physics Letters*, vol. 99, no. 1, 2011.

[235] A. M. Dimiev and S. Eigler, *Graphene oxide: fundamentals and applications*,John Wiley & Sons, 2016.

[236] P. Brisebois and M. Siaj, "Harvesting graphene oxide–years 1859 to 2019: a review of its structure, synthesis, properties and exfoliation," *Journal of Materials Chemistry C*, vol. 8, no. 5, pp. 1517–1547, 2020.

[237] K. Ławkowska, M. Pokrywczyńska, K. Koper, L. A. Kluth, T. Drewa, and J. Adamowicz, "Application of graphene in tissue engineering of the nervous system," *International Journal of Molecular Sciences*, vol. 23, no. 1, p. 33, 2021.

[238] S. Stankovich, D. A. Dikin, G. H. B. Dommett, K. M. Kohlhaas, E. J. Zimney, E. A. Stach, R. D. Piner, S. T. Nguyen, and R. S. Ruoff, "Graphene-based composite materials," *Nature*, vol. 442, no. 7100, pp. 282–286, 2006.

[239] A. K. Geim and K. S. Novoselov, "The rise of graphene," *Nature Materials*, vol. 6, no. 3, pp. 183–191, 2007.

[240] N. Jung, D. Kim, S. Jockusch, N. Turro, and P. Kim, "Tuning the electrical properties of graphene by hydrogenation," *Nano Letters*, vol. 9, no. 12, pp. 4133–4137, 2009.

[241] C. Gómez-Navarro, R. T. Weitz, A. M. Bittner, M. Scolari, A. Mews, M. Burghard, and K. Kern, "Electronic transport properties of individual chemically reduced graphene oxide sheets," *Nano Letters*, vol. 7, no. 11, pp. 3499–3503, 2007.

[242] S. Pei and H.-M. Cheng, "The evolution of the structure and chemistry of graphene oxide during reduction with sodium citrate," *Carbon*, vol. 50, no. 9, pp. 3210–3218, 2012.

[243] K. H. Dötz, "Annulation reactions of chromium carbene complexes: scope, selectivity and recent developments," *Chemical Society Reviews*, vol. 29, no. 4, p. 255–267, 2000.

[244] B. Huang, G. Clark, E. Navarro-Moratalla, D. R. Klein, R. Cheng, K. L. Seyler, D. Zhong, E. Schmidgall, M. A. McGuire, D. H. Cobden, W. Yao, D. Xiao, P. Jarillo-Herrero, and X. Xu, "Quantum spin hall effect in two-dimensional transition metal dichalcogenides," *Nature Nanotechnology*, vol. 9, no. 10, pp. 765–769, 2014.

[245] M. Bacon, S. J. Bradley, and T. Nann, "Graphene quantum dots," *Particle & Particle Systems Characterization*, vol. 31, no. 4, pp. 415–428, 2014.

[246] A. D. Güçlü, P. Potasz, M. Korkusinski, P. Hawrylak, *et al.*, *Graphene quantum dots*,Springer, 2014.

[247] X. T. Zheng, A. Ananthanarayanan, K. Q. Luo, and P. Chen, "Glowing graphene quantum dots and carbon dots: properties, syntheses, and biological applications," *small*, vol. 11, no. 14, pp. 1620–1636, 2015.

[248] W. Chen, G. Lv, W. Hu, D. Li, S. Chen, and Z. Dai, "Synthesis and applications of graphene quantum dots: a review," *Nanotechnology Reviews*, vol. 7, no. 2, pp. 157–185, 2018.

[249] P. Tian, L. Tang, K. Teng, and S. Lau, "Graphene quantum dots from chemistry to applications," *Materials today chemistry*, vol. 10, pp. 221–258, 2018.

[250] Y. Yan, J. Gong, J. Chen, Z. Zeng, W. Huang, K. Pu, J. Liu, and P. Chen, "Recent advances on graphene quantum dots: from chemistry and physics to applications," *Advanced materials*, vol. 31, no. 21, p. 1808283, 2019.

[251] M. Li, T. Chen, J. J. Gooding, and J. Liu, "Review of carbon and graphene quantum dots for sensing," *ACS sensors*, vol. 4, no. 7, pp. 1732–1748, 2019.

[252] Y. Tan, C. Liu, Y. Chen, W. Wang, C. Lu, and M. Yang, "Graphene oxide: An emerging material for biosensing," *Sensors and Actuators B: Chemical*, vol. 178, pp. 631–640, 2013.

[253] Y. Liu, D. Yu, C. Zeng, J. Miao, and Z. Dai, "A high-performance biosensor based on graphene nanosheets for detection of carcinoembryonic antigen," *Biosensors and Bioelectronics*, vol. 64, pp. 408–414, 2015.

[254] D. Shahdeo, A. Roberts, A. Tiwari, V. K. Singh, R. Chauhan, B. P. Malhotra, S. B. Singh, and R. Verma, "Graphene-based biosensor for detection of biotin with high sensitivity and specificity," *Biosensors and Bioelectronics*, vol. 168, p. 112535, 2020.

[255] R. Nandee, M. A. Chowdhury, M. A. Kowser, S. K. Nondy, N. Hossain, M. Rasadujjaman, A. Al Mostazi, M. B. Molla, S. Barua, M. M. Rana, *et al.*, "Bandgap formation in graphene doped with bn, tio2, al2o3 and zno by sintering process," *Results in Chemistry*, vol. 6, p. 101229, 2023.

[256] S. Günes, H. Neugebauer, and N. S. Sariciftci, "Conjugated polymer-based organic solar cells," *Chemical Reviews*, vol. 107, no. 4, pp. 1324–1338, 2007.

[257] K. S. Novoselov, A. K. Geim, S. V. Morozov, D. Jiang, Y. Zhang, S. V. Dubonos, I. V. Grigorieva, and A. A. Firsov, "Electric field effect in atomically thin carbon films," *Science*, vol. 306, no. 5696, pp. 666–669, 2004.

[258] F. Bonaccorso, Z. Sun, T. Hasan, and A. C. Ferrari, "Graphene photonics and optoelectronics," *Nature Photonics*, vol. 4, no. 9, pp. 611–622, 2010.

[259] S.-I. Na, S.-S. Kim, J. Jo, and D.-Y. Kim, "Efficient and flexible ito-free organic solar cells using highly conductive polymer anodes," *Advanced Materials*, vol. 20, no. 21, pp. 4061–4067, 2008.

[260] H.-F. Pang, J. Xu, G. Fang, and S. Wang, "Applications of graphene in electrochemical sensors and biosensors," *TrAC Trends in Analytical Chemistry*, vol. 30, no. 10, pp. 1406–1415, 2011.

[261] X. Li, Y. Zhu, W. Cai, M. Borysiak, B. Han, D. Chen, R. D. Piner, L. Colombo, and R. S. Ruoff, "Transfer of large-area graphene films for high-performance transparent conductive electrodes," *Nano Letters*, vol. 9, no. 12, pp. 4359–4363, 2009.

[262] K. S. Kim, Y. Zhao, H. R. Jang, S. Y. Lee, J. S. Kim, K. S. Kim, J.-H. Ahn, B. H. Kim, B. H. Hong, *et al.*, "Large-area synthesis of high-quality and uniform graphene films on copper foils," *Nature*, vol. 457, no. 7230, pp. 706–710, 2009.

[263] Y. Wang, X. Chen, Y. Zhong, F. Zhu, and K. P. Loh, "Large area, continuous, few-layered graphene as anodes in organic photovoltaic devices," *Applied Physics Letters*, vol. 95, no. 6, 2009.

[264] Z. Wu, Z. Chen, X. Du, J. M. Logan, J. Sippel, M. Nikolou, K. Kamaras, J. R. Reynolds, D. B. Tanner, A. F. Hebard, and A. G. Rinzler, "Transparent, conductive carbon nanotube films," *Science*, vol. 305, no. 5688, pp. 1273–1276, 2004.

[265] S. Bae, H. Kim, Y. Lee, X. Xu, J.-S. Park, Y. Zheng, J. Balakrishnan, T. Lei, H. R. Kim, Y. I. Song, Y.-J. Kim, K. S. Kim, B. Ozyilmaz, J.-H. Ahn, B. H. Hong, and S. Iijima, "Roll-to-roll production of 30-inch graphene films for transparent electrodes," *Nature Nanotechnology*, vol. 5, no. 8, pp. 574–578, 2010.

[266] N. Hill, W. Milne, S. Silva, and G. Amaratunga, "Field emission from carbon nanotubes," *Journal of Applied Physics*, vol. 84, no. 6, pp. 3121–3127, 1998.

[267] A. Reina, X. Jia, J. Ho, D. Nezich, H. S. Son, V. Bulovic, M. S. Dresselhaus, and J. Kong, "Large area, few-layer graphene films on arbitrary substrates by chemical vapor deposition," *Nano Letters*, vol. 9, no. 1, pp. 30–35, 2009.

[268] K. S. Kim, Y. Zhao, H. R. Jang, S. Y. Lee, J. S. Kim, K. S. Kim, J.-H. Ahn, B. H. Kim, B. H. Hong, *et al.*, "Large-area synthesis of high-quality and uniform graphene films on copper foils," *Nature*, vol. 457, no. 7230, pp. 706–710, 2009.

[269] J. Park, L. Yang, Y.-W. Son, M. L. Cohen, and S. G. Louie, "Graphene field-effect transistors with tunable bandgap," *Nature Physics*, vol. 4, no. 3, pp. 213–217, 2008.

[270] Y. Gao, H.-L. Yip, S. K. Hau, K. M. O'Malley, N. C. Cho, H. Chen, and A. K.-Y. Jen, "Anode modification of inverted polymer solar cells using graphene oxide," *Applied Physics Letters*, vol. 97, no. 20, 2010.

[271] X. Li, L. Colombo, and R. S. Ruoff, "Graphene growth and transfer: A review," *Nano Today*, vol. 10, no. 4, pp. 415–432, 2012.

[272] C. Gómez-Navarro, J. Meyer, R. Sundaram, A. Chuvilin, S. Kurasch, M. Burghard, K. Kern, and U. Kaiser, "Graphene-based materials for energy storage in lithium batteries," *Nano Letters*, vol. 10, no. 4, pp. 1144–1148, 2010.

[273] H. A. Becerril, J. Mao, Z. Liu, R. M. Stoltenberg, Z. Bao, and Y. Chen, "Evaluation of solution-processed reduced graphene oxide films as transparent conductors," *ACS Nano*, vol. 2, no. 3, pp. 463–470, 2008.

[274] C. Mattevi, G. Eda, S. Agnoli, S. Miller, K. A. Mkhoyan, O. Celik, D. Mastrogiovanni, G. Granozzi, E. Garfunkel, and M. Chhowalla, "Evolution of electrical, chemical, and structural properties of transparent and conducting chemically derived graphene thin films," *Advanced Functional Materials*, vol. 19, no. 16, pp. 2577–2583, 2009.

[275] Y. S. Yun and H.-J. Jin, "Transparent and conductive films based on graphene and silver nanowires hybrid structure," *Synthetic Metals*, vol. 161, no. 21-22, pp. 2466–2469, 2011.

[276] I. Khrapach, F. Withers, T. H. Bointon, D. K. Polyushkin, W. L. Barnes, S. Russo, and M. F. Craciun, "Novel highly conductive and transparent graphene-based conductors," *Advanced Materials*, vol. 24, no. 21, pp. 2844–2849, 2012.

[277] J. B. Bult, R. Crisp, C. L. Perkins, and J. L. Blackburn, "Role of dopants in long-range charge carrier transport for p-type and n-type graphene transparent conducting thin films," *ACS nano*, vol. 7, no. 8, pp. 7251–7261, 2013.

[278] V. Georgakilas, M. Otyepka, A. B. Bourlinos, V. Chandra, N. Kim, K. C. Kemp, P. Hobza, R. Zboril, and K. S. Kim, "Functionalization of graphene: covalent and

non-covalent approaches, derivatives and applications," *Chemical Reviews*, vol. 112, no. 11, pp. 6156–6214, 2012.

[279] D. R. Dreyer, S. Park, C. W. Bielawski, and R. S. Ruoff, "The chemistry of graphene oxide," *Chemical Society Reviews*, vol. 39, no. 1, pp. 228–240, 2010.

[280] S. Z. Butler, S. M. Hollen, L. Cao, Y. Cui, J. A. Gupta, H. R. Gutiérrez, T. F. Heinz, S. S. Hong, J. Huang, A. F. Ismach, E. Johnston-Halperin, M. Kuno, V. V. Plashnitsa, R. D. Robinson, R. S. Ruoff, S. Salahuddin, J. Shan, L. Shi, M. G. Spencer, H. Terrones, W. Windl, and J. E. Goldberger, "Progress, challenges, and opportunities in two-dimensional materials beyond graphene," *ACS Nano*, vol. 7, no. 4, pp. 2898–2926, 2013.

[281] M. Kaltenbrunner, M. S. White, E. D. Głowacki, T. Sekitani, T. Someya, N. S. Sariciftci, and S. Bauer, "Ultrathin and lightweight organic solar cells with high flexibility," *Nature Communications*, vol. 3, p. 770, 2012.

[282] A. Cataldo, A. Cannavó, C. Lodato, A. Pecora, D. Antonino, G. Marrocco, A. Ascoli, and S. Milici, "Stretchable and flexible electronics using liquid metals and graphene: a review," *Micromachines*, vol. 7, no. 10, p. 168, 2016.

[283] F. Schwierz, "Graphene transistors," *Nature Nanotechnology*, vol. 5, no. 7, pp. 487–496, 2010.

[284] X. Li, C. W. Magnuson, A. Venugopal, R. M. Tromp, J. B. Hannon, E. M. Vogel, L. Colombo, and R. S. Ruoff, "Chemically derived, ultrasmooth graphene nanoribbon semiconductors," *Science*, vol. 327, no. 5966, pp. 662–662, 2010.

[285] S. H. Kim, J.-W. Nah, J. Jo, D. Shahrjerdi, L. Colombo, Z. Yao, E. Tutuc, and S. K. Banerjee, "Work-function engineering of graphene electrodes by self-assembled monolayers for high-performance organic field-effect transistors," *ACS Nano*, vol. 4, no. 10, pp. 5131–5136, 2010.

[286] Y. Xu, H. Bai, G. Lu, C. Li, and G. Shi, "Tuning the electronic structure of graphene by surface modification," *ACS Nano*, vol. 7, no. 5, pp. 4042–4049, 2013.

[287] Z. Cheng, Q. Zhou, C. Wang, Q. Li, Y. Wang, and Y. Fang, "Interface engineering in graphene devices with high-k gate dielectrics," *Nano Letters*, vol. 14, no. 1, pp. 507–512, 2014.

[288] A. J. Heeger, "Semiconducting and metallic polymers: the fourth generation of polymeric materials," *Chemical Society Reviews*, vol. 43, no. 2, pp. 435–446, 2014.

[289] K.-J. Kim, J. Y. Park, S.-J. Cho, J.-H. Lee, W. Yoon, J.-H. Kim, J. W. Park, and J.-Y. Kim, "Chemical vapor deposition-grown graphene: the thinnest solid lubricant," *ACS Nano*, vol. 9, no. 8, pp. 8601–8610, 2015.

[290] L. Jiang, C. Qin, H. Lin, L. Li, B. Wang, X. Zhang, T. Yu, and Q. Bao, "Chemical doping of graphene for high-performance transparent electrodes," *Carbon*, vol. 82, pp. 31–39, 2015.

[291] Q. Li, Q. Zhang, Y. K. Yap, R. F. Klie, X. Wang, Q. Huo, and H. Zhang, "Large-area graphene single crystals grown by low-pressure chemical vapor deposition of methane on copper," *Journal of Materials Chemistry C*, vol. 4, no. 4, pp. 658–665, 2016.

[292] Y. Liu, X. Dong, and P. Chen, "Patterned graphene structures for flexible electronics," *Advanced Materials*, vol. 30, no. 4, p. 1705551, 2018.

[293] X. Xu, A. Tang, Y. Liu, J. Yuan, Y. Chen, Z. Xie, W. Ma, and E. Zhou, "Ternary organic solar cells based on a small molecule acceptor with a complementary absorption spectrum," *Advanced Energy Materials*, vol. 9, no. 8, p. 1803581, 2019.

[294] J. Wang and X. Zhan, "Nonfullerene acceptor: The rise of organic solar cells to 18% efficiency and beyond," *Advanced Energy Materials*, vol. 10, no. 25, p. 2000858, 2020.

[295] C. Li, L. Zhan, Z. Wang, Y. Yang, S. Li, Y. Chen, J. Min, H. Zhu, C. Zhu, X. Xu, *et al.*, "Tandem organic solar cells with 20.6enabled by reduced voltage losses," *Nature*, vol. 598, pp. 444–450, 2021.

[296] T. Liu, Z. Luo, Y. Zhou, H. Sun, X. Xu, F. Zhang, H. Zhu, and G. Li, "Stability of organic solar cells: challenges and strategies," *Materials Today*, vol. 36, pp. 63–88, 2020.

[297] C. Li, J. Min, B. Zhao, L. Zhan, C. Zhu, X. Xu, L. Yu, F. Zhang, H. Zhu, and G. Li, "Hydrophobic passivation enables high-performance organic solar cells with exceptional moisture stability," *Nature Communications*, vol. 11, no. 1, pp. 1–9, 2020.

[298] X. Liu, X. Zhang, X. Xu, and G. Li, "Interface engineering for high-performance organic solar cells," *Advanced Materials*, vol. 33, no. 34, p. 2007804, 2021.

[299] Y. Wang, K. Zhao, J. Liu, H. Zhang, and W. Li, "Dft study of electronic and optical properties of non-fullerene acceptors for organic solar cells," *Journal of Molecular Modeling*, vol. 28, no. 5, pp. 1–10, 2022.

[300] Q. Van Le, J.-Y. Choi, and S. Y. Kim, "Recent advances in the application of two-dimensional materials as charge transport layers in organic and perovskite solar cells," *FlatChem*, vol. 2, pp. 54–66, 2017.

[301] Y. Liu, J. Zhao, Z. Li, C. Mu, W. Ma, H. Hu, H. Ade, H. Yan, and Y. Li, "Interface engineering in solution-processed organic photovoltaics: Concepts, recent progress and challenges," *Advanced Energy Materials*, vol. 6, no. 7, p. 1502104, 2016.

[302] F. Zhang, H. Zhu, J. Lv, X. Xu, and G. Li, "Interfacial engineering for highly efficient and stable planar p–i–n perovskite solar cells," *Advanced Energy Materials*, vol. 7, no. 1, p. 1601204, 2017.

[303] W. Chen, Z. Xu, Y. Li, and X. Gong, "Zno interface modification for high efficiency polymer solar cells," *Advanced Functional Materials*, vol. 22, no. 10, pp. 2027–2031, 2012.

[304] B. Lim, J. Lee, Y. S. Park, K. H. Lee, and J.-J. Kim, "Solution-processed zno thin film for efficient polymer solar cells," *ACS Applied Materials & Interfaces*, vol. 2, no. 3, pp. 616–620, 2010.

[305] J. M. Park and D. H. Choi, "The role of bathocuproine in organic solar cells as an exciton and electron blocking layer," *Journal of Materials Chemistry*, vol. 22, no. 36, pp. 18988–18994, 2012.

[306] E. Wang, W. Mammo, and M. R. Andersson, "Highly efficient inverted polymer solar cells with an electron transport layer of poly[(9,9-bis(3 -(n,n-dimethylamino)propyl)-2,7-fluorene)-alt-2,7-(9,9-dioctylfluorene)]," *Journal of Materials Chemistry A*, vol. 1, no. 14, pp. 3586–3592, 2013.

[307] Y. Liang, Z. Liu, X. Xu, and E. Wang, "New indene–c60 bisadducts as acceptors for high-performance polymer solar cells," *Advanced Materials*, vol. 26, no. 28, pp. 4691–4697, 2014.

[308] Q. Zheng, J. W. Jung, J. Li, X. Wan, and Y. Kim, "A review on graphene-based materials in the field of organic photovoltaics," *Energy Environmental Science*, vol. 9, no. 2, pp. 347–373, 2016.

[309] W. Huang, Z.-G. Wang, J. Kang, W. Wang, and R. Peng, "Ternary organic solar cells: a promising strategy to simultaneously enhance power conversion efficiency and stability," *Journal of Materials Chemistry A*, vol. 6, no. 39, pp. 19074–19083, 2018.

[310] T. Liu, X. Li, X. Xu, F. Zhang, H. Zhu, and G. Li, "Graphene and graphene oxide as novel materials for interfacial engineering in organic photovoltaic devices," *Journal of Materials Chemistry A*, vol. 7, no. 34, pp. 19500–19517, 2019.

[311] N. T. Ho, T. V. Tam, H. N. Tien, S.-J. Jang, T. K. Nguyen, W. M. Choi, S. Cho, and Y. S. Kim, "Solution-processed transparent intermediate layer for organic tandem solar cell using nitrogen-doped graphene quantum dots," *Journal of Nanoscience and Nanotechnology*, vol. 17, no. 8, pp. 5686–5692, 2017.

[312] L. M. Malard, M. A. Pimenta, G. Dresselhaus, and M. S. Dresselhaus, "Electronic properties of graphene: A perspective from scanning tunneling microscopy and magnetotransport," *Physical Review B*, vol. 82, no. 12, p. 125403, 2010.

[313] Z. Liu, J. T. Robinson, X. Sun, and H. Dai, "Graphene-based materials: an overview of their synthesis, properties, and applications," *Chemical Society Reviews*, vol. 39, no. 7, p. 228–240, 2010.

[314] A. Iwan and A. Chuchmała, "Perspectives of applied graphene: Polymer solar cells," *Progress in Polymer Science*, vol. 37, no. 12, pp. 1805–1828, 2012.

[315] Z. Pan, H. Gu, M.-T. Wu, Y. Li, and Y. Chen, "Graphene-based functional materials for organic solar cells," *Optical Materials Express*, vol. 2, no. 6, pp. 814–824, 2012.

[316] Y. Sun and G. Shi, "Graphene/polymer composites for energy applications," *Journal of Polymer Science Part B: Polymer Physics*, vol. 51, no. 4, pp. 231–253, 2013.

[317] B. M. Itapu and A. H. Jayatissa, "A review in graphene/polymer composites," *Chem. Sci. Int. J*, vol. 23, no. 1, 2018.

[318] N. Mustapha, Z. Fekkai, and A. Alkaoud, "Enhanced efficiency of organic solar cells based on (meh-ppv) with graphene and quantum dots," *Optik*, vol. 127, no. 5, pp. 2755–2760, 2016.

[319] J. Wu, Y. Lu, S. Feng, Z. Wu, S. Lin, Z. Hao, T. Yao, X. Li, H. Zhu, and S. Lin, "The interaction between quantum dots and graphene: the applications in graphene-based solar cells and photodetectors," *Advanced Functional Materials*, vol. 28, no. 50, p. 1804712, 2018.

[320] M. Burgelman, P. Nollet, and S. Degrave, *SCAPS 1D Solar Cell Capacitance Simulator Manual*. Department of Electronics and Information Systems (ELIS), University of Gent, 2000.

[321] M. T. Dang, L. Hirsch, and G. Wantz, "P3ht: Pcbm, best seller in polymer photovoltaic research," 2011.

[322] Y.-J. Jeon, J.-M. Yun, D.-Y. Kim, S.-I. Na, and S.-S. Kim, "High-performance polymer solar cells with moderately reduced graphene oxide as an efficient hole transporting layer," *Solar Energy Materials and Solar Cells*, vol. 105, pp. 96–102, 2012.

[323] B. Y. Kadem, M. Al-Hashimi, A. S. Hasan, R. G. Kadhim, Y. Rahaq, and A. K. Hassan, "The effects of the pedot: Pss acidity on the performance and stability of p3ht: Pcbm-based oscs," *Journal of Materials Science: Materials in Electronics*, vol. 29, no. 22, pp. 19287–19295, 2018.

[324] D. Tiwari, S. K. Dwivedi, P. Dipak, and T. Chandel, "Pedot: Pss: rgo nanocomposite as a hole transport layer (htls) for p3ht: Pcbm based organic solar cells," in *AIP Conference Proceedings*, vol. 1953, p. 100065, AIP Publishing LLC, 2018.

[325] X. Liu, H. Kim, and L. J. Guo, "Optimization of thermally reduced graphene oxide for an efficient hole transport layer in polymer solar cells," *Organic Electronics*, vol. 14, no. 2, pp. 591–598, 2013.

[326] M. Hilal and J. I. Han, "Significant improvement in the photovoltaic stability of bulk heterojunction organic solar cells by the molecular level interaction of graphene oxide with a pedot: Pss composite hole transport layer," *Solar Energy*, vol. 167, pp. 24–34, 2018.

[327] T. A. Amollo, G. T. Mola, and V. O. Nyamori, "High-performance organic solar cells utilizing graphene oxide in the active and hole transport layers," *Solar Energy*, vol. 171, pp. 83–91, 2018.

[328] I. C. Ghosekar and G. C. Patil, "Review on performance analysis of p3ht: Pcbm-based bulk heterojunction organic solar cells," *Semiconductor Science and Technology*, vol. 36, no. 4, p. 045005, 2021.

[329] L. Hrostea, M. Girtan, R. Mallet, and L. Leontie, "Optical and morphological properties of p3ht and p3ht: Pcbm thin films used in photovoltaic applications," in *IOP Conference Series: Materials Science and Engineering*, vol. 374, p. 012015, IOP Publishing, 2018.

[330] D.-Y. Lee, S.-I. Na, and S.-S. Kim, "Graphene oxide/pedot: Pss composite hole transport layer for efficient and stable planar heterojunction perovskite solar cells," *Nanoscale*, vol. 8, no. 3, pp. 1513–1522, 2016.

[331] H. S. Dehsari, E. K. Shalamzari, J. N. Gavgani, F. A. Taromi, and S. Ghanbary, "Efficient preparation of ultralarge graphene oxide using a pedot: Pss/go composite layer as hole transport layer in polymer-based optoelectronic devices," *Rsc Advances*, vol. 4, no. 98, pp. 55067–55076, 2014.

[332] X. Huang, H. Guo, J. Yang, K. Wang, X. Niu, and X. Liu, "Moderately reduced graphene oxide/pedot: Pss as hole transport layer to fabricate efficient perovskite hybrid solar cells," *Organic Electronics*, vol. 39, pp. 288–295, 2016.

[333] Y. Zhou, S. Mei, J. Feng, D. Sun, F. Mei, J. Xu, and X. Cao, "Effects of pedot: Pss: Go composite hole transport layer on the luminescence of perovskite light-emitting diodes," *RSC advances*, vol. 10, no. 44, pp. 26381–26387, 2020.

[334] S. Rafique, S. M. Abdullah, M. M. Shahid, M. O. Ansari, and K. Sulaiman, "Significantly improved photovoltaic performance in polymer bulk heterojunction solar cells with graphene oxide/pedot: Pss double decked hole transport layer," *Scientific reports*, vol. 7, no. 1, p. 39555, 2017.

[335] S. Rafique, N. A. Roslan, S. M. Abdullah, L. Li, A. Supangat, A. Jilani, and M. Iwamoto, "Uv-ozone treated graphene oxide/pedot: Pss bilayer as a novel hole transport layer in highly efficient and stable organic solar cells," *Organic Electronics*, vol. 66, pp. 32–42, 2019.

[336] J. H. Lee, S. Yoon, M. S. Ko, N. Lee, I. Hwang, and M. J. Lee, "Improved performance of organic photovoltaic devices by doping f4tcnq onto solution-processed graphene as a hole transport layer," *Organic Electronics*, vol. 30, pp. 302–311, 2016.

[337] A. Daraie and A. Fattah, "Performance improvement of perovskite heterojunction solar cell using graphene," *Optical Materials*, vol. 109, p. 110254, 2020.

[338] S. B. Hacène and T. Benouaz, "Influence of charge carrier mobility and surface recombination velocity on the characteristics of p3ht: Pcbm organic solar cells," *physica status solidi (a)*, vol. 211, no. 4, pp. 862–868, 2014.

[339] B. M. Omer, "Influence of characteristic energy of the valence band tail on performance of p3ht: Pcbm bulk-heterojunction solar cell: Amps-1d simulation study," in *2014 IEEE 40th Photovoltaic Specialist Conference (PVSC)*, pp. 1770–1775, IEEE, 2014.

[340] E. K. Chiew, M. Yahaya, and A. P. Othman, "Electrical characterization of p3ht/pcbm bulk heterojunction organic solar cell," *International Journal of Computational Materials Science and Engineering*, vol. 1, no. 01, p. 1250004, 2012.

[341] K. Nithya and K. Sudheer, "Device modelling and optimization studies on novel itic-oe based non-fullerene organic solar cell with diverse hole and electron transport layers," *Optical Materials*, vol. 123, p. 111912, 2022.

[342] S.-F. Wang, L.-Y. Chen, Y. Zhang, J.-M. Zhang, V. Ji, and K.-W. Xu, "First-principle study on structural and electronic properties of pristine and adsorbed lif nanotubes," *The Journal of Physical Chemistry C*, vol. 116, no. 2, pp. 1650–1657, 2012.

[343] G. A. Nowsherwan, A. Samad, M. A. Iqbal, T. Mushtaq, A. Hussain, M. Malik, S. Haider, P. V. Pham, and J. R. Choi, "Performance analysis and optimization of a pbdb-t: Itic based organic solar cell using graphene oxide as the hole transport layer," *Nanomaterials*, vol. 12, no. 10, p. 1767, 2022.

[344] W. Abdelaziz, A. Zekry, A. Shaker, and M. Abouelatta *Sol. Energy*, vol. 211, 2020.

[345] M. Q. Khokhar, S. Q. Hussain, D. P. Pham, S. Lee, H. Park, Y. Kim, E.-C. Cho, and J. Yi *Energies*, vol. 13, no. 7, 2020.

[346] H. Niu, C. Fang, X. Wei, H. Wang, L. Wan, Y. Li, X. Mao, J. Xu, and R. Zhou, "Magnetron sputtered zno electron transporting layers for high performance perovskite solar cells," *Dalton Transactions*, vol. 50, no. 19, pp. 6477–6487, 2021.

[347] V. Srikant and D. R. Clarke, "On the optical band gap of zinc oxide," *Journal of applied physics*, vol. 83, no. 10, pp. 5447–5451, 1998.

[348] M. Q. Khokhar, S. Q. Hussain, D. P. Pham, M. Alzaid, A. Razaq, I. Sultana, Y. Kim, Y. H. Cho, E.-C. Cho, and J. Yi *Mater. Sci. Semicond. Process.*, vol. 134, 2021.

[349] B. Hussain, A. Aslam, T. M. Khan, M. Creighton, and B. Zohuri, "Electron affinity and bandgap optimization of zinc oxide for improved performance of zno/si heterojunction solar cell using pc1d simulations," *Electronics*, vol. 8, no. 2, p. 238, 2019.

[350] A. Umar, P. Tiwari, Sadanand, V. Srivastava, P. Lohia, D. K. Dwivedi, H. Qasem, S. Akbar, H. Algadi, and S. Baskoutas, "Modeling and simulation of tin sulfide (sns)-based solar cell using zno as transparent conductive oxide (tco) and nio as hole transport layer (htl)," *Micromachines*, vol. 13, no. 12, p. 2073, 2022.

[351] M. V. Jacob *Sci. Technol. Adv. Mater.*, vol. **6**, no. 8, 2005.

[352] M. Dadashbeik, D. Fathi, and M. Eskandari *Sol. Energy*, vol. **207**, 2020.

[353] M. Singh, R. Kumar, V. Singh, *et al. Mater. Res. Express*, vol. **6**, no. 11, 2019.

[354] A. S. Khune, V. Padghan, R. Bongane, V. N. Narwade, B. Dole, N. N. Ingle, M.-L. Tsai, T. Hianik, and M. D. Shirsat, "Highly selective chemiresistive so2 sensor based on a reduced graphene oxide/porphyrin (rgo/tapp) composite," *Journal of Electronic Materials*, vol. 52, no. 12, pp. 8108–8123, 2023.

[355] L. Sygellou, G. Paterakis, C. Galiotis, and D. Tasis, "Work function tuning of reduced graphene oxide thin films," *The Journal of Physical Chemistry C*, vol. 120, no. 1, pp. 281–290, 2016.

[356] C. Yuwen, B. Liu, L. Zhang, S. Guo, and J. Peng, "Synthesis high-qulity graphene oxide and temperature-dependent dielectric properties of reduced graphene oxide," *Materials Research Express*, vol. 6, no. 9, p. 0950b4, 2019.

[357] Y. Wang, Y. Chen, S. D. Lacey, L. Xu, H. Xie, T. Li, V. A. Danner, and L. Hu, "Reduced graphene oxide film with record-high conductivity and mobility," *Materials Today*, vol. 21, no. 2, pp. 186–192, 2018.

[358] K. Chakraborty, R. Mandal, and D. K. Mandal, "A comprehensive study on utility of carrier transportation layer for efficiency improvement of organic photovoltaic devices using GPVDM modeling," *International Journal of Engineering and Applied Physics*, vol. 2, no. 3, pp. 515–523, 2022.

[359] N. Singh, K. C. Dubey, S. K. Singh, A. Srivastava, N. Wadhwani, and R. K. Shukla, "Optimizing parameters for enhanced conversion efficiency in P3HT/PCBM-based solar cells through computer simulations," *Next Research*, vol. 2, no. 3, Art. 100601, 2025.

[360] G. Li, V. Shrotriya, Y. Yao, J. Huang, and Y. Yang, "High-efficiency solution processable polymer photovoltaic cells by self-organization of polymer blends," *Nature Materials*, vol. 4, no. 11, pp. 864–868, 2005.

[361] J. Y. Kim, S. H. Kim, H. H. Lee, K. Lee, W. Ma, X. Gong, and A. J. Heeger, "New architecture for high-efficiency polymer photovoltaic cells using solution-based titanium oxide as an optical spacer," *Advanced Materials*, vol. 18, no. 5, pp. 572–576, 2006.

[362] S. H. Park, A. Roy, S. Beaupré, S. Cho, N. Coates, J. S. Moon, D. Moses, M. Leclerc, K. Lee, and A. J. Heeger, "Bulk heterojunction solar cells with internal quantum efficiency approaching 100%," *Nature Photonics*, vol. 3, no. 5, pp. 297–302, 2009.

[363] K. Chakraborty, R. Mandal, and D. K. Mandal, "A comprehensive study on utility of carrier transportation layer for efficiency improvement of organic photovoltaic devices using GPVDM modeling," *International Journal of Engineering and Applied Physics*, vol. 2, no. 3, pp. 515–523, 2022.

[364] N. Singh, K. C. Dubey, S. K. Singh, A. Srivastava, N. Wadhwani, and R. K. Shukla, "Optimizing parameters for enhanced conversion efficiency in P3HT/PCBM-based solar cells through computer simulations," *Next Research*, vol. 2, no. 3, Art. 100601, 2025.

[365] B. Balraj, M. Raja, T. G. Vignesh Prabhu, M. Balaji, J. Chandrasekaran, S. K. Nagarajan, M. Bharathi, S. Lee, and C. Sivakumar, "A critical review on decade progress and future prospects of P3HT:PCBM bulk heterojunction solar cells," *Solar Energy*, vol. 297, Art. 113574, 2025.

[366] L. Ye, W. Zhao, S. Li, S. Mukherjee, J. H. Carpenter, O. Awartani, X. Jiao, J. Zhao, H. Ade, and H. Yan, "A comparison study of non-fullerene and fullerene acceptor based organic solar cells: The influence of molecular packing on device performance," *Advanced Energy Materials*, vol. 8, no. 8, p. 1702657, 2018.

[367] C. An, J. Wang, K. Gao, M. Zhang, Y. Kan, X. Hao, F. Zhang, T. P. Russell, and Y. Cao, "Energy loss: The key parameter determining the efficiency of organic solar cells," *Advanced Energy Materials*, vol. 8, no. 3, p. 1701721, 2018.

[368] J. Zhang, B. Kan, A. J. Pearson, A. J. Parnell, J. F. Cooper, X.-K. Liu, P. J. Conaghan, T. R. Hopper, Y. Wu, X. Wan, *et al.*, "Efficient non-fullerene organic solar cells employing sequentially deposited donor–acceptor layers," *Journal of Materials Chemistry A*, vol. 6, no. 37, pp. 18225–18233, 2018.

[369] Y. Kan, F. Zhang, F. Liu, X. Wan, C. Li, Y. Zhang, J. Huang, and Y. Chen, "Fine-tuning the phase separation of nonfullerene organic solar cells by introducing a third component for an enhanced fill factor," *Advanced Energy Materials*, vol. 8, no. 32, p. 1801830, 2018.

[370] Y. Kan, X. Wan, F. Liu, X. Ke, Y. Wang, Y. Wang, Y. Zhang, J. Huang, and Y. Chen, "Chlorinated nonfullerene acceptor enables over 13organic solar cells with low energy loss," *Advanced Materials*, vol. 30, no. 47, p. 1801894, 2018.

[371] A. Siddiqui, B. Suman, and S. Singh, "An indacenodithiophene core moiety for organic solar cells," *Materials Chemistry Frontiers*, vol. 5, no. 21, p. 7724–7736, 2021.

[372] M. Singh, R. Kumar, V. Singh, *et al.*, "Investigating the impact of layer properties on the performance of p-graphene/ch3nh3pbi3/n-csi solar cell using numerical modelling," *Superlattices and Microstructures*, vol. 140, p. 106468, 2020.

[373] F. Zheng, W.-L. Xu, H.-D. Jin, X.-T. Hao, and K. P. Ghiggino, "Charge transfer from poly (3-hexylthiophene) to graphene oxide and reduced graphene oxide," *RSC advances*, vol. 5, no. 109, pp. 89515–89520, 2015.

[374] P. Molaei and I. Kazeminezhad, "One-step in situ synthesis of antimony sulfide/reduced graphene oxide composite as an absorber layer with enhanced photocurrent performances for solar cells," *Journal of Nanoparticle Research*, vol. 21, no. 3, p. 54, 2019.

[375] M. Nawaz, E. Marstein, and A. Holt, "Design analysis of zno/csi heterojunction solar cell," in *2010 35th IEEE Photovoltaic Specialists Conference*, pp. 002213–002218,IEEE, 2010.

[376] E. Widianto, Y. Firdaus, L. M. Pranoto, K. Triyana, I. Santoso, N. M. Nursam, *et al.*, "Device modeling of two-dimensional hole transport materials for boosting the performance of non-fullerene acceptor bulk heterojunction organic solar cells," *Optical Materials*, vol. 132, p. 112771, 2022.

[377] S. Ghosh, S. Yasmin, J. Ferdous, and B. B. Saha, "Numerical analysis of a czts solar cell with mos2 as a buffer layer and graphene as a transparent conducting oxide layer for enhanced cell performance," *Micromachines*, vol. 13, no. 8, p. 1249, 2022.

[378] W. Abdelaziz, A. Shaker, M. Abouelatta, and A. Zekry, "Possible efficiency boosting of non-fullerene acceptor solar cell using device simulation," *Optical Materials*, vol. 91, pp. 239–245, 2019.

[379] J. Cameron and P. J. Skabara, "The damaging effects of the acidity in pedot: Pss on semiconductor device performance and solutions based on non-acidic alternatives," *Materials Horizons*, vol. 7, no. 7, pp. 1759–1772, 2020.

[380] Z.-H. Hao, Z.-Y. Hu, J.-J. Zhang, Q.-Y. Hao, and Y. Zhao, "Influence of doped pedot: Pss on performance of polymer solar cells," *Acta Phys Sin*, vol. 60, p. 117106, 2011.

[381] N. Fauji, Kardiman, V. Efelina, M. F. Hakim, F. C. Suci, R. Hanifi, I. N. Gusniar, and E. Widianto, "Optimization of non-fullerene organic photovoltaics through interface engineering with graphene oxide: A numerical simulation," *Journal of Electronic Materials*, vol. 53, no. 3, pp. 1539–1550, 2024.

[382] D. Davis and K. Sudheer, "Numerical investigation on efficiency enhancement and influence of electrical parameters on pbdbt-intic bulk heterojunction organic solar cells," in *AIP Conference Proceedings*, vol. 3196, p. 030002, AIP Publishing LLC, 2024.

[383] S. S. Alarfaji, D. Fatima, B. Ali, A. Sattar, R. Hussain, R. Hussain, and K. Ayub, "Computational investigation of near-infrared-absorbing indeno [1, 2-b] indole analogues as acceptors in organic photovoltaic devices," *ACS omega*, vol. 8, no. 1, pp. 1430–1442, 2022.

[384] B. Hu, W. Zhang, J. Wu, Z. Pang, S. Zhao, Z. Lu, and Y. Huang, "An easily available near-infrared absorbing non-fullerene photovoltaic electron acceptor with indeno [1, 2-b] indole as the central core," *Dyes and Pigments*, vol. 166, pp. 467–472, 2019.

[385] D. Davis and K. Sudheer, "Numerical investigation of pbdb-t: Intic based bulk heterojunction organic solar cell with graphene derivatives as htl," *Results in Surfaces and Interfaces*, vol. 19, p. 100474, 2025.

[386] M. M. Shabat and G. Zoppi, "Simulation on the perovskite-based solar cell with graphene derivative," in *2023 8th International Engineering Conference on Renewable Energy & Sustainability (ieCRES)*, pp. 1–8, IEEE, 2023.

[387] R. Bhujel, S. Rai, U. Deka, G. Sarkar, J. Biswas, and B. P. Swain, "Bandgap engineering of pedot: Pss/rgo a hole transport layer for sinws hybrid solar cells," *Bulletin of Materials Science*, vol. 44, no. 2, p. 72, 2021.

[388] V. Hebbar, R. Bhajantri, and J. Naik, "Influence of graphene nanoparticles on optical and dielectric properties of pva-pedot: Pss blend composite," in *AIP Conference Proceedings*, AIP Publishing LLC,vol. 1832, p. 050046, 2017.

[389] Y.-J. Lin, J.-J. Zeng, and C.-L. Tsai, "Enhancement of the carrier mobility of poly (3, 4-ethylenedioxythiophene) doped with poly (4-styrenesulfonate) by incorporating reduced graphene oxide," *Applied Physics Letters*, vol. 101, no. 5, 2012.

[390] B. Zhao, X. Huang, S. Chung, M. Zhang, Y. Zhong, A. Liang, Z. Zhao, C. Zhu, J. Zhao, S. Kim, *et al.*, "Hole-selective-molecule doping improves the layer thickness tolerance of pedot: Pss for efficient organic solar cells," *eScience*, vol. 5, no. 1, p. 100305, 2025.

[391] J. Ouyang, ""secondary doping" methods to significantly enhance the conductivity of pedot:pss for its application as transparent electrode of optoelectronic devices," *Displays*, vol. 34, no. 5, pp. 423–436, 2013.

[392] M. Javadi, A. Mazaheri, H. Torbatiyan, and Y. Abdi, "Mechanism of charge transport in hybrid organic-inorganic pedot:pss/silicon heterojunctions," *Phys. Rev. Appl.*, vol. 12, no. 8, 2019.

[393] Z. Xu, J. P. Madalaimuthu, J. B. Slowik, R. Meitzner, A. Anand, S. Alam, H. Corte, S. Stumpf, U. S. Schubert, and H. Hoppe, "Compatible solution-processed interface materials for improved efficiency of polymer solar cells," *Advanced Materials Interfaces*, vol. 10, no. 19, p. 2201740, 2023.

[394] S. Chen, *Dielectric constant measurement of P3HT, polystyrene, and polyethylene*. PhD thesis, Faculty of Science and Engineering, 2017.

[395] J. Yao, B. Qiu, Z.-G. Zhang, L. Xue, R. Wang, C. Zhang, S. Chen, Q. Zhou, C. Sun, C. Yang, *et al.*, "Cathode engineering with perylene-diimide interlayer enabling over 17% efficiency single-junction organic solar cells," *Nature communications*, vol. 11, no. 1, p. 2726, 2020.

[396] F. Bonaccorso, A. Lombardo, T. Hasan, Z. Sun, L. Colombo, and A. C. Ferrari, "Production and processing of graphene and 2d crystals," *Materials today*, vol. 15, no. 12, pp. 564–589, 2012.

[397] X. Hu and F. Meng, "Structure and gap opening of graphene with fe doped bridged trivacancy," *Computational Materials Science*, vol. 117, pp. 65–70, 2016.

[398] R. Quhe, J. Zheng, G. Luo, Q. Liu, R. Qin, J. Zhou, D. Yu, S. Nagase, W.-N. Mei, Z. Gao, *et al.*, "Tunable and sizable band gap of single-layer graphene sandwiched between hexagonal boron nitride," *NPG Asia Materials*, vol. 4, no. 2, p. -e6, 2012.

[399] R. Quhe, J. Ma, Z. Zeng, K. Tang, J. Zheng, Y. Wang, Z. Ni, L. Wang, Z. Gao, J. Shi, *et al.*, "Tunable band gap in few-layer graphene by surface adsorption," *Scientific Reports*, vol. 3, no. 1, p. 1794, 2013.

[400] M. Velasco-Soto, S. Pérez-García, J. Alvarez-Quintana, Y. Cao, L. Nyborg, and L. Licea-Jiménez, "Selective band gap manipulation of graphene oxide by its reduction with mild reagents," *Carbon*, vol. 93, pp. 967–973, 2015.

[401] Z. Fakharan, L. Naji, K. Madanipour, and A. Dabirian, "Complex electrochemical study of reduced graphene oxide/pt produced by nd: Yag pulsed laser reduction as photo-anode in polymer solar cells," *Journal of Electroanalytical Chemistry*, vol. 880, p. 114927, 2021.

[402] S. Angizi, P. R. Selvaganapathy, and P. Kruse, "Graphene-silicon schottky devices for operation in aqueous environments: Device performance and sensing application," *Carbon*, vol. 194, pp. 140–153, 2022.

[403] A. Samuels, "Organic and metallo-organic doping of graphene,"

[404] Y. Gao, C. Wang, J. Li, and S. Guo, "Adjustment of dielectric permittivity and loss of graphene/thermoplastic polyurethane flexible foam: Towards high microwave absorbing performance," *Composites Part A: Applied Science and Manufacturing*, vol. 117, pp. 65–75, 2019.

[405] L. J. Romasanta, M. Hernández, M. A. López-Manchado, and R. Verdejo, "Functionalised graphene sheets as effective high dielectric constant fillers," *Nanoscale research letters*, vol. 6, pp. 1–6, 2011.

[406] T. Bayer, S. R. Bishop, N. H. Perry, K. Sasaki, and S. M. Lyth, "Tunable mixed ionic/electronic conductivity and permittivity of graphene oxide paper for electrochemical energy conversion," *ACS applied materials & interfaces*, vol. 8, no. 18, pp. 11466–11475, 2016.

[407] S. Gupta, P. Joshi, and J. Narayan, "Electron mobility modulation in graphene oxide by controlling carbon melt lifetime," *Carbon*, vol. 170, pp. 327–337, 2020.

[408] A. T. Smith, A. M. LaChance, S. Zeng, B. Liu, and L. Sun, "Synthesis, properties, and applications of graphene oxide/reduced graphene oxide and their nanocomposites," *Nano Materials Science*, vol. 1, no. 1, pp. 31–47, 2019.

[409] X. Liu, B. Xie, C. Duan, Z. Wang, B. Fan, K. Zhang, B. Lin, F. J. Colberts, W. Ma, R. A. Janssen, *et al.*, "A high dielectric constant non-fullerene acceptor for efficient bulk-heterojunction organic solar cells," *Journal of Materials Chemistry A*, vol. 6, no. 2, pp. 395–403, 2018.

[410] K. Sreedhar Ram, H. Mehdizadeh-Rad, D. Ompong, D. D. Y. Setsoafia, and J. Singh, "Characterising exciton generation in bulk-heterojunction organic solar cells," *Nanomaterials*, vol. 11, no. 1, p. 209, 2021.

[411] M. Mativenga, D. Geng, J. H. Chang, T. J. Tredwell, and J. Jang, "Performance of 5-nm a-igzo tfts with various channel lengths and an etch stopper manufactured by back uv exposure," *IEEE electron device letters*, vol. 33, no. 6, pp. 824–826, 2012.

[412] J. H. Seo and T.-Q. Nguyen, "Electronic properties of conjugated polyelectrolyte thin films," *Journal of the American Chemical Society*, vol. 130, no. 31, pp. 10042–10043, 2008.

[413] C.-S. Chuang, T.-C. Fung, B. G. Mullins, K. Nomura, T. Kamiya, H.-P. D. Shieh, H. Hosono, and J. Kanicki, "P-13: Photosensitivity of amorphous igzo tfts for active-matrix flat-panel displays," in *SID Symposium Digest of Technical Papers*,Wiley Online Library, vol. 39, pp. 1215–1218, 2008.

[414] H. Lee, S. Lee, Y. Kim, A. B. Siddik, M. M. Billah, J. Lee, and J. Jang, "Improvement of stability and performance of amorphous indium gallium zinc oxide thin film transistor by zinc-tin-oxide spray coating," *IEEE Electron Device Letters*, vol. 41, no. 10, pp. 1520–1523, 2020.

[415] A. Marroun, N. A. Touhami, and T.-E. El Hamadi, "Improved igzo-tft structure using high-k gate dielectric materials," in *2019 International conference on wireless technologies, embedded and intelligent systems (WITS)*, IEEE, pp. 1–4, 2019.

[416] H. Su, W. M. Tang, and P. T. Lai, "Effect of dopant redistribution in gate electrode on surface plasmon resonance in ingazno thin-film transistors," *AIP Advances*, vol. 12, no. 11, 2022.

[417] N. Walsh, *Passivation of amorphous indium-gallium-zinc oxide (IGZO) thin-film transistors*. Rochester Institute of Technology, 2015.

[418] M. Hina, K. Kamran, S. Bashir, J. Ahmed, D. Ameer, M. Jahanzaib, and S. Mubarik, "Extra ordinary properties of graphene," in *Graphene: Fabrication, Properties and Applications*, pp. 21–52, 2023.

[419] D. Sahu, H. Sutar, P. Senapati, R. Murmu, and D. Roy, "Graphene, graphene-derivatives and composites: fundamentals, synthesis approaches to applications," *Journal of Composites Science*, vol. 5, no. 7, p. 181, 2021.

[420] L. Velasco Davoise, A. M. Díez-Pascual, and R. Peña Capilla, "Application of graphene-related materials in organic solar cells," *Materials*, vol. 15, no. 3, p. 1171, 2022.

[421] X. Wan, G. Long, L. Huang, and Y. Chen, "Graphene–a promising material for organic photovoltaic cells," *Advanced Materials*, vol. 23, no. 45, pp. 5342–5358, 2011.

[422] J. Zhao, P. Ji, Y. Li, R. Li, K. Zhang, H. Tian, K. Yu, B. Bian, L. Hao, X. Xiao, *et al.*, "Ultrahigh-mobility semiconducting epitaxial graphene on silicon carbide," *Nature*, vol. 625, no. 7993, pp. 60–65, 2024.

[423] R. J. Lewis, "An evaluation of phosgene exposure health effects," *Toxicology and Industrial Health*, vol. 16, no. 6, pp. 265–281, 2000.

[424] G. Li, R. Zhu, and Y. Yang, "Interface engineering of organic electronics: Principles, applications, and perspectives," *Advanced Materials*, vol. 27, no. 31, pp. 5166–5196, 2015.

[425] D. Akinwande, C. J. Brennan, J. S. Bunch, P. Egberts, J. R. Felts, H. Gao, R. Huang, J. Kim, T. Li, Y. Li, *et al.*, "Progress, challenges, and opportunities in two-dimensional materials beyond graphene," *Extreme Mechanics Letters*, vol. 13, pp. 42–77, 2017.

[426] F. Azri, A. Meftah, N. Sengouga, and A. Meftah *Sol. energy*, vol. **181**, 2019.

[427] J. Wang, Z. Xie, and J. T. Yeow, "State-of-the-art organic solar cells based on carbon nanotubes and graphene," *ECS Journal of Solid State Science and Technology*, vol. 9, no. 10, p. 105004, 2020.

[428] E. Muchuweni, B. S. Martincigh, and V. O. Nyamori, "Organic solar cells: Current perspectives on graphene-based materials for electrodes, electron acceptors and interfacial layers," *International Journal of Energy Research*, vol. 45, no. 5, pp. 6518–6549, 2021.

[429] P. Kumar, "Carbon nanotubes and graphene in photovoltaics," in *Emerging Applications of Carbon Nanotubes and Graphene*, pp. 131–159, CRC Press, 2023.

[430] A. Kumar, S. Singh, D. Varshney, S. Sreenivasa, and N. Beemkumar, "Graphene-based materials for solar cells: Recent advances, performance optimization, and future prospects," *physica status solidi (a)*, p. 2500144,2025.

List of Publications

Notable International Journal Publications

1. Davis, D., & Sudheer, K. S. (2024). Numerical investigation of graphene derivatives as HTL in PBDB-T:NCBDT bulk heterojunction organic solar cell. *Results in Optics*, **17**, 100748. https://doi.org/10.1016/j.rio.2024.100748.

2. Davis, D., & Sudheer, K. S. (2025). Numerical investigation of PBDB-T:INTIC based bulk heterojunction organic solar cell with graphene derivatives as HTL. *Results in Surfaces and Interfaces*, **19**, 100474. https://doi.org/10.1016/j.rsurf.2025.100474.

3. Davis, D., & Sudheer, K. S. (2025). Graphene oxide and reduced graphene oxide as hole transport layers for improved efficiency in fullerene based bulk heterojunction organic solar cells: A numerical simulation study. *East European Journal of Physics*, **3**(1), 217–232. https://doi.org/10.26565/2312-4334-2025-1-23.

Conference proceedings

1. Davis, D., Shamna, M. S., Nithya, K. S., & Sudheer, K. S. (2022). Graphene as a hole transport layer for enhanced performance of P3HT:PCBM bulk heterojunction organic solar cell: A numerical simulation study. In *Proceedings of IOP Conference Series: Materials Science and Engineering* (Vol. 1248, No. 1, p. 012011). IOP Publishing. https://doi.org/10.1088/1757-899X/1248/1/012011.

2. Davis, D., & Sudheer, K. S. (2024). Numerical investigation on efficiency enhancement and influence of electrical parameters on PBDBT-INTIC bulk heterojunction organic solar cells. In *Proceedings of AIP Conference Proceedings* (Vol. 3196, No. 1, p. 030002). AIP Publishing LLC. https://doi.org/10.1063/5.0203492.

Conference Presentations

1. Davis, D. (2021, March). "Simulation study of PEDOT:PSS/PTB7:$PC_{70}BM$ organic solar cell". Poster presented at *Annual Physics Symposium 2020–2021*, St. Teresa's College (Autonomous), Cochin, Kerala, India.

2. Davis, D. (2022, February). "Graphene as a hole transport layer for enhanced performance in P3HT:PCBM bulk heterojunction organic solar cell: A numerical simulation study". Oral presentation at *CNCER*, University of Rajasthan, Jaipur, India.

3. Davis, D. (2022, April). "Numerical simulation study on P3HT:PCBM based bulk heterojunction organic solar cell with graphene as a hole transport layer". Poster presented at *ICEPV 2022*, Ankara, Turkey.

4. Davis, D. (2022, December). "Modelling and simulation study of PTB7:PCBM organic solar cell with graphene as the hole transport layer using SCAPS-1D". Oral presentation at *National Conference on Recent Trends in Material Science and Technology (NCMST-2022)*, IIST, Trivandrum, Kerala, India.

5. Davis, D. (2024, January). "Numerical investigation on efficiency enhancement and influence of varying bandgap, thickness and electron affinity of PBDB-T:INTIC NFA based bulk heterojunction organic solar cells". Oral presentation at *International Conference on Advances in Novel Materials: Towards Sustainable Future (ICAN-2024)*, Ranchi, Jharkhand, India.

6. Davis, D. (2024, November). "Numerical simulation study on fullerene derivatives based bulk heterojunction organic solar cells". Oral presentation at *SCIENTIA-2 Multidisciplinary International Conference and Research Expo 2024*, Christ College (Autonomous), Irinjalakuda, Kerala, India.

7. Davis, D. (2025, February). "Electrical simulation of organic solar cells using GPVDM software". Oral presentation at *Two-Day Multidisciplinary National Conference and Research Expo 2024*, Christ College (Autonomous), Irinjalakuda, Kerala, India.